Thesis Consent Form

This thesis may be consulted for the purposes of research or private study provided that due acknowledgement is made where appropriate and that permission is obtained before any material from the thesis is published. Students who do not wish their work to be available for reasons such as pending patents, copyright agreements, or future publication should seek advice from the Graduate Centre as to restricted use or embargo.

Author of thesis	Diana PAJUELO APARICIO
Title of thesis	The Role of a High Altitude Active Geothermal System in Mobilizing Metals through a Miocene ore deposit at Jaraña hot springs, Puno-Peru
Name of degree	Master of Science (MSc) in Earth Sciences
Date Submitted	14th March 2019

Print Format (Tick the boxes that apply)

☑ I agree that the University of Auckland Library may make a copy of this thesis available for the collection of another library on request from that library.

☑ I agree to this thesis being copied for supply to any person in accordance with the provisions of Section 56 of the Copyright Act 1994.

Digital Format - PhD theses

I certify that a digital copy of my thesis deposited with the University is the same as the final print version of my thesis. Except in the circumstances set out below, no emendation of content has occurred and I recognise that minor variations in formatting may occur as a result of the conversion to digital format.

Access to my thesis may be limited for a period of time specified by me at the time of deposit. I understand that if my thesis is available online for public access it can be used for criticism, review, news reporting, research and private study.

Digital Format - Masters theses

I certify that a digital copy of my thesis deposited with the University is the same as the final print version of my thesis. Except in the circumstances set out below, no emendation of content has occurred and I recognise that minor variations in formatting may occur as a result of the conversion to digital format.

Access will normally only be available to authenticated members of the University of Auckland, but I may choose to allow public access under special circumstances. I understand that if my thesis is available online for public access it can be used for criticism, review, news reporting, research and private study.

Copyright (Digital Format Theses) (Tick **ONE box only**)

☑ I confirm that my thesis does not contain material for which the copyright belongs to a third party, ***(or)*** that the amounts copied fall within the limits permitted under the Copyright Act 1994.

☑ I confirm that for all third party copyright material in my thesis, I have obtained written permission to use the material and attach copies of each permission, ***(or)*** I have removed the material from the digital copy of the thesis, fully referenced the deleted materials and, where possible, provided links to electronic sources of the material.

Signature

Date 05th September 2019

Comments on access conditions

Faculty Student Centre / Graduate Centre only: Digital copy deposited ☐ Signature Date

THE ROLE OF A HIGH ALTITUDE ACTIVE GEOTHERMAL SYSTEM IN MOBILIZING METALS THROUGH A MIOCENE ORE DEPOSIT AT JARAÑA HOT SPRINGS; PUNO-PERU

---

by

Diana Pajuelo Aparicio

A thesis submitted in fulfilment of the requirements for the degree of
Master of Science in Earth Science

The University of Auckland

2019

ABSTRACT

The Jaraña hot springs deposits are located in a highland (>4570 meters above sea level), on a backarc environment in southern Peru, 90 km east of the present day volcanic front of the Central Andes. Regional faults control the exhumation of Cretaceous to Miocene rocks (sandstone, limestone, conglomerates and volcanic rocks) and Miocene copper ore bodies. Thirty-two samples from subrecent deposits, recent deposits and host rocks were collected from northern, central and eastern zones at Jaraña hot springs. The field and sample description defined the emergence of hot springs as thermal pools that generate run-off channels; the description also recognized varieties of nodular and botryoidal morphologies for recent deposits and network fabrics for subrecent deposits. The laboratory analysis employed x-ray diffraction, optical microscopy and cathodoluminescence methods for two purposes: identify two varieties of gypsum crystals for recent subaerial deposits, and, differentiate two types of subaqueous deposits based on iron and manganese oxide minerals that are related to calcite minerals and carbonate composition in their matrix. Moreover, laboratory analysis further allowed to recognize jarosite minerals on subrecent deposits and to determine the quartz mineral composition for surrounding host rocks. Additionally, hot spring deposits contain variable abundance of diatoms. By using 4-acid digestion and laser ablation ICP-MS, the chemical analysis also allowed to determine high concentrations of Ca, Fe and Si (above 1 Wt %) in hot spring deposits, and the perfect correlation between Ca and Sr for subrecent and recent deposits. Consequently, four types of deposits were identified at Jaraña hot springs: jarosite, gypsum, iron-travertine and manganese-travertine. The hot spring deposits are highly influenced by microbial communities, which concentrate, precipitate minerals, and, later induce mineral crystallization. Likewise, iron-travertine deposits proved to be good hosts for base metals (Cu, Pb, Zn) and As, as well as, for the formation of oxide and sulfide mineral crystals. The host rocks are source for providing Ca, Fe, Si, Cu and As. Thermal waters carries these elements, whereas, hot springs are hosts for metal concentration. Finally, the present study is the first ever undertaken in Peru concerning the Jaraña hot spring deposits. Its findings, together with the variety of mineral and chemical composition of the deposits, will definitely enrich the environmental, geothermal and mining research in that region.

DEDICATION

Dedicated to the memory of my grandmother, Zoraira Revilla.

ACKNOWLEDGEMENTS

First of all thanks to God for permitting me to live this wonderful experience.

I would like to thank my supervisor Dr. Michael Rowe very much, who gave me the opportunity to come to New Zealand. Thanks to belief in this project, for your commitment during all the process of this thesis including the laboratory analysis, your support during the writing process and infinite patience. Also, I would like to thank to Dr. Kathleen Campbell for shearing all her knowledge and passion for hot spring deposits and suggestions for the writing procedure. Thanks for giving me a general overview during the field trips and for introducing me with other students under your supervision during social meetings, which were useful to change ideas.

My thanks to Liz Stone and Chris Naughton, for the proofreading, on the result and discussion sections on this thesis. Also, thanks to Ana Maria from ELE. And to Alonso Robles. I would like to thank to PRONABEC (Scholarship loans from Peru), specifically to Milagros Céspedes for provide the necessary conditions to reach one of my dreams and the completion of this project. My thanks to LatinoAustralia group, specifically to Gladys Galvez, for the support and guidance during the application process to the University. Special thanks to Ana Cecilia Anastacio, for joining without hesitation to the adventure of collecting samples, in a remote area, and her emotional support during my stay in Auckland. Thanks to the driver Mr. Elmer Castillo who also helped us in the safe driving to our destination, helped in sampling collection and provided good music. Special thanks to my cousin Waldo and her wife, for receiving us in their house at Arequipa and providing us with food and tools before embarking to the trip.

My appreciation also goes to the technical assistance of Louise Cotterall, Neville Hudson, Natalia Abrego, Andrés Arcila, Stuart Morrow and Catherine Hobbis, thanks for the advices and good environment for working. Special thanks to Jie Wu who gave me instructions for a better development during the lab analysis and the images edition. Thanks to Sian Camp, Yuli Yaled and Michaela Dobson for the exchange of knowledge during the lab analysis.

My special thanks and considerations to Dr. Julie Rowland, Dr. Bridget Lynne and Irene Wallis for their amazing knowledge in geothermal research and industry, their experience gave me a different overview about this area.

I would like to thank to those people who made a good environment for me during my stay at Auckland. Special thanks to Meghna Sengupta, for giving me all the emotional support during the year, the long talks with the amazing view to Rangitoto Island, her positive spirit and amazing friendship were important factors for me. My thanks to David Wackrow who with his great sense of humour always make me laugh even in my worst days. Also, I would like to thank to Carlos Carvajal, Danielle Johnson, Joao Albuquerque, Daniel Dela Torre, Roselyn Naidu, Khanh, Paul Oluwunmi, Ben, Daniela, Juan, Bill Howie and Lyndsay Blue, for the good times talking in the kitchen area and to encourage me to don’t give up over the course of this year (See you around!). To my MSc office mates Ella, Noah, Elliot, Kayo and Esther, who bring me comfortable and enjoyable moments inside the master office.

To the Tertiary Catholic Group who received me as a family and to Study Auckland Group who gave me the opportunity to know more about the New Zealand culture. Also to my flatmates Vale Villa and Andrea Guzman who orientated me in my first days in the city; to Peggy Hazou, Neha Yadav and Giang Nguyen (Moon) who always knocked my door for bringing me nice surprises, laughs, talks and hugs.

I would like to thank the support of my relatives and friends who from one way or another always encouraged me during this year. Special thanks to my cousins Américo Aparicio and Mónica Pallardel, who despite the distance were always concern about me.

Finally, but the most important for me, infinity thanks to my mum Vicky, who always supported all my crazy dreams, and despite the distance and time differences between countries, she always was there able to send a lovely text or funny pictures. Your strength and your courage were always my inspiration to follow.

TABLE OF CONTENTS

LIST OF FIGURES

CHAPTER 1: INTRODUCTION

CHAPTER 2: METHODOLOGY

CHAPTER 3: FIELD AND SAMPLE DESCRIPTION

CHAPTER 4: METHODOLOGY

CHAPTER 5: DISCUSSION

APPENDICES

APPENDIX I: MINERALOGY

LIST OF TABLES

CHAPTER 1: INTRODUCTION

CHAPTER 2: METHODOLOGY

CHAPTER 5: DISCUSSION

APPENDICES

APPENDIX II: CHEMICAL DATA

APPENDIX III: LIST OF CODE NUMBER

1 INTRODUCTION

Hot springs deposits are surface manifestations part of a complex cycle of an active geothermal system. Hot spring deposits precipitate from thermal fluids, which could carry saturated elements. The variation of element concentrations and pH conditions on thermal fluids are important features to generate sinter (silica-based), travertine (carbonate-based), iron-rich (Fe (III) based), jarosite (Fe (III) and acid pH based), gypsum (Ca and SO_4 based) or manganese (manganese based) deposits. Moreover, biotic factors can induce the element oxidation and concentration from thermal waters to produce mineral nucleation and later crystallization (Chafetz, Akdim, Julia, & Reid, 1998; Ferris, 2000; Renaut & Jones, 2000; Takashima, Okumura, Nishida, Koike, & Kano, 2011). However, abiotic factors could also have similar effects on mineral crystallization (Ferris, 2000; Handley, Campbell, Mountain, & Browne, 2005; Merinero, Hernández, & Martínez, 2010). Likewise, hot spring deposits can incorporate precious (Au, Ag) and base metals (Cu, Pb, Zn) into their structure and generate minerals with grainy morphologies (Kanellopoulos, Mitropoulos, Valsami-Jones, & Voudouris, 2017; Merinero et al., 2010; Uchida, Yokoyama, Watanabe, & Izawa, 2001). The incorporation and crystallization processes are related with high As, Fe and/or Sr concentrations. Sinter and travertine deposits, on the other hand, mainly contain economically important metals as registered on different cases from Devonian to recent times (Rice et al., 1995; Smith, 2008).

The aim of the study is to understand the presence of economically important metals in hot spring deposits inside the dynamism of an active geothermal system at high altitudes. To address this issue, my research focuses on the Jaraña hot spring deposits in southern Peru. Hot springs in Peru are distributed along the Central Andes mountains at high altitudes (>3000 m), over exhumed ore mineral outcrops (Acosta et al., 2010; Vargas & Cruz, 2010). The Jaraña hot springs are located 90 km east of the active volcanic arc, and their spatial location is above Cu-Fe ore bodies hosted on Miocene volcanic rocks (Valdivieso, 2015). Hot springs on Jaraña emerge with neutral pH, mesothermal temperatures (55-74ºC) and alkali-chloride and acid-sulfate water composition (Cruz, 2016). Thermal waters precipitate colourful terraces (red, orange, yellow and black) around vents with a thin (from milimetric to centimetric thickness) white coverture. Also, hot spring deposits at Jaraña contain halite, gypsum and minerals enriched in metals (Ag, Cu, Pb, As, Sn and Fe) (Pajuelo, Condorhuaman, Cruz, & Zegarra, 2016).

1.1 Background

1.1.1 The dynamism of a Geothermal System

Hot springs and precipitates are controlled by the dynamism of a geothermal system. A geothermal system mainly depends on three aspects; meteoric water filtering, physical and chemical changes of fluids, and the ascent of fluids to the surface. Meteoric water filters from surface and circulates along faults, fractures and permeable rocks (Figure 1.1). The heated water is influenced by factors such as geothermal gradient (25-30ºC km^{-1}), deep faults (Faulds, Hinz, Kreemer, & Coolbaugh, 2012), or active magma systems (International Geothermal Association, 2014). Meteoric water is usually heated at mid-crustal to upper crustal depths leading a large-scale hydrothermal convection (Rowland & Sibson, 2004); also, heated meteoric fluids are mixed with minor proportions of hydrothermal fluids derived from magmatic or metamorphic water (Renaut & Jones, 2011).

The ascendant heated fluids typically evolve to become saline and chloride-rich, forming geothermal reservoirs in permeable horizons economically important for geothermal energy (International Geothermal Association, 2014; Renaut & Jones, 2011). The ascendant geothermal fluids react with rocks (hydrothermal alteration) according to their temperature and leach elements from country rocks. The chemical characteristic of heated fluids (chloride fluids) acts as a favourable solvent to leach and transport metals at high temperatures and pressures (Giggenbach, 1980). Moreover, fluids enriched in metals will precipitate minerals along the transit to the surface where the environmental conditions change. Proximal to the surface, the fluids will rise convectively and will boil and produce liquid and steam phases below the surface (Renaut & Jones, 2011). The interception between the groundwater table and topography ultimately results in discharging thermal water at the surface, enriched in soluble elements. Thermal waters are rich carriers of anions from the deep geothermal system circulation and its saturation produces the precipitation around spring vents, also known as hot spring deposits. Hot springs (liquid phase) are formed when hot fluids and shallow groundwater mix at the surface, during discharge, modifying fluid composition, temperature, and pH. Additionally, thermal waters are classified according to the main anion component e.g. alkali-chloride water (Cl-), sulfate water (SO-4) and bicarbonate (HCO-3) (Nicholson, 1993).

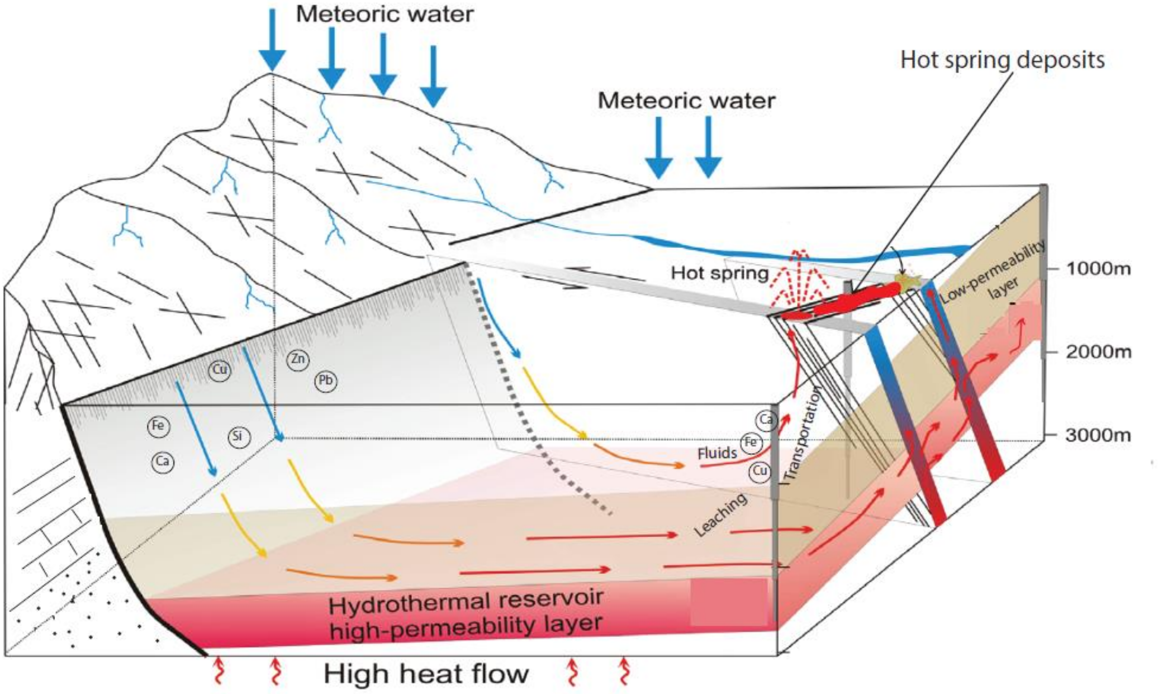

Figure 1.1 Active geothermal model system (Modified from (Moeck, 2014)*).*

1.1.2 Hot spring deposits

Hot springs deposits, located around vents, are part of surface manifestation of geothermal systems; groundwater oscillation can generate the extinction and activation of hot spring vents. Therefore, lithic terraces could be found around extinct hot springs, or as layers with different level position of the actual thermal water discharge. These “old precipitates” or “ancient deposits” represent a register of earlier geothermal systems (Hamilton, Campbell, Rowland, & Browne, 2017; Lynne, 2012). Moreover, the hydrodynamic variation generates subaerial or subaqueous deposition, which produces varieties of morphologies on hot spring deposit surfaces (Campbell et al., 2015). Hot spring deposits contain a record of physical characteristics such as colour variation caused by a predominant element concentration, and layering thickness with various forms (parallel or wave) caused by flow rate conditions. Furthermore, hot spring deposits can entomb flora (leaf) and fauna (insects) during a rapid precipitation (Guido & Campbell, 2018; Lynne, 2012; Lynne & Campbell, 2003); also, the saturation of other minerals (e.g., Fe-Mn oxides, metal sulfides, zeolites, and clays) and pH variation (e.g., acidic, neutral) on thermal waters generates other types of hot spring deposits (Riding & Awramik, 2000).

The complex anion saturation defines two main types of hot spring deposits: “sinter” (silica based) and “travertine” ($CaCO_3$ based). If mixed together, sinter and travertine deposits could generate sinter-carbonate deposits (Campbell, Rodgers, Brotheridge, & Browne, 2002; Smith, 2008). Under oxidations conditions, thermal waters, when saturated on Fe (II), generate the precipitation of Fe (III) (oxide-hydroxides or ferrihydrite) on surface. The precipitation of Fe (III) may be influenced by biotic or abiotic factors, generating the ”iron-rich deposits” precipitation that form red to orange coloured terraces (Parenteau, Jahnke, Farmer, & Cady, 2014). The iron-rich deposits may also be intermixed with sinter or travertine, which generate the “iron-sinter deposits” or “iron-travertine deposits”. The register of iron-rich deposits can be found at Chocolate Pots in Yellowstone, United States of America (Parenteau et al., 2014), Shionoha and Okuoku-Hachikurou hot springs, Japan (Takashima et al., 2011) and Sperchios, Greece (Kanellopoulos et al., 2017). The reduction of pH (<3) and the rise of SO_4 concentration on thermal waters produce mineralogical changes on iron-rich deposits. Thus, the hydrous ferric oxides (Fe (III)) and thermal water conditions induce the jarosite precipitation, as reported in a case at Waiotapu geothermal area, New Zealand (Jones & Renaut, 2007). On the other hand, thermal waters carrying high amounts of Ca and SO_4, induce the gypsum precipitation in hot spring terrains; the conditions are similar to those found on evaporitic environment (Warren, 2016). Gypsum deposits form a white crust on the surface deposits, and the evaporative processes induce the presence of other common evaporate salts such as halite and anhydrite (Warren, 2016). Moreover, gypsum deposits in hot spring terrains could contain a wide range of crystal habits; mainly influenced by geochemistry of fluids and microbial communities. This case has a register at Kamchatka hot springs, Russia (Tang, Ehreiser, & Li, 2014). Microorganisms have a strong influence on Fe precipitation, and also can induce the Mn precipitation from waters with almost undetectable concentrations of Mn (Chafetz et al., 1998; Mita & Maruyama, 1994; Sasaki et al., 2013). The manganese deposits in hot spring terrains precipitate under neutral pH conditions in shallow water areas, and generate black shrubs or/and banded manganese, as indicated in the Idelsane Skoura and Tinjidad hot springs, Morocco (Chafetz et al., 1998) and Sambe hot springs registers, Japan (Sasaki et al., 2013).

Additionally, hot spring deposits studies are important for economic and environmental purposes. For example, the importance on sinter deposits depends on the identification of hidden geothermal systems (Guido & Campbell, 2011, 2018; Lynne, 2012; Lynne, Campbell, Perry, Browne, & Moore, 2006) and is related to epithermal systems at depth (Hedenquist & Lowenstern, 1994). Although, travertine deposits represent a distal up flow facie of a geothermal system; travertine deposits rich in iron, they are related to an active metallogenic process with an active hydrothermal system at depth (Kanellopoulos et al., 2017). Moreover, the studies on sinter, iron-rich and jarosite deposits represent an analogous with extraterrestrial materials on Mars (Campbell et al., 2015; McHenry, Carson, Dixon, & Vickery, 2017; Scarlett, Grey, & Brand, 2012). Overall, hot spring deposits record the dynamism of a geothermal system, hydrothermal overprinting overtime, and provide information about the chemistry of fluids.

1.1.3 Biotic and abiotic factors for crystal nucleation in hot spring deposits

The hot spring deposits could derive from thermal waters with hyperthermal conditions (>75°C), which is mainly influenced by abiotic factors. Also, precipitations could derive from warm (20-40ºC) and mesothermal (40–75ºC) thermal waters, which are controlled by biotic factors (microbial influence) (Riding & Awramik, 2000). These two factors (biotic and abiotic) induce the authigenic mineral deposition and other aggregates forms. The summary of the process for crystal nucleation, influenced by biotic and abiotic factors, is presented in a flowchart (Figure 1.2) and the description is as follows:

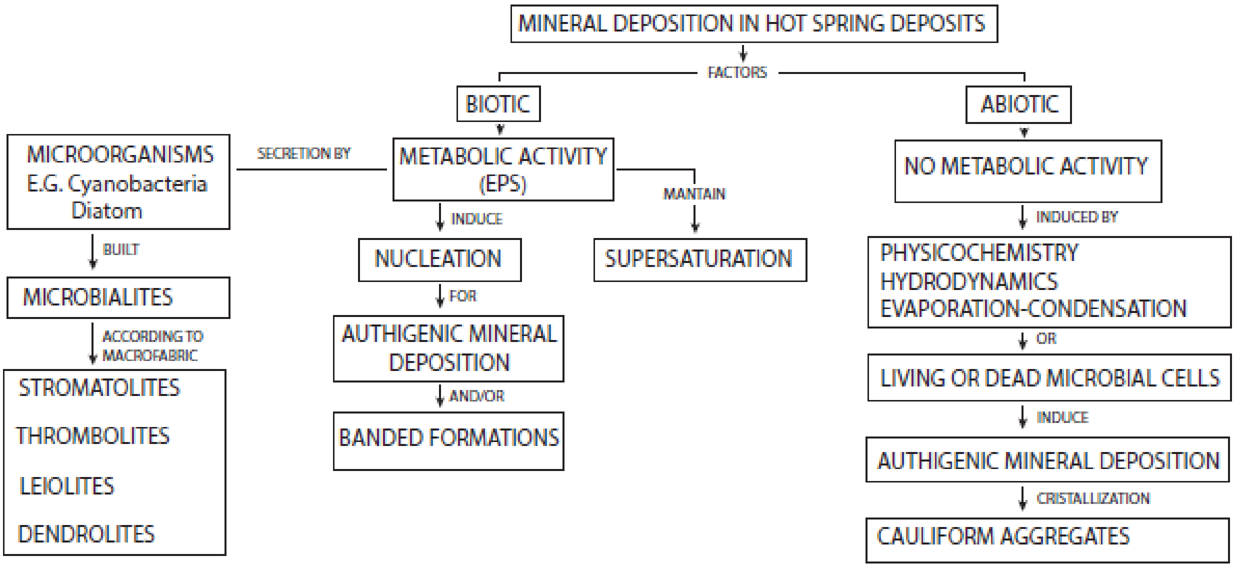

Figure 1.2 Mineral deposition flowchart influenced by biotic and abiotic factors.

Biotic factors are influenced by microbial communities, which are common in hot spring terrains. The microbes extend as a colourful covertures (e.g. green, orange) above surface manifestations as microbial mats (above aqueous surface) or biofilms (above solid surfaces) (Stolz, 2000). The affluence of microbes increases away from spring vents (Renaut & Jones, 2000). Most of the microbial communities such as cyanobacteria are thermophilic microorganisms capable of resisting extreme temperatures of more than 55ºC; however, other microorganisms such as diatoms are capable of living in hot springs terrains between 30º to 44ºC (Brock, 1978). Cyanobacteria are resistant to survive on high temperature environments with a wide range of salinity, they grow as micrometric cells building a long chain of filaments with open lumens (Jones & Renaut, 2003). On the other hand, diatoms exist in carbonate areas and take silicon from the waters where they live. These microorganisms occur as solitary cells or in colonies with regular size between 5 micrometers to 0.5 millimeters and build a cell wall made of silica (frustule) (Kale & Karthick, 2015; Winsborough, 2000). Cyanobacteria and diatoms are important microorganisms because they both produce high amounts of oxygen survive by converting light to chemical energy (photosynthesis). Moreover, cyanobacteria and diatoms have the same capability to trap and bind sediments; the result of this process generates the deposition and construction of layered mounds (authigenic accumulations) better known as "microbialites" (Alshuaibi & Khalaf, 2015; Brock, 1978; Warren, 2016; Winsborough, 2000). Microbialites generate a diversity of morphologies during their growth and the names (stromatolites, thrombolites, leiolites and dendrolites) are based into their physical characteristics. Stromatolites contain columns with sheet likes and sediments could be trapped on the layering. Column growth generates laterally-linked hemispheroids, stacked hemispheroids, laterally-linked stacked hemispheroids and spheroids (oncoids) (Figure 1.3) (Scholle & Ulmer-Scholle, 2003). Thrombolites contain a patchy clotted macro fabrics and leiolites are structureless. The thrombolite and stromatolite macro fabrics could grow together (Alshuaibi & Khalaf, 2015; Warren, 2016). Furthermore, stromatolites could also have branched type shapes as reported on carbonate terrains (Terra et al., 2010). The branched type shapes generates arborescent, arbustiform and dendriform morphologies (Figure 1.3); also, this branched type classification could be comparable with dendrolites (Warren, 2016).

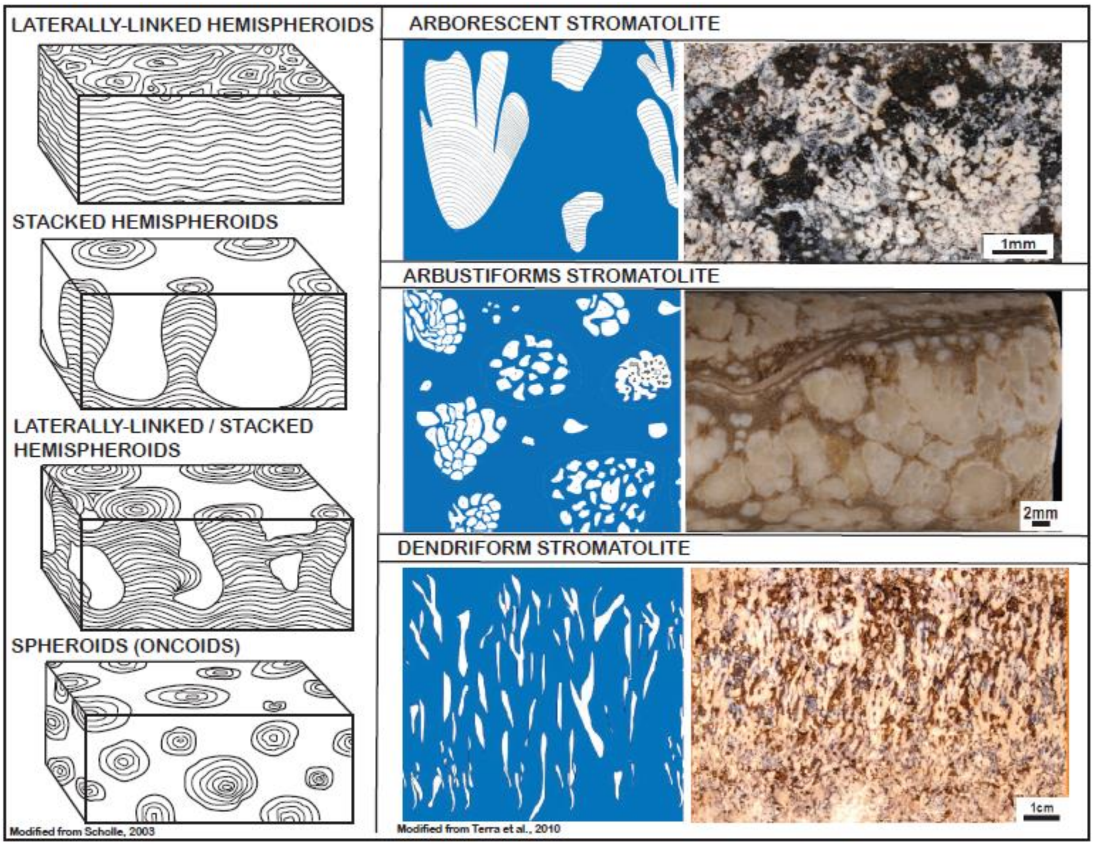

Figure 1.3 Microbial column grow forms. Stromatolite classification according to Scholle, Peter A.; Ulmer-Scholle, 2003; Terra et al., 2010*.*

The microorganisms generate metabolic activities and secrete extracellular polymeric substances (EPS). The EPS is inside microbial mats matrix, induces elements nucleation and maintains mineral saturation level (Renaut & Jones, 2000). Moreover, EPS generates oxidation and reduction process; for example, during carbonate crystallization, the acidity produced by bacteria dissolves carbonate minerals, and the empty space is filled with gypsum, this process is the result from sulfide oxidation to sulfate phase. At the same time, gypsum is attacked by sulfate-reducing bacteria (SRB) process and generates H_2S concentrations (Warren, 2016). The generation of H_2S produces a reaction with Fe and then the reaction induces an iron-banded precipitation (Takashima et al., 2011). The EPS substance produces reactive inorganic ligands (sulfide, phosphate, dissolved inorganic carbon) inducing metal precipitation and authigenic mineral deposition (Ferris, 2000). For example, Fe (III) in travertine deposits precipitates as magnetite and hematite mineral laminations influenced by iron-oxidizing bacteria (Kanellopoulos et al., 2017; Takashima et al., 2011). Overall, microorganisms generate extracellular capsules and sheets where metals (e.g. calcium, molybdenum, and zinc) are accumulated with high Fe concentrations (Ferris, 2000); this process induces authigenic sulfide crystallization as cluster of spheroids (framboid texture) induced by bacteria under reducing conditions (Merinero et al., 2010; Taylor, 2009).

On the other hand, the mineral depositions in hot spring terrains without a metabolic activity (abiotic factors) have influence of physicochemistry, hydrodynamics, and evaporation-condensation shifts (Handley et al., 2005). The living or dead microbial cells on hot spring deposits behave as a solid sorbent phase allowing the dissolution of metals and inducing crystallization as cauliform aggregates or framboid textures. These spherical shapes (cluster of spheroids) are the result of authigenetic crystallization, where shape and size are similar to bacterial cells (Ferris, 2000). Spherical shapes in sulfide minerals (pyrite, chalcopyrite, bornite and chalcocite) are common on sedimentary environments (Merinero et al., 2010). Also, metal and metalloids can crystallize as grains inside cavities of hot spring deposits. For example, Nicolau (2013) reported a Cahnite ($Ca_4B_2As_2O_{12}*4H_2O$) inside the cavities of a sinter layering matrix. Uchida et al. (2001) described small grains of pyrite and native gold inside sinter deposits matrix. Similarly, Kanellopoulus et al., (2017) identified grains of sulfide minerals such as chalcopyrite, Au-Cu-Ag alloy, As-rich pyrite, sphalerite, galena and cassiterite inside the pores of iron-rich deposits.

Therefore, biotic and abiotic factors have a strong influence to generate a stable nucleus using the supersaturated element concentration in thermal waters (Renaut & Jones, 2000). The stable nucleus continues their growing and generates crystals; the crystal habits are similar with other geological environments. The most common mineral habits founded in hot spring deposits are based on the following names and characteristics according with Dana, & Hurlbut, (1993) and have a graphic representation in figure 1.4:

a) Massive: Mineral lacking crystal face.
b) Granular: A group of minerals with approximately same size.
c) Lamellar: Finely layers as in books.
d) Bladed: Crystals or grains flattened elongate.
e) Fibrous: Group of needle-like grains or fibres.
f) Acicular: Mineral with a needle like habit.
g) Radiating: Acicular crystals radiate from a central point.
h) Dendritic: Branching pattern.
i) Banded: Parallel banding.
j) Concentric: Layers arranged in parallel positions about one or more centre.
k) Colloform: Rounded prominences surface similar to mammillary, botryoidal, globular and reniform textures.
l) Oolitic: Small, round or ovate accretionary bodies
m) Pisolitic: Oolitic aggregates but coarser in grain size.

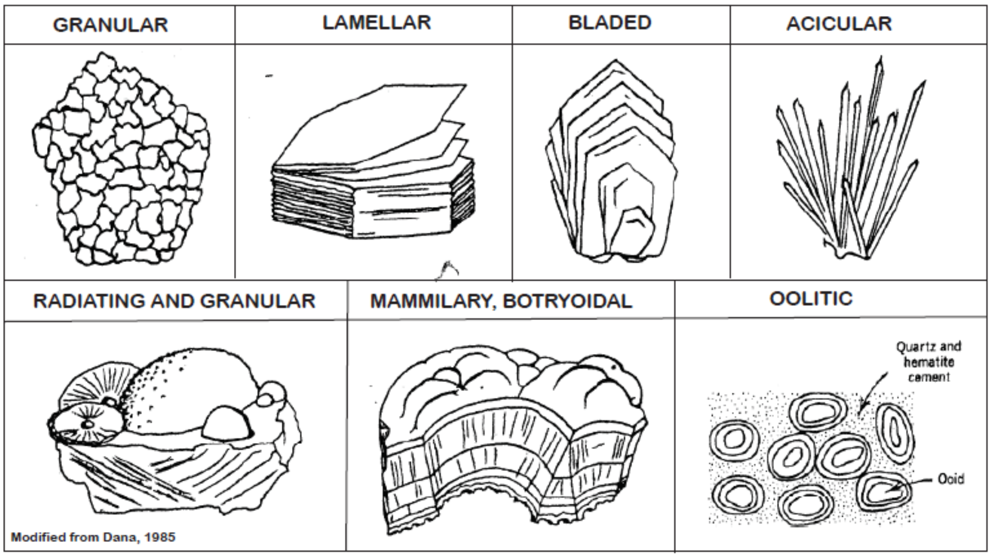

Figure 1.4 Common mineral habits and crystal aggregates by nucleation.

Other morphologies generated under abiotic conditions are comparable with the morphologies generated under sedimentary process. The oscillation of currents generates morphological changes at the time of crystallization of minerals; rounded and/or spherical components grow under water flow conditions, the common terms for these morphologies are oolites and oncolites, a brief description is as follows (Figure 1.5):

a) Oolites: The term for a single component is ooid and for a group of ooids is oolites. Ooids have concentric cortical laminations, composed of calcium carbonate and organic matter; the concentric structure could be fibrously radiated. Ooids may vary from superficial ooids (few thin coatings), collapsed ooids (with partial dissolution and internal collapse of remaining undissolved materials), composite ooids (coalescence of two or more ooids with concentric layers) to deformed ooids (reflect compaction or tectonic compression) (Scholle & Ulmer-Scholle, 2003; Terra et al., 2010). The ooids grow during coating processes over a crystal or a grain, and the group of oolites form lobules and brain textures (Terra et al., 2010).

b) Oncolites: The term for a single component is oncoid. Oncoids are organic grains formed by the accretion of cyanobacteria and usually present agglomerate grains. Oncoids shape is not spherical as ooids (Scholle & Ulmer-Scholle, 2003; Terra et al., 2010).

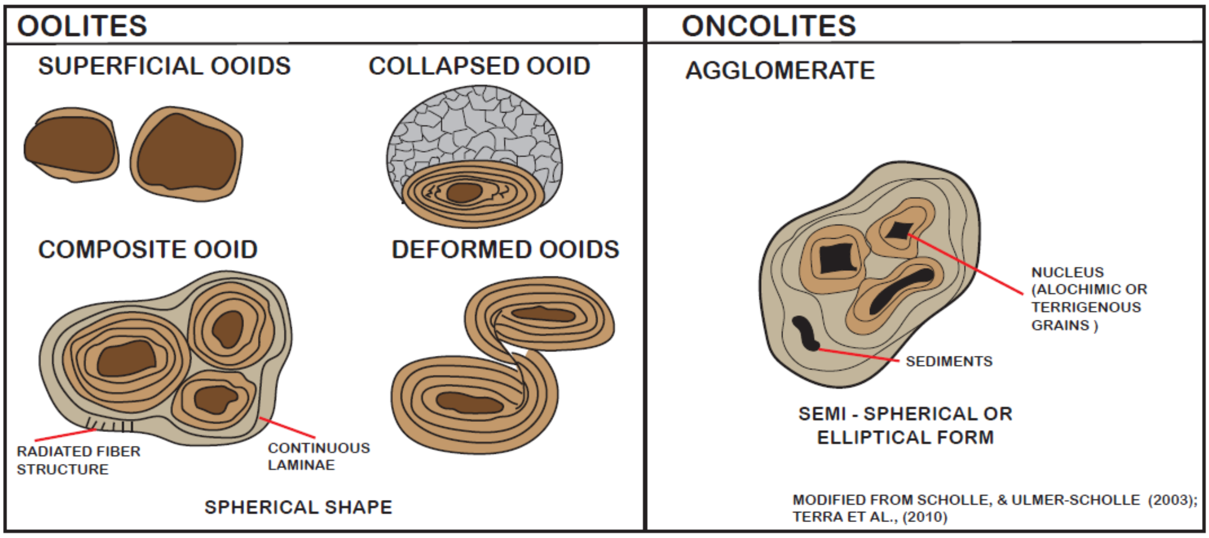

Figure 1.5 Oolites and oncolites morphologies (Modified from Sholle & Ulmer-Scholle (2003) and Terra et al. (2010)).

1.1.4 Precious and base metal concentrations in hot spring deposits

Precious (Au, Ag) and base metals (Cu, Pb, Zn) concentrations in hot springs deposits are studied around the world, mostly in sinter and travertine deposits. Two hypotheses suggest the register of precious and base metal concentration on sinter and travertine deposits from an active hydrothermal system perspective. The first hypothesis is focus on sinter deposits, it suggests that volatile elements; e.g. mercury, drag some precious metals to the surface in a vapour phase and have a later deposition during sinter precipitation (Sillitoe, 2015). The second hypothesis is focus on travertine deposits, it suggests that precious and base metals form as sulfide minerals and alloys at depth; later on, they are transferred as clastic grains into surface by hydrothermal fluids and gases. The sulfide minerals and alloys have a clastic grain shape, and are captured during a fast travertine precipitation (Kanellopoulos et al., 2017).

Precious and base metals could be incorporated as an amorphous element into hot spring deposit structure, during their first stages of precipitations (Jones & Renaut, 2003). The concentrations of these elements (Au, Ag, Cu, Pb and Zn) are generally associated with metalloids (As, Sb) and high Fe concentrations. Moreover, the Fe (III) has a relevant influence for As concentrations but it is not significant for Sb concentrations. Arsenic (As) is incorporated to sinter deposit structure during their first stages of precipitation influenced by high Fe amounts; however, As has a better compatibility with carbonates rather than silica and are concentrated in highest amounts on travertine deposits (McKenzie, Brown, Cady, & Campbell, 2001; Smith, 2008).

Cases about sinter and travertine deposits containing precious and base metals are reported around the world from Devonian to recent times (Table 1.1). The ancient sinter deposits have more documented cases related to Au and Ag compared to recent sinter deposits, but only one case at Savo Volcano (Salomon Islands) report Ag in travertine deposits. The highest concentration of Au (1.62 ppm) has a register in recent sinter deposits at Yellowstone National Park, United States of America (Fournier, Kennedy, Aoki, & Thompson, 1994). In contrast, the highest amount of Ag (10.1 ppm) has a register in ancient sinter deposits at Kohuamuri, New Zealand (Hamilton et al., 2017). On the other hand, travertine deposits register no more than 0.04 ppm of Ag concentrations at Savo volcano, Salomon Islands (Smith, 2008).

Base metals have a greater amount of Fe, As and Sr on sinter rather than travertine deposits. The highest concentrations on Cu (<10-220 ppm) and Zn (<30-410 ppm) were registered at El Tatio, Chile, with high amounts of Fe_2O_3 (0.01-18.8 Wt %) and As (420-20528 ppm) (Landrum et al., 2009; Nicolau, 2013). Also, sinter deposits could contain a high amount in Pb (8-69 ppm) with high Sr concentrations (356-6081 ppm) such as at Savo volcano, Salomon Islands (Smith, 2008).

Similarly, sinter deposits register a high concentration on base metals comparing with travertine deposits but influenced by high amounts of Sr such as at El Tatio, Chile and Atiamuri, Champagne Pool, Ohaaki Pool and Tokaanu Springs, New Zealand (Landrum et al., 2009; K. Nicholson & Parker, 1990). Travertine deposits register concentrations of Cu (3.6-14.7 ppm), Pb (0.35-10.6 ppm) and Zn (2.52-25.9 ppm) with high amounts of As (66-18300 ppm) and Fe (0.01-28.9 Wt %) such as at Northern Euboea Island and Sperchios, Greece (Kanellopoulos et al., 2017) (Table 1.1).

Table 1.1 Sinter, travertine and carbonate-silica deposits with metal and metalloid concentrations from Devonian to recent times.

Location	Age	Description	Au (ppm)	Ag (ppm)	Cu (ppm)	Pb (ppm)	Zn (ppm)	As (ppm)	Sb (ppm)	Fe (Wt%)	Fe2O3 (Wt%)	Sr (ppm)	Reference
Savo volcano (Salomon Islands)	Recent	Travertine	-	0.003-0.04	0.20-0.78	0.03-1.25	0.30-21.0	0.60-625	0.09	0.06-2.29	-	1151-3974	Smith, 2008
Savo volcano (Salomon Islands)	Recent	Mixed	0.002	-	4.19	0.13-3.00	3.60	186-287	3.00	0.10-1.43	-	1589-4206	Smith, 2008
Savo volcano (Salomon Islands)	Recent	Sinter	0.001-0.003	-	-	8.00 - 69.0	-	9.00-280	2.00 - 44.0	0.85 - 2.82	-	356-6081	Smith, 2008
Northern Euboea Island and Sperchios (Greece)	Recent	Travertine	-	-	3.60-14.7	0.35-10.6	2.52-25.9	66.0-18300	0.03-4.58	0.01-28.9	-	254-3960	Kanellopoulos et al., 2017
Atiamuri, Champagne Pool, Ohaaki Pool, Tokaanu Springs (New Zealand)	Recent	Sinter	-	-	<1.00-23.0	4.00 -18.0	<1.00-18.0	<1.00-246	-	0.14-0.71	0.11-0.55	5.00-584	Nicholson & Parker, 1990
Taupo Volcanic Zone (New Zealand)	Recent	Sinter	-	-	-	-	-	13.0-1646	157-494	-	0.08-8.85	-	Mckenzie et al., 2001
Yellowstone National Park (United States)	Recent	Sinter	0.002-1.62	<0.20-0.80	1.00-6.00	<1.00-8.00	<1.00-44.0	1.00-1120	1.20-150	0.05-1.40	0.14-4.00	-	Fournier et al., 1994
El Tatio (Chile)	Recent	Sinter	-	-	420-20528	2398-7293	10.8-68.0		-	-	-	64.8-315	Landrum et al., 2009
El Tatio (Chile)	Recent	Sinter	-	<0.50-2.40	<10.0-220	<5.00-56.0	<30.0-410	5.00->2000	0.50->200	-	0.01-18.8	-	Nicolau, 2013
Osorezan (Japan)	Holocene	Sinter	0.01-0.03	-	-	-	-	35.0-650	209-3100	-	-	-	Hayashi, 2013
Kohuamuri (New Zealand)	Miocene - Pliocene	Sinter	0.001-0.12	0.05-10.1	-	-	-	2.00-344	1.36-96.7	-	-	-	Hamilton et al., 2017
San Agustin (Argentina)	Jurassic	Sinter	0.001-0.003	<0.05-0.22	-	-	-	<0.10-78.8	0.48-3.03	-	-	-	Guido et al., 2010
La Marciana (Argentina)	Jurassic	Sinter	<0.05	0.02-0.36	5.60-8.10	3.70-7.50	2.00-4.00	4.00 - 7.00	1.10-2.70	-	-	-	Guido et al., 2002
Queensland (Australia)	Devonian-Carboniferous	Sinter	<0.01	<1.00	-	-	-	<2.00-50	4.00 - 13.0	-	-	-	Cunneen & Sillitoe, 1989
Rhynie (Scotland)	Devonian	Chert	0.05-0.18	<2.00	-	-	-	15.0-66.0	<5.00 - 22.0	-	-	-	Rice & Trewin, 1988

1.2 Aims and objectives

The study focuses on metal concentrations in hot spring deposits, showing in detail precious and base metals (economically important metals). This was done in order to understand the role of an active geothermal system in re-mobilizing metals at high altitudes above ore deposits. For this purpose, it is necessary to analyse the discharge conditions of thermal waters and their precipitations, and the mineralogical and chemical characteristics of hot spring deposits. To address this issue, my research focuses on the Jaraña hot spring deposits in southern Peru, which contain the necessary conditions for this study.

1.3 Regional Geologic Overview

Peru is located on the boundary of subduction zone between the Nazca and South American plates, with a convergence rate of 7,4 cm/yr, in the direction N78°E (NW to SE) (Tassara, 2005). The tectonic and magmatic processes were developed throughout the geodynamic evolution of the Andes (Jaillard, Soler, Carlier, & Mourier, 1990) and produced the right conditions to generate varieties of ore deposits (porphyry, epithermal, skarn, MVT, VMS, IOCG and gold veins deposits) all throughout the Peruvian territory (Acosta et al., 2010).

Nowadays, the Nazca Ridge (latitude: 15° S) causes a change in the angle subduction of the Nazca Plate (Gutscher, Olivet, Aslanian, Eissen, & Maury, 1999), therefore, in the north of Peru, subduction is flat (less than 10°) and to the south, subduction is at a "normal angle" (around 30° S). The steeper subduction angle allows the generation of magmas and the presence of active volcanoes (Rosenbaum et al., 2005; Tassara, 2005), specifically in the southern region of Peru (Figure 1.6A). Moreover, the geothermal systems in Peru are emplaced above exhumed mineralized ore bodies from ancient times. Pinaya is one of the main geothermal systems located in the back-arc area with 36.8 MW estimate for electricity generation (Figure 1.6B) (West Japan Engineering Consultants, 2012), and the surface manifestations are over Cu-Mo (Au-Zn) porphyry–skarn and Cu-Au-Fe exhumed deposits associated with Eocene–Oligocene intrusive rocks (Figure 1.6C) (INGEMMET, 2018). The Pinaya geothermal system is a group of hot springs near local hamlets; the group of hot springs near the Jaraña hamlet receives the name of "Jaraña hot springs".

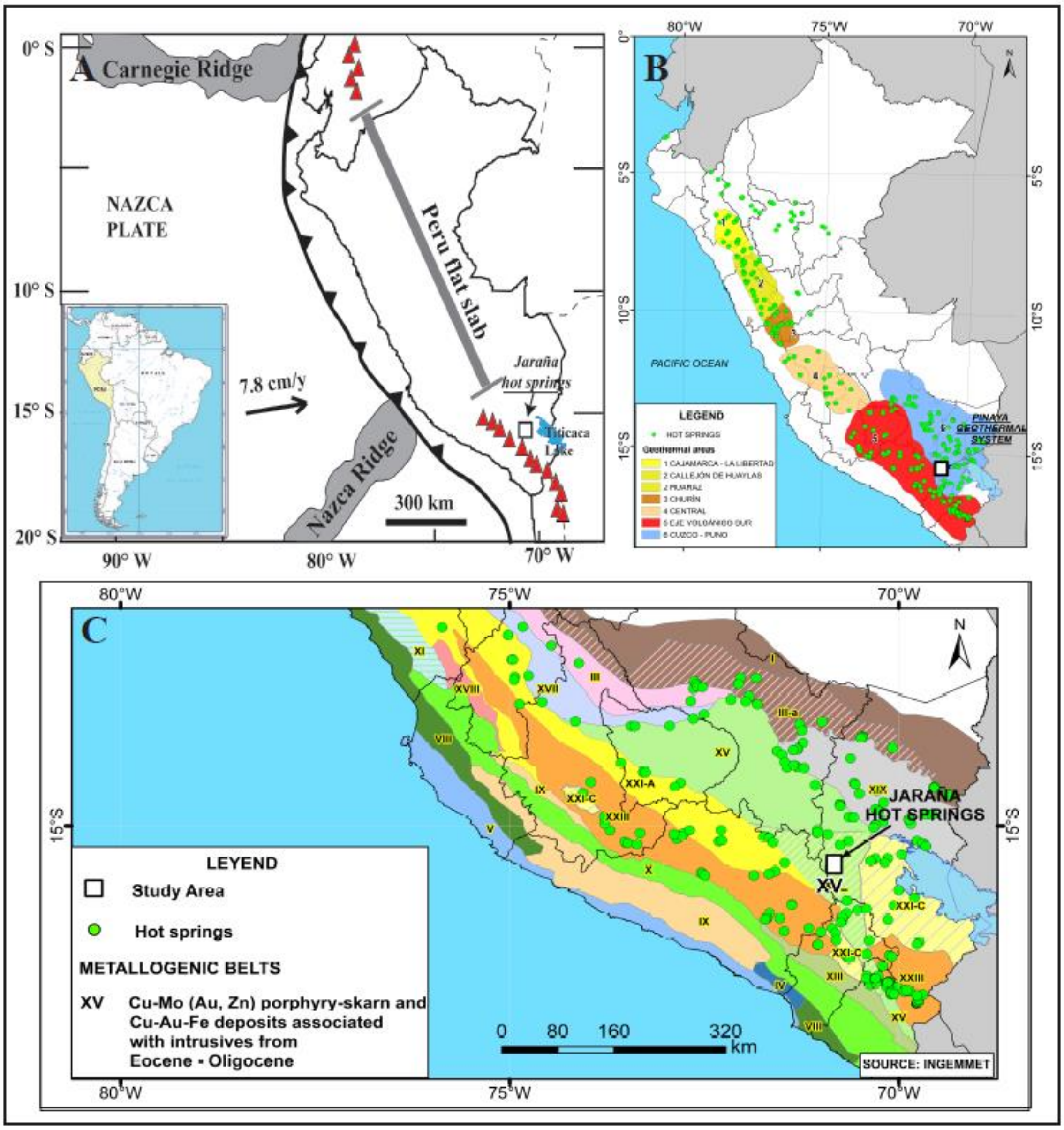

Figure 1.6 Location maps: A) Peru in South America and tectonic settings (modified from Rosenbaum et al., 2005), the red triangles represent the active volcanoes; B) geothermal areas map of Peru and location of Pinaya geothermal system (modified from Vargas & Cruz, 2010); (C) metallogenic map, hot springs and Jaraña hot springs location on the southern side of Peru (Modified from INGEMMET, 2018).

1.3.1 Geographic Overview

The Jaraña hot springs are located in the southern region of Peru, in the Puno province (latitude 15°30,21'S, longitude 70°50,80'W) at high altitude (4570 meters); between the eastern side of the Occidental Cordillera (Sillapaca Cordillera) and the Altiplano area, around 90 km east of the active volcanic arc. The hot springs are inside a hollow valley surrounded by high mountain peaks (5300 m). The mountains preserve volcanic centre morphology, which is inactive since Miocene ages. The pluvial precipitation is higher from December to March (around 183 mm) and decreases between April to November (3 to 61 mm) (CLIMATE-DATA.ORG, 2018); therefore, the rainfall reduction causes dry conditions and extremely cold weather. Hence, the annual range of temperature varies from minus 7 to 17°C.

1.3.2 Geological Setting

The regional geology exposes old rock units enabling information about the geology at depth. The oldest rocks are Cretaceous sandstone (Hualhuani Formation) and limestone (Arcurquina Formation), overlapped by Paleocene–Eocene red bedding sandstone and conglomerates within a calcareous matrix (Puno Group). The

Cretaceous and Paleocene–Eocene rocks are folded and covered under an angular discordance by Oligocene andesitic lavas (Tacaza Group; 29 Ma) (Fornari et al., 2002). Subsequently, the area is overlaid by a thicker white tuff deposit (Palca Group) from lower Miocene times (22-18 Ma) (Cereceda et al., 2010) and lacustrine units interbedded with volcaniclastic deposits (Maure Group) (Aguilar, 2012). Finally, Miocene andesitic and basaltic andesite lavas (Sillapaca Group) cover a high percentage of the exhumed zone (Valdivia & Rodríguez, 2003). The lithological sequences were intruded by tonalitic, granodioritic rocks around 25.7 Ma, and dacitic-andesitic rocks around 19 Ma, causing a mineralization process around. A roughly circular lava dome near to Pinaya hamlet, dated at 0.842 Ma, represents the youngest rock unit inside this area (Figure 1.7).

The Cusco–Lagunillas–Mañazo (CLMF) is a regional fault (NW-SE direction) (Carlotto et al., 2005), which has control on the lithology and influence on tectonic evolution through time (Figure 1.7). The CLMF changes from transtensional during the Mesozoic, to transpressional during the Cenozoic, followed by localized deformation allowing the magmatism during the Oligocene (Cerpa et al., 2012).

Miocene volcanic rocks surround the hot springs at Jaraña; the andesitic and basaltic-andesitic lava rocks are affected by hydrothermal alteration (argillic–advanced argillic) and silicification. The hot springs are above a magmatic-phreatic breccia controlled by local faults with a WNE–ESE trending and strike-slip direction movement (Aguilar, 2012; Valdivieso, 2015). In a recent study, Valdivieso (2015) described that hot springs in Jaraña are above mineralized ore bodies located at depth; the hypothesis is based on core sample analysis placed at the north side on Jaraña (Sabina project exploration, figure 1.7). The core drill samples registered sulfide minerals such as pyrite (FeS_2), rutile (TiO_2), arsenopyrite (FeAsS), enargite (Cu_3AsS_4), luzonite (Cu_3AsS_4), covellite (CuS), digenite (Cu_9S_5); also, iron minerals such as hematite (Fe_2O_3) and limonite ($FeO(OH).nH_2O$) and jarosite minerals hosted in volcanic rocks.

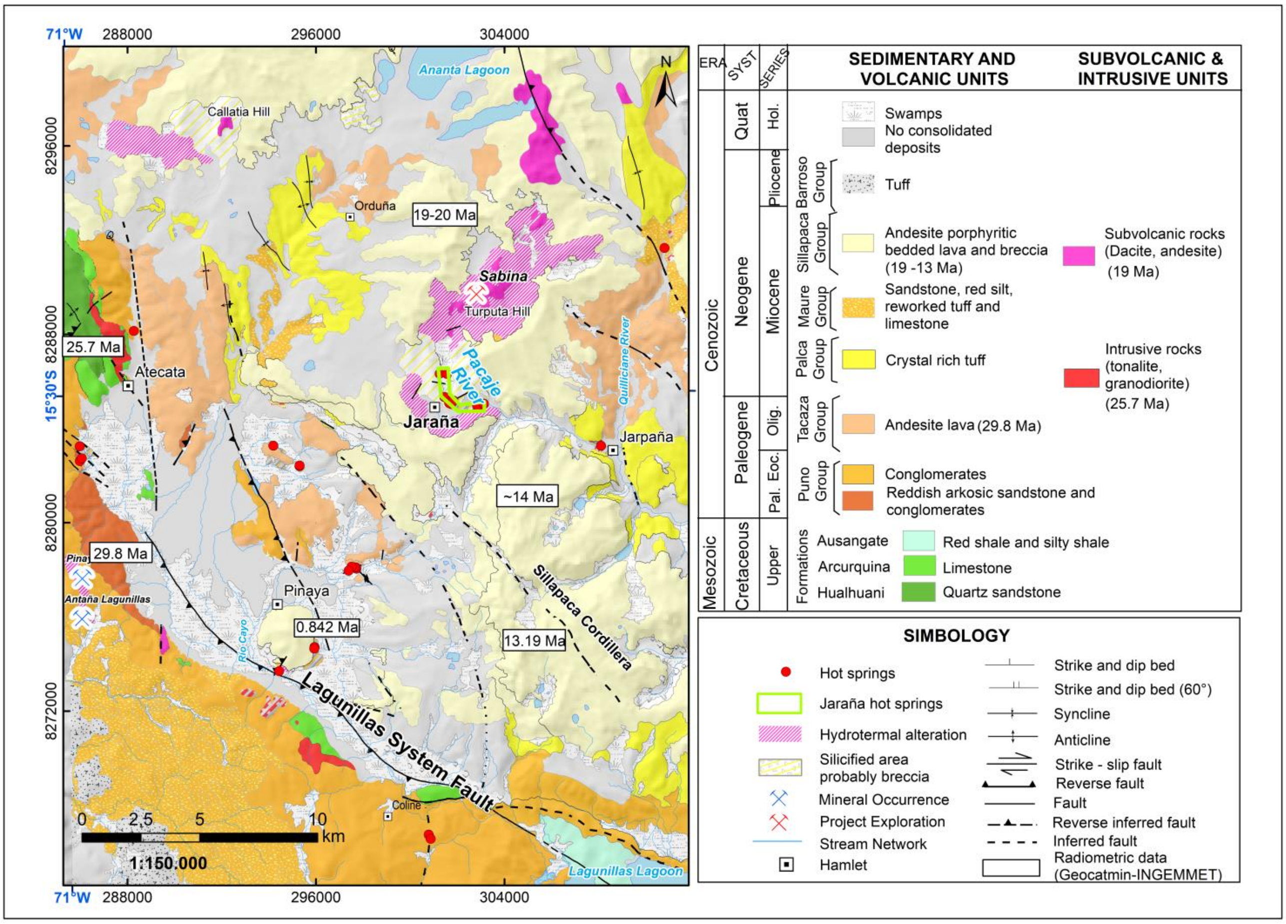

Figure 1.7 Regional geologic map and location of Jaraña hot springs (Modified from INGEMMET, 2018).

1.3.3 Surface manifestations at Jaraña

The hot springs at Jaraña are surrounded by mountains, which is suitable for a meteoric recharge in geothermal systems. The Jaraña thermal area covers around one km^2 and the hot springs are located near the Pacaje River. The river extends from north to south and then turns toward the east, as an L-form (Figure 1.7). The hot springs are distributed along a flat surface, inside a hollow valley, precipitating red, orange and yellow coloured materials; also, a thin white layer interpreted in the field as salts, covers hot spring deposits.

Cruz (2016) determined the hot springs pH (6–6.7), temperature (55 to 74°C) and water chemical composition (alkali-chloride and acid-sulfate waters) at Jaraña and pointed out that these thermal waters derive from a deep reservoir at less than 140°C. Thermal waters contain a major concentration (above 100 mg/L) of cations such as Na and Ca, and anions such as Cl, SO_4, HCO_3, and SiO_2. K, Mg and SiO_2 are in the range of 10 to 100 mg/L. Other trace elements, such as Li, F, B, As, Sr, Fe, Rb, Cs and Mn, register concentrations between 0.1 and 10 mg/L. The Rb, Cs, and Mn elements have moderate concentrations in the range of 0.1 to 1 mg/L. Trace metals with low concentrations are Co, Cu, Mo, Ni, Pb, Sb, Se, Ti, Tl, V. W and Zn below 0.1 mg/L. The discharge of thermal waters generate hot springs deposits with halite, gypsum, and minerals enriched in elements such as Ag Cu, Pb, As, Sn and Fe (Pajuelo et al., 2016).

2 METHODOLOGY

This chapter presents the field sampling process and the analytical methods used to characterize hot spring deposits and host rocks at the Jaraña hot springs site. Field sampling methods include sample collection criteria, the treatment of samples during collection, and condition with respect to being moved from Peru to New Zealand. Sample analysis utilized the following laboratory methods: x-ray diffraction, scanning electron microscopy and energy dispersive spectroscopy (SEM-EDS), optical microscopy, cathodoluminescence, 4 Acid –Digest using ICP-MS and ICP–AES and Laser Ablation Inductively Coupled Plasma Mass Spectrometry (LA-ICP-MS).

2.1 Field sampling

Before field sample collection, a mosaic Google Earth map (scale: 1:2,000) was prepared with hot spring spatial locations according to Cruz (2016). Sample collection at Jaraña was based on hot spring distributions along three zones; northern, central and eastern (Figure 2.1). Samples were collected during the dry season (Mid-November) and the sample nomenclature contains the first two letters of Jaraña (JR: Jaraña), and consecutive numbers were assigned the order of collection (01, 02, 03). Where samples were collected from the same position, a consecutive alphabetical letter was added (A, B, C). The main criterion for sample collection was to collect representative characteristics in the precipitates, both in terms of colour and morphologies as well as position relative to the vent and precipitate conditions (subaerial or subaqueous).

Thirty-two samples of geothermal precipitates and host rocks were collected around hot springs vents and extinct hot springs. Of these, a total of twenty-two samples were collected from recent hot spring deposits, specifically from white subaerial deposits and black and orange subaqueous deposits. Four samples were collected from red and yellow terraces and two samples of silicified rocks were taken from outcrops around hot spring deposits in the central zone (Figure 2.2A, B and C; Table 2.1).

While the aim was to collect a hand sample size for each, most of the subaqueous samples began to disintegrate upon collection. Some of the fragile samples (JR-10, JR-19, JR-20, JR-21, JR-23, and JR-25) required multiple sample fragments to serve as a quality control for analytical results. The samples weighed around 500 g to 1 kg and were initially dried (solar) in the field at the time of collection. The samples were then heated between 5 and 10 minutes at 200 ºC before being moved to New Zealand. One sample (JR-13) was dismissed because of damage during the drying process. The collection was located on a geologic/sampling map of the site based on field observations and satellite imagery.

After biosecurity control inspections in New Zealand, samples were carefully cleaned from dust and classified according to the collection site. Subsequently a macroscopic sample description focused on representative sample colours, layering, and any diagnostic sedimentary features. The identification of colour and texture characteristics was used for spatial correlation among the hot spring deposits along the three zones (northern, central, and eastern), over a distance of 2 km approximately.

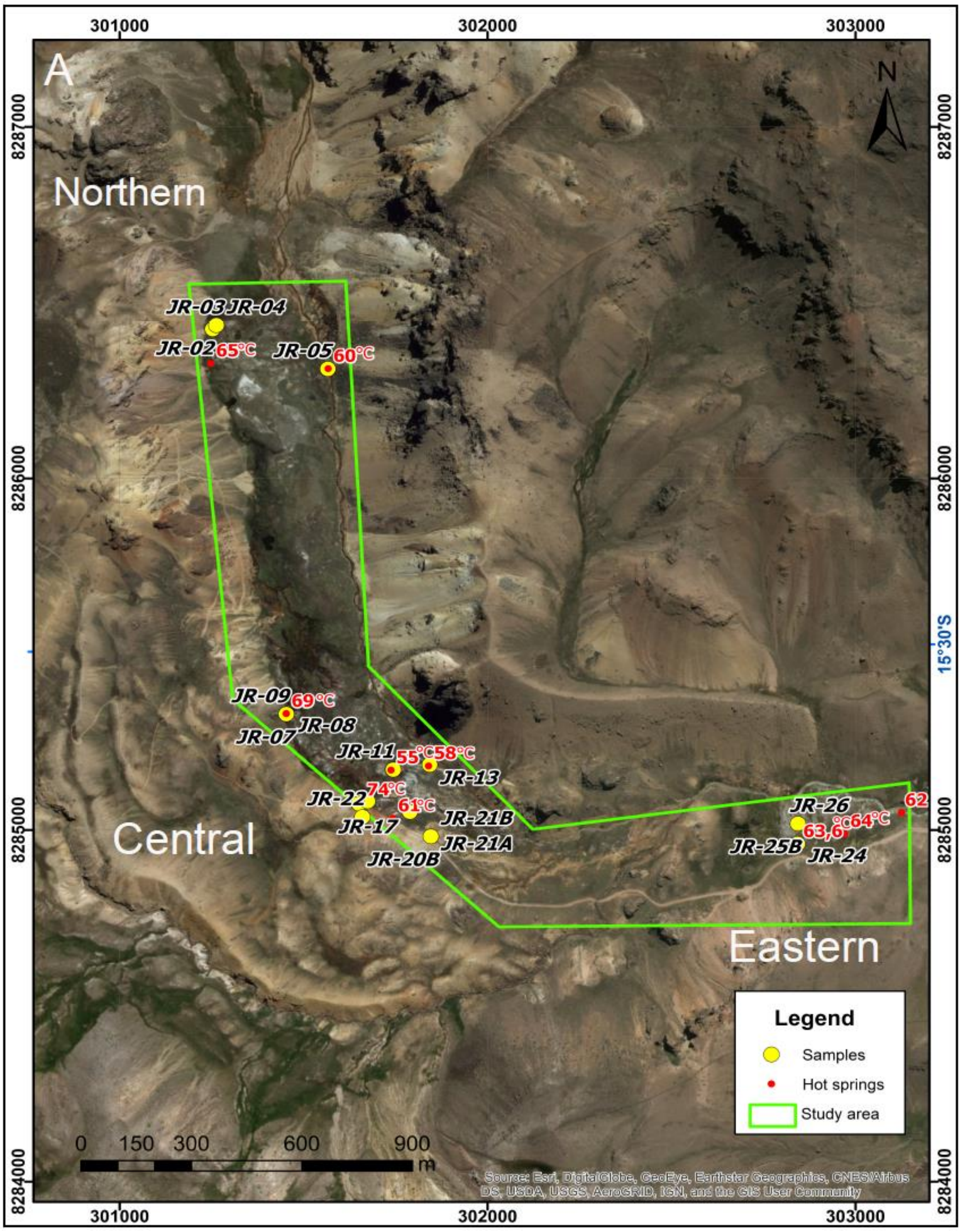

Figure 2.1 Hot springs and samples collection in the northern, central and eastern zones on a Google Earth map.

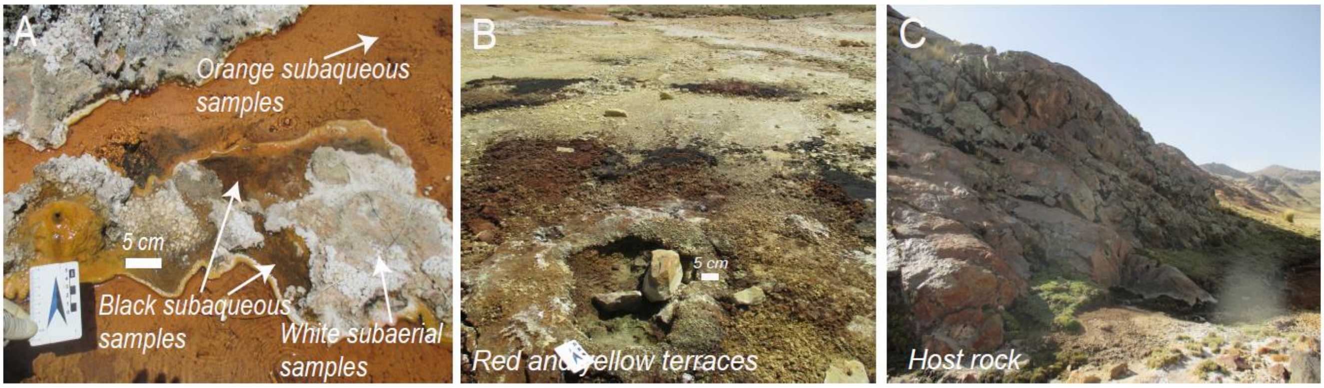

Figure 2.2 Samples collection from: A) active hot spring; sample collection on subaerial and subaqueous areas (white, orange and black colours); B) inactive hot spring; samples from yellow and dark red terraces (central zone); C) host rock sample collected near an active hot spring (central zone).

Table 2.1 ID Sample collection in the northern, central and eastern zones, detailing sample collection areas (SA=subaerial and SQ=subaqueous).

ZONE	SAMPLE	COLLECTION AREA	ZONE	SAMPLE	COLLECTION AREA	ZONE	SAMPLE	COLLECTION AREA
NORTH	JR-01	SQ	CENTRE	JR-06	SA	EAST	JR-23A	SA/SQ
	JR-02	SQ		JR-07	SA/SQ		JR-23B	SA/SQ
	JR-03	SQ		JR-08	SQ		JR-24	SA/SQ
	JR-04	SQ		JR-09	Host rock		JR-25A	SA/SQ
	JR-05	SQ		JR-10A	SQ		JR-25B	SA/SQ
				JR-10B	SQ		JR-26	SA/SQ
				JR-10C	SQ			
				JR-11	SA/SQ			
				JR-12	SQ			
				JR-14	SQ			
				JR-15	SQ			
				JR-16	SQ			
				JR-17	SQ			
				JR-18	SQ			
				JR-19A	SA/SQ			
				JR-19B	SA/SQ			
				JR-20A	Terrace			
				JR-20B	Terrace			
				JR-21A	Terrace			
				JR-21B	Terrace			
				JR-22	Host rock			

2.2 Analytical Methods

2.2.1 X-Ray Diffraction (XRD)

Samples were collected from hot spring deposit layers and host rocks, and later stored in sample vials. Precipitates from different coloured layers were extracted with spatula and milled using an agate mortar. On the other hand, rocks were reduced by means of a ring mill at Earth Science Processing Lab. Smear mounts were created on glass plates using acetone. The powder distribution was homogeneous and carefully concentrated in the middle of the glass.

A total of 58 samples were analysed using the PANalytical Empyrean X-ray Diffractometer at The University of Auckland. The powder samples were analysed in four batches; each batch used a silica standard as a reference, and a 2-degree anti-scatter slit. The three first batches took around 10 hours and the fourth batch around 3 hours. Seven of the samples had a repeated analysis for further pattern comparison and quality control.

The diffraction patterns were processed with the High Score Plus software. The procedure for the mineral identification was based on the similitudes with the highest intensity percentage peaks and their position at the 2Theta axis. For example, the analysed pattern reported a minimum of three peaks, with the main intensities shown with a black arrow and, then, matched with the standard mineral in blue lines. The highest intensities and the position in the 2Theta axis were verified in the standard mineral peak list; therefore, the standard mineral has certitude to be included as mineral result (Figure 2.3A and B). However, mixed samples often result in complex and overlapping diffraction patterns; hence, mineral identification may result in a non-unique solution.

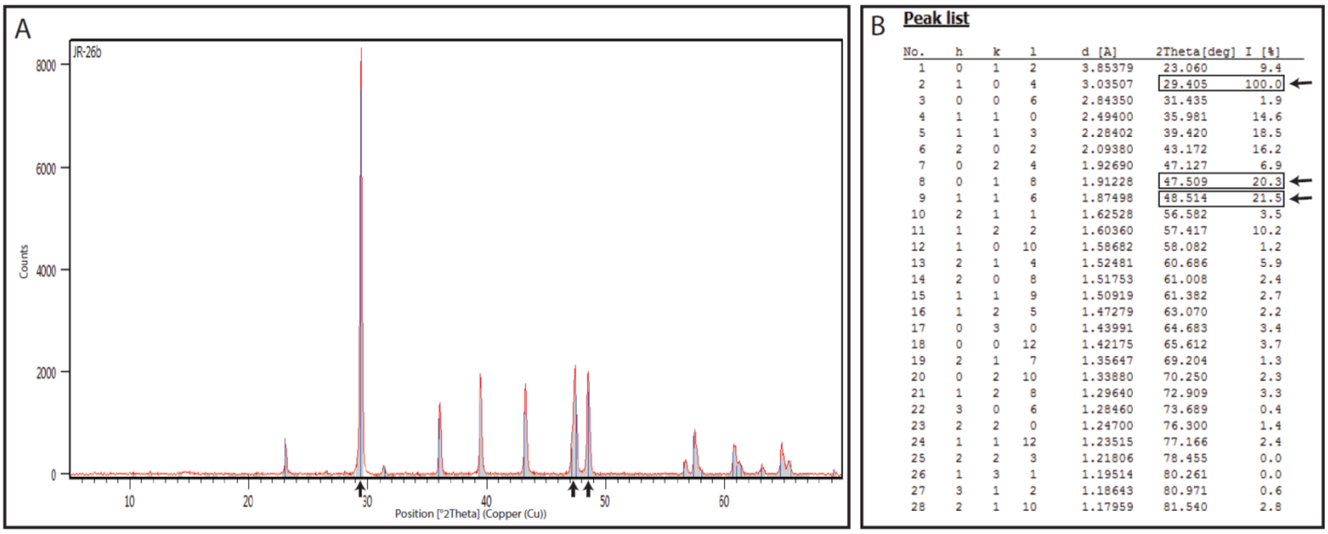

Peak list

No.	h	k	l	d [A]	2Theta[deg]	I [%]
1	0	1	2	3.85379	23.060	9.4
2	1	0	4	3.03507	29.405	100.0
3	0	0	6	2.84350	31.435	1.9
4	1	1	0	2.49400	35.981	14.6
5	1	1	3	2.28402	39.420	18.5
6	2	0	2	2.09380	43.172	16.2
7	0	2	4	1.92690	47.127	6.9
8	0	1	8	1.91228	47.509	20.3
9	1	1	6	1.87498	48.514	21.5
10	2	1	1	1.62528	56.582	3.5
11	1	2	2	1.60360	57.417	10.2
12	1	0	10	1.58682	58.082	1.2
13	2	1	4	1.52481	60.686	5.9
14	2	0	8	1.51753	61.008	2.4
15	1	1	9	1.50919	61.382	2.7
16	1	2	5	1.47279	63.070	2.2
17	0	3	0	1.43991	64.683	3.4
18	0	0	12	1.42175	65.612	3.7
19	2	1	7	1.35647	69.204	1.3
20	0	2	10	1.33880	70.250	2.3
21	1	2	8	1.29640	72.909	3.3
22	3	0	6	1.28460	73.689	0.4
23	2	2	0	1.24700	76.300	1.4
24	1	1	12	1.23515	77.166	2.4
25	2	2	3	1.21806	78.455	0.0
26	1	3	1	1.19514	80.261	0.0
27	3	1	2	1.18643	80.971	0.6
28	2	1	10	1.17959	81.540	2.8

Figure 2.3 Procedure to pattern identification in samples: A) pattern sample in red lines and black arrows represent the coincidences between the sample and standard mineral; B) peak list of standard mineral, the arrows show the position of the main peak intensity and their position in the 2Theta axis.

2.2.2 Scanning Electron Microscopy and Energy Dispersive Spectroscopy (SEM-EDS)

A small representative amount of subsample was taken from the top side of the sample according to location (northern, central and eastern zones), colours and layering. Sample orientation was an important characteristic for the analysis of morphologies, textures, crystals and microbial presence.

A total of six samples was imaged and analysed for Scanning Electron Microscopy (SEM) and Energy Dispersive Spectrometer (EDS) analysis at the Research Centre for Surface and Material Science, Faculty of Engineering–The University of Auckland. Samples were placed onto pin mounts and carefully orientated, photographed and, then, double-coated with platinum, using a Quorum Q150R S vacuum cycle for 10 minutes. The samples were analysed using the XL30 S-FEG Philips and Quanta 200 SEM instruments. The analysis was carried out with an XL30 S-FEG Philips instrument, using an accelerating voltage of 5, 20 and 30 kV, a beam current of less than 1 µA, and a resolution at 1.5 nm. Sample analysis were carried out with Quanta 200 instrument using an average pressure of 0.60 Torr, an accelerating voltage of 10 and 20 kV, current of less than 1 µA, and a resolution of approximately 3 nm. Furthermore, SEM analysis allowed simultaneous collection of elemental data using EDS. The EDS data compositions were collected over a regular and flat surface.

2.2.3 Optical microscopy

Seventeen samples from Jaraña hot spring deposits with representative morphologies from the centre and east zone were selected to prepare for thin sections. Representative samples were cut along transverse and longitudinal areas for a better analysis.

Six of the samples were prepared at the University of Iowa, Department of Geoscience Petrographic Facilities and eleven at the University of Auckland (Earth Science processing Lab). Sample preparation of the friable samples was extremely challenging and required vacuum impregnation with epoxy. Soft samples and water soluble components required extreme care while producing thin sections.

Petrographic observations were made on a Nikon eclipse LV100POL microscope. Samples impregnated inside an epoxy were polished and description was based on optical properties in reflected light; thin section mineral description was based on optical properties in plane polarized (PP) and crossed polarized (XP) light.

2.2.4 Cathodoluminescence

Eleven thin sections from Jaraña hot spring deposits at the central and eastern zones were selected for cathodoluminescence method analysis. The aim was to identify the carbonate precipitation and distribution in laminated horizons, for that reason, sample orientation was important for the analysis.

The optical cathodoluminescence microscope analysis was carried out with a CITL CL Mk5-2 electron beam source, under operating conditions of 15 kV, 350 µA at University of Auckland (Faculty of Science). Samples were exposed to the electron beam source between five to ten minutes for a better result; the voltage was accelerated to 20 kV to detect silica horizons.

Samples with luminescence were compared with a thin section sample from previous work results in cathodoluminescence methods (Campbell, Farmer, & Des Marais, 2002). The analysis was based on luminescence identification; e.g. dull, bright, dark. The light orange luminescence represents the presence of the Mn element activator and dark orange luminescence represents the presence of the Fe element quencher (Mackenzie & Adams, 1951).

2.2.5 4 Acid–Digest using ICP-MS and ICP-AES

Sample selection was based on spatial distributions and distinguishing features between precipitates and host rock. Samples were milled and powder samples packed inside a plastic bag with a total weight of 0.500 g.

Twenty-one samples were analysed at ALS laboratories (Vancouver) using ICP-MS instrumentation to detect the lowest Limit SuperTrace Multi-Element Analysis (ME-MS61L) and Rare earth (ME-MS61L). Samples were dissolved using the 4-acid digestions (HNO_3, $HClO_4$, HF and HCl) and the final solution was analysed by inductively coupled plasma-mass spectrometry (ICP-MS) as well as inductively coupled plasma-atomic emission spectrometry (ICP-AES). The 4-acid digest method was capable of detecting 48 elements and 12 rare earth elements considering a lower and upper limit (Table 2.2 and 2.3).

Table 2.2 Analyte and detection limit for 48 elements using 4-acid digest method.

ANALYTE	SYMBOL	UNITS	LOWER LIMIT	UPPER LIMIT
Silver	Ag	ppm	0.002	100
Aluminum	Al	%	0.01	25
Arsenic	As	ppm	0.05	10000
Barium	Ba	ppm	1	10000
Beryllium	Be	ppm	0.02	1000
Bismuth	Bi	ppm	0.005	10000
Calcium	Ca	%	0.01	25
Cadmium	Cd	ppm	0.005	1000
Cerium	Ce	ppm	0.01	500
Cobalt	Co	ppm	0.005	10000
Chromium	Cr	ppm	0.3	10000
Cesium	Cs	ppm	0.01	500
Copper	Cu	ppm	0.02	10000
Iron	Fe	%	0.002	50
Gallium	Ga	ppm	0.01	10000
Germanium	Ge	ppm	0.01	500
Hafnium	Hf	ppm	0.004	500
Indium	In	ppm	0.005	500
Potassium	K	%	0.01	10
Lanthanum	La	ppm	0.005	10000
Lithium	Li	ppm	0.2	10000
Magnesium	Mg	%	0.01	25
Manganese	Mn	ppm	0.2	50000
Molybdenum	Mo	ppm	0.02	10000
sodium	Na	%	0.001	10
Niobium	Nb	ppm	0.005	500
Nickel	Ni	ppm	0.08	10000
Phosphorus	P	%	0.001	1
Lead	Pb	ppm	0.01	10000
Rubidium	Rb	ppm	0.02	10000
Rhenium	Re	ppm	0.002	50
Sulphur	S	%	0.01	10
Antimony	Sb	ppm	0.02	10000
Scandium	Sc	ppm	0.01	10000
Selenium	Se	ppm	0.2	1000
Tin	Sn	ppm	0.02	500
Strontium	Sr	ppm	0.02	10000
Tantalum	Ta	ppm	0.01	500
Tellerium	Te	ppm	0.04	500
Thorium	Th	ppm	0.004	10000
Titanium	Ti	%	0.001	10
Thallium	Tl	ppm	0.004	10000
Uranium	U	ppm	0.01	10000
Vanadium	V	ppm	0.1	10000
Tungsten	W	ppm	0.008	10000
Ytrium	Y	ppm	0.01	500
Zinc	Zn	ppm	0.2	10000
Zirconium	Zr	ppm	0.1	500

Table 2.3 Analyte and detection limit for rare earth elements using 4-acid digest method.

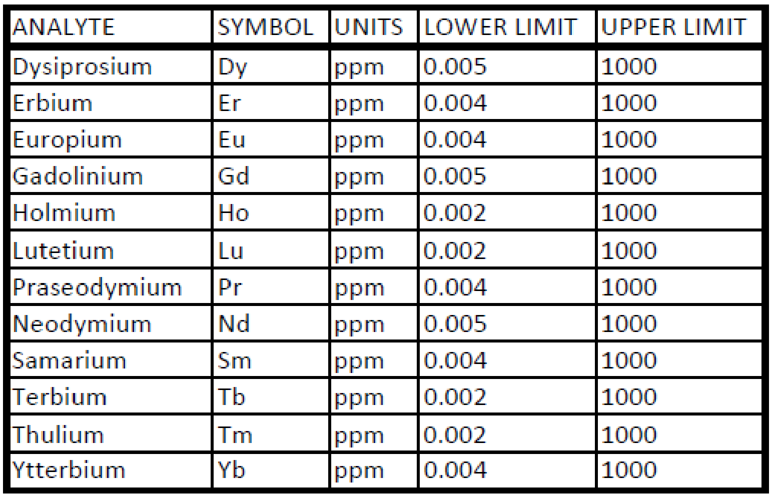

ANALYTE	SYMBOL	UNITS	LOWER LIMIT	UPPER LIMIT
Dysiprosium	Dy	ppm	0.005	1000
Erbium	Er	ppm	0.004	1000
Europium	Eu	ppm	0.004	1000
Gadolinium	Gd	ppm	0.005	1000
Holmium	Ho	ppm	0.002	1000
Lutetium	Lu	ppm	0.002	1000
Praseodymium	Pr	ppm	0.004	1000
Neodymium	Nd	ppm	0.005	1000
Samarium	Sm	ppm	0.004	1000
Terbium	Tb	ppm	0.002	1000
Thulium	Tm	ppm	0.002	1000
Ytterbium	Yb	ppm	0.004	1000

2.2.6 Laser Ablation Inductively Coupled Plasma Mass Spectrometry (LA-ICP-MS)

Six samples selected from recent precipitates with representative textures and components (clasts) were selected to determine trace element abundances between horizons. The samples were epoxy - impregnated and polished before the analysis (Figure 2.4A).

Trace elements were determined by LA-ICP-MS method at the University of Auckland using an Agilent 7700 ICP-MS coupled with a 193 nm New Wave Excimer laser ablation system. The laser beam energy was ~7 J/cm2 with a beam diameter of 75 µm. A rep rate of 5 Hz with an ablation time of 60 seconds, followed by 45 seconds of washout time was used for all analyses.

Two standard samples (GSE-1G, GSD-1G) were used during the analysis for calibration (GSE-1G) and as a secondary standard (GSD-1G). Standards were analysed every 20 unknowns. Accepted standard abundances were from GeoRem (http://georem.mpch-mainz.gwdg.de). For each horizon/target, samples were analysed in replicates of 5 to account for the sample heterogeneity (Figure 2.4A). A total of 48 elements were analysed: ^{7}Li, ^{9}Be, ^{11}B, ^{25}Mg, ^{27}Al, ^{29}Si, ^{35}Cl, ^{43}Ca, ^{47}Ti, ^{51}V, ^{52}Cr, ^{55}Mn, ^{57}Fe, ^{59}Co, ^{60}Ni, ^{63}Cu, ^{66}Zn, ^{71}Ga, ^{72}Ge, ^{75}As, ^{77}Se, ^{85}Rb, ^{88}Sr, ^{95}Mo, ^{107}Ag, ^{111}Cd, ^{118}Sn, ^{121}Sb, ^{125}Te, ^{133}Cs, ^{138}Ba, ^{139}La, ^{140}Ce, ^{146}Nd, ^{147}Sm, ^{157}Gd, ^{163}Dy, ^{166}Er, ^{172}Yb, ^{182}W, ^{185}Re, ^{197}Au, ^{201}Hg, ^{205}Tl, ^{208}Pb, ^{209}Bi, ^{232}Th, ^{238}U.

Data processing was completed by hand using Microsoft Excel software. The heterogeneity of the samples meant significant variation during analysis of samples, limiting the amount of time considered to represent “good” data. An average of 47 seconds to detect the ablation peaks was considered for the analysis, with the first five or ten and the last ten seconds removed from the process. The first stage of seconds was variable and depended on the peaks shapes; thus, if peaks were not coherent with the rest of the diagram they were not considered for the analysis (Figure 2.4B). Standard normalized trace elements were normalized to Ca using 4 acid-digest results and solution ICPMS data from GeoREm (http://georem.mpch-mainz.gwdg.de/sample_query_pref.asp). The average of major element concentration (Mg, Al, Si, Ca, Ti, Fe and As) allowed detect ion of anomalous amounts in samples (more than 100%). As a consequence, some of the spots (JR-06-CLAST-1, JR-06-CLAST-4, JR-06-CLAST-5 AND JR-19B-HB-4) were removed from the data result.

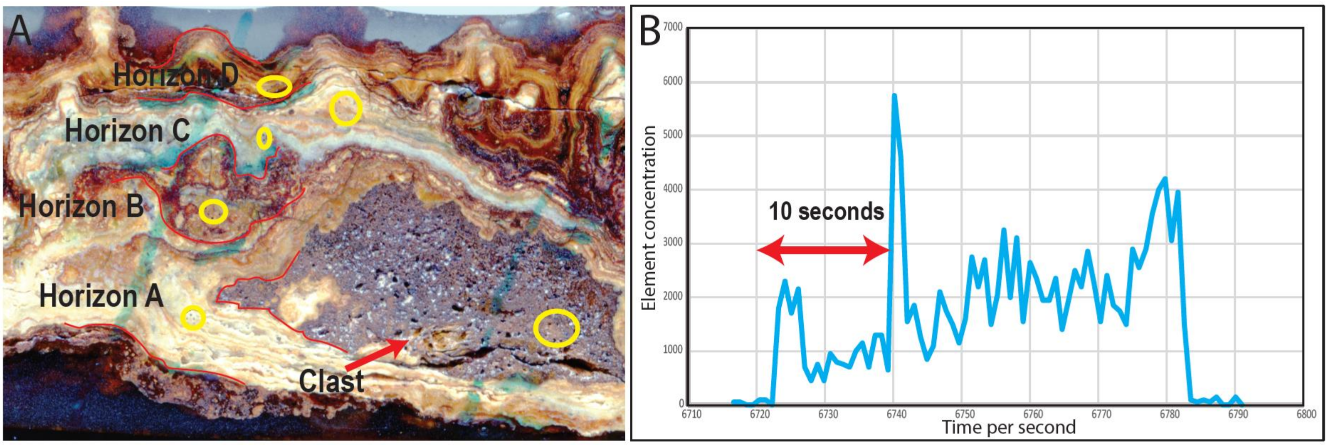

Figure 2.4 A) Sample JR-15 epoxy-impregnated and polished showing horizon layers, clast (red lines) and spots (yellow circles) for LA-ICPMS analysis; B) ablation peaks in sample JR-15 - Horizon C, first 10 seconds show no coherent pattern with the rest of the diagram. Time in seconds ("X" axis) and count rate ("Y" axis).

3 FIELD AND SAMPLE DESCRIPTIONS

This chapter describes the main characteristics of rocks surrounding hot springs, fluid discharge, and hot spring deposits at the Jaraña hot springs. These field and samples descriptions aid in the interpretation of laboratory results (Chapter 4), and include three topics: field observations, hot spring areas and deposits around vents, and features of hot spring deposit samples. In addition, they also focus on geological and geothermal features in the northern, central and eastern zones at Jaraña.

3.1 Field observation

Special geographical and geological characteristics surround the Jaraña hot springs deposits. Geographically, the hot springs are located on a flat valley floor at high altitude (4597 m), with moderate sloping hills, covered by colluvial deposits. The floor has a particular “L” shape, lightly inclined towards the east. The mountains on the northern side are the main source for the Pacaje River, which is located on the eastern edge of the valley floor (Figure 3.1A). Geologically, the surrounding mountains are silicified rocks (Figure 3.2A), which have an off-grey colour with quartz grains or an aphanitic texture. The rock structure has centimetre-sized cavities that may contain oxides or yellow disaggregated material (Figure 3.2B). A brecciated outcrop is located along the central zone of the Pacaje riverbank. The breccia is composed of small white angular fragments (0.5–2 cm) bound together by red cement (Figure 3.2C). Moreover, the Pacaje riverbank comprises an unconsolidated deposit, 3 meters thick, which has an interbedding of thin brown and white laminations (Figure 3.2D). Hot springs and their precipitates, as well as swamps and dry grassland, can be seen on the valley floor, covering rocks and thick (1-10 cm) unconsolidated deposits. Precipitates around hot springs have three main colours: white, red and yellow. The white unconsolidated deposits have the largest surface area and cover red deposits and dry grasslands. Red deposits surround the spring discharge and cover both channel bottoms, and yellow deposits form terraces mostly in the central zone (Figure 3.1 and figure 3.2A).

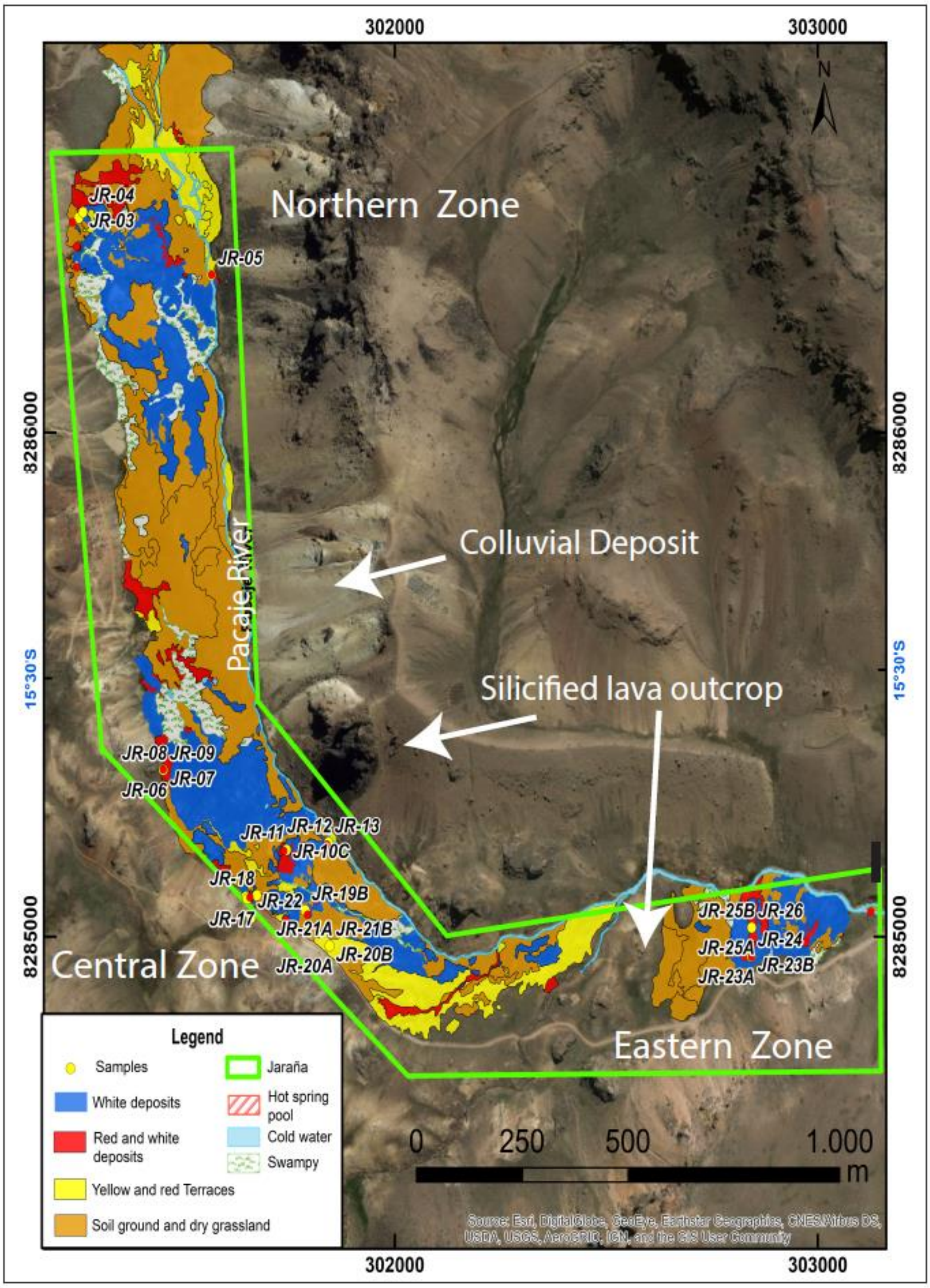

Figure 3.1 Jaraña hot springs location. Google Earth map overlain with outcrop features, sample collection sites (yellow circles), and mapping of main deposit materials over the flat valley.

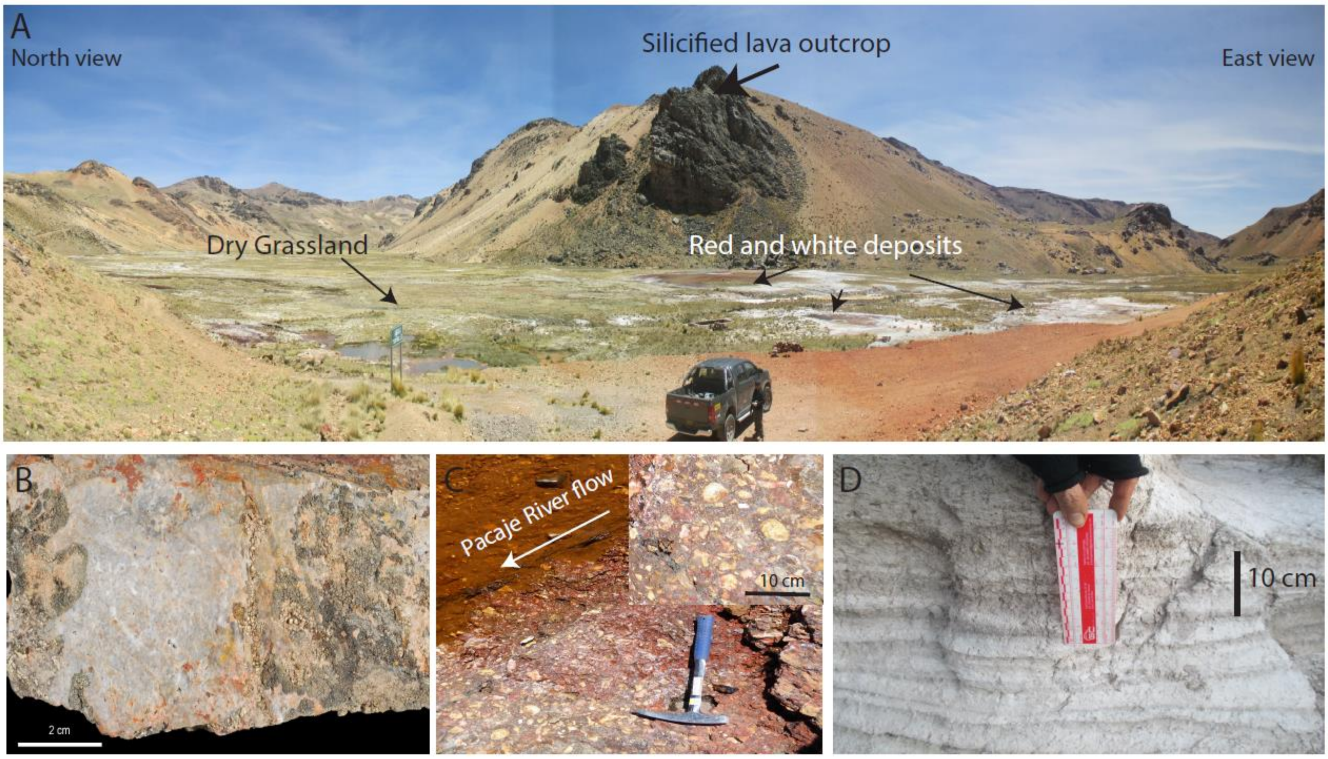

Figure 3.2 Field outcrops: A) panoramic photo through the northern and eastern zones with rock out crops and deposits over a flat base; B) silicified lava rock sample next to hot springs; C) breccia with red cement next to the Pacaje River; D) unconsolidated black and white laminations below the hot spring deposits.

3.2 Hot spring areas and their precipitation

The northern, central, and eastern zones of the valley floor contain hot springs forming in groups. Hot springs emerge from a vent, sustaining thermal pools with variable deepness, as well as generating run-off channels with their outflow. All three zones have subaqueous orange deposits and subaerial white terraces. Another finding disclosed subaqueous black deposits below orange deposits. Likewise, orange, green and yellow mats were found floating over the water surface. Furthermore, the central zone contains red and yellow terraces that represent past precipitation around now inactive hot springs at Jaraña. A description of the active and inactive hot springs sites and their precipitates inside the three zones, is presented below:

a) Northern Zone

Thermal pools at the northern zone are located at the lateral edges of the flat valley. The western edge contains thermal pools with stagnant water. The stagnant water accumulated in thermal pools and channels generates both, white mats floating over the water surface, and orange deposits built up as islets (Figure 3.3A). The eastern edge contains thermal pools with shallow depths near the Pacaje River. There are orange mats floating over the water surface and green mats located at the rim of the thermal pool. Also, orange deposits occur with network texture precipitate below the water surface whereas black deposits are notably close to the vent (Figure 3.3B). Generally, subaerial precipitates are at the rim of the thermal pools, covering solid surfaces and dry grassland; thickness is usually very thin (<1 cm thick).

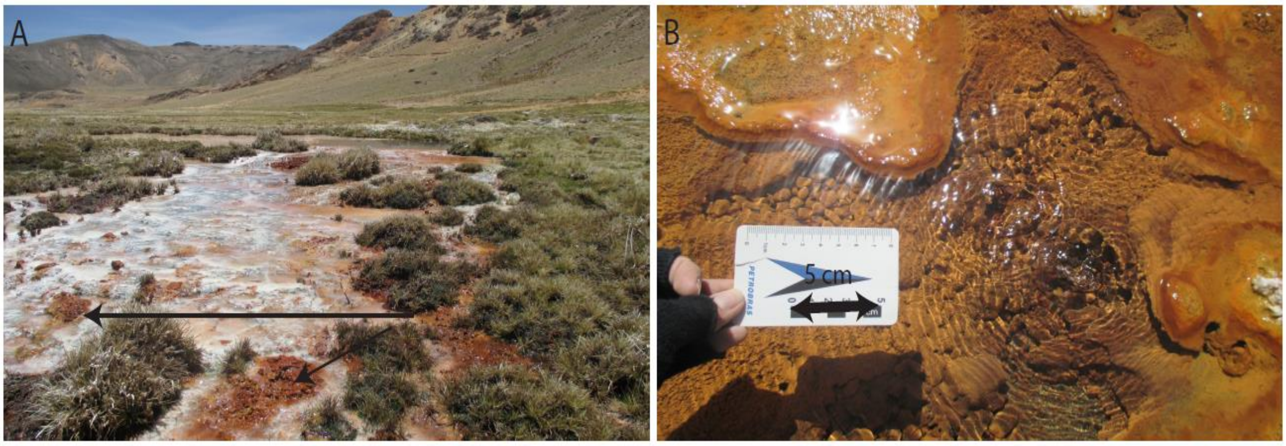

Figure 3.3 Hot springs and precipitates in the northern zone: A) stagnant water with orange islets (black arrows); B) shallow thermal pool with floating orange mat and subaqueous orange and black precipitates.

b) Central zone

The central zone contains the greatest number of thermal pools of varying depths, as well as extinct hot springs, located on the west and middle side of the valley floor. Thermal pools release steam and precipitate subaerial and subaqueous deposits; thickness of subaerial deposits, and colours in subaqueous deposits, are different from north to south. Thermal pools at the northern area are located on the west edge near a silicified rock outcrop; an ellipsoidal vent emerges from the ground sustaining shallow pools. These pools generate discharge channels, which merge with secondary channel branches, resulting in secondary warm pools. The thermal water in channels contains subaqueous orange deposits, and subaerial white deposits are at the rim of pool (Figure 3.4A) Furthermore, subaerial deposits with greater thickness (2-3 cm) precipitate above the orange deposits, while a lighter orange layer is positioned the register of water level (Figure 3.4B).

The central area contains steamy thermal pools and run off channels; thermal pools may be shallow or deep. The deep thermal pool is 5 meters in diameter, and its steam can be observed from a distance. This thermal pool is the largest thermal pool in Jaraña (Figure 3.4C). The water surface covers orange to dark orange subaqueous deposits, and water level oscillations generate a ramp covered by subaerial deposits; which are notable at the rim of the thermal pool (Figure 3.4D). In contrast, shallow thermal pools generate run-off channels, while steam rises from the surface of secondary shallow thermal pools (Figure 3.4E). The deposits below the water surface are orange and host white subaerial terraces at their rims. The latter kind of pool shows that white subaerial deposits are capable of floating over the water surface (Figure 3.4F). Likewise, orange and green mats float over the water surface (Figure 3.4G). Furthermore, this area comprises small thermal pools with shallow depth and has multiple run-off channels that generate secondary thermal pools. The shallow thermal pools have white terraces surrounding discharge channels, and green and yellow mats float over the water surface (Figure 3.4H).

Figure 3.4 Hot springs and precipitate characteristics in the central zone (northern and central areas): A) channels containing subaqueous orange deposits with subaerial white deposits at the rim; B) subaqueous and subaerial precipitates with a light orange layering; C) steamy thermal pool with a 5-metre diameter; D) ramp surface with subaerial white deposits and subaqueous orange deposits; E) steamy channels with subaqueous dark orange deposits; F) white subaerial deposit floating over the water surface; G) thermal pool with red rounded material below the water surface and orange to green mats; H) vent with run-off channel sustaining thermal pools with subaerial deposits at the rim and green mats.

Thermal pools located in the southern area have circular morphologies, with considerable depth and green water colour. Similar to those in the northern area, orange deposits are below the water surface and thin (<1 cm) white deposits are around the rim of the pool (Figure 3.5A). Shallow water on shelves covers orange deposits, that contain irregular spheroids with a weathered nucleus. Also, black deposits are noticeable below the orange deposits (Figure 3.5B and C). Finally, the centre zone contains red to yellow terraces close to a small hole. The circular shape is interpreted as an extinct thermal pool. A thin (1-3 mm) white deposit covers the red and yellow terraces (Figure 3.5D).

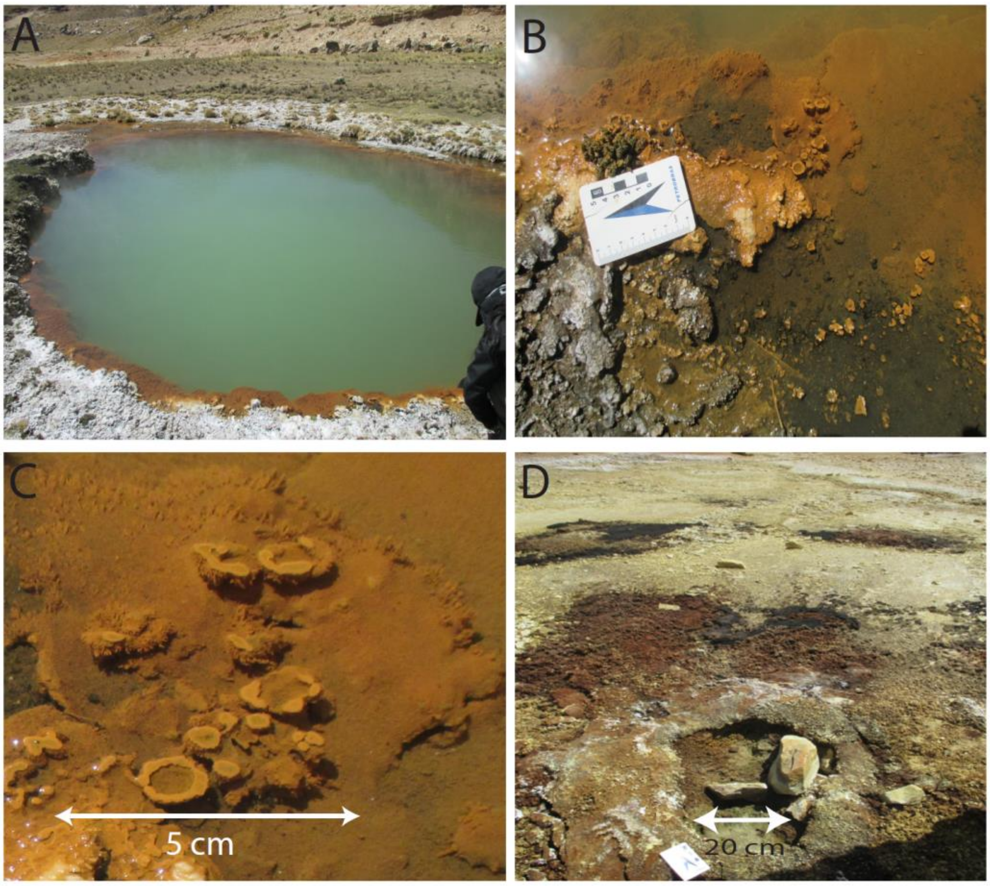

Figure 3.5 Hot springs and precipitate characteristics in the central zone (southern area): A) thermal pool with green watercolour; B) shallow rim of the thermal pool with subaqueous orange and black deposit; C) a zoom image of subaqueous orange deposits with irregular discoidal shapes; D) subrecent precipitates around an extinct hot spring.

c) Eastern zone

Hot springs in the eastern zone are located at the southern edge of the valley floor. Hot springs emerge from the ground, sustaining shallow thermal pools and generating run-off channels. Thermal pools and run-off channels have yellow and green mats floating at the edges. Orange deposits lie below the water surface and white deposits cover subaqueous and rock surfaces. Subaqueous deposits have black precipitates below the orange deposits at shallow depths. Furthermore, shallow thermal pools contain spring conduits, 10 cm in diameter. The mounds are circular with a cylindrical central hole, and are covered by a light orange coloured mat (Figure 3.6A). Run-off channels contain subaqueous orange deposits, but colours change to green and black according to distance from vent areas. Similarly, subaerial white deposits located at the rim of thermal pools and channels increase in thickness away from vent areas (Figure 3.6 B).

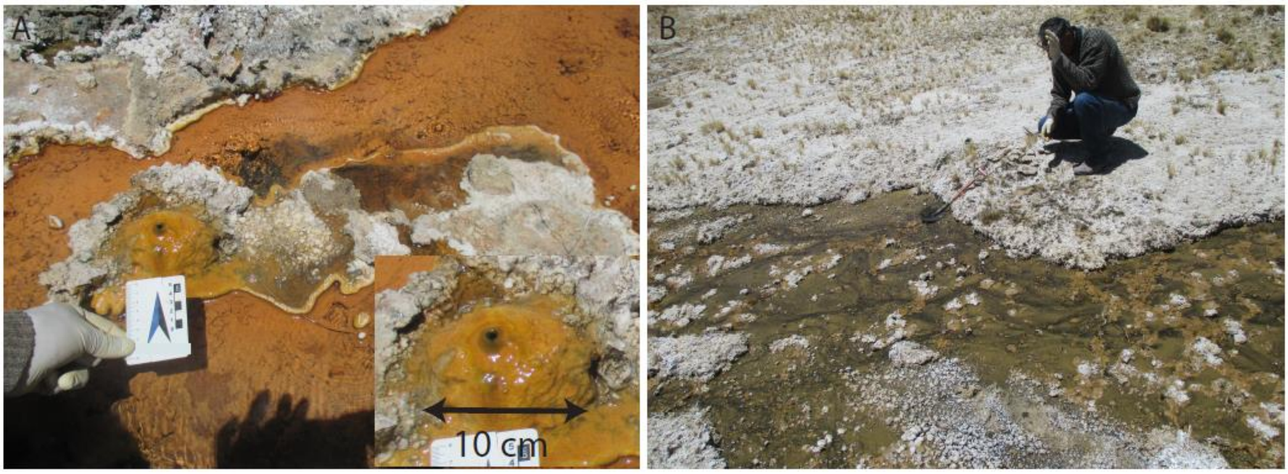

Figure 3.6 Hot springs and precipitates in the eastern zone: A) shallow thermal pool with spring conduit mound, subaerial white deposits and subaqueous orange and black deposits. A zoom image show the spring conduit (10 cm) covered by yellow mat; B) run-off channel with subaqueous black and green deposits, and subaerial white deposits with thick thickness.

3.3 Features of hot spring deposit samples

a) Northern Zone

The five representative samples (See table 2.1) from the north zone have orange colours and are small, massive fragments (Figure 3.7A). Samples were from subaqueous areas and some of the fragments contain colourless acicular crystals, e.g. sample JR-02 (Figure 3.7B). Furthermore, samples have a massive aspect with polygenetic grains, e.g. sample JR-05 (Figure 3.7C).

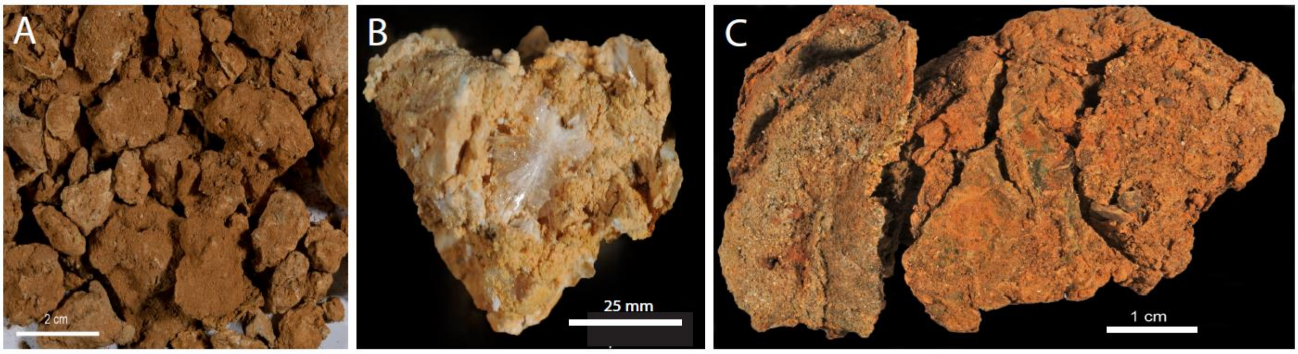

Figure 3.7 Sample characteristics at the northern zone: A) small massive fragments, sample JR-03; B) fragment with acicular crystals; C) fragment with polygenetic grains, sample JR-05.

b) Central Zone

Representative samples from the central zone have variable characteristics in colours, morphologies and layering. There are four samples from terraces interpreted as subrecent precipitates, four samples from subaerial areas, and 14 samples from subaqueous areas (See table 2.1).

Subrecent precipitates are identified as red and yellow terraces in the central zone. Samples JR-20A and JR-20B represent the red terraces and samples JR-21A and JR-21B the yellow terraces. The red samples (JR-20A and JR-20B) have a greater porosity and may contain yellow disaggregated deposits; likewise, a white thin deposit is covering the sample (Figure 3.8A). Morphologically, these samples have a braided appearance similar to a network fabric. The braided texture contains long tubes making connections and forming cavities (Figure 3.8C and D); also, when long tubes connect with other tubes, they form circular knots, with off-white deposits filling the cavities (Figure 3.8B).

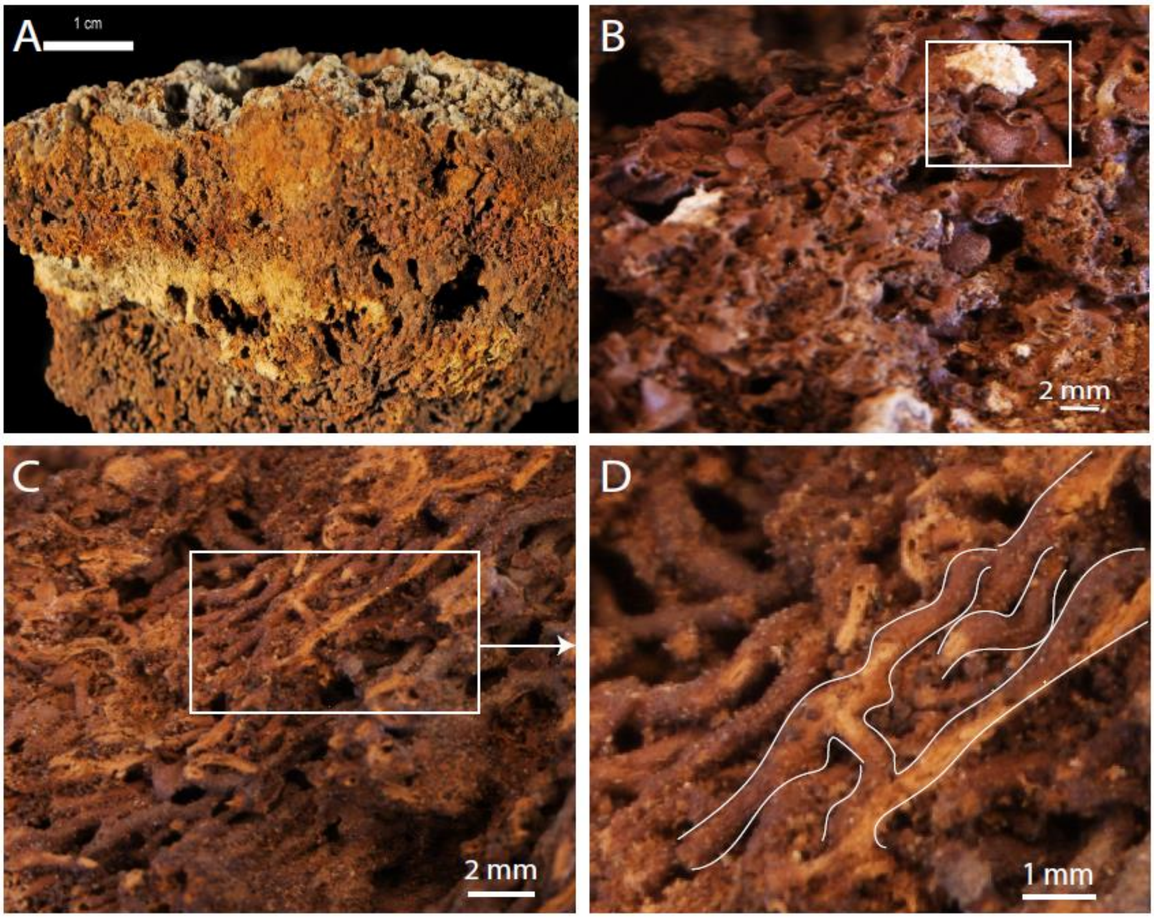

Figure 3.8 Subrecent precipitate sample of irregular morphologies: A) sample JR-20A with a thin white layer at the upper side of the sample; B) circular knots and white precipitation filling cavities; C) network fabric; D) long tubes making connections.

Subaerial deposits are identified as white terraces in the central zone. Sample JR-06 represents the white deposit, and sample JR-07 both the orange and white deposits (Figure 3.9A). Subaerial deposits have a thicker thickness in northern areas, which is the opposite to the southern areas that have a thin coverture over subaqueous surfaces. The increase of thickness develops morphologies; for example, sample JR 06 has elongated nodules that are laterally and continuously linked, giving a cerebroid appearance from the top view. This cerebroid appearance is chaotic, with curved walls and a smooth ending surface. The curved walls have continuous corridors, probably part of the weathering during precipitation process (Figure 3.9B). Nodules have a convex lamination growth and the build-ups have cavities. Furthermore, the bases of subaerial samples with thicker thickness have round orange fragments of variable size from 0.5 x 0.2 cm to 2 x 0.5 cm (Figure 3.9C).

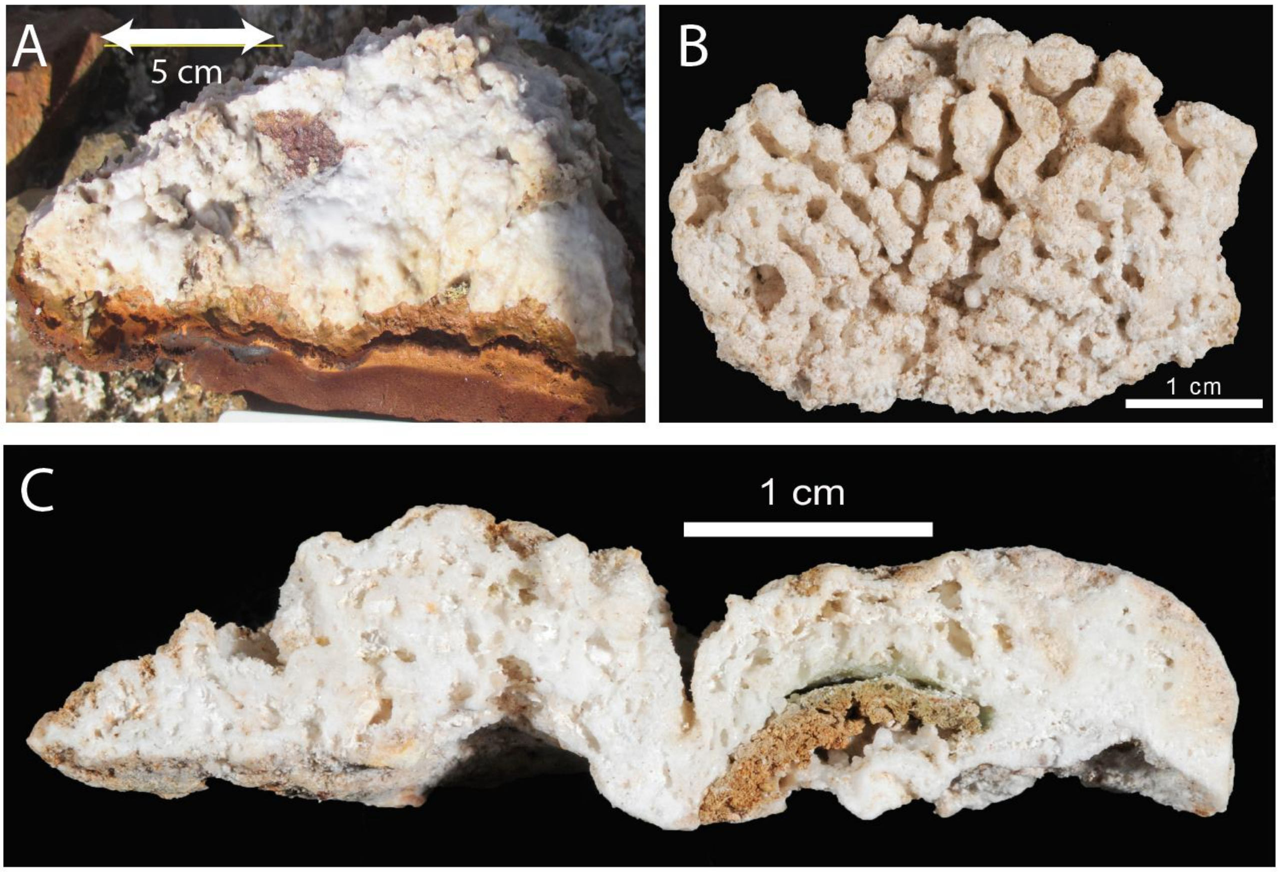

Figure 3.9 Subaerial samples with irregular morphologies from the central zone: A) sample JR-07 with subaerial and subaqueous deposits; B) sample JR-06 with a cerebroid appearance; C) sample JR-06 with nodules and cavities, the base contain a round fragment.

Subaqueous deposits are identified as orange and black deposits. Subaqueous orange samples have two characteristics, a disaggregated appearance and nodular morphologies. Samples with a disaggregated appearance are mainly from central thermal pools areas; samples have small orange fragments (JR-07, JR-10A, JR-10B, JR-12 and JR-16) and a massive corrugated aspect with polygenetic grains (JR-17 and JR-18). In contrast, other samples from the centre zone have nodular morphologies with variable elongation (JR-10C, JR-11, JR-14, JR-15, JR-19A and JR-19B). Nodular morphologies are common in samples JR-10C, JR-14 and JR-15; the nodules appear as columns ranging from 0.2 to 0.5 cm long with a spherical termination, and a rounded base ranging from 0.1 to 0.2 cm wide (Figure 3.10A and B). Some of the columns are laterally linked and some of the spherical shapes have a weathered nucleus at the top (e.g. JR-10C); also, spherical nodules show circular laminations (Figure 3.10C). Nodules grow over laminated horizons with variable thicknesses, a wide range of colours and different lustre types. Thickness varies from millimetric to centimetric size; colours are orange, red, white, grey, black or white; and lustre may be opaque, vitreous or metallic. Laminations cover or trap concave-shaped fragments (e.g. sample JR-15). Generally, fragments are at the base of the samples or at initial phases of deposition, with red colours and uniform porosity; their size varies from 1.1 x 0.7 cm to 4 x 3 cm (Figure 3.10D). Furthermore, clusters of round nodules were found on both sides of sample JR-11 (Figure 3.10E) and small nodules with a grainy aspect and weathered nucleus, overlying laminated structures were found on the upper surface of samples JR-19A and JR-19B (Figure 3.10F). Additionally, samples JR-19A and JR-19B have small black spherical nodules with a smooth surface and granular appearance; their growth form and direction is normal to water surface (Figure 3.10G).

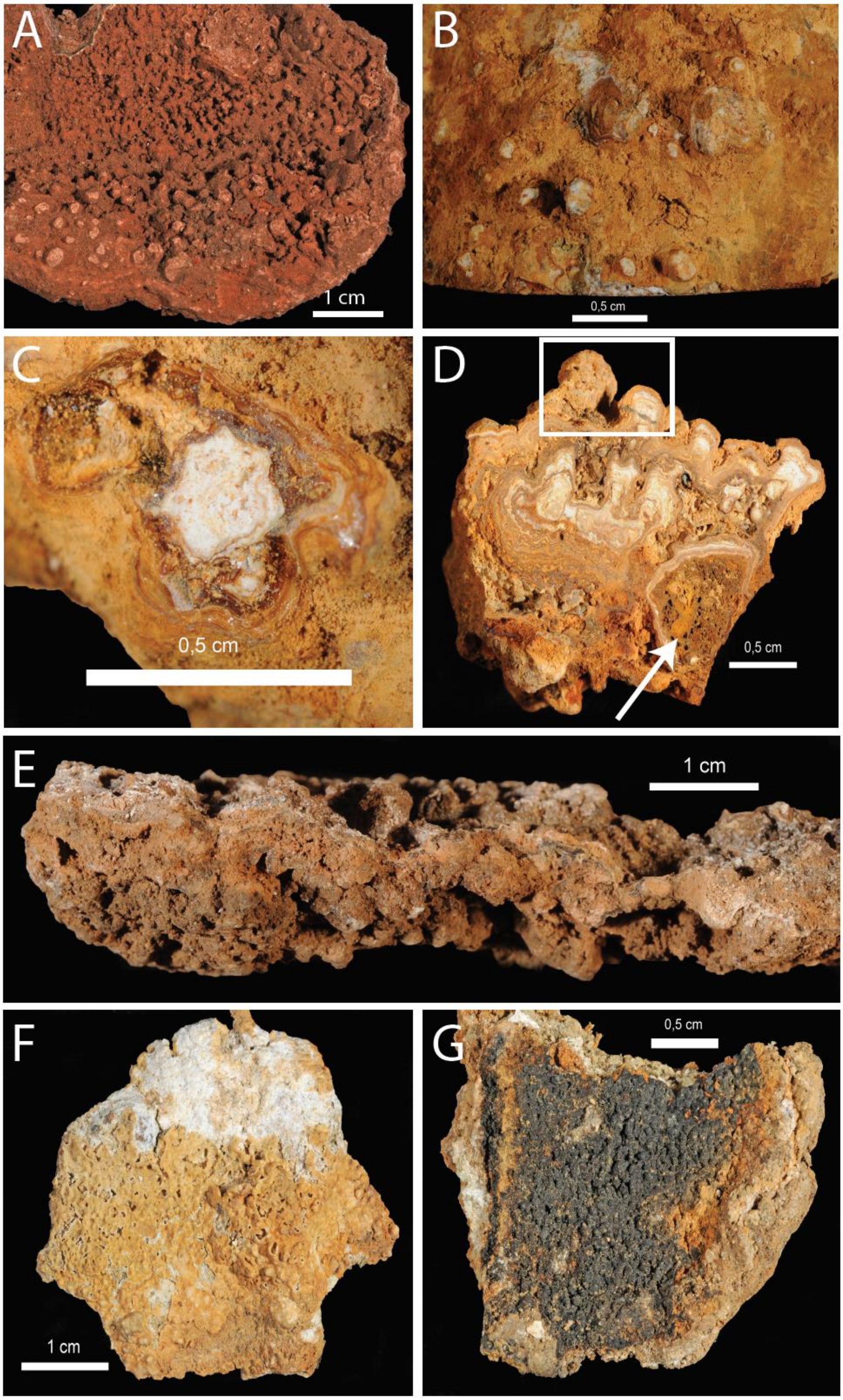

Figure 3.10 Subaqueous samples with nodular morphologies from the central zone: A) sample JR-10C with small size nodules; B) sample JR-14 with spherical nodules; C) sample JR-15 with horizontal cut of spherical nodule show circular laminations; D) sample JR-15 with spherical ending nodules, white laminations (white square) and fragment trapped by wave continuous laminations (white arrow); E) sample JR-11 with cluster of round nodules; F) upper surface of sample JR-19B with grainy aspect and weathered nucleus; G) under surface of sample JR-19B with black granular aspect.

c) Eastern zone

The east zone contains six samples from subaerial and subaqueous deposits (See Table 2.1). Subaerial samples have similar white colours but variable characteristics in morphologies. In contrast, subaqueous samples have variable characteristics in colours and morphologies. Subaerial samples above orange deposits have a white granular aspect; but above black deposits, they contain elongated nodules with laterally linked columns resulting in a dendriform or rounded appearance. For example, sample JR-24 has elongated nodules, which are laterally linked or not, similar to a branch, giving a dendriform appearance (Figure 3.11A). The length of the branches varies from 0.5 to 1 cm; thus, the length is greater than the width (Figure 3.11B). The branches have a smooth granular surface with millimetric to centimetric holes. Sample JR-25A has round nodules, which may have divergent rounded columns toward the top. The small rounded columns are about 1 cm long and the top surface could present cavities (Figure 3.11C). Furthermore, nodules have a convex lamination and the build-ups have cavities; also, nodules occur over a white laminated surface that covers a green mat layer. (Figure 3.11D). Subaqueous samples have two representative colours, black and orange. Black deposits are from run-off channels and have botryoidal morphologies in the lower surface of the sample. For example, samples JR-25A, JR-25B and JR-26 have botryoidal morphologies comparable to a cluster of nodules; surfaces have a smooth convex appearance, and horizons with off-white colours are overlying black nodules. The off-white horizons have acicular crystals growing perpendicular to the black nodule surfaces (Figure 3.11E and F). On the other hand, orange deposits are from hot spring feeders located at shallow thermal pools and have colloform morphologies. For example, sample JR-23A has smooth and convex surfaces, and its colloform morphology is over a continuous wave lamination (Figure 3.11G). Laminations have similar characteristics to samples in the central zone (samples JR-14 and JR-15); thus, laminations have variable thicknesses, orange to black colours and opaque to metallic lustre without magnetism (Figure 3.11H). Moreover, laminations cover or trap concave-shaped fragments, with orange colours and high porosity similar to sample JR-15 at the centre zone.

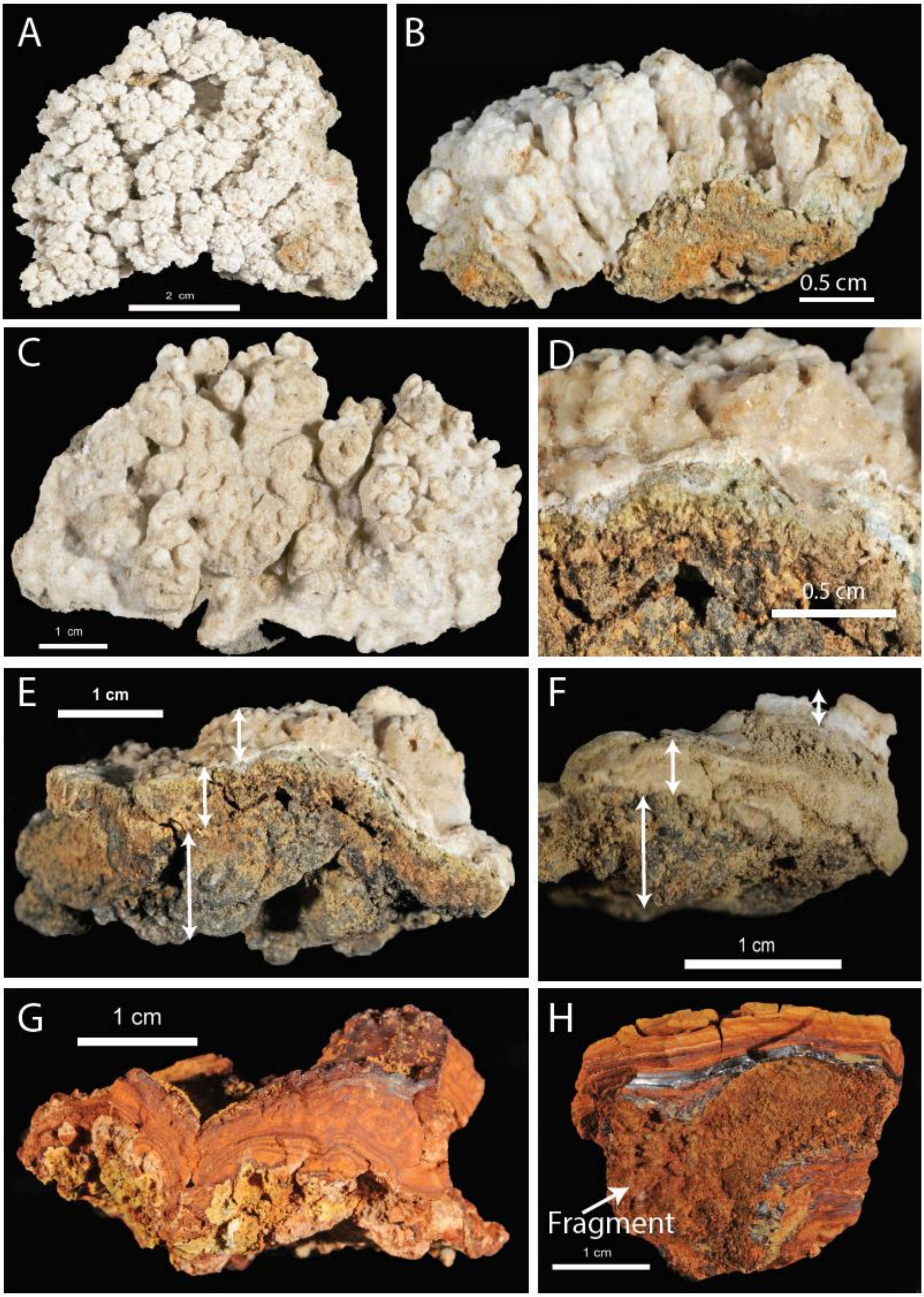

Figure 3.11 Subaerial and subaqueous samples with morphologies from the eastern zone: A) sample JR-24 with nodules laterally-linked with dendriform appearance; B) elongated nodules with a branched appearance (sample JR-24); C) sample JR-25B with small rounded columns; D) a zoom image (sample JR-25B) of the laminated surface overlying a green mat; E) and F) samples JR-25B and JR-26 with subaerial and subaqueous precipitates. Subaqueous black precipitates have botryoidal morphologies with a cluster of nodules, below an off-white horizon.

4 LABORATORY RESULTS

This chapter presents the laboratory results of subrecent precipitate, recent hot spring deposits and host rock samples distributed along the northern, central and eastern zones on the Jaraña hot springs. The laboratory results are divided into two main sections: the first section includes the mineralogy, microtexture and carbonate precipitation identified in samples and the second section contains the chemical analysis. The mineralogy, microtextures and carbonate precipitation describes the results obtained using X-ray diffraction (XRD), optical microscopy, SEM-EDS and cathodoluminescence techniques. Moreover, the chemical analysis contains the results using the four acid digest and laser ablation ICP-MS methods. The chemical methods results contain the trace element concentration amount in subrecent and recent deposits and host rock samples. The analysis of trace element concentrations is divided into three topics: the trace element concentration in laminated samples, the major and trace amount in subrecent and recent deposits and host rocks, and, finally, the analysis of correlation between elements using binary diagrams in recent precipitates.

4.1 Mineralogy, microtextures and carbonate precipitation

4.1.1 Mineralogy

The x-ray diffraction results are based on 65 bulk samples from subrecent precipitates, recent hot spring deposits and host rocks. X-ray diffraction patterns showed that the most significant mineral for the subrecent precipitates is jarosite, for the subaerial deposits is gypsum and for the subaqueous deposits are mainly calcite followed by iron-oxide and manganese-oxide minerals. Besides host rocks contain quartz as the main mineral. The mineral description for the ancient and recent deposits at the northern, central and eastern zones are as follows (Figure 4.1 and for more details sees Appendix I):

The minerals results from the northern zone are different from minerals from the central or eastern zones.

The northern zone contains recent subaqueous samples with gypsum as the main mineral; however secondary minerals are incorporated in small proportion such as hydrotalcite ($Mg_6Al_2(CO_3)(OH)_{16}.4(H_2O)$), sylvite (KCl), periclase (MgO), sodalite ($Na_8Al_6Si_6O_{24}.Cl_2$) and calcite ($CaCO_3$).

The central zone contains subrecent and recent precipitates; the minerals identified on subrecent precipitates were completely different to those identified in recent precipitates. The subrecent deposits have jarosite mineral ($KFe^{3+}_3(OH)_6(SO_4)_2$) as the main mineral; however, alabandite minerals (MnS) are incorporated as a minor component in red and yellow terraces. The subaerial deposits have gypsum ($CaSO_4.2H_2O$) as the main mineral; however, samples with a thin layer located in southern areas yielded calcite minerals in moderate proportion. Other minerals such as sulfides enriched in Cu, As and Sb (freibergite ($Cu_{12}Sb_4S_{13}$) and colusite ($Cu_{12-13}V(As,Sb,Sn,Ge)_3S_{16}$)) and halite (NaCl) were identified in small proportions. The sulfide minerals were identified in samples JR-06 and JR-14c_d_rpt and halite in sample JR-11a, which result different from minerals on the eastern zone (Figure 4.2A). In contrast, subaqueous deposits are heterogeneous materials and contain a variable range of pattern results, where calcite is the predominant mineral. Iron-oxide minerals such as hematite (Fe_2O_3), goethite (FeO(OH)), magnesioferrite ($MgFe^{3+}_2O_4$) and franklinite ($ZnFe^{3+}_2O_4$) were identified in most of the samples (JR-07a, JR-10A, JR-10B, JR-15a, JR-16 and JR-19Ba) in moderate proportion (Figure 4.2B) and manganese-oxides such as bunsenite ($Ni_{25.8}Mn_{3.20}O_2$) were identified in one sample (JR-19Aa) in small proportions (Figure 4.2C). Three subaqueous samples (JR-12, JR-16 and JR-19Ba) reported quartz (SiO_2) as a secondary mineral; however, a repeated analysis in sample JR-12 gave a different pattern result and identified a sulfide mineral (colusite) as a new result. Furthermore, there are other secondary minerals incorporated as a small proportion, such as halite, alabandite, gypsum, lime (CaO) and renierite ($(Cu,Zn)_{11}(Ge,As)_2Fe_4S_{16}$), which are not common in all subaqueous samples. An identification of minerals according to their morphology indicated that disaggregated samples have quartz as a main mineral (samples JR-12 and JR-16) and also calcite and hematite (samples JR-10A and JR-10B) as secondary minerals (Figure 4.2D). Corrugated samples (JR-17 and JR-18) contain calcite minerals in high proportion and nodular shape samples have calcite and iron oxide minerals. Additionally, silicified host rock gave a predictable result of quartz mineral as the main mineral.

The eastern zone contains recent subaerial and subaqueous deposits; the main minerals identified were gypsum for subaerial deposits and calcite for subaqueous deposits. Subaerial deposits incorporate calcite in moderate proportion, calcite phases is mainly concentrated at the bottom surface of samples such as sample JR-24a (Figure 4.2A); also, green mats have calcite as a main mineral composition. A detailed comparison between black and orange subaqueous deposits demonstrated that both deposits have different mineral composition. While subaqueous black deposits contain mainly calcite and manganese-oxide minerals in small proportion, subaqueous orange deposits contain iron-oxide and sulfide minerals. Black subaqueous deposits contain bunsenite and henritermierite ($Mn_{10.11}Ca_{24}Si_{19.44}O_{96}$) minerals in small proportions. Bunsenite is a mineral also found in the central zone, incorporated into calcite minerals (Figure 4.2C). Orange subaqueous deposits contain other minor mineral phases such as ilmenite ($FeTiO_3$) and magnetite (Fe_3O_4), and small proportion phases of magnesite ($MgCO_3$), proustite (Ag_3AsS_3) and sulfides minerals enriched in silver and arsenic (Figure 4.2D).

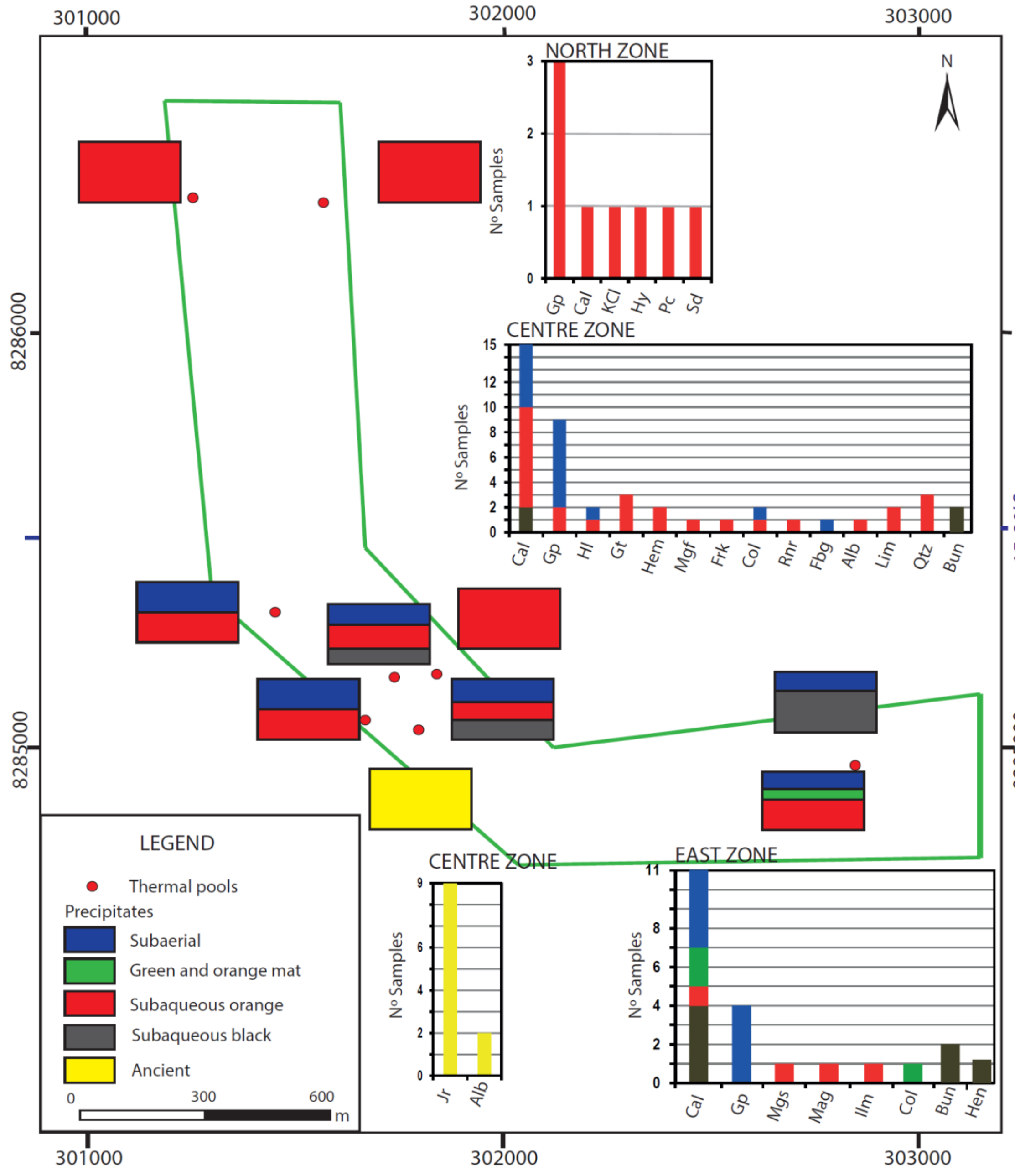

Figure 4.1 Map with x-ray diffraction results. The chart illustrates the number of samples containing specific minerals at the north, centre and east zones in Jaraña hot springs. See key below:

Gp = gypsum
Gt = goethite
Alb = alabandite
Bun = bunsenite

Cal = calcite
Hem = hematite
Lim = Lime
Hen = Henritermierite

KCl = sylvite
Mgf = magnesioferrite
Qtz = quartz

Hy = hydrotalcite
Frk = franklinite
Jr = jarosite

Pc = periclase
Col = colusite
Mgs = magnesite

Sd = sodalite
Rnr = renierite
Mag = magnetite

Hl = halite
Fbg = freibergite
Ilm = ilmenite.

The recent subaerial deposits have gypsum as a main mineral; however, calcite incorporates in moderate proportion towards the southern areas at the central and eastern zones. Only the northern areas at the central zone report a sulfide mineral (freibergite) in small proportion, e.g. sample JR-06 (Figure 4.2A).

Subaqueous deposits with black colours have calcite as the main mineral (central and eastern zones), only one sample (JR-19Ba) contains secondary minerals such as goethite and quartz (Figure 4.2B) and bunsenite minerals incorporate in small proportion to calcite (central and eastern zones) (Figure 4.2C). Also, minerals in subaqueous orange deposits from the northern zone are completely different from those located at the central and eastern zone. The northern areas at the central zone contains calcite minerals (JR-10A, JR-10B, JR-10C and JR-11) in major proportion comparing to southern areas at the central zone; and iron-oxide minerals are commonly found at the eastern zone (Figure 4.2D).

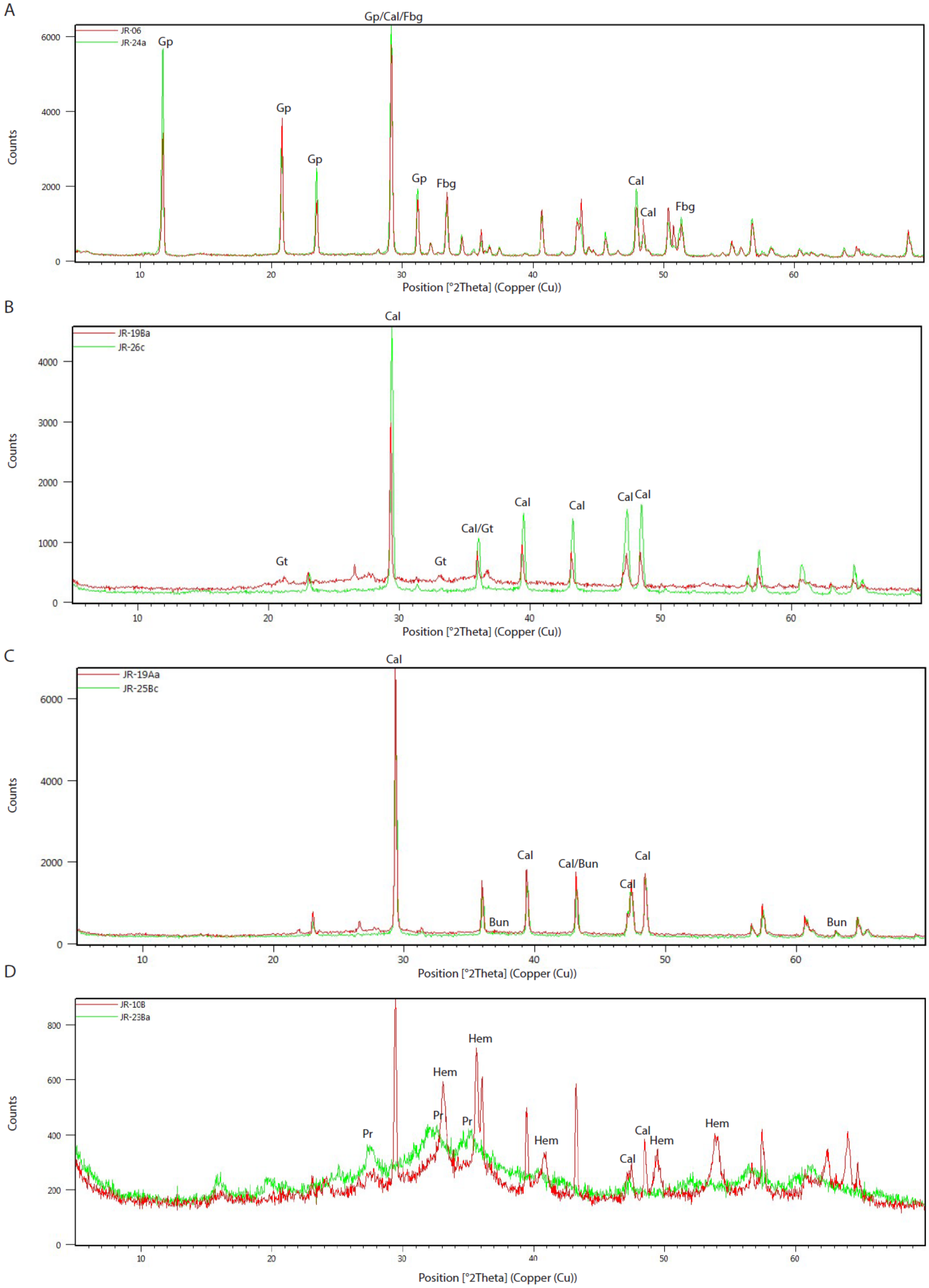

Figure 4.2 X-ray diffraction patterns at the central and eastern zones: A) subaerial samples show gypsum mineral as the main mineral in samples; and freibergite in small proportion (JR-06 and JR-24a); B) subaqueous black samples show calcite mineral in major proportion and bunsenite mineral in minor proportion (JR-19Ba, JR-26c); C) subaqueous black samples show calcite mineral in major proportion and goethite incorporated in minor proportion (JR-19Aa; JR-25Bc); C) subaqueous orange samples show calcite and iron-oxide mineral (sample JR-10B) and proustite mineral (sample JR-23Ba).

4.1.2 Microtextures

Optical microscopy and SEM-EDS analysis allowed recognizing microtextures in subrecent and recent deposits. Crystals, cement, clasts and biologic components (e.g. diatoms) were found inside the microtexture analysis. The following paragraphs will describe the microtextures found on one sample from a subrecent deposit from the central zone (JR-20A), on three samples from subaerial deposits from the central and eastern zones (JR-06, JR-24 and JR-25B), and nine samples from subaqueous deposits from the northern, central and eastern zones (JR-03, JR-10C, JR-11, JR-14, JR-15, JR-19B, JR 25B and JR 26).

Optical microscopic analysis revealed that subrecent deposits contain curly-shaped filaments with red colours; and that these have perpendicular lines and external walls. The white thin (milimetric) coverture that covers the sample is a clastic horizon with angular colourless fragments (Figure 4.3A). SEM-EDS analysis showed that the curly filaments have spherical grains shapes with smooth surface, with the filament surface containing Fe-oxide minerals with trace elements of Si, Mn, As, Ca, and minor amount of C and S. Also, filament surface may contain small plates, which correspond to weathering process. The SEM images showed that the iron-oxide coverture trapped plant stems, which in turns contain small filaments (Figure 4.3B). The iron-oxide coverture also contains white grainy microtextures, the EDS analysis indicated that surrounding surfaces had a similar composition (iron–oxide mineral) but with a slight increase in arsenic (As). Besides, iron surfaces have well-preserved tabular diatoms over their surface (Figure 4.3C).

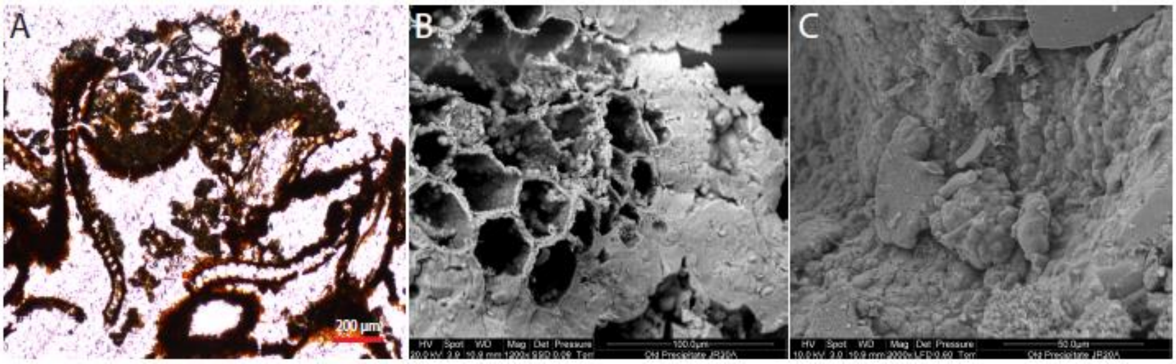

Figure 4.3 Microtextures for subrecent deposits: A) thin section with filaments and detrital coverture at the top of the sample JR-20A; B) SEM photography of plant stem entombed with iron precipitation; C) SEM photography of spherical shaped grains of iron and diatoms.

Subaerial samples on the central (JR-06) and eastern (JR-24 and JR-25B) zones contain two gypsum crystallization, the first one is an anhedral and the second is prismatic. Optical microscopy, using transmitted light, showed colourless anhedral gypsum with sharp to rounded edges (Figure 4.4A). Anhedral gypsum grows over a convex lamination and may form rounded branches during its growth. In crossed polarized light, anhedral gypsum showed cleavages and contact twinning. The prismatic crystals are as a cluster of crystals distributed along a convex lamination. The cluster of prismatic crystals could form a crown group. Crossed-polarized light analysis of sample JR-24 showed prismatic crystals with a high interference colour. On the other hand, SEM analysis showed that anhedral gypsum has lentil-shaped microtexture and forms nodules or spherical shapes. Prismatic crystals are needle-like, and crystals are randomly grouped forming convex roof (Figure 4.4C). Between the surface of the anhedral gypsum and prismatic crystals there is a brown cement coverture; also, the brown cement is commonly found surrounding anhedral gypsum as well as filling gaps left by convex laminations. The brown cement has spherical grain shape (Figure 4.4D) and may contain subrounded polymictic clasts.

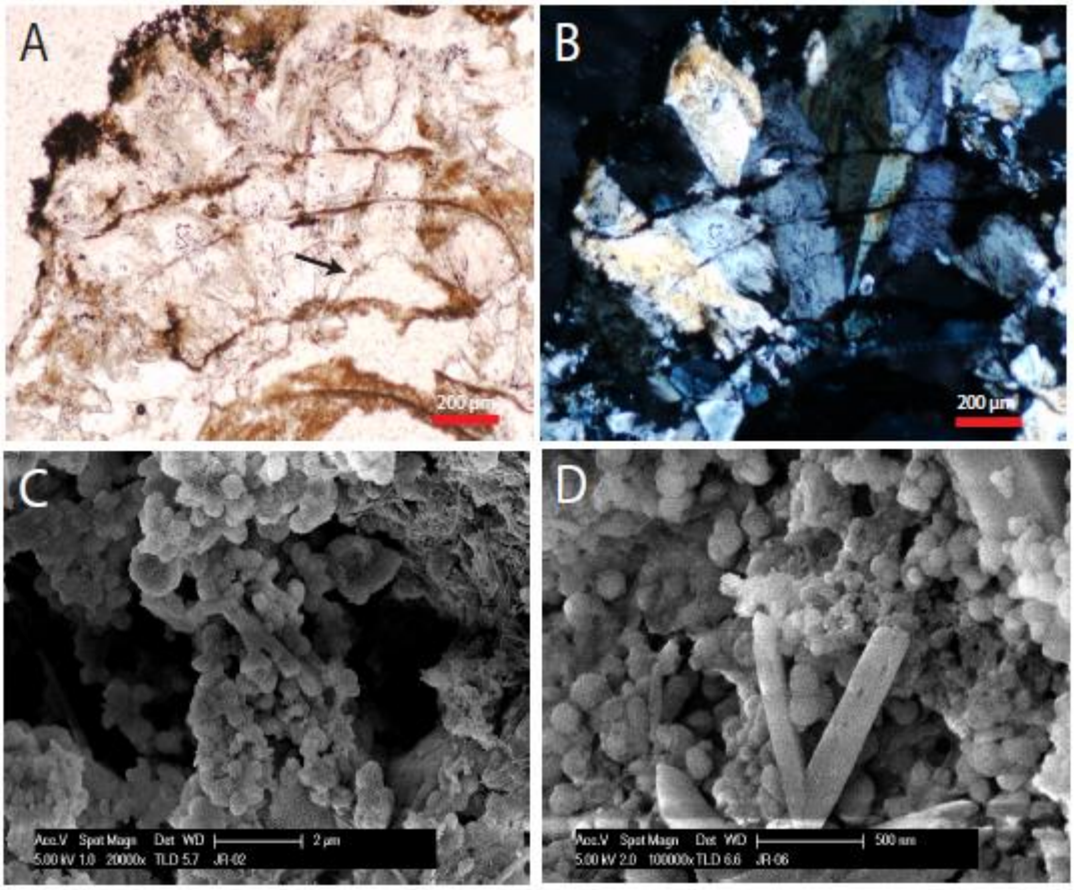

Figure 4.4 Microtextures on subaerial deposits: A) optical microscopy using transmitted light shows gypsum crystal growth forming convex laminations; B) crossed-polarized light shows gypsum twinning; C) SEM images show platy gypsum crystals forming a linear group; D) SEM photography shows prismatic crystals overlying spherical grains.

Other components such as diatoms (boat or rectangular shaped) are around or between the anhedral and prismatic crystals in smaller quantities. It seems that diatoms had a parallel existence during the crystal growth and generated a reaction or dissolution over crystal surfaces, similar examples were found on the central and eastern zone (Figure 4.5A and B). The bottom surface of subaerial deposits can have fluidal texture of gypsum crystals, which could be interbedded with grainy calcite crystals. Also, gypsum crystals can grow over a clastic and irregular surface. For example, sample JR-25B from the eastern zone contains parallel laminations, gypsum crystals have a fluidal orientation and brown cement fills the gaps between crystals; the brown cement may contain polymictic clasts. Sample JR-19B from the central zone contains wave-laminated horizons at the bottom surface; the base is an interbedding of gypsum and grainy calcite. Samples JR-06 and JR-24, from the central and eastern zones, respectively, have brown to orange trapped semi-round fragments. Gypsum crystals grow above irregular fragment surfaces and can dissolve and incorporate small fragments into their structure. The fragments in samples JR-06 and JR-24 have a heterogeneous composition of polymictic clasts, diatoms and filaments. Polymictic clasts join inside brown cement similarly as diatoms and filaments, and their amount increases towards the outer sides (Figure 4.6A).

Additionally, optical microscopy using reflected light showed that sample JR-06 from the central zone contains opaque minerals. The opaque minerals are overlapping or filling cavities of gypsum crystals and present outstanding characteristics of a sulfide mineral. The first opaque mineral identified has a subrounded shape, yellow colours, and a non-pleochroic and weakly anisotropic view with blue to orange internal reflections. The second opaque mineral has a pink colour with a yellow background, and the edges of the crystal vary from blue to green colours. It is non-pleochroic but it is isotropic. Optical characteristics suggest that opaque minerals are chalcopyrite and copper sulfides such as bornite (Figure 4.6B).

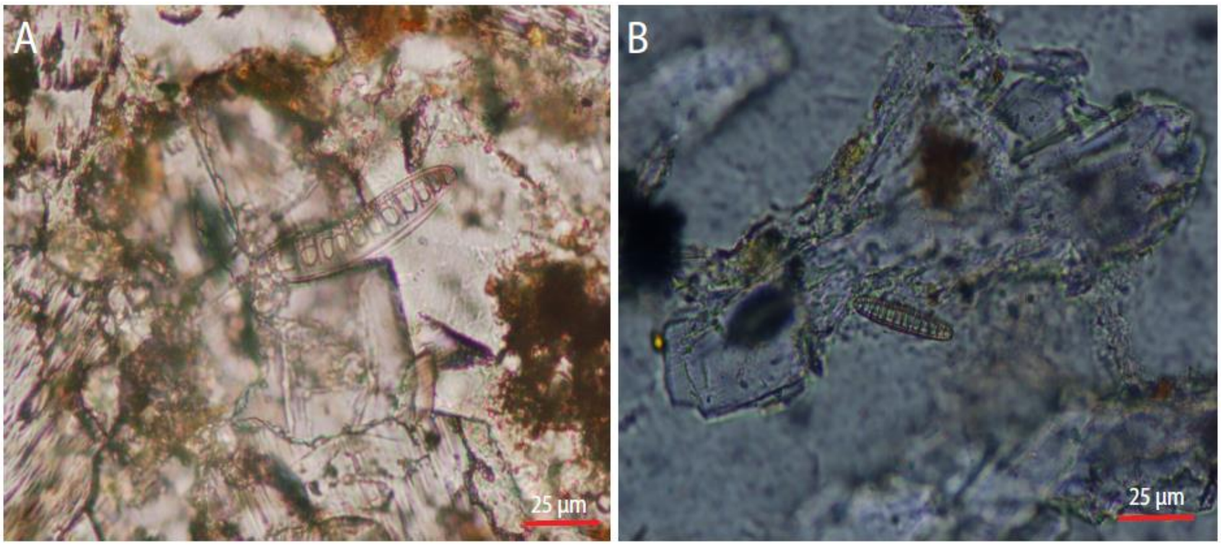

Figure 4.5 Gypsum crystals with diatoms: A) diatom between two crystals, sample JR-24 in the eastern zone; B) diatoms creating dissolution over crystal surface, sample JR-06 in the central zone.

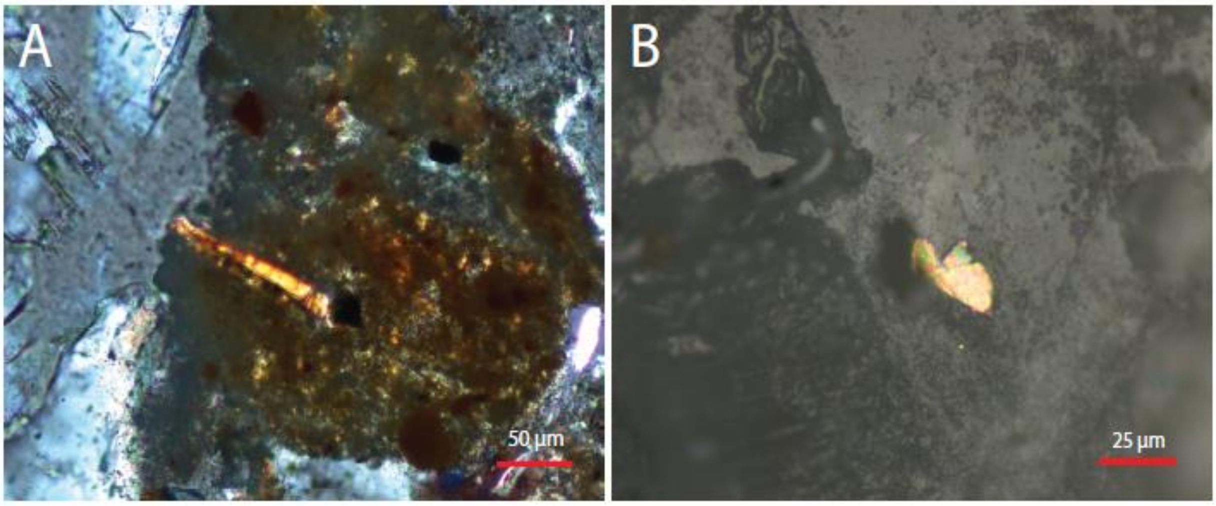

Figure 4.6 A) Transmitted light shows a gypsum crystal overlying a fragment; B) optical microscopy using reflected light shows opaque mineral above gypsum surface.

There is a wide variation in the microtextures of the subaqueous samples among the northern (JR-03), central (JR-10C, JR-11, JR-14, JR-15 and JR-19B) and eastern zones (JR-23A, JR-25B and JR-26). Calcite crystals with grainy, acicular or fragmented shapes could be recognized in samples along the three zones but with variable size. The subaqueous samples from the central and eastern zones have cemented laminations with variable colour, polymictic clasts and a high proportion of biological components. Laminated horizons contain grainy calcite and may be interbedded with other laminated horizons with variable composition such as reported on the central and eastern zones (samples JR-10C, JR-19B and JR-25B). Acicular crystals increase their size from the central to eastern zones. Acicular crystals could form fan shaped microtextures and could be randomly distributed inside laminated horizons (e.g. JR-10C, JR-14 and JR-15). The fan-shaped crystals have a larger size on the eastern zone (JR-25B and JR-26); crystals are interbedded with grainy calcite minerals. Also, acicular crystals grow over a black laminated horizon as elongated prismatic crystals and this black cement fills the joins between crystals (Figure 4.7A).

SEM analysis showed that samples JR-03, JR-10C and JR-25B (from the northern, central and eastern zones, respectively) contain acicular crystals with spherical shaped grains over their surface. For example, sample JR-03 from the northern zone contains acicular crystals and a cluster of spherical morphologies is above their surface (Figure 4.7B). Sample JR-10C from the central zone contains tabular crystals with sharp edges covered by two different cement type textures: spherical and spiky. The EDS result indicated that these grainy textures have a carbonate composition enriched in elements such Fe, As, Si and Na. In contrast, sample JR-25B from the eastern zone, contains elongated acicular crystals, and can cover filament surfaces (Figure 4.7C). Besides, clusters of white grainy crystals with carbonate composition enriched in Fe and Si can cover the surface of the elongated acicular crystals. Fragmented calcite crystals were found on the central zone in samples JR-11 and JR-14. Sample JR-11 contains fragmented calcite crystals forming circular patterns with successive laminations, a black cement could be filling the gaps left during crystal growth (Figure 4.7D). Similarly, sample JR-14 contains laminated horizons with fragmented calcite crystal in smaller proportions.

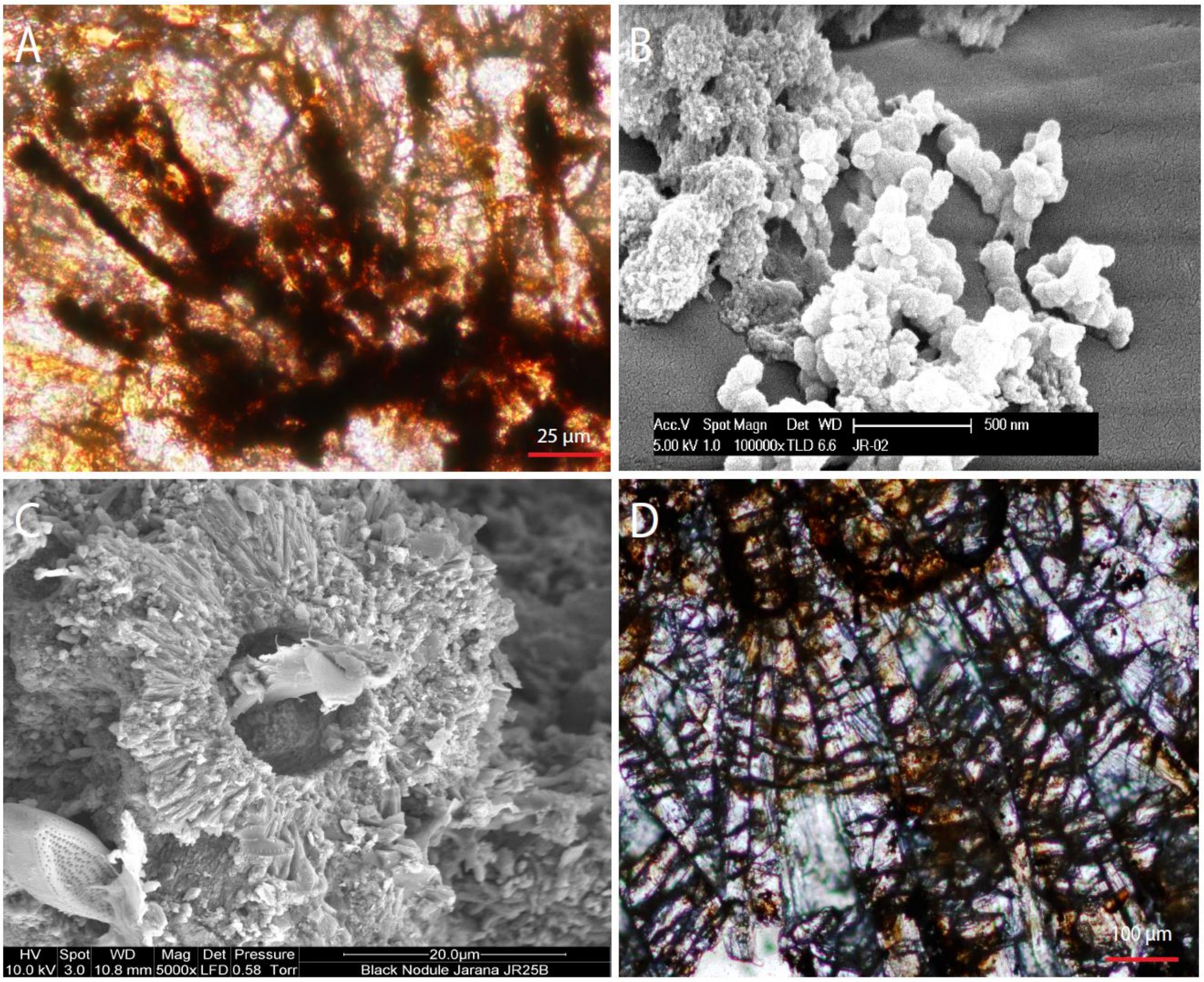

Figure 4.7 A) Black cement filling calcite crystal gaps, sample JR-26; B) spherical microtextures over acicular crystal surface, sample JR-03; C) acicular crystals surrounding a filament, sample JR-25B; D) fragmented calcite crystals with black cement, sample JR-11.

The cemented laminations have an aphanitic texture view under the microscope, but the EDS analysis showed that cemented black laminations contain irregular spherical-shaped grains and bury communities of diatoms (Figure 4.8A). Looking at specific samples, microscope analysis of samples JR-14 and JR-15 showed that cement laminations in some horizons contain randomly distributed polymictic clasts, filaments and diatoms. The clasts have a variable shape and size, the diatoms are boat shaped, and the filaments appear in red horizons forming criss-crossed shapes with knots along their extension (Figure 4.8B). The clasts appear above crystal surfaces joined by cement as in samples JR-11 (central zone) and JR-26 (eastern zone). Diatoms may appear singly or in clusters; for example, optical microscope analysis of sample JR-19B (central zone) showed an ellipsoidal-shaped group of diatoms over black and orange cemented laminations. Furthermore, sample JR-26 (eastern zone) contains a greater presence of diatoms inside nodule morphologies; however, the acicular crystals above nodules contain a singly diatom orientated according to crystal direction.

SEM analysis of sample JR-25B showed laminated horizons with diatoms and leaves randomly distributed inside nodules; diatoms and plants are over crystal surfaces or entombed by the cement. The EDS analysis showed that black cemented laminations have a carbonate composition with high concentrations of Mn and Fe, a moderate amount on Si and Ca, and with just low levels of As. Also, there is a high concentration in oxygen (O:

23.76 Wt%), which may suggest the precipitation of manganese-oxide minerals. On the other hand, the orange laminated horizons have a carbonate composition with high concentrations on Fe, moderate amounts on Si, and traces of Ca, As and Mn. Also, the high concentration in oxygen (23.76 Wt %), may have influence into the precipitation of iron-oxide minerals. Generally, those samples with greater cement laminations (JR-10C, JR-14, JR-15 and JR-23A) came from the central and eastern zones. Clasts, filaments or biological components vary laterally and horizontally in each laminated horizon. Samples JR-14 and JR-15 showed iron-laminated horizons with high concentrations of clasts, filaments and diatoms at the bottom side of samples; these components decrease in the middle of sequences and slightly increase again in the upper sequences. The crystals in samples JR-14 and JR-15, though, are largely found in the middle to upper sequences. Samples JR-15 and JR-23A present laminations deposited over a convex–concave-shaped fragment; the deposition process of the laminated horizons can allow the incorporation of small clasts from the big size fragment (Figure 4.8C). The fragments mainly contain non-colour filaments with an irregular waved surface and the centre side could contain an empty hollow (Figure 4.8D).

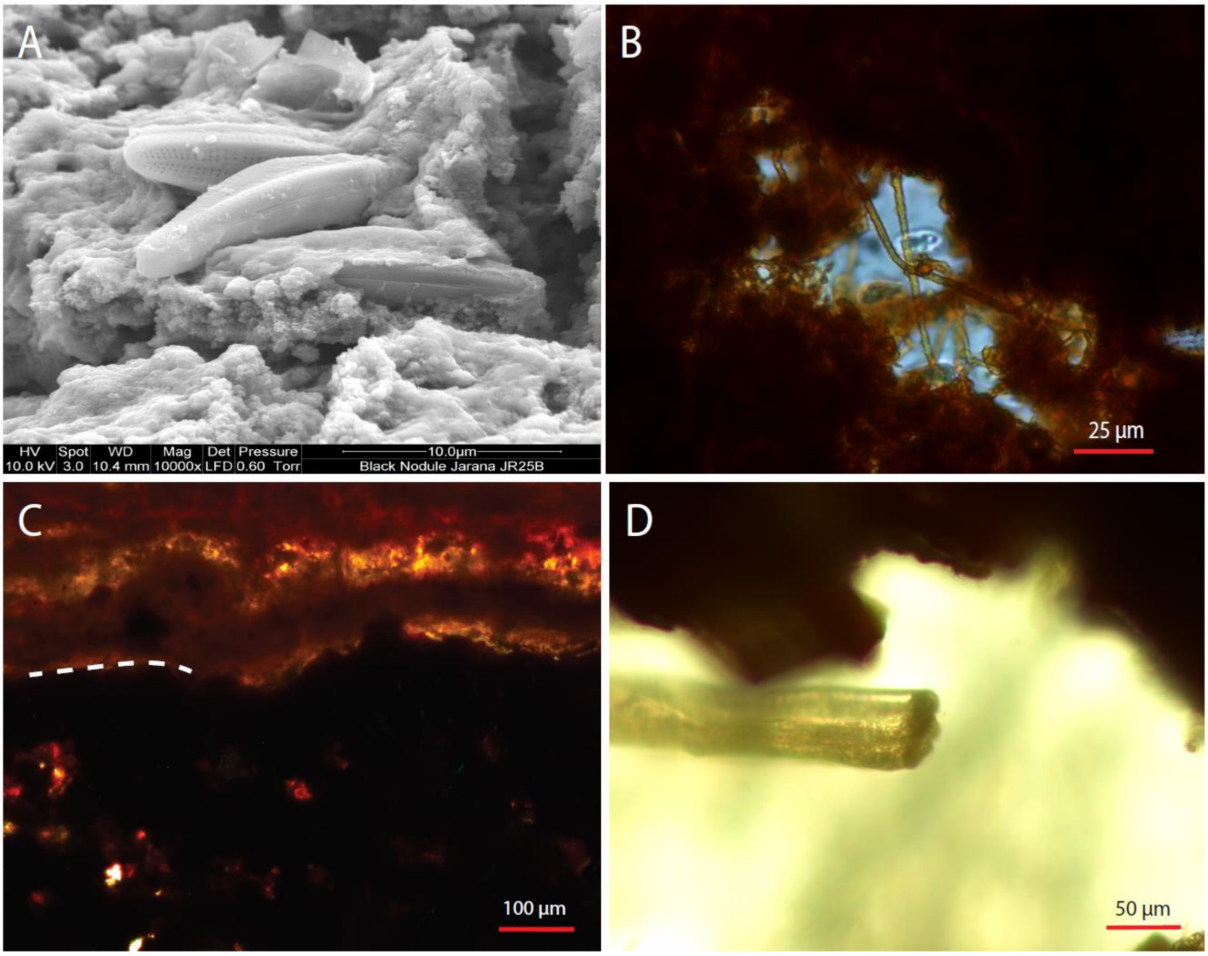

Figure 4.8 A) Spherical grains of manganese cement entombing diatoms; B) criss-crossed shaped filaments with knots in iron cement laminations; C) iron cement precipitation over a fragment; D) non-colour filament inside fragment.

Optical microscopy using reflected light showed that laminated horizons in samples (JR-10C, JR-14, JR-15 and JR-23A) are a good host for disseminated opaque minerals. Samples JR-10C and JR-23A contain a random dissemination for each layer; also, samples JR-14 and JR-15 show an increase of opaque minerals towards the upper sequences. Opaque minerals are over the matrix and have a small size in samples JR-14 and JR-15 but a big size in samples JR-10C and JR-23A. The optical properties indicate the presence of pyrite and copper minerals. A detailed analysis showed that sample JR-10C have isotropic anhedral crystals with pale yellow colours and no pleochroism; which in turn suggests a pyrite mineral. Sample JR-23A shows a large isotropic anhedral mineral with yellow, pink and blue colours and no pleochroism; these optical properties suggests the presence of copper sulfide mineral (Figure 4.9A). The SEM-EDS analysis on sample JR-10C showed shiny crystals overlying a calcareous matrix, and other four distinct minerals. The first mineral has a platy crystal habit; it forms a bunch of plaques attached by a filament line (Figure 4.9C). The EDS indicated that the platy crystals are a mixture of carbonates and oxides mainly enriched in Fe, moderately enriched in Ca, Mn, Si and Sr, and with trace elements of As, Na, Al and K. The second mineral is a small platy crystal, which the EDS identified as a Sr-oxide mineral enriched in Fe and Ca and with trace elements of As, Si, Mn, Ba, P and Na. The third crystal has a pseudo-octahedral shape, which the EDS identified as a Fe-oxide mineral with trace elements of As, Si, Sr, Al, Mn, P, Na and Ba. The fourth crystal overlies the pseudo-octahedral crystal and it has a bunch of spherical shapes, similar to a framboid texture. The framboid shape mineral is mainly enriched in Fe and Cu; it also has low concentrations of Sr, Ca, As, Si, Al, Na and Mn; as well as low concentrations of C, O and S anions (Figure 4.9C). For more details about EDS trace element results see Appendix II.

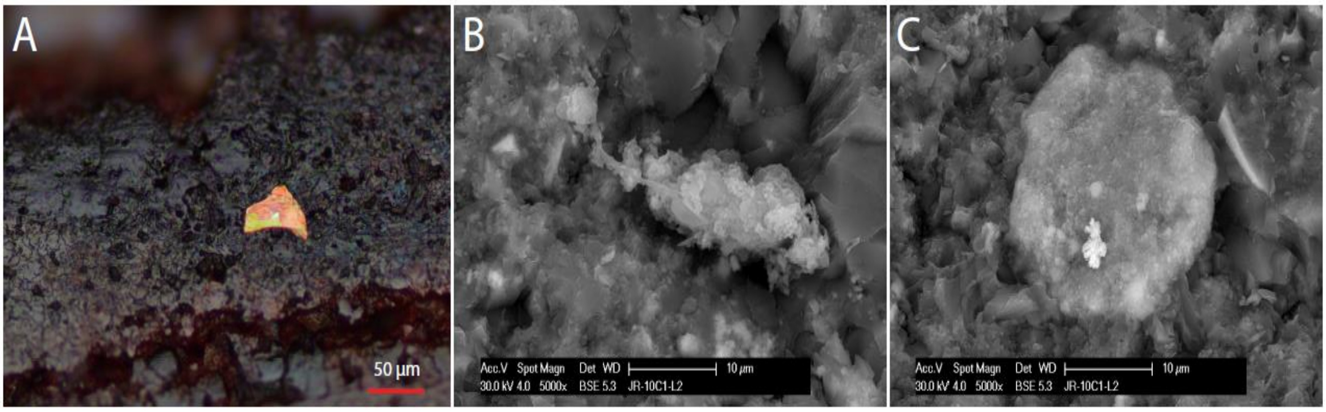

Figure 4.9 A) Sample JR-23A with opaque mineral under reflected light; B) SEM photography of plaques attached by a thin filament inside a carbonate cavity; C) SEM photography of a pseudo-octahedral crystal (iron-oxide mineral), which contains a framboid microtexture, the mineral enriched in Fe and Cu.

4.1.3 Carbonate precipitation

The analysis of eleven thin sections from subrecent and recent deposits using the cathodoluminescence method allowed the identification of carbonate composition with wide variable orange luminescence. From all thin sections, only eight samples from the central (JR-10C, JR-11, JR-14, JR-15 and JR-19B) and eastern zones (JR-24, JR-25B and JR-26) registered orange luminescence. Also, two samples (JR-06 and JR-25B) from the central and eastern zones showed a blue colour luminescence. The results using cathodoluminescence method indicated that carbonate precipitation is frequent in subaqueous deposits rather than subrecent deposits or subaerial deposits.

The central zone contains samples from subaqueous areas with laminated horizons (JR-10C, JR-14 and JR-15) and calcite crystals (JR-11 and JR-19B) with a wide variety of colour luminescence. Samples with parallel continuous lamination, such as JR-10C, JR-14 and JR-15, registered different stages of carbonate deposition. Sample JR-10C represents the best sample for a continuous carbonate precipitation: the thin laminations in this sample registered dark orange luminescence and the upper sequences a light orange luminescence, which represents carbonate changes between iron and manganese elements. The different sequences limit stages of precipitation and register weathered stages covered by other precipitation processes (Figure 4.10A). Iron carbonate horizons could register cavities, which are filled by a lighter orange carbonate precipitation or a variable deposition with luminescence ranging from dark to light orange (Figure 4.10B). Samples JR-14 and JR-15 showed an orange luminescence only in layers with carbonate composition. Laminations show the growth of nodules growth; the nodule builds up with continuous carbonate sequences forming convex groups and is later covered by a thin carbonate lamination (Figures 4.10C and D). Crystalline sample JR-11 registered orange to light orange luminescence, which represents the successive calcite crystal growth, interbedded with a black manganese lamination (Figure 4.10E). The inner area has a lighter orange luminescence and contains small cavities filled with carbonates enriched in iron (dark orange colours) (Figure 4.10F). Sample JR-19B registered dark orange colours distributed in layers, the dark orange colours change to orange through the top sides.

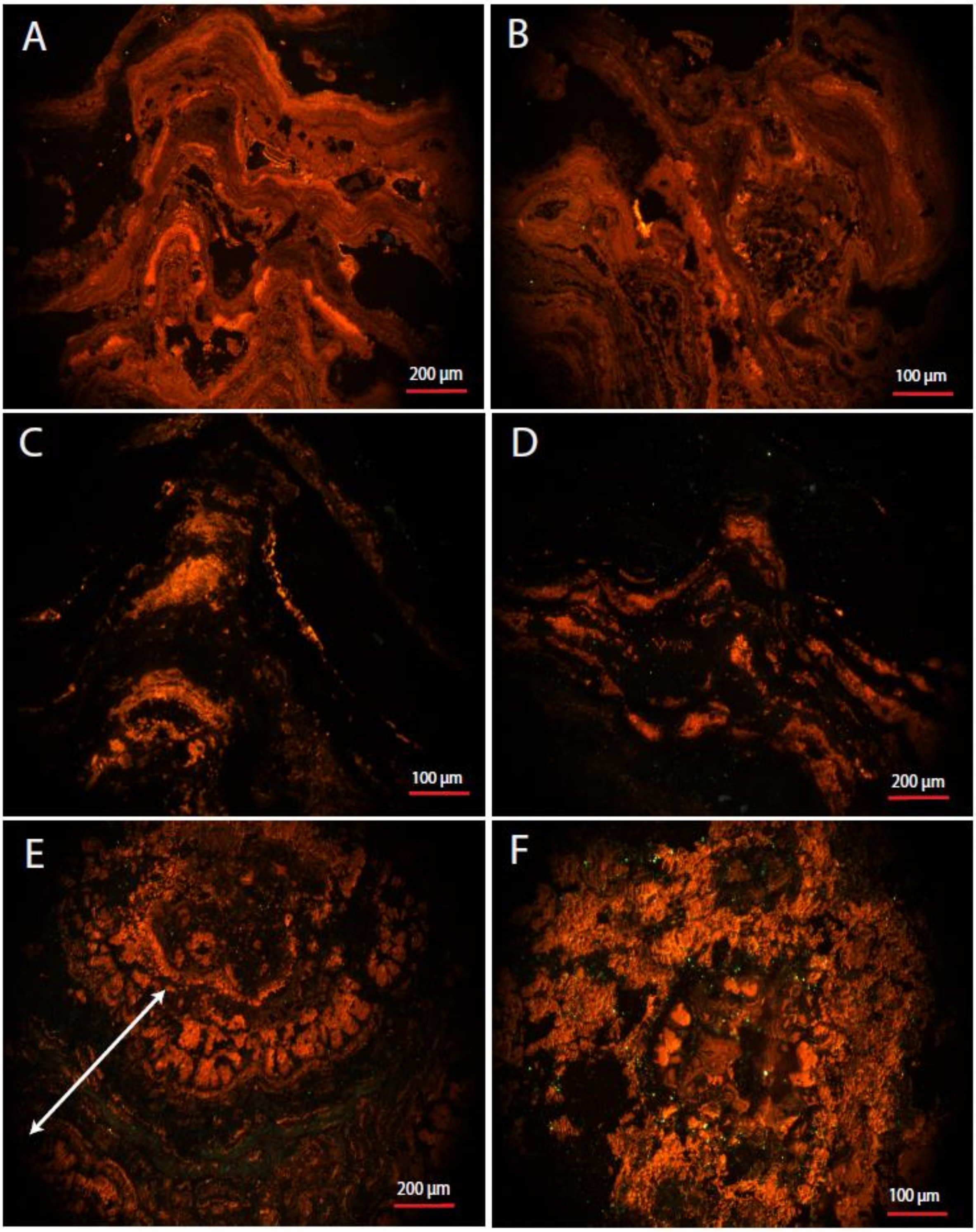

Figure 4.10 Carbonate concentrations in samples from the central zone: A) sample JR-10C shows changes from dark orange to light orange in three horizons; B) cavities in sample JR-10C show a light orange colour; C) sample JR-14 shows carbonate concentrations forming convex laminations covered by a thin carbonate precipitation; D) sample JR-15 shows laminated horizons with carbonate composition; E) sample JR-11 shows a circular shape with fragmented calcite crystals in the inner side; F) a zoom into the inner circular shape of sample JR-11 shows cavities filled by carbonate precipitation.

In contrast, subaerial deposits contain carbonate composition at the bottom part of their base, as shown in sample JR-19B. Carbonates have a dark orange luminescence forming a wave lamination; wave laminations contain carbonate precipitation enriched on Fe interbedded with other laminated horizons (Figure 4.11A). However, sample JR-06 from subaerial deposits registered blue colours inside its structure, which suggests high concentrations on Si element (Figure 4.11B).

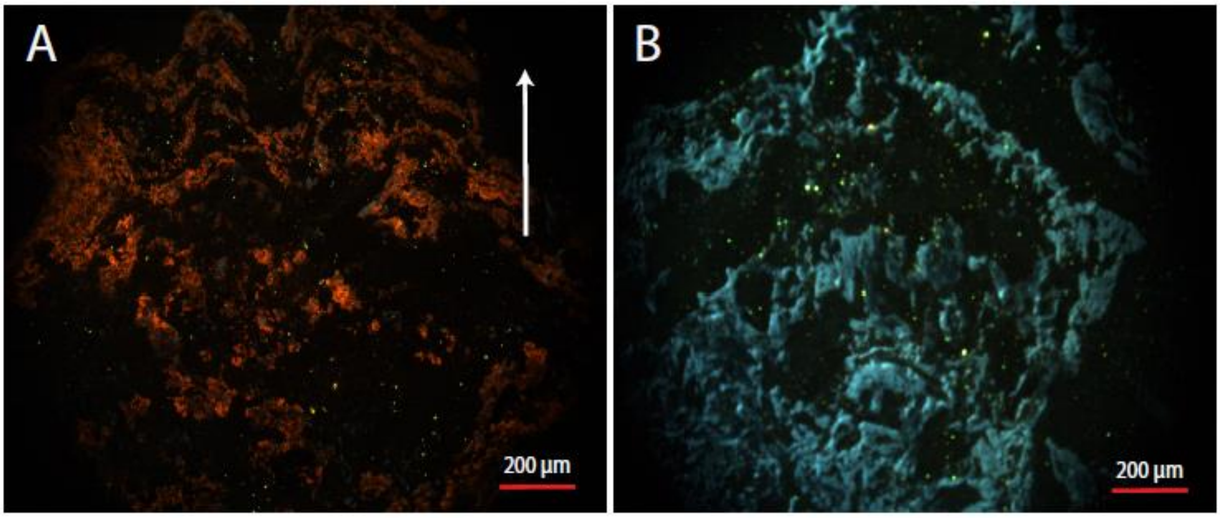

Figure 4.11 Subaerial deposits from the central zone: A) sample JR-19B shows wave-laminated horizons; B) sample JR-06 show blue colour luminescence.

The eastern zone contains three samples (JR-24, JR-25B and JR-26) from subaqueous areas with calcite crystals and carbonated clasts. Samples register orange lightning colours, which represents the carbonate composition enriched on Fe and Mn. The luminescence register the continuous crystal growth of calcite minerals (Figure 4.12A), and the contact between crystals and clastic horizons. Clastic horizons change to carbonate crystals progressively from inner to outer sides (Figure 4.12A); also, clasts are covered by manganese laminations and separated from carbonate crystals (Figure 4.12B). Furthermore, sample JR-24 is a representative example of the transition from subaqueous to subaerial deposits. The orange luminescence represents the carbonate areas and blue luminescence represents a horizon enriched in silica. Moreover, sample JR-24 shows that subaerial deposits can incorporate carbonate fragments (orange circles) into their structure (Figure 4.12C). Also, the analysis under transmitted light showed brown cemented horizons and cathodoluminescence analysis showed an orange light luminescence, defining carbonate clast as horizons inside convex laminations (Figure 4.12D and E).

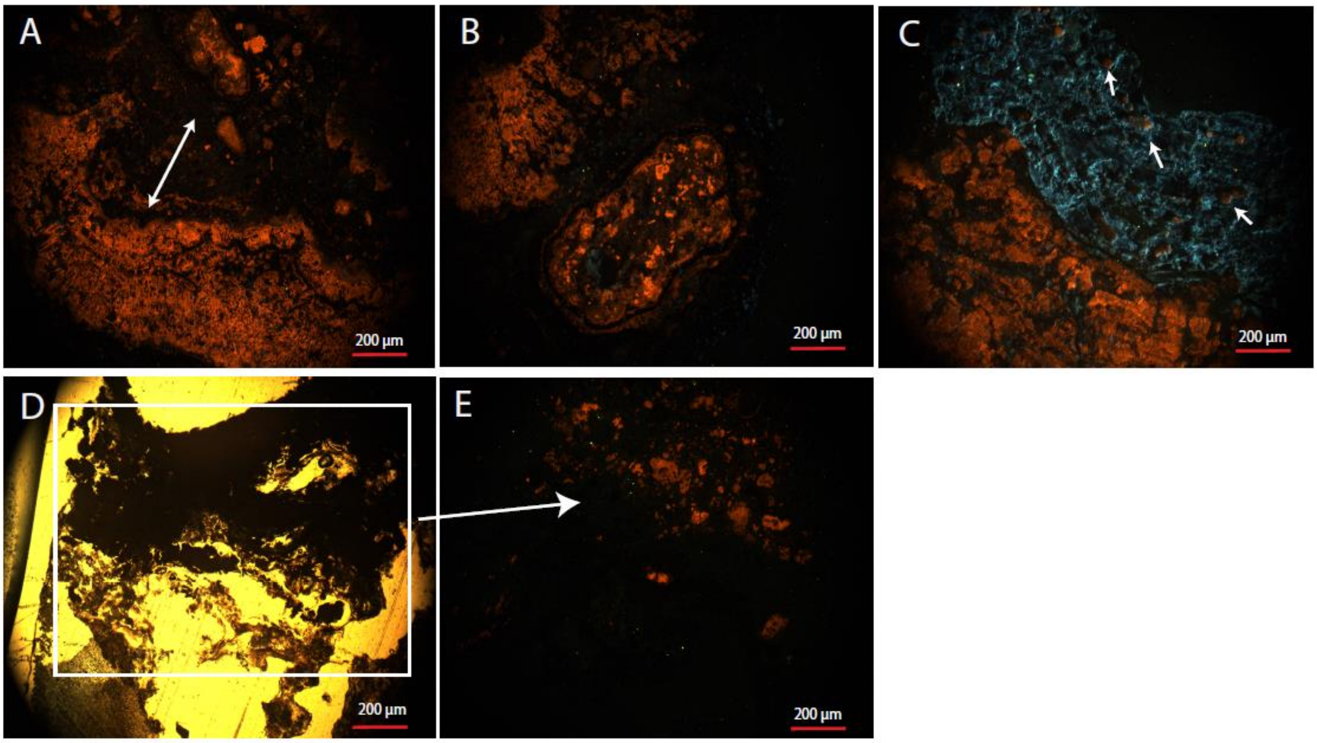

Figure 4.12 Carbonate concentrations in samples from the eastern zone: A) sample JR-19B shows wave-laminated horizons; B) sample JR-06 shows blue colour luminescence.

4.2 Chemical composition

Laser ablation ICP-MS and 4-acid digest methods have been used to analyse the chemical composition of the sample precipitates. The chemical results turned out convenient to recognize the element concentrations and allowed to do an analysis of three topics: The element amount in horizons with vitreous and metallic lustre for recent subaqueous deposits; the trace element concentrations in hot spring deposits and host rocks using spider diagrams; and the correlation among elements for recent hot spring deposits using binary diagrams.

4.2.1 Element concentration in laminated horizons

Subaqueous samples at the central and eastern zones have laminated structures with a wide range of colours and lustre characteristics. Chemical results were convenient to identify and confirm the main element inside laminated horizons with vitreous and metallic lustre. Two samples were considered for the following description (JR-15 and JR-23A), the resulting analysis was important to understand the anomalous element enrichment in samples.

4.2.1.1 Horizons with vitreous lustre

Samples JR-14 and JR-15 from the central zone, both register particular horizons with vitreous lustre. The analysis of sample JR-15 allowed the identification of five colourful horizons (A, B, C, CC and D). Horizons contain an opaque and vitreous lustre, but particularly, horizon C shows a clear vitreous lustre with grey and white colours (Figure 4.13A). The Laser Ablation ICP-MS results indicated that horizons A and C register a high concentration of Si compared to other horizons (Figure 4.13B). An average of Si inside each horizon showed that horizons A and C contain Si element above 60 Wt %, and trace concentration of Fe, Mg, Ti, Al, B and As (Figure 4.13C). Thus, chemical results confirmed a brief silica precipitation in subaqueous precipitates with laminated structures.

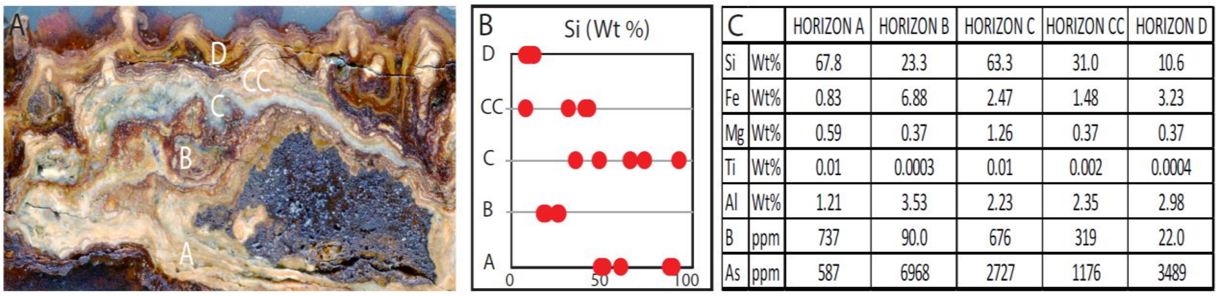

		HORIZON A	HORIZON B	HORIZON C	HORIZON CC	HORIZON D
Si	Wt%	67.8	23.3	63.3	31.0	10.6
Fe	Wt%	0.83	6.88	2.47	1.48	3.23
Mg	Wt%	0.59	0.37	1.26	0.37	0.37
Ti	Wt%	0.01	0.0003	0.01	0.002	0.0004
Al	Wt%	1.21	3.53	2.23	2.35	2.98
B	ppm	737	90.0	676	319	22.0
As	ppm	587	6968	2727	1176	3489

Figure 4.13 A) Sample JR-15 shows horizons A, B, C, CC and D; B) laser ablation ICP MS results in sample JR-15 horizons; C) table with an average of results for each horizon in sample JR-15.

4.2.1.2 Horizons with metallic lustre

Samples JR-14, JR-15 and JR-23A from the central and eastern zones register laminations with a black colour and metallic lustre, the thickness increases in sample JR-23A (eastern zone). The increase in thickness was convenient to use the 4 acid-digest method. The analysis of sample JR-23A was based on the comparison between the horizon with metallic lustre and orange laminations (Figure 4.14A). The 4-acid digestion identified a higher iron amount in horizons with metallic lustre (34.5 Wt %) compared with orange laminations (27.5 Wt %). The high iron amount is contrasted with the trace element amount in Ca, Al, S, Ti, Mn and Sr, but, at the same time, register an anomalous amount of As (Above detection limit). Additionally, precious (Ag) and base metals (Cu, Zn and Pb) register trace concentrations but Zn registers a higher amount (423 ppm) in orange laminations and Pb has higher amount in horizons with metallic lustre (Figure 4.14 B). Thus, chemical results confirmed the precipitation of iron, as a mineral, interpreted as an iron-oxide mineral (hematite) enriched Pb.

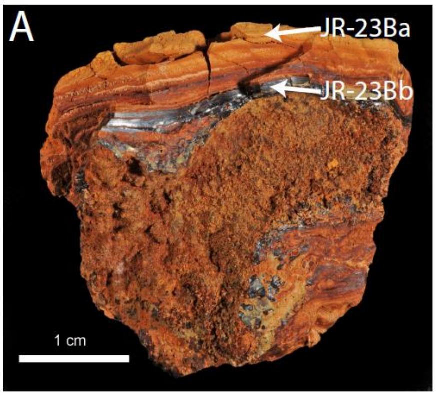

B		JR-23Bb	JR-23Ba
Fe	Wt%	34.5	27.5
Ca	Wt%	2.77	3.91
Al	Wt%	0.04	0.01
S	Wt%	0.06	0.1
Ti	Wt%	<0.001	0.001
Sr	Wt%	0.13	0.15
As	ppm	>10000	>10000
Ag	ppm	<0.002	0.01
Cu	ppm	0.03	0.15
Zn	ppm	297	423
Pb	ppm	415	27.9

Figure 4.14 A) Hand sample (JR-23A) with orange (JR-23Ba) and metallic lustre (JR-23Bb) horizons; B) table with 4-acid digestion results of horizon JR-23Bb and JR-23Ba.

4.2.2 Trace elements in Jaraña hot spring deposits and host rocks

The results obtained from 21 bulk samples, using 4-acid digestion method and 148 spots from sample horizons, in addition to using laser ablation ICP-MS method, allowed the identification of trace element concentration in hot spring deposits and host rock. The trace elements values can be measured in weight percentage (Wt %) and part per million (ppm) units. All samples from the northern, central and eastern zones contain variable concentrations and anomalous enrichment in elements; thus, it was convenient to analyse the chemical results using spider diagrams dividing the samples into five groups of samples: subrecent deposits, subaerial deposits, subaqueous deposits with calcite crystals, subaqueous deposits with laminated structures and host rock. The analysis of these five groups of samples was useful in identifying the factors such as spatial distribution, mode of emplacement or particular characteristics in samples, which may represent an influence for anomalous peaks. Additionally, chemical results took into consideration the values obtained from the following samples: JR-03 from the northern zone; JR-06, JR-07, JR-10C, JR-11, JR-12, JR-14, JR-15, JR-19A, JR-19B, JR-20A, JR-20B, JR-21B and JR-22 from the central zone and JR-23A, JR-23B, JR-24, JR-25B and JR-26 from the eastern zone (Detailed results are in Appendix II).

4.2.2.1 Major element concentration (Wt%)

Subrecent samples contain Fe, K and S abundances above 1 Wt %. Arsenic, Ca, Al, Na and P contain moderate abundances in the range of 0.1 to 1 Wt %, and other elements such as Mg, Ti, Sr and Mn register a wide range of values below 0.1 Wt % (Figure 4.15A). Fe element shows the highest concentrations in the range between 26.9 and 38.3 Wt %; as opposed to Ca which contains the lowest amount in the range from 0.06 to 0.09 Wt %. K (0.15-4.29 Wt %) and S (4.08-9.51 Wt %) also contain high amount followed in order of concentrations by As (1090->10000 ppm). Al (0.07-0.84 Wt %), Na (0.39-0.47 Wt %), Mg (<0.01-0.05 Wt %) and P (0.08-0.56 Wt %) which contains the lowest amount. However, Mn (5-28.8 ppm) and Sr (25.5-387 ppm) represent the elements with minor concentrations on subrecent precipitates.

Chemical results for subaerial samples, obtained from laser ablation ICP-MS and 4 acid-digest methods showed that Ca, Si and S have major concentrations (above 1 Wt %), but Fe, Al and Na could contain a variable range of concentration, from minor to major amounts (from 0.01 to 1 Wt %) and K, Mg, P, Ti, Mn, Sr and As have minor concentrations (less than 0.1 Wt %). Both methods showed different ranges of concentrations only for Fe and Al (Figure 4.15B). While laser ablation ICP-MS results show low quantities for Fe (0.001-0.05 Wt %) and Al (0.001-0.36 Wt %); the 4 acid-digest methods show a high concentration for Fe (0.04-13.25 Wt %) and Al (0.02-1.87 Wt %). Of all the elements; Ca, Si and S have the highest concentrations (above 1 Wt %) in subaerial samples. Besides, Ca, Na, Mg, Si, Sr and S contain positive enrichment, while Fe, Al, K, P, Ti, Mn and As show the opposite (Figure 4.15B). The concentrations for Fe, Al, Na and K are in the range from 0.01 to 10 Wt % and Mg and Sr contain low concentrations in the range between 0.1 and 1 Wt %. Subaerial samples contain Ca in the range from 5.75 to >25 Wt %, but Si and Sr present similar amounts. Si is in the range of 0.98 Wt % and Sr is in the range of 1370-3153 ppm. However, basal fragments contain a notable lowest concentration for Si (0.008 Wt %) and Sr (123-124 ppm) compared with subaerial deposits. Na (0.09-3.51 Wt %), K (<0.02-0.28 Wt %) and Mg (0.09-1.05 Wt %) contain variable range of concentrations according to 4 acid digest results. However, subaerial samples from the central zone contain the highest amounts of Na, K and Mg comparing to the eastern zone (Figure 4.15B). Moreover, As and Mn show a wide range of concentrations; the laser ablation ICP-MS results showed concentrations for As in the range of 49.01-891.959 ppm and for Mn in the range of 0.81-320 ppm, but basal fragments show the lowest amount for As (1.54-1.63 ppm) and Mn (0.06-0.08 ppm). In contrast, the 4 acid-digest methods showed the highest amounts for As (150- >10000 ppm) and Mn (23.3-3920 ppm). Of all the group of subaerial samples, only sample JR-14c_d contains anomalous concentrations as compared with other subaerial samples. Sample JR-14c_d contains anomalous enrichment on As (>10000 ppm) and Al (1.87 Wt %) but a notable decrease in Ca (5.75 Wt %) and Sr (1815 ppm). This result may be due to the bulk of sample used for the analysis; in this case, the JR-14c_d sample was taken from a thin layering may have included information about the precipitates below.

Chemical results for subaqueous samples with calcite crystals, obtained from LA-ICPMS and 4 acid-digest methods (one sample: JR-25Bc) present similar results. Concentrations are variable from 0.01 to 10 Wt %, approximately, for Ca, Fe, Al, Na, K Mg, Si, Mn, Sr, As and S. Only P and Ti show concentrations below 0.01 Wt %. Ca contains a concentration above 25 Wt %, according to 4 acid-digest results. Fe, Si and Mn contain a variable range of concentration from 0.01 to more than 10 Wt % (Figure 4.15C). Thus, Fe concentration varies from 0.25 to 10.4 Wt %, Si is in the range of 0.17 to 26.4 Wt % and Mn is in the range of 112 to 319428 ppm. The variable concentration of these elements (Fe, Si and Mn) in the central zone is different from that in the eastern zone. Subaqueous samples with calcite crystals from the eastern zone contain a higher concentration of Fe, Si and Mn than that of the central zone. However, samples JR-11 and JR-19B from the central zone show different quantities; sample JR-11 shows a slight increase if compared with sample JR-19B (Figure 4.15C). Al, Sr and As contain concentrations in the range of 0.01 to 1 Wt %. Al concentrate amounts from 0.01 to 0.27 Wt %, Sr has concentrations in the range of 683 to 8405 ppm and As has concentration amounts in the range of 544 to 18919 ppm. Similarly, these three elements (Al, Sr and As) show a slight increase in the eastern zone. The 4 acid-digest methods showed results for Na, K, Mg, P and S. Na contains 0.19 Wt % amount, K has 0.07 Wt %, Mg has 0.12 Wt % and S has 0.73 Wt %. Moreover, P (0.005 Wt %) and Ti (0.004 Wt %) register the lowest concentrations.

Subaqueous samples with laminated structures present results from laser ablation ICP-MS and 4 acid-digest methods. Both methods show similar results. Ca, Fe and Si are the elements with concentrations above 1 Wt %. Al and As has a variable range of concentration amount from 0.01 to 10 Wt % (Figure 4.15D). Na, K, Mg, P, Ti, Mn, Sr and S contain concentrations below 1 Wt %. Ca has concentrations in the range of 1.17 to 24.3 Wt %, only the basal fragment registers 0.06 Wt%. Fe contains 0.38 to 60.2 Wt % and Si has from 0.09 to 92.6 Wt %. Of these three elements (Ca, Fe and Si), Ca has the highest concentrations in sample JR-10C from the central zone and the lowest concentrations is in sample JR-03 from the northern zone, the basal fragment contains a notable decrease compared with subaqueous samples. Fe has highest concentrations in sample JR-23A from the eastern zone and Si presents the highest concentrations in sample JR-15 from the central zone (Figure 4.15D). In the case of Al their concentrations are on the range of 0.01 to 6.55 Wt % and for As on the range of 173 to 71204 ppm. Al registers its highest amount on samples JR-03 from the northern zone and samples JR-15, JR-07, JR-12 and JR-19B from the central zone. As registers its highest amount in sample JR-14 from the central zone, but some of the horizons in the sample, register the lowest concentrations (Figure 4.15D). The results for Mn and Sr show concentrations on the range of 46.5 to 8997 ppm and 85.9 to 1056 ppm, respectively. Mn and Sr have their highest concentrations on sample JR-10C from the central zone. However, the lowest concentrations for Mn are on sample JR-03 from the northern zone and some horizons from sample JR-15 from the central zone. Sr register their lowest concentrations on the basal fragment, results are totally different from subaqueous deposits. Other elements with values below 1 Wt % are Na (0.09-1.29 Wt %), K (0.03-0.68 Wt %), Mg (0.05-0.54 Wt %), P (0.01-0.17 Wt %), Ti (<0.001-0.56 Wt %) and S (0.06-1.43 Wt %). Na, K and Ti contain highest concentrations in samples from the central zone. S contains highest concentrations in samples from the northern zone (JR-03) and in sample JR-10C (Figure 4.15D).

The host rock sample contains results from 4 acid-digest methods. The results showed that the elements analysed for subrecent and recent deposit samples have concentrations below 1 Wt % (Figure 4.15E). Ti is an element that has the lowest concentrations in subrecent and recent deposits; however, host rock contains a slightly increase on 0.56 ppm. In this case, Mn contains the lowest concentrations (1 ppm), followed by Sr (10.1 ppm). Other elements present the following results: Ca contains 0.02 Wt %, Fe contains 0.09 Wt %, Al contains

0.11 Wt %, Na contains 0.013 Wt %, K contains 0.05 Wt %, Mg contains less than 0.01 Wt %, P contains 0.003 Wt %, As contains 30.5 ppm and S contains 0.03 Wt %.

The most important findings in the chemical results for major elements in Wt % amounts is that subrecent and recent deposits contain different amount of major elements comparing to host rocks; while hot spring deposits register their lowest values on Ti host rock shows an opposite result. Subrecent and recent deposits contain similar high amount of Fe. Recent deposits contain high amount of Ca comparing to subrecent deposits. Subrecent deposits contain the highest values on K comparing to recent deposits. Recent deposits register high amount on Si. Subrecent and recent deposits contain similar values of S (above 1 Wt %). Subaqueous samples with calcite minerals contain the highest amount of Mn. Subaqueous samples with laminated structures contain the highest amount on As (above 1 Wt %) for samples with high amount in Fe (above 1 Wt %).

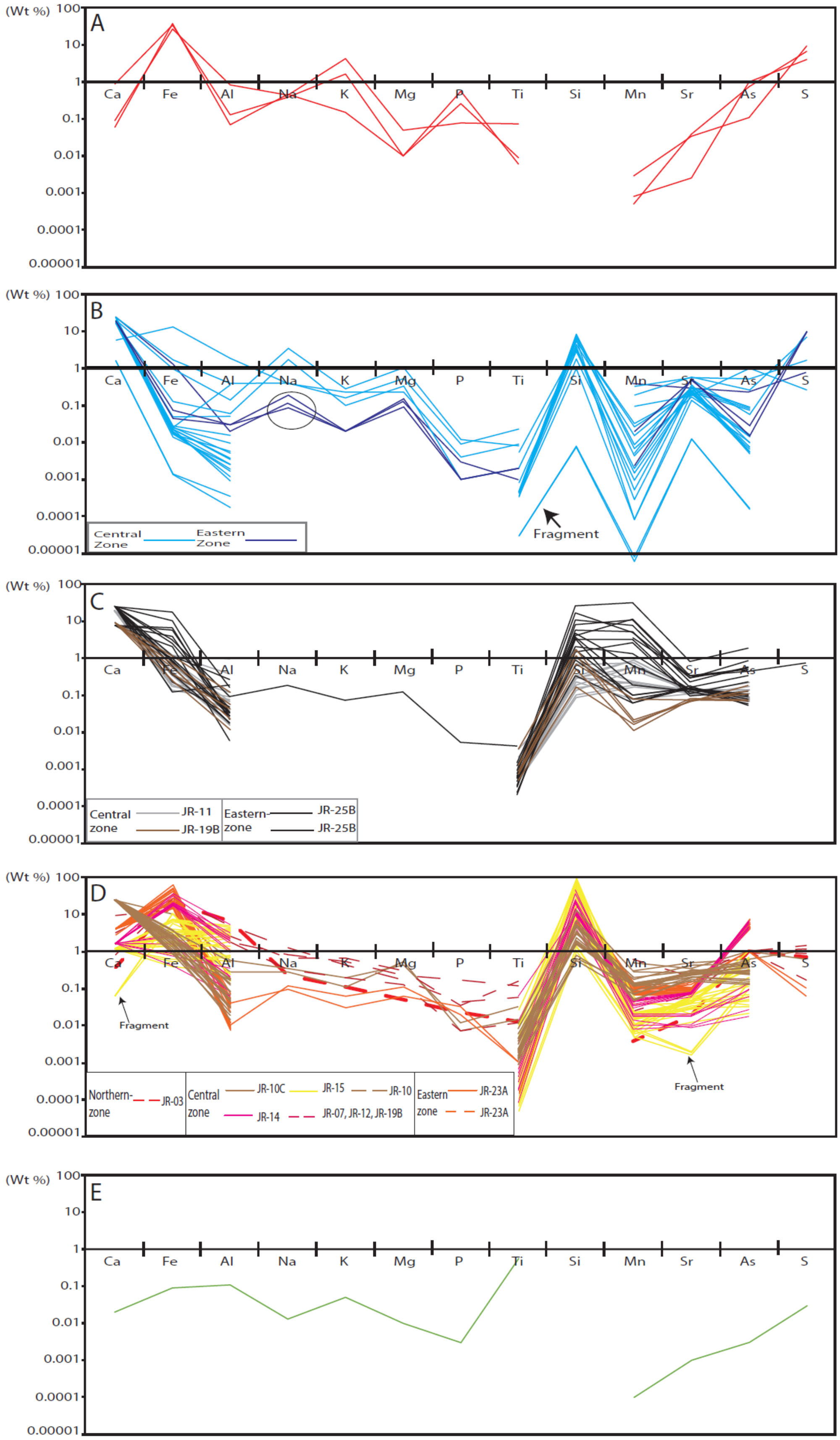

Figure 4.15 Spider diagrams with elements in major amount concentration (Wt %) for: A) subrecent deposits; B) subaerial deposits; C) subaqueous deposits with calcite crystals; D) subaqueous deposits with laminated structures; E) host rock outcrop. (For diagrams B, C and D; continues lines represent Laser Ablation ICP-MS method and dashed lines represent 4 acid-digest methods).

4.2.2.2 Low element concentration (ppm)

The chemical results from the four-acid digestion and laser ablation analysis indicate variable concentrations of trace elements (i.e. below 1000 ppm) in the ancient and recent precipitates; chemical values were compared with the host rock. The chemical results were normalized to the average composition of the Upper Continental Crust (Rudnick and Gao, 2003) and new values were illustrated in spider diagrams. Spider diagrams plot elements ordered according to periodic table position – i.e. metals, metalloids and non metals against numerical values in ppm. The description focuses on chemical values of ancient precipitates, subaerial deposits, subaqueous samples with calcite crystals, subaqueous samples with laminated structures and their comparison with a host rock.

Subrecent samples contain abundances above 1 ppm for the metal Mo (8.15-111 ppm) and the metalloid Sb (1.71-7.72 ppm); also, the metals Cs (6.51-31.8 ppm), Y (0.09-1.04 ppm), Cd (0.05-0.12 ppm) y Tl (0.39-7.93 ppm) show moderate enrichment. Li, U, Ta, Cu, Zn, Ga, In, Sn and Pb appeared in moderate amounts, ranging from 0.01 to 1 ppm. Rare earth elements (REE) ranged in concentration from 0.001 to 0.01 ppm. Metalloids registered a moderate trace concentration (0.01–1 ppm) for Bi and Ge, Ag contains the lowest concentration on the range of 0.011 to 0.028 ppm.

Subaerial samples contain abundances above 1 ppm for B (2.19-1070 ppm) and abundances above 0.1 ppm for Cs (0.03-72.4 ppm), Mo (0.17-6.33 ppm), W (0.4-9.92 ppm), Cd (0.01-15.9 ppm) and Tl (0.02-2.94 ppm). Li also contains values above 0.1 ppm, only basal fragments concentrate Li element below 0.1 ppm. Chemical results, using the 4 acid-digest method, indicated that U (3.62 ppm), Co (58.8 ppm), Ni (37 ppm), Cu (108.5 ppm) and Zn (565 ppm) contain positive peaks showing anomalous enrichment in some samples, which is frequent in samples from the central zone. Rare earth elements (REE) contain values below 0.01 ppm; however, there is a slight increase of concentrations for samples from the central zone. Moreover, Sc shows similar differences of concentration between the central and the eastern zone, samples from the central zone contain the highest concentration on Sc compared with to the eastern zone (Figure 4.16B).

Subaqueous samples with calcite crystals contain the results from laser ablation ICP-MS and 4 acid digest methods, which present similar results. Subaqueous samples with calcite crystals show abundances above 1 ppm Mo (0.15-45.8 ppm) and W (0.37-620 ppm) based on 4 acid-digest results, whereas the results for B (14.9-198 ppm) and Sb (1.1-132 ppm) were based on laser ablation ICP-MS. Moreover, the metals Li, Cs, Be, Sn, Tl and metalloid Ge have concentrations above 0.1 ppm; these elements show a notable difference in concentration between the central and eastern zone. Samples from the eastern zone contain a slight increase in concentrations on Li, Cs, Be, Sn, Tl and Ge compared with the central zone. Also, there is an anomalous positive peak (198 ppm) registered on sample JR-25B from the eastern zone. The central zone register indicates that sample JR-11 contains the highest amount of Ni (0.35-2.83 ppm), Cu (0.74-6.88 ppm), Zn (1.52-8.87 ppm) and Tl (0.48-16.3 ppm) in comparison with sample JR-19B (Ni: 0.3-0.64 ppm, Cu: 0.17-0.8 ppm, Zn: 1.19-2.83 ppm, and Tl: 0.14-0.58 ppm). Pb contains its highest concentrations in sample JR-25B from the eastern zone, decreases in samples JR-11 and is low in sample JR-19B (Figure 4.16C). Rare earth elements (REE) have concentrations of around 0.01 ppm and the trace elements with the lowest concentrations were Sc and Ag.

Subaqueous samples with laminated structures contain the results from laser ablation ICP-MS and 4 acid digest methods, which present similar results. The subaqueous deposits show abundances above 1 ppm for Cs (1.39-727 ppm), Mo (0.38-12 ppm), W (0.13-200 ppm), Ge (1.25-80 ppm), B (16.3-1221 ppm) and Sb (1.68-227 ppm), and abundances above 0.1 ppm for Li (1.42-150 ppm), Be (0.37-48.3 ppm), Cd (0.52-18.3) and Tl (0.24-30.9 ppm). Moreover, rare earth elements (REE) have concentrations above 0.01 ppm and Ag register the lowest concentrations between <0.002 to 0.1ppm obtained using 4 acid-digest result methods. The northern zone contains a sample (JR-03) that contains the highest concentrations in Mo. The central zone contains a sample (JR-15) that has the highest concentrations on Co, Ni and B, sample JR-14 from the same zone (central) contain the highest concentrations on Cu, Zn and Cd and sample JR-10C contains the highest amounts on Li and Ge. The eastern zone registers a sample (JR-23A) that contains high concentrations on Pb and Sb. Samples from the northern, central and eastern zones contain the same range of values for each element in ppm; however, the V, Cr, Co, Ni, Cu, Zn and B show a wide range of values. Specifically, samples from the central zone show different values for each one; for example, sample JR15 contains high values on Co, Ni, Cu and Zn, but sample JR-10C contains the lowest amount for the same elements. The Co, Ni and Cu elements show similar high values for samples JR-14, JR-15 (central zone) and sample JR-03 (northern zone); but low values for sample

JR-10C (central zone) and JR-23A (eastern zone). Only for Zn, samples from the three zones show an increase yielding similar values, but sample JR-10C shows only a slight increase forming a different range of values (Figure 4.16D).

The host rock presents results obtained using 4 acid-digest method. The host rock (sample JR-22) contains abundance above 1 ppm for Cs (11.74 ppm), Mo (7.42 ppm), W (710 ppm), Co (62.7 ppm), Cd (0.43 ppm), Sn (2.96 ppm), Pb (47.3 ppm), Bi (0.39 ppm), Sb (5.72 ppm) and Se (0.5 ppm). The rare earth elements (REE) are in the range of 0.01 to 0.1 ppm (Figure 4.16E). Li (19.4 ppm), U (1.11 ppm), Zr (26.6 ppm), Nb (6.35 ppm), Hf (0.71 ppm), Ta (0.33 ppm) and Tl (0.57 ppm) contain a slight increase above 0.1 ppm. Cu and Zn register values of 5.23 ppm and 7.9 ppm, respectively.

The most important finding in the results for trace elements in ppm amounts is that subrecent and recent deposits and host rock contain similar concentrations above 1 ppm for Cs, Mo and Sb. An analysis between hot spring deposits and host rocks allowed to identify that only subrecent precipitates contain the highest concentrations on V (above 1 ppm). Subaerial samples contain the highest amount in B (above 1 ppm). Subaqueous samples represented by laminated horizons contain the highest amounts on REE’s and Sb. Host rocks contain high concentration on W and similar amounts of REE’s compared to recent subaerial and subaqueous samples with calcite minerals and subrecent deposits (Figure 4.16).

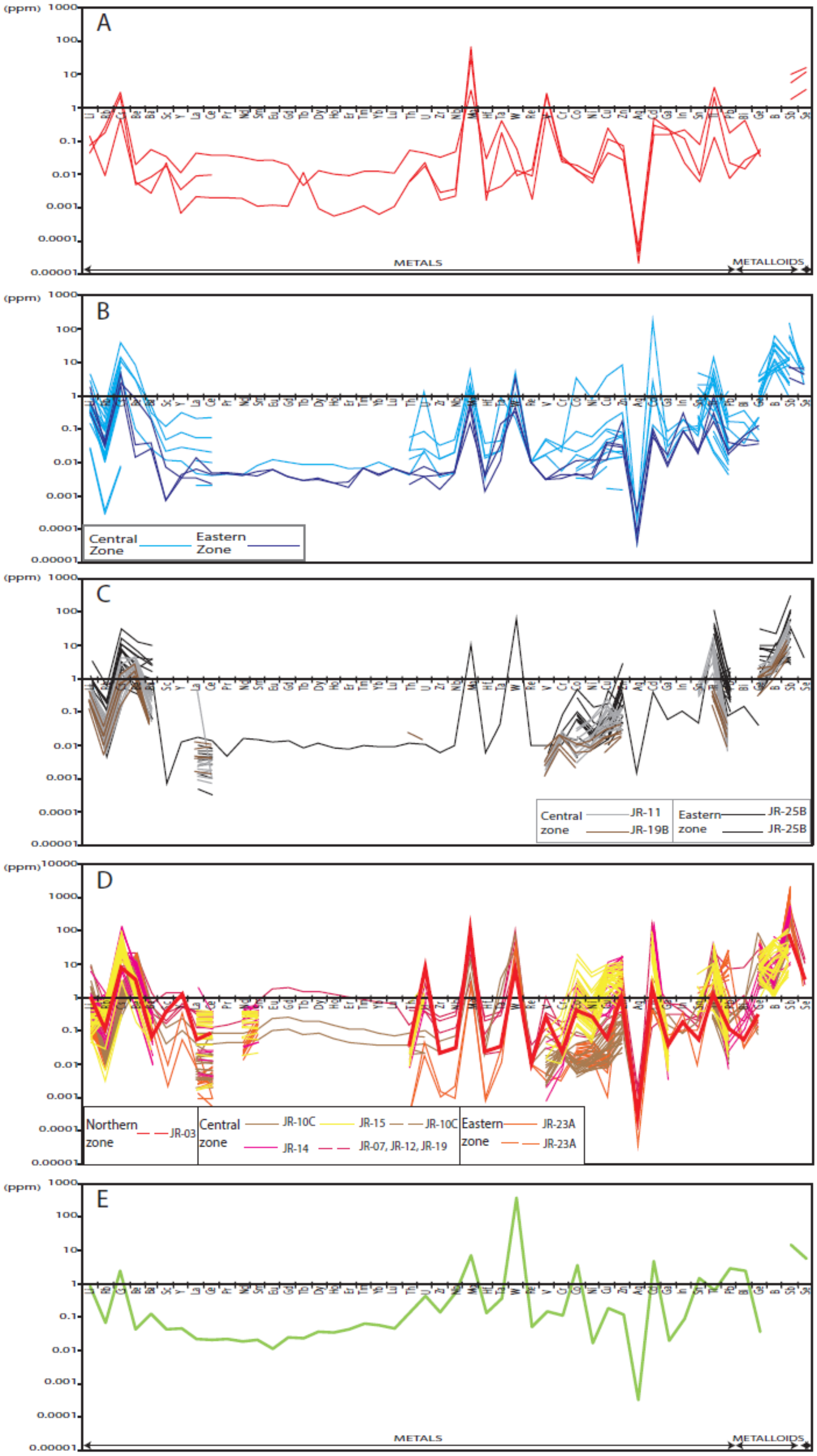

Figure 4.16 Spider diagrams with elements in minor amount concentration (ppm) normalized against average Upper Continental Crust (Rudnick & Gao, 2013) *for: A) ancient precipitate samples; B) subaerial precipitate samples; C) subaqueous samples with calcite crystals; D) subaqueous samples with laminated structures; E) host rock outcrop. (On diagrams B, C and D; continues lines represent Laser Ablation ICP-MS method and dashed lines represent 4 acid-digest method).*

4.2.3 Correlation between trace elements for recent precipitates

The following description presents the analysis of the correlation between elements for recent deposits using binary diagrams. Binary diagrams illustrate the correlation and affinity between two elements to coexist together for subaerial and subaqueous (with calcite crystals and laminated structures) deposits. The description is based on chemical results obtained from laser ablation ICP MS and four-acid digest analysis, and it contains two subsections: first, the analysis for major elements in Wt %; and second, the analysis for trace elements in ppm.

4.2.3.1 Correlation for major elements

The description is based on the analysis of Ca and Fe in order to understand their compatibility with other elements. The first analysis shows diagrams comparing Ca with Fe, Na, Sr and As, while the second analysis shows a comparison between Fe and Al, Mg, Mn and As. Finally, comparisons are shown between Al vs Ti, As vs Al, Si vs Sr and Fe vs Si. It should be noted that the four-acid digest results registered a high detected limit for Ca (25 Wt %) and As (1 Wt %); thus, for the first group of analyses, only 4-acid digest results will be shown.

Ca and Sr are elements that present a perfect correlation for recent precipitates (Figure 4.17C). However, there is no correlation between Ca and Fe or Ca and As (Figure 4.17A and D). The increase in Ca amounts generates a constant value for Fe on subaqueous samples but the increase in Fe generates a constant value for subaerial precipitates. Similarly, the increase of Ca generates a constant value for As for subaqueous samples, but the increase of As generates a constant value for subaerial samples. Also, Na shows scattered plots compared with Ca, which represents the mobility of Na during Ca precipitation. Samples from the northern zone (JR-03) present low Ca concentration; and then, form a separated group with samples from the central and eastern zones (Figure 4.17). Subaerial samples present more affinity to form groups with subaqueous samples from the eastern zone (Figure 4.17C).

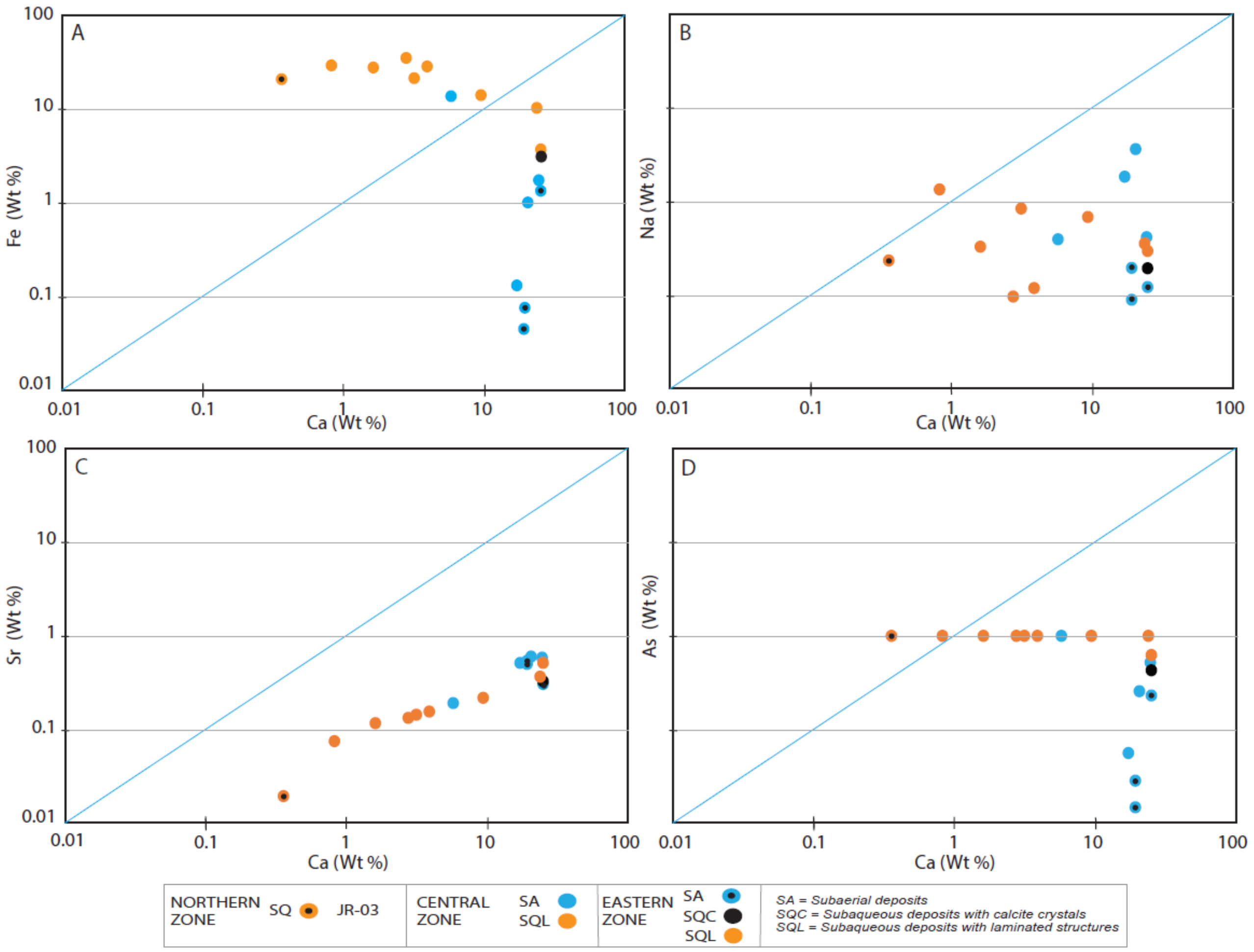

Figure 4.17 Binary diagrams (Wt %) between: A) Ca vs Fe; B) Ca vs Na; C) Ca vs Sr; D) Ca vs As.

The comparison between Fe and Al, Mg, Mn and As in Wt % shows that the subaerial and subaqueous samples fall into two groups depending on Fe concentrations (Figure 4.18). Most of the subaerial samples have a Fe concentration below 0.1 Wt % whereas the Fe concentrations in the subaqueous samples are above 0.1 Wt %. The subaerial samples generally show scattered plots, although the binary diagrams for Fe vs Al and Fe vs As show moderately positive correlations. The binary diagram for Fe vs Al shows no correlation between the two metals in some of the subaerial samples but correlation in others (Figure 4.18A). The diagram of Fe vs As shows scattered plots of subaerial samples with a positive correlation (Figure 4.18D).

Subaqueous samples show scattered plots in Fe vs Al and Fe and Mn, but positive correlation in the binary diagrams for Fe vs Mg and Fe vs As. The binary diagram for Fe vs Al shows scattered plots for subaqueous samples with a positive correlation; specifically, sample JR-23A from the east zone form an outliner. Besides, the binary diagram shows a positive trend with a perfect correlation for sample JR-14 (Figure 4.18A). The binary diagram of Fe vs Mg shows different results for every sample. Samples JR-11 and JR 19B at the centre zone have no correlation between Fe and Mg, but JR-25A from the east zone shows a positive correlation with a different trend. Likewise, sample JR-14 from the centre zone shows a negative correlation and samples JR-15 and JR-23A have a positive correlation (Figure 4.18B). The binary diagram for Fe vs Mn shows a positive perfect correlation for subaqueous samples with calcite crystals JR-11 and JR-25A and scattered plots for sample JR-19B. In contrast, subaqueous samples with laminated structures show different group trends for every sample; thus, samples JR-15 and JR-23A show a positive correlation between Fe and Mn, but sample JR-15 has a different trend from sample JR-23A. Besides, the data from sample JR-10C form a circular plot whereas these are scattered for sample JR-14 (Figure 4.14C). Finally, the binary diagram of Fe vs As shows a positive correlation between the two metals for samples JR-25A, JR-14 and JR-15; however, the diagram shows no correlation for samples JR 10C, JR-19B, JR-10 and JR-23A (Figure 4.18D).

Thus, the subaerial samples had a higher affinity to precipitate with As while Fe was precipitating; however, Al, Mg and Mn were mobile during iron precipitation. For subaqueous samples, the behaviour of Al, Mg, Mn and As was different for every sample during iron precipitation. The subaqueous samples with calcite crystals had an affinity for Mn, As and Fe to precipitate together. The subaqueous samples with laminated structures showed positive correlation trends for Al, Mg, Mn and As with different trends; however, sample JR-10C showed negative correlation between Fe and Mg, and samples JR-10C and JR-23A showed a no correlation between Fe and As. From the results, it is deduced that the spatial distribution of samples is not an influence for a recent precipitate description.

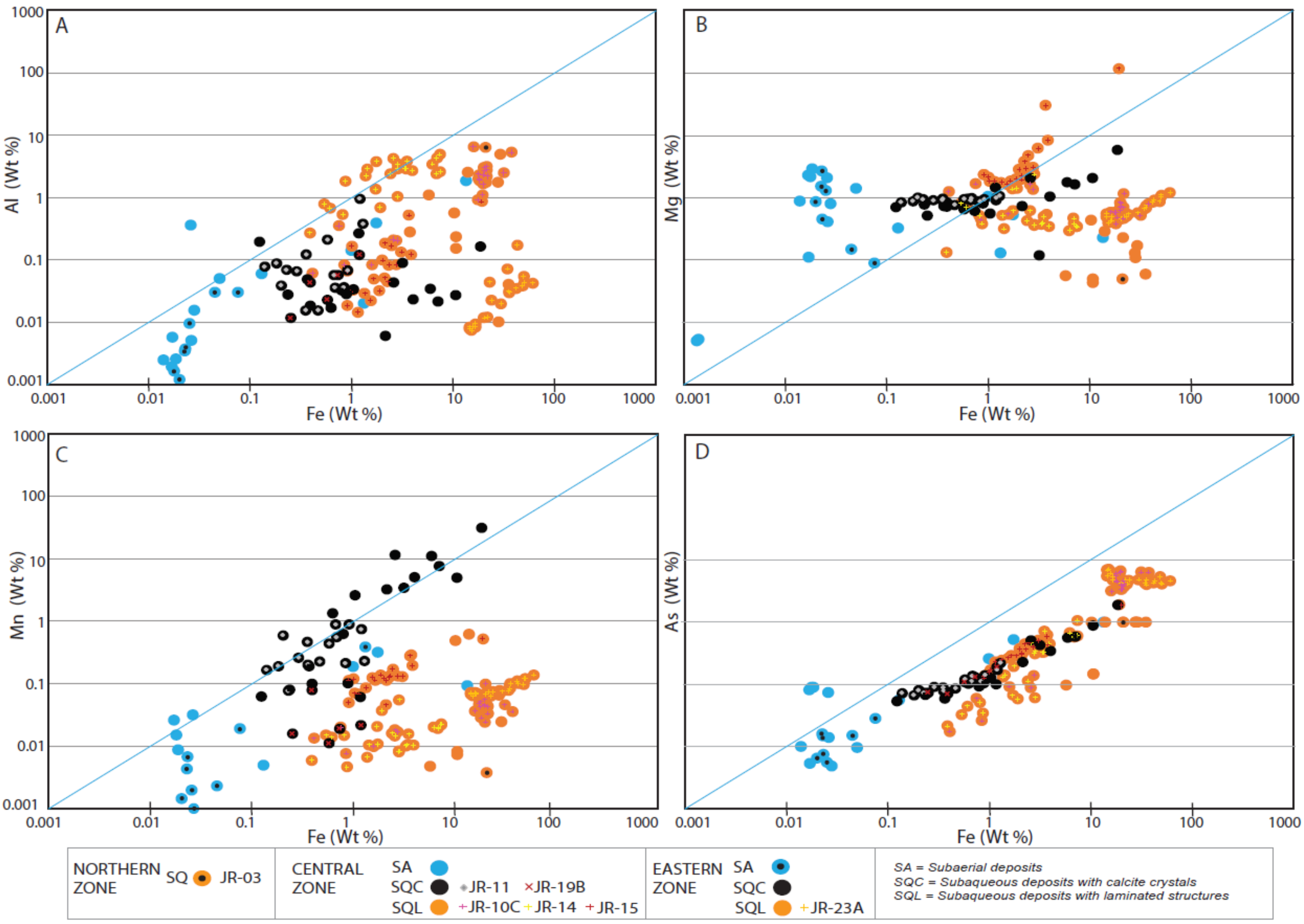

Figure 4.18 Binary diagrams (Wt %) between: A) Fe vs Al; B) Fe vs Mg; C) Fe vs Mn; D) Fe vs As.

The comparison between Al vs Ti, As vs Al, Si vs Sr and Fe vs Si is represented in binary diagrams for major concentrations. The first binary diagram, Al vs Ti, shows scattered plots; however, a detailed analysis showed no correlation for a group of subaerial precipitates from the centre and east zone (Figure 4.19A). The second binary diagram, As vs Al, also shows scattered plots, and no correlation between As and Al in for sample JR-23A (Figure 4.19B). The third diagram shows no correlation between Si and Sr in the precipitates; however, sample JR-14 shows a positive correlation (Figure 4.19C).

Subaerial samples show scattered plots in binary diagram of Fe vs Si but a positive perfect correlation for subaqueous samples. There is a perfect correlation between Fe and Si for subaqueous samples with calcite crystals, as there is one with subaqueous samples JR-10C, JR-15 and JR-23A. However, sample JR-14 has a scattered plot with a negative trend; thus, the increase in Fe reduces the amount of Si in sample JR-14 (Figure 4.19D).

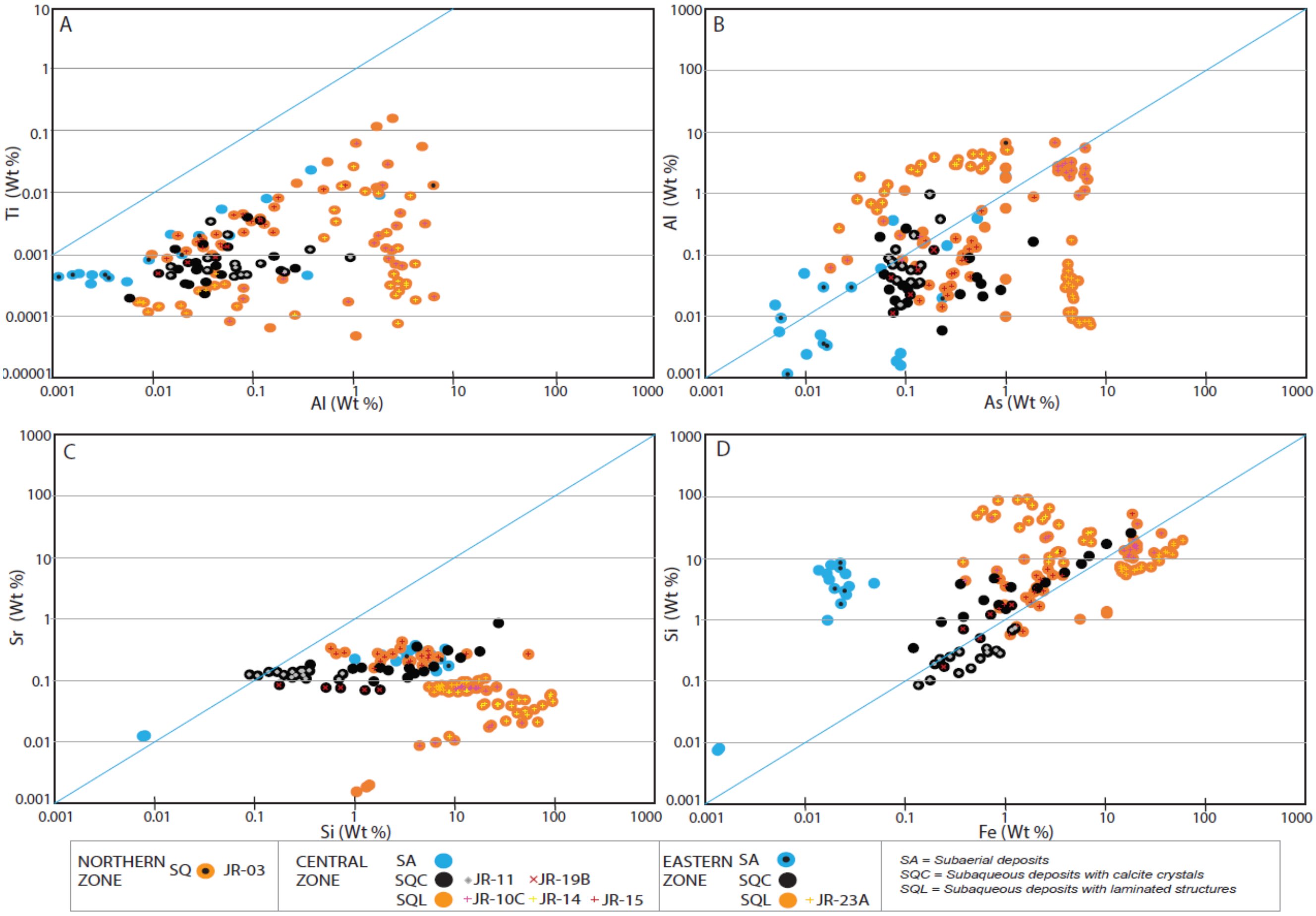

Figure 4.19 Binary diagrams (Wt %) between: A) Al vs Ti; B) As vs Al; C) Si vs Sr; D) Fe vs Si.

4.2.3.2 Correlation for trace elements

The analysis between metals and metals in ppm concentration is represented in binary diagrams, as shown in the analysis. The first analysis shows binary diagrams of Cs vs Rb, Ba vs Mo, Ba vs W, and Ba and Zn. The second analysis shows binary diagrams predominantly of the base metal Zn: Zn vs Ni, Zn vs Mo, Zn vs W, Mo vs W, Zn vs Cu and Zn vs Pb. Finally, the last set of binary diagrams shows the analysis between metals and metalloids (Ga vs Cu, Sb vs Pb, Sb vs Zn, and Ge vs Pb). The metals and metalloids selected for the analysis were based on positive peaks in trace concentrations and the analysis is focused on the behaviour of metals, base metals and metalloids in recent precipitates.

The analysis between Cs vs Rb, Ba vs Mo, Ba vs W, and Ba vs Zn shows positive correlations for recent precipitates. The binary diagram between alkaline metals Cs and Rb shows a positive perfect correlation for recent precipitates (Figure 4.20A). Diagram Ba vs Mo shows scattered plots with a positive trend. Subaqueous samples with calcite crystals show a positive correlation trend, similarly, sample JR-23A from the east zone shows a trend with a positive correlation (Figure 4.20B). Diagram Ba vs W shows a positive correlation with a low ratio for the subaqueous samples with calcite crystals, whereas the subaqueous samples with laminated structures show no correlation between these two metals (Figure 4.20C). Diagram Ba vs Zn shows no correlation for subaerial samples, which is in contrast to the subaqueous samples with calcite crystals that show a positive correlation. Sample JR-15 has a different trend compared with the other subaqueous samples with laminated structures; in this case, sample JR-15 shows characteristics similar to those of the subaqueous samples with calcite crystals (Figure 4.20D). Additionally, the spatial distribution of precipitate samples does not seem to represent a factor for chemical concentrations.

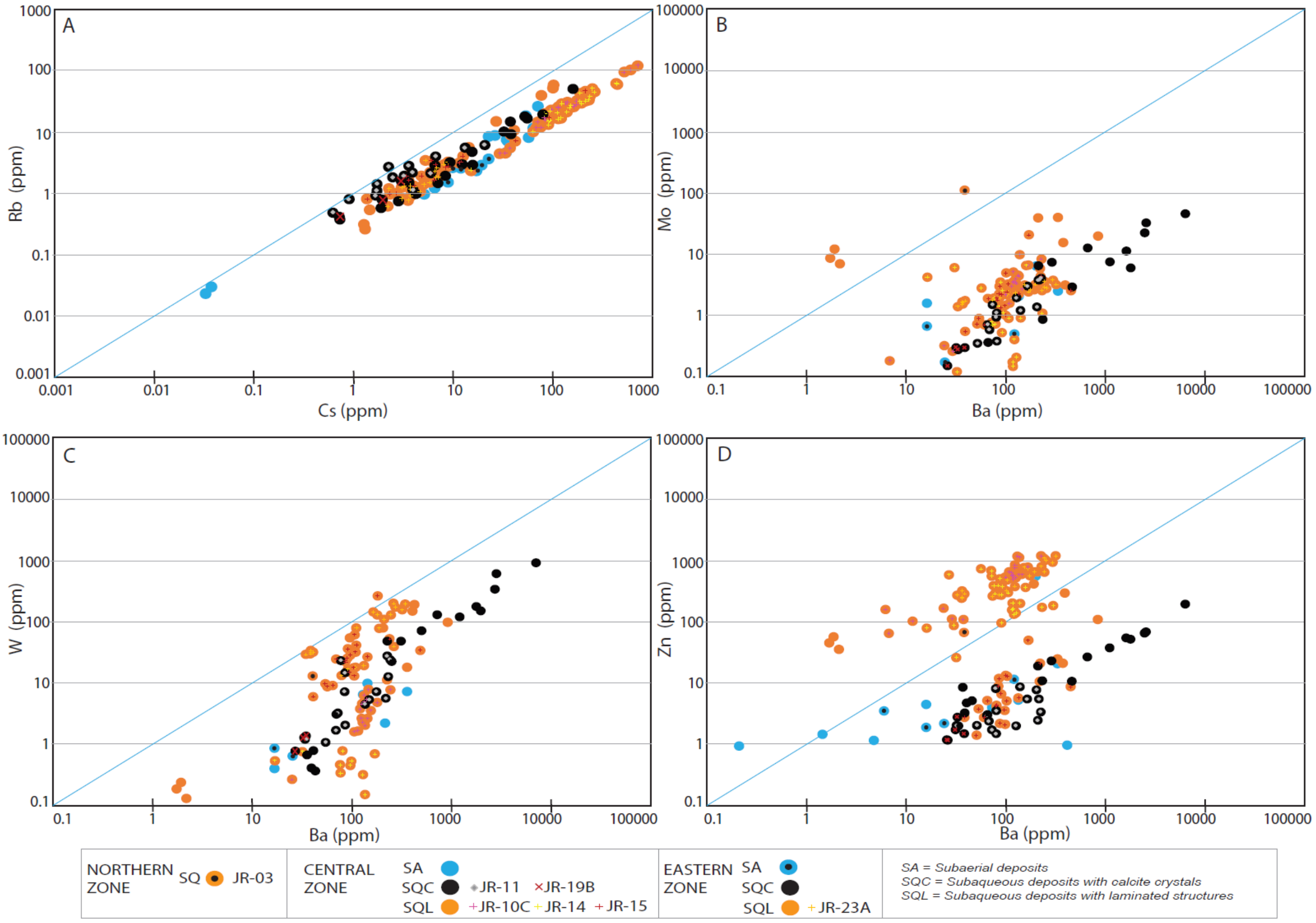

Figure 4.20 Binary diagrams (ppm) between: A) Cs vs Rb; B) Ba vs Mo; C) Ba vs W; D) Ba vs Zn.

The analysis for Zn and Ni, Mo, W, Cu and Pb, and Mo and W shows positive correlations with different trends. The binary diagram of Zn vs Ni shows a scattered plot with a positive correlation for both subaerial and subaqueous samples. Subaqueous sample JR-23A is an outlier, still with a positive correlation but different trend (Figure 4.21A). The binary diagram of Zn vs Mo shows a positive correlation between the two metals with two trends. The first trend shows a scattered plot with a positive correlation; this group contains subaerial and subaqueous samples. The second trend also has a positive correlation for samples JR-10C, JR-14 and JR-23A from the centre and east zones (Figure 4.21B). The binary diagram of Zn vs W shows a positive correlation with three trends. The first trend represents a group of subaqueous samples with calcite crystals (JR-11, JR-19B and JR-25A) and sample JR-15. The second trend represents sample JR-23A. The third trend is a group sample JR-10C and sample JR-14 with scattered plots; also, subaerial samples have no correlation between Zn and W (Figure 4.21C). The binary diagram of Mo vs W clearly shows positive correlation for subaqueous samples with calcite crystals and subaqueous sample JR-15; also, sample JR-14 presents a positive correlation but different trend. Furthermore, there is a no correlation between Mo and W, in sample JR-23A (Figure 4.21D).

The analysis between Zn and Cu in a binary diagram shows correlation between these elements. The binary diagram shows scattered plots with positive correlation for both subaerial and subaqueous samples However, once again, subaqueous laminated sample JR-23A is an outlier, with a positive correlation but different trend (Figure 4.21E). The binary diagram for base metals Zn vs Pb also shows positive correlation between these two metals in subaerial and subaqueous samples. However, there is no correlation between Zn and Pb in the sample JR-25A at the east zone (Figure 4.21F).

From this analysis, it is evident that Zn shows affinity with most of the metals during precipitation. However, sample JR-23A shows a tendency to be an outlier, subaqueous samples with calcite crystals and sample JR-15 show a stronger affinity between Mo and W. Furthermore, there is no correlation between Zn and Pb in sample JR-25A and spatial distribution of samples not shows no influence in trace element concentrations.

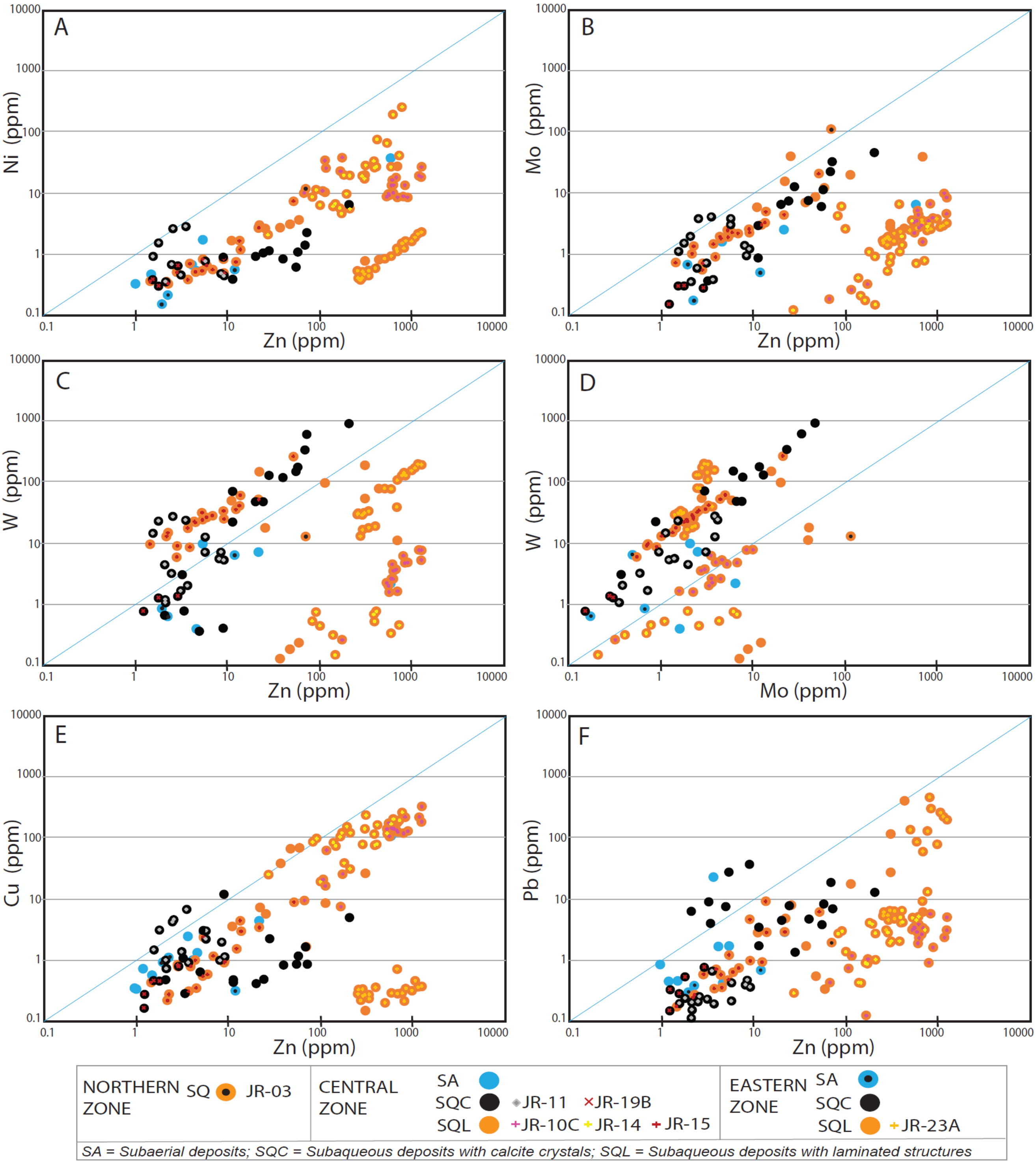

Figure 4.21 Binary diagrams (ppm) between: A) Zn vs Ni; B) Zn vs Mo; C) Zn vs W; D) Mo vs W; E) Zn vs. Cu; F) Zn vs. Pb.

The analysis to correlate metals (Ga), base metals (Cu, Pb and Zn) and metalloids (Sb and Ge) is shown in binary diagrams. The binary diagram of Ga vs Cu shows two trends with positive correlation. The first trend shows scattered plots for subaerial and subaqueous samples. This trend shows that Ga and Cu are more strongly correlated in subaqueous samples JR-15, JR-19B and JR-25A than in sample JR-11, which has a more scattered plot. Furthermore, samples JR-10C and JR-14 show a positive correlation with a different trend (Figure 4.22A). The binary diagram of Sb vs Pb shows one trend with positive correlation for the subaerial and subaqueous samples (Figure 4.22B). The binary diagram of Sb vs Zn shows scattered plots with positive correlation; indeed, sample JR-25A has perfect positive correlation. The subaqueous samples with laminated structures present two trends. The first trend represents samples JR-10C, JR-14 and JR-15 from the centre zone. The second trend represents subaqueous samples JR-11, JR-15 and JR-19A from the centre zone (Figure 4.22C). The binary diagram of Ge vs Pb shows scattered plots with positive correlation; however, there is no correlation between Ge and Pb in sample JR-25A (Figure 4.22D). Finally, Cu shows a good affinity to precipitate with Ga; also, Sb shows a good affinity for precipitation with base metals such as Pb and Zn.

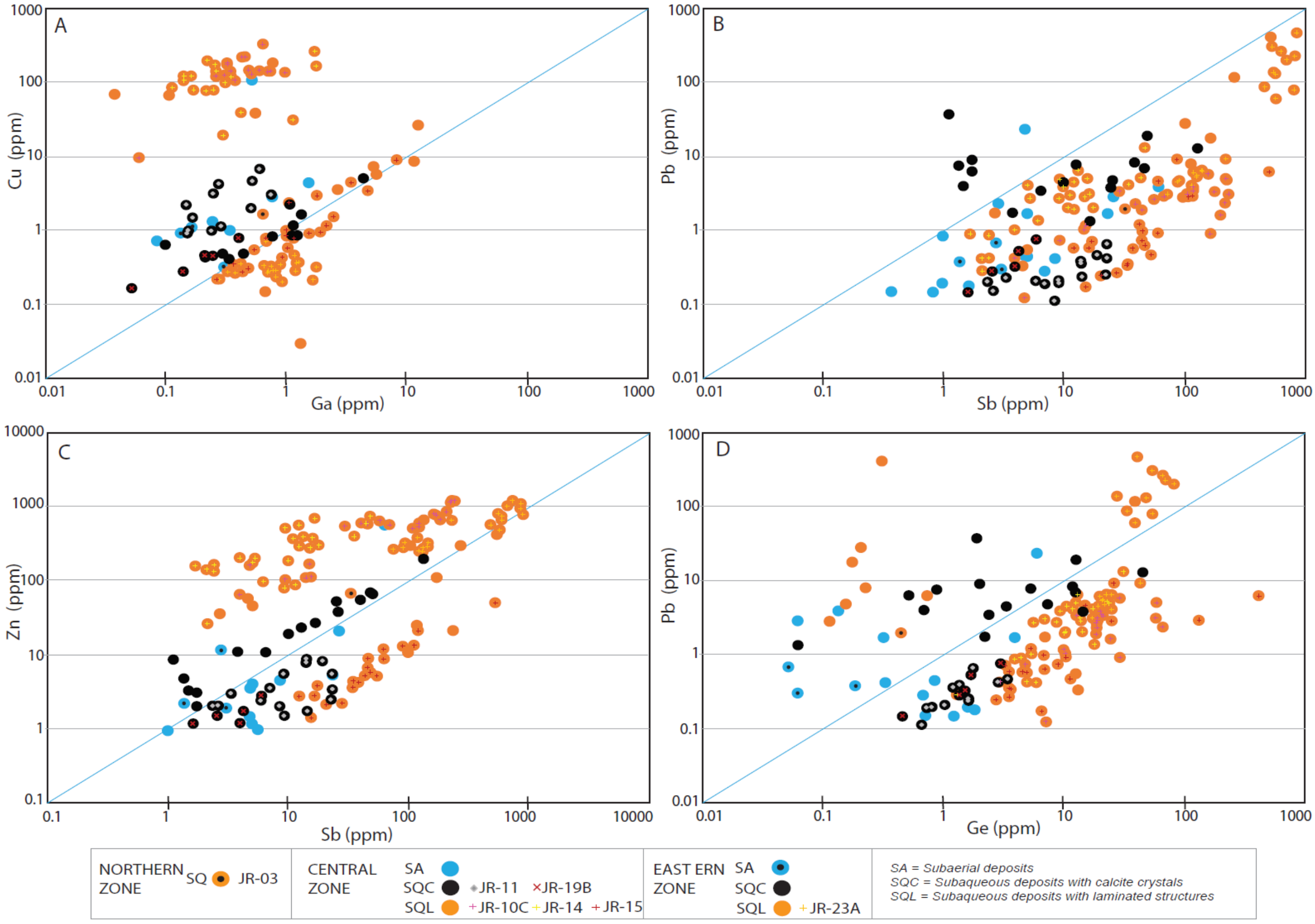

Figure 4.22 Binary diagrams (ppm) between: A) Ga vs Cu; B) Sb vs Pb; C) Sb vs Zn; D) Ge vs Pb.

5 DISCUSSION

The following discussion is presented in three topics: The first topic focus on the deposit types identified at Jaraña; the second topic compares diagenetic events along the northern, central and eastern zones. The last topic illustrates the geothermal system using an idealized conceptual model to understand the interactions among rock, water and precipitates.

5.1 Deposit types identified

Jaraña hot springs preserved four main deposit types: jarosite, gypsum, manganese-travertine and iron-travertine deposits. The first two are based on the sulfate component and the last two on the carbonate component. Jarosite deposits are part of the subrecent Jaraña deposits and record the chemical change of the waters within the geothermal system. Gypsum and travertine deposits are part of the recent precipitation in the Jaraña hot springs, with their precipitation subaerial and subaqueous, respectively. The identification of these four types of deposits is based on mineralogy and chemical composition. The main characteristics of the four deposit types are as follows:

Jarosite deposits: The red, jarosite rich terraces preserve a network fabric morphology. The main chemical constituent is Fe, with moderate abundances of K and As. In addition, jarosite deposits contain filamentous microbes and diatoms.

Gypsum deposits: The emplacement of the deposit is subaerial; gypsum builds up in convex laminations producing a branched morphology. The main chemical constituents are Ca and Si; with moderate abundances of Sr. Gypsum deposits contain diatoms and Fe-Cu sulfide crystals.

Manganese-travertine deposits: The emplacement of the deposit is subaqueous; manganese-travertine deposits preserve nodular morphologies in shallow thermal water areas (thermal pools and run-off channels). The main chemical constituents are Ca and Si, with moderate abundances of Mn. The manganese-travertine deposits contain diatoms.

Iron-travertine deposits: The emplacement of the deposit is subaqueous; iron-travertine deposits preserve nodular morphologies with laminated structures in thermal waters. The main chemical constituents are Ca, Fe and Si, with moderate abundances of Al and As. Iron-travertine deposits contain microbes such as diatoms and filamentous, as well as iron-oxide minerals and Fe-Cu sulfide minerals.

5.1.1 Jarosite deposits

Jarosite deposits are in the subrecent rock record at Jaraña hot springs. They receive the name “jarosite deposits” because of the identification of jarosite minerals obtained using x-ray diffraction. The jarosite deposit is precipitation-derived as, in some places, it records stems from plants trapped inside an iron coverture. This precipitate has a network fabric that yields a porous appearance.

The source of jarosite precipitation at Jaraña is unknown. Generally, jarosite deposits are related to acidic groundwater, mineral deposits, and acid sulfate soils; and it precipitates in areas with very low pH, moderately oxidizing conditions and availability of a high amount of sulfate ligands (Herbert Jr, 1995; Stahl, Fanning, & James, 1993). The geological setting contains sulfide minerals enriched in Fe and Cu (Valdivieso, 2015) that might influence the acidity of the waters. However, Jaraña thermal waters currently have neutral pH of alkali-chloride and acid-sulfate composition (Cruz, 2016), which are not suitable for jarosite precipitation. Therefore, the jarosite deposits at Jaraña may be part of the evidence of a previous hot springs emergence with acid pH or may be part of secondary alteration products.

The mineralogical composition of jarosite ($KFe^{3+}_3(OH)_6(SO_4)_2$) is supported by its chemical composition. The 4-acid digest and EDS analysis registered the highest concentrations on Fe and S rather than only S. However, the results obtained from these analyses showed different ranges of concentrations for Fe (4-acid digest analysis: 26.9–38.3 Wt %; EDS detection: 64.34–67.04 Wt %) and S (4-acid digest analysis: 6.92–7.07 Wt %; EDS detection: 4.08–9.51 Wt %). These results may suggest the presence of other iron minerals such as oxides or sulfides incorporated in small proportions. Additionally, jarosite deposits contain iron (Fe) as their main constituent preserved as hydrous ferric oxides (Jones & Renaut, 2007). Also, jarosite deposits are enriched in trace elements such as As, Cs, Mo, V and Tl, which are typical of these deposits (Scarlett et al., 2012).

5.1.1.1 Microbial influence during precipitation

Jarosite deposits in the study area preserve two microorganism types. The first corresponds to an interpretation that filamentous, inside plants, are part of microbial record and the second is that pennate diatoms are over jarosite surfaces. Normally, bacterial communities influence the change from Fe^{+2} to Fe^{+3} in jarosite deposits (Herbert Jr, 1995). However, the conditions for jarosite precipitation influenced by microbial communities remains unclear, but it could be deduced that diatoms have no influence during jarosite precipitation; rather, their presence may indicate the end of jarosite precipitation.

5.1.2 Gypsum precipitates

The Jaraña hot springs has large white gypsum deposits overlying rocks, dry grass, and even water surface (subaerial precipitation). It is known as “gypsum deposits” because of the predominant gypsum mineral, identified by using the x-ray diffraction and optical microscopy. Initial field impressions are of a salt deposit; supported in previous x-ray diffraction patterns of halite (Pajuelo et al., 2016). It is important to mention that the drying process, between collecting samples in Peru and the arrival of the samples in New Zealand, could have produced a reduction in thickness of the white layering, which represents halite loss. Only one sample (JR-11) contains halite minerals using x-ray diffraction. Gypsum deposits at Jaraña could be compared to other gypsum deposits in shallow areas of sedimentary environments because of two particular reasons; the precipitation conditions (subaerial) and the affinity to precipitate with halite minerals (Tang et al., 2014; Vogel et al., 2010).

The Jaraña gypsum deposits contain two gypsum crystal varieties: platy and prismatic; layer thickness has no influence on gypsum crystal growth. Generally, gypsum crystals grow in sedimentary environments and hot spring terrains (Tang et al., 2014; Vogel et al., 2010). Gypsum deposits in hot springs have been observed to contain six varieties of gypsum crystals: prismatic, prismatic pseudo-hexagonal, fibrous, tabular, lenticular and twinned crystals, as is the case in Kamchatka hot springs at Russia (Tang et al., 2014). Consequently, gypsum crystal growth and varieties are common in hot spring terrains.

The first stages of gypsum precipitation contain gypsum crystals with fluidal texture, representative of flow rate of thermal waters. These first gypsum precipitations could incorporate carbonate composition into the structure as carbonate fragments or calcite crystals. The laminated horizons are usually found in areas with fast flow such as run-off channels.

Cathodoluminescence results showed a blue luminescence only in samples JR-06 and JR-25B from the central and eastern zones. The blue luminescence is typically from the Si element activator (Mackenzie & Adams, 1951). Gypsum deposits contain Si concentrations in the range of 0.98 to 8.46 Wt %. Not all gypsum samples showed this blue luminescence, which may indicate that Si is not the only activator for these blue colours.

Finally, the gypsum deposits contain different concentration amounts in Na, Mg and K between the central and eastern zones. Gypsum deposits in the central zone contain the highest concentrations of Na, Mg and K compared to gypsum deposits at the eastern zone. Normally, Na, Mg and K elements register high concentrations in sedimentary environments above 0.1 Wt % (Vogel et al., 2010), comparable to gypsum deposits from the central zone of Jaraña.

5.1.2.1 Microbial influence during precipitation

Gypsum deposits at Jaraña contain two types of microbial evidence. The first is a thin green to orange, calcareous mat floating above the thermal water surface, and the second is diatoms near gypsum crystals. The green and orange mats are usually found below the gypsum deposits and the diatoms seem to be contemporary with gypsum crystal growth. Diatoms generate a reaction at the edges of gypsum crystals, such as dissolution into surfaces. Microbial mats and diatoms generate metabolic activities and produce EPSs (Extracellular polymeric substances); the EPS induces nucleation and maintains mineral saturation, thereby, causing the gypsum precipitation under sulfate oxidation (Renaut & Jones, 2000). Therefore, diatoms have a strong influence on gypsum crystallization from the earliest stages. The trapping and binding of sediments is representative of diatoms (Brock, 1978; Warren, 2016).

Additionally, the nodular-branched type morphology in Jaraña gypsum deposits is similar to macrofabrics of gypsum in carbonate or evaporitic environments (Laurent et al., 2016; Scholle & Ulmer-Scholle, 2003; Terra et al., 2010; Warren, 2016). The branched morphology with convex laminations could represent stromatolitic macrofabrics, build-up by microbial communities such as diatoms.

5.1.2.2 Metal Crystallization

X-ray diffraction and optical microscopy detected sulfide minerals incorporated into gypsum deposits at the central zone of Jaraña. Specifically, XRD of two samples (JR-06 and JR-14) in the central zone suggests the presence of small proportions of sulfides minerals (freibergite and colusite) enriched in Ag, Cu, Fe, V, As and Sb. This finding is supported by the identification of a Cu-Fe sulfide inside gypsum cavities in sample JR-06, using optical microscopy. Similarly, the chemical analysis using the 4-acid digest and laser ablation ICP-MS data results identified a higher amount of Cu, Fe, V and Sb elements in the central zone (See table 5.1). Ag showed no relevant changes between the central and eastern zones. From this analysis, the highest amount of Cu, Fe, V and Sb in the central zone result appropriate for metal concentration and mineralization compared to other zones.

Table 5.1 Chemical results from 4-acid digest and Laser ablation ICP-MS methods, comparing element amounts (Ag, Cu, Fe, V, As and Sb) on gypsum horizons at the central and eastern zones of Jaraña.

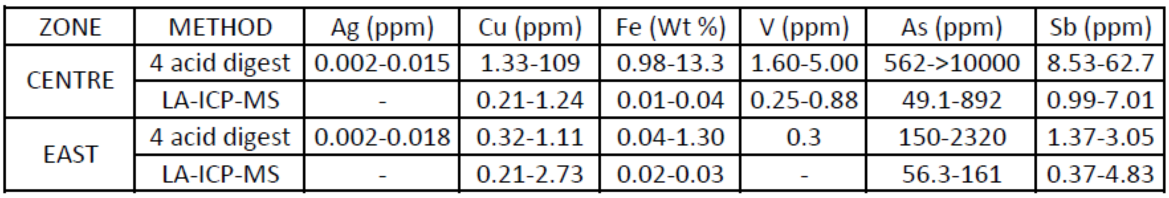

ZONE	METHOD	Ag (ppm)	Cu (ppm)	Fe (Wt %)	V (ppm)	As (ppm)	Sb (ppm)
CENTRE	4 acid digest	0.002-0.015	1.33-109	0.98-13.3	1.60-5.00	562->10000	8.53-62.7
	LA-ICP-MS	-	0.21-1.24	0.01-0.04	0.25-0.88	49.1-892	0.99-7.01
EAST	4 acid digest	0.002-0.018	0.32-1.11	0.04-1.30	0.3	150-2320	1.37-3.05
	LA-ICP-MS	-	0.21-2.73	0.02-0.03	-	56.3-161	0.37-4.83

5.1.3 Manganese-travertine deposits

Jaraña has manganese-travertine deposits precipitates around shallow thermal water or run-off channels and that contain a distinct black colouration. It receives the name of “manganese-travertine deposits” because of the calcite and manganese-oxide minerals detected from XRD patterns and anomalous abundances (11.6 Wt %) of Mn. This type of deposit has nodular morphologies at the bottom side of the samples.

The manganese-travertine deposits at Jaraña precipitate as manganese layering, interbedded with iron-rich layers. The interbedding between manganese and iron layers, and calcite crystals represents changes in pH composition in thermal waters (Chafetz et al., 1998). The manganese-laminated horizons are occasionally interbedded with clast breccia. Also, manganese laminations form botryoids and may contain angular fragments (Figure 5.1A and B). The carbonate clasts could be caused by the flow rate within run-off channels. Generally, manganese deposits and calcite crystals precipitate together. The manganese precipitation is likely induced by manganese oxidation in fresh waters and calcite minerals induced by high saturation of Ca in thermal waters. However, “Ca^{+2} ions are difficult to incorporate to in Mn oxides” as reported by Sasaki et al., 2002 manganese-travertines at Japan.

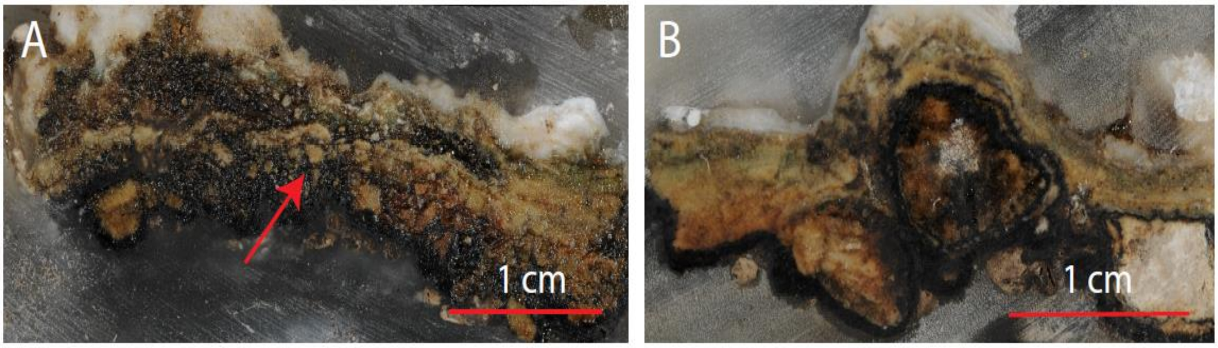

Figure 5.1 Manganese-travertine deposits at Jaraña from run-off channel areas: A) travertine clast breccia inside manganese laminations (sample JR-25A); B) botryoids form and interbedding of calcite and manganese-oxide mineral laminations, (sample JR-25B).

The eastern zone within run-off channels contains big size calcite crystals and a slight increase in metal concentrations (Mn, Fe, Si and As, Li, Cs, Tl, Sb, Mo, W, Cu and Zn) compared to thermal pools at the central zone. However, manganese-travertine deposits do not register sulfide minerals as crystals. The banded manganese-oxide minerals and calcite crystals present different conditions to concentrate elements. For example, Si element has a higher concentration within manganese laminated horizons (horizon 1: 2.09 to 26.36 Wt % and horizon 2: 1.51 to 11.12 Wt %), rather than calcite crystal horizons (horizon 3: 0.35 to 3.86 Wt %) (Figure 5.2B). This work suggests that the processes of Mn precipitation lead to enrichments in Si in the deposits compared to relatively low Si in the zones of calcite enrichment (Figure 5.2A and B).

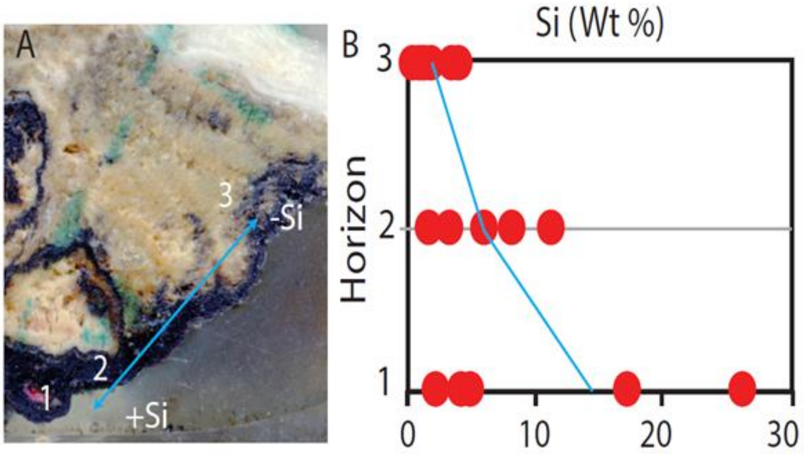

Figure 5.2 Sample JR-25A on the eastern zone (run-off channel): A) sample JR-25A with three horizons: two with manganese layers and the third with calcite crystals; B) Laser ablation ICP-MS data of Si element concentrations among three horizons.

The manganese-travertine deposits from central and northern zones at Jaraña show a good correlation between Mn and Ba (Figure 5.3A). The Ba incorporates into manganese deposits easily (Sasaki et al., 2013), this can be explained by the facility that has Ba to displace earth alkaline metals from oxide minerals such as MnO_2 (Finland, 2005). While manganese-travertine deposits from shallow thermal pools in the central zone show no correlation between Mn and Sr, manganese-travertine deposits from run-off channels in the eastern zone have a good correlation between these two elements (Figure 5.3B). Sr chemically replaces Ca which has difficulties into incorporate to manganese structures (Sasaki et al., 2013); therefore, Sr has the same analogy. The anomalous concentrations in Mn (above 10000 ppm) from run-off channels at the eastern zone show a good correlation with Sr. The banded manganese-oxide minerals at the eastern zone show affinity to incorporate Sr or Ca into their structure, as recorded in EDS results where Mn contains 24.51 Wt % and Ca 9.18, Wt%. Thus, manganese-travertine deposits in the eastern zone are suitable to incorporate into Ca or Sr because of their anomalous amount; however, the decrease in Mn concentrations causes the exclusion of Ca element as registered at the central zone.

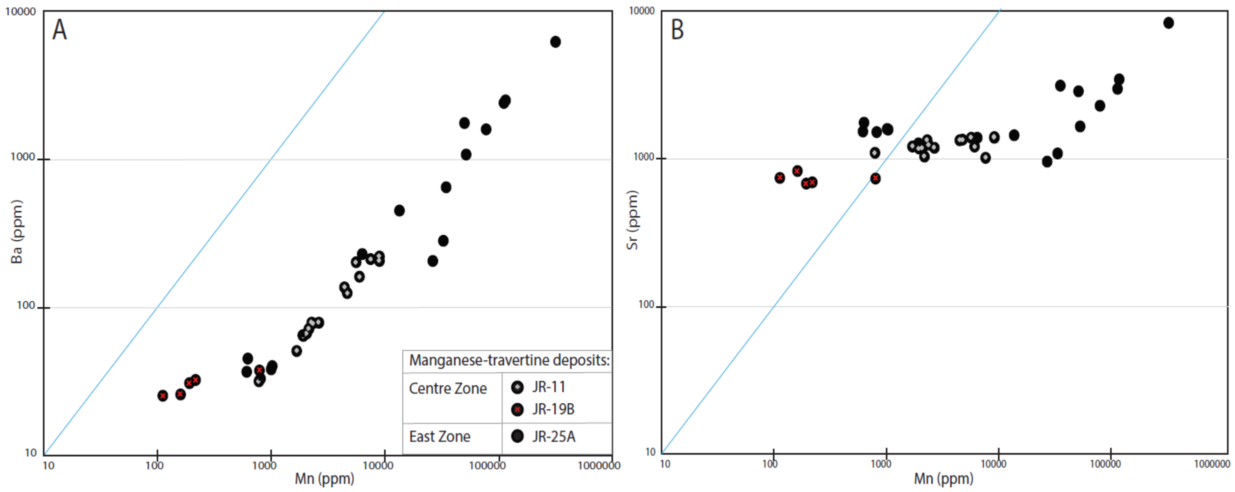

Figure 5.3 Binary diagrams for manganese-travertine deposits at Jaraña: A) Mn vs. Ba (ppm); B) Mn vs. Sr (ppm).

5.1.3.1 Microbial influence during precipitation

Manganese-travertine deposits preserve one microbial species: diatoms. The abundance of diatoms is higher around calcite clasts and manganese laminations, but diatoms decrease in abundance around calcite acicular crystals. Moreover, diatoms have been found buried by manganese precipitation within run-off channels, which is typical in manganese hot spring deposits with neutral pH (Sasaki et al., 2013). The decrease in diatom amount in calcite crystals is related to the decrease in Si amount, as described above. This record is coherent considering that diatoms require silica to build their cell wall (Kale & Karthick, 2015; Winsborough, 2000). Besides, diatoms have the ability to cause the manganese-oxidizing reaction (Chafetz et al., 1998; Mita & Maruyama, 1994) and to induce manganese precipitation and later concentration inside shallow thermal pools and run-off channels at Jaraña. Thus, it seems that diatoms have a greater concentration in run-off channels than thermal pools at Jaraña, one reason for this is the distance from the vent (Sasaki et al., 2013) which generates low temperatures in thermal waters and is suitable for diatoms existence (Brock, 1978).

5.1.4 Iron-travertine deposits

Jaraña iron-travertine deposits precipitate inside Jaraña thermal pools and show red and orange colouration. It receives the name of “iron-travertine deposits” because calcite and iron-oxide minerals are observed from XRD patterns and the variable concentrations of Ca (2.77->25 Wt %) and Fe (0.89-60.19 Wt %) obtained by using 4-acid digest and laser ablation ICP-MS analysis. Iron-travertine deposits consist of nodular shaped morphologies and precipitate with parallel laminations; these subaqueous deposits contain anomalous enrichments in Si element concentrations, in the range of 0.09 to 92.6 Wt %.

Vertical cross-sections showed laminated structures with variable physical characteristics, which allowed three subdivisions based on Ca and Fe concentrations. For example, iron-travertine deposits with high Ca (23.6->25 Wt %) concentrations but low Fe (0.89-3.78 Wt %) amounts, contain high carbonate concentrations in laminated horizons. According to cathodoluminescence results, carbonate horizons contain more Fe during the first stages of deposition and change to Mn through upper sequences. This type of deposit also allows the crystallization of small calcite grains. A second example of the iron-travertine deposits contains low Ca (1.61 Wt %) concentration but moderate Fe (0.40-36.93 Wt %) abundances, resulting in iron, carbonate, silica and hematite precipitation. The iron and carbonate layers occasionally mix among them, silica layers mix with carbonates and hematite precipitate as thin laminations. Furthermore, this type of deposits shows crystallization of small calcite grains, whereas laminations trap large iron fragments at their bottom surfaces. Finally, iron deposits contain low Ca (2.77-3.91 Wt %) concentrations but high Fe (12.29-60.19 Wt %) occur as spring conduits and precipitate iron-oxide minerals forming thin layers. This type of deposit also contains laminations, which trap large fragments at the bottom surface. The description of the three cases suggests three subdivisions based on Ca and Fe; concentrations, the names are: Carbonate-iron deposits, iron-travertine deposits and iron deposits (Table 5.2).

Table 5.2 Jaraña iron-travertine subdivision and characteristics.

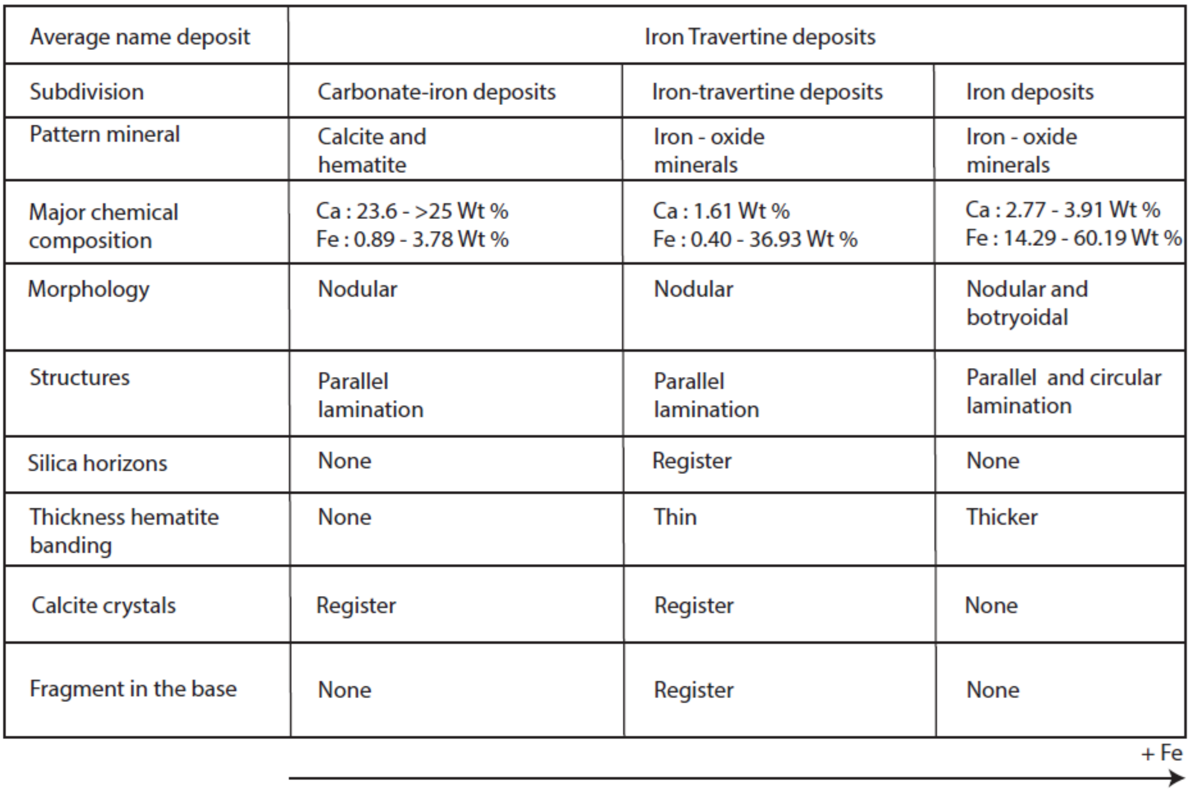

Average name deposit	Iron Travertine deposits		
Subdivision	Carbonate-iron deposits	Iron-travertine deposits	Iron deposits
Pattern mineral	Calcite and hematite	Iron - oxide minerals	Iron - oxide minerals
Major chemical composition	Ca : 23.6 - >25 Wt % Fe : 0.89 - 3.78 Wt %	Ca : 1.61 Wt % Fe : 0.40 - 36.93 Wt %	Ca : 2.77 - 3.91 Wt % Fe : 14.29 - 60.19 Wt %
Morphology	Nodular	Nodular	Nodular and botryoidal
Structures	Parallel lamination	Parallel lamination	Parallel and circular lamination
Silica horizons	None	Register	None
Thickness hematite banding	None	Thin	Thicker
Calcite crystals	Register	Register	None
Fragment in the base	None	Register	None

Generally, iron-travertine deposits contain banded hematite structures caused by ferrihydrite precipitation, which is influenced by iron-oxidizing bacteria (Kanellopoulos et al., 2017; Takashima et al., 2011). Also, laminated horizons enriched in Fe with variable amounts of Si and Sr (which replaces Ca) could be a mechanism to concentrate base metals (Cu, Pb and Zn) and metalloids (As). For example, iron-travertine deposits with high Sr concentrations (carbonate-iron deposits represented by sample JR-10C) but low Fe and Si amounts, afford the lowest quantities in base metals (Zn: 0-40 ppm; Pb: 0-10 ppm; Cu: 0-5 ppm); however, the increase in Fe in laminated horizons is related with a slight increase in As (Figure 5.5A). Iron-travertine deposits with layers with variable composition bring the opportunity to evaluate the base metal and arsenic concentrations (represented in samples JR-14 and JR-15). The high concentrations for Zn (around 1000 ppm) seem to be related to horizons (Horizons 1 and 2, sample JR-14) with high amounts on Fe (20-40 ppm) and Sr (500-1000 ppm) (Figure 5.5B). However, the high concentrations on Si (50-100 Wt %) and a moderate amount in Fe (5-10 Wt %) and Sr (around 500 ppm) allow to concentrate more Cu (around 200 ppm) inside the laminated horizons such as horizon 3 in sample JR-15 (Figure 5.5C). Also, the increase in Fe (25-70 Wt %) and Sr (around 1000 ppm) generates the highest concentrations in Pb (250 ppm) such as horizons 1 and 4 in sample JR-23A (Figure 5.5D). Moreover, horizons in sample JR-23A and horizons 1 and 2 in sample JR-14 contain a considerable amount of Fe (25-70 Wt %) and Sr (500-1000 ppm) but low Si (less than 25 Wt %) concentrations (Figure 5.5B and D). This high Fe and Sr but low Si concentrations, seem to influence the generation of high As amounts; therefore, As shows affinity to precipitate with anomalous quantities of Fe and Sr.

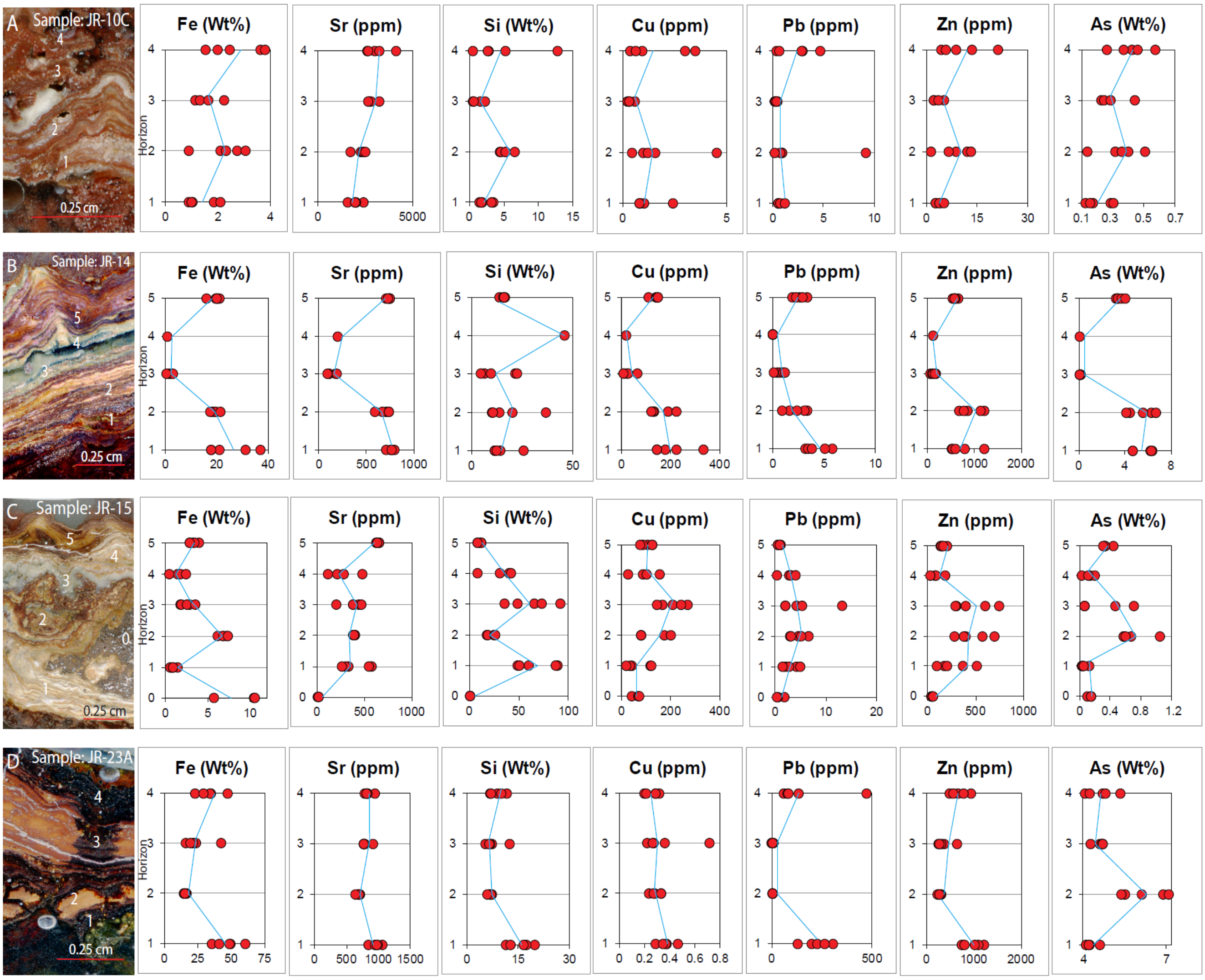

Figure 5.5 Jaraña iron-travertine deposits with laminated horizons and element concentrations of Fe, Sr, Si, Cu, Pb, Zn and As: A) four horizons in sample JR-23A represent carbonate-iron deposits; B) five horizons in sample JR-15 represent iron-travertine deposits; C) five horizons in sample JR-14 represent iron-travertine deposits D) four horizons in sample JR-10C represent iron deposits.

The variable range of concentrations on Fe, Sr and Si inside laminated horizons of iron-travertine deposits allowed concentrating economically important metals at Jaraña. The concentrations of Ag at Jaraña (< 0.002-0.06 ppm) are similar to other travertine deposits (0.003-0.04 ppm) as reported at Savo volcano, Salomon Islands (Smith, 2008). However, sinter deposits are suitable to concentrate more Ag into the structure such as reported at National Park, United States (Fournier et al., 1994) and El Tatio, Chile (Nicolau, 2013), probably because of low Fe and As concentrations (Table 5.3). Cu has a variable range of concentration (0.03-333 ppm) at Jaraña iron-travertine deposits. Cu amounts are greater at Jaraña compared with other travertine deposits at Savo volcano, Salomon Islands or Northern Euboea Island and Sperchios, Greece (Kanellopoulos et al., 2017; Smith, 2008). However, sinter deposits at El Tatio (Chile) report a greater amount of Cu (420-20528 ppm) related with high concentrations of Sr (64.8-315 ppm) (Landrum et al., 2009). Similarly, the high concentration of Pb (0.12-308 ppm) at Jaraña is greater than that at other travertine or mixed deposits. However, sinter deposits at El Tatio, Chile register a greater concentration of Pb (2398-7293 ppm) also related with high Sr (64.8-315 ppm) concentrations (Landrum et al., 2009). The Jaraña iron-travertine deposits register the highest concentrations of Zn (173-71204 ppm) compared with other travertine or sinter deposits around the world. As described above, the high Zn concentrations are related to high Fe and Sr concentrations; but according to the case at El Tatio, Chile in sinter deposits, the high Zn concentrations (<30-410 ppm) could also be influenced by high As amounts (0.01-18.8 ppm) (Table 5.3).

Table 5.3 Comparative trace and major element concentration between Jaraña iron-travertine deposits and recent and ancient sinter and travertine deposits cases.

Location	Age	Description	Ag (ppm)	Cu (ppm)	Pb (ppm)	Zn (ppm)	As (ppm)	Fe (Wt%)	Fe2O3 (Wt%)	Sr (ppm)	Reference
Jaraña hot springs (Peru)	Recent	Travertine	<0.002-0.06	0.03-333	0.12-308	2.14-1213	173-71204	0.38-60.2	-	85.9-4900	Current work thesis
Savo volcano (Salomon Islands)	Recent	Travertine	0.003-0.04	0.20-0.78	0.03-1.25	0.30-21.0	0.60-625	0.06-2.29	-	1151-3974	Smith, 2008
Savo volcano (Salomon Islands)	Recent	Mixed	-	4.19	0.13-3.00	3.60	186-287	0.10-1.43	-	1589-4206	Smith, 2008
Savo volcano (Salomon Islands)	Recent	Sinter	-	-	8.00 - 69.0	-	9.00-280	0.85 - 2.82	-	356-6081	Smith, 2008
Northern Euboea Island and Sperchios (Greece)	Recent	Travertine	-	3.60-14.7	0.35-10.6	2.52-25.9	66.0-18300	0.01-28.9	-	254-3960	Kanellopoulos et al., 2017
Atiamuri, Champagne Pool, Ohaaki Pool, Tokaanu Springs (New Zealand)	Recent	Sinter	-	<1.00-23.0	4.00 -18.0	<1.00-18.0	<1.00-246	0.14-0.71	0.11-0.55	5.00-584	Nicholson & Parker, 1990
Taupo Volcanic Zone (New Zealand)	Recent	Sinter	-	-	-	-	13.0-1646	-	0.08-8.85	-	Mckenzie et al., 2001
National Park (United States)	Recent	Sinter	<0.20-0.80	1.00-6.00	<1.00-8.00	<1.00-44.0	1.00-1120	0.05-1.40	0.14-4.00	-	Fournier et al., 1994
El Tatio (Chile)	Recent	Sinter	-	420-20528	2398-7293	10.8-68.0		-	-	64.8-315	Landrum et al., 2009
El Tatio (Chile)	Recent	Sinter	<0.50-2.40	<10.0-220	<5.00-56.0	<30.0-410	5.00->2000	-	0.01-18.8	-	Nicolau, 2013

Laminations with moderate Fe concentrations but low Ca contain iron fragments on their bases. The iron fragments show physical characteristics such as high porosity and red colours comparable with physical characteristics found in jarosite deposits. The spatial location (central zone) of the jarosite deposits and iron–travertine deposits suggests that those fragments could be part of the jarosite deposits. Furthermore, chemical results show similarities of Ca, Fe, Al, Mn, Sr and As concentrations within fragments and jarosite deposits, which suggests that iron-travertine deposits precipitated over a jarosite deposit surface and incorporated eroded fragments in their structure (Figure 5.6).

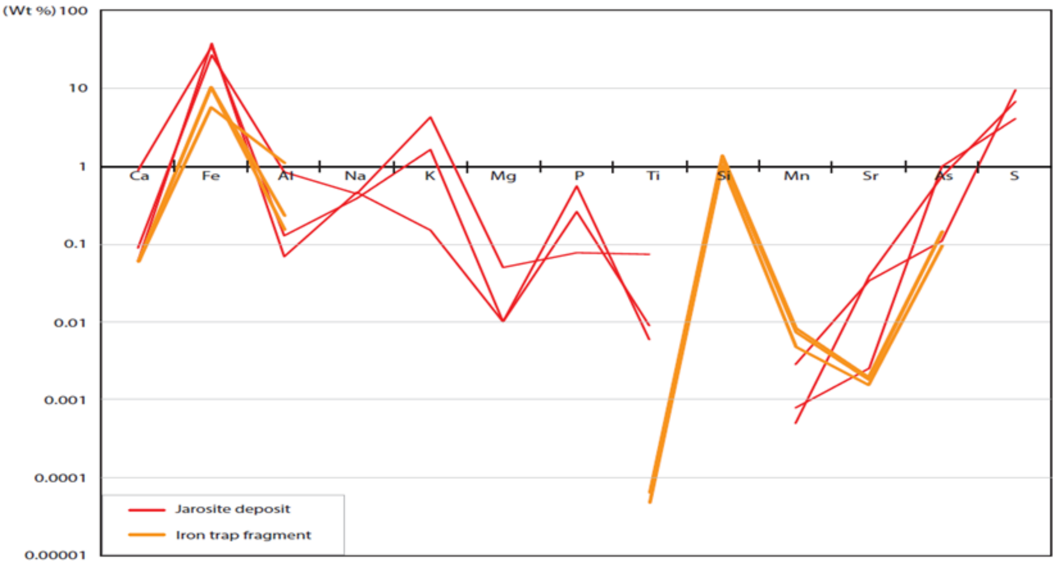

Figure 5.6 Spider diagram show elements with major concentrations. The chart compares jarosite deposits and iron fragments inside iron-travertine deposits.

Finally, the variety of trace elements concentrations in iron-travertine samples among the northern, central and eastern zones, could be caused by the differences of hot springs discharge. Thus, the stagnant thermal pools at the northern zones are not suitable for laminated structures precipitation; the thermal pools with big diameter and depth at the central zone present favourable conditions to precipitate gradually, laminated structures with nodules and concentrate Ca, Fe and Si elements in high amount. On the other hand, thermal pools with shallow depth form spring conduits, gave favourable results to concentrate Fe in high amounts and precipitate iron-oxide banded structures.

5.1.4.2 Microbial influence during precipitation

Iron-travertine deposits at Jaraña contain three types of microbial evidence. The first a thin green to orange mat, frequently found floating over the thermal water surface. The second evidence is diatoms inside laminated structures. The third one constitutes filaments inside iron-laminated horizons. Diatoms and filaments were found in laminated horizons with moderate concentrations of Fe and also of iron fragments trapped by laminated structures. The diatom shapes have a similitude with *Surirella* species (Bramburger, Haffner, Hamilton, Hinz, & Hehanussa, 2006). The optical analysis showed a high concentration of filaments inside iron laminations; thus, the filament intensity appears in the precipitation of iron and its decrease contributes to carbonate precipitation (Takashima, Kano, Naganuma, & Tazaki, 2008) (Figure 5.7A, B and C). Furthermore, the iron-travertine deposits at Jaraña are based on ferrihydrite precipitation, which is caused by microbial metabolism that oxides the iron in hot spring environments (Takashima et al., 2008). Microbial metabolism stimulates metal precipitation, produces ligands and generates crystals (Ferris, 2000). The influence of microbial metabolism on the generation of crystals could be represented in the metal crystals enriched in Sr and Fe found in carbonate-travertine deposits. These particular bunches of platy crystals are connected by an elongated filament, which could suggest microbial influence during metal crystallization.

Additionally, the nodular morphologies and convex laminated characteristics found in iron-travertine deposits could be comparable to macrofabrics such as stromatolites and thrombolites commonly found in evaporitic and calcareous environments (Alshuaibi & Khalaf, 2015; Terra et al., 2010; Warren, 2016). The laterally linked columns, convex laminations forming columns and conical shapes trapped inside laminated structures indicate an important influence of microbial communities (Scholle & Ulmer-Scholle, 2003), even if filaments are not always preserved.

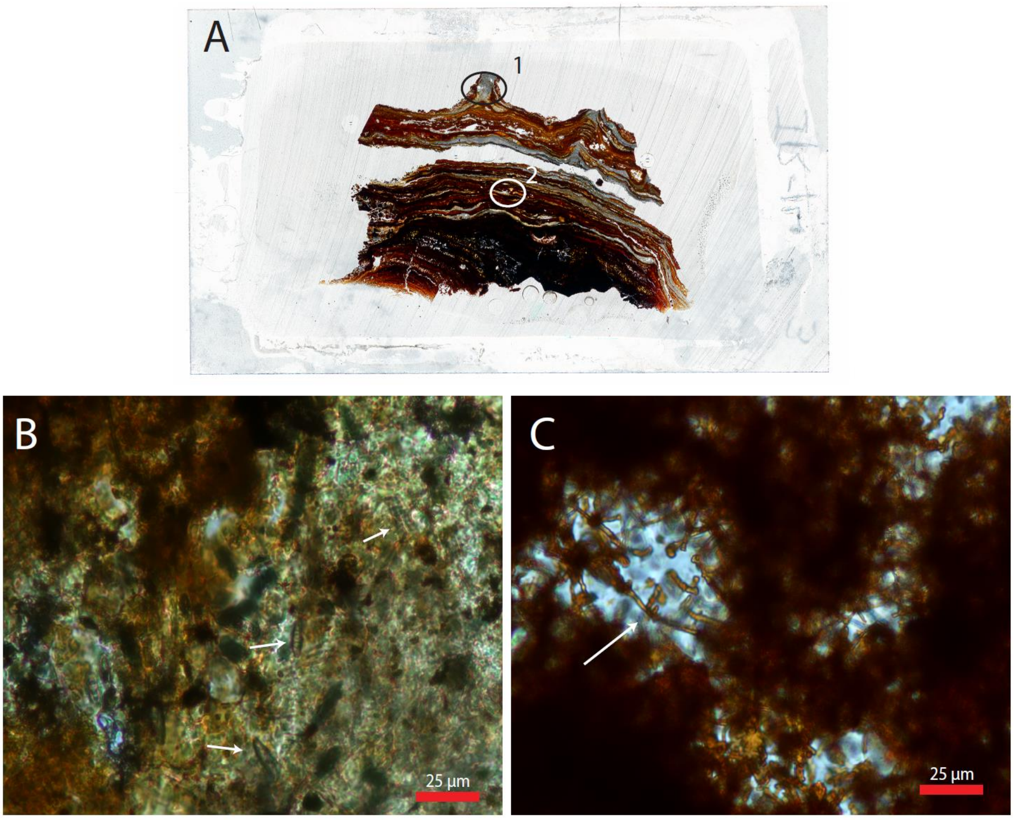

Figure 5.7 Sample JR-14 from the central zone shows: A) thin section with location of high concentration on diatoms (1) and filaments (2); B) Diatoms shown in white arrows inside calcareous horizon; C) filaments shown in white arrows inside iron horizon.

5.1.4.3 Metal Crystallization

The oxide (franklinite) and sulfide minerals (renierite, colusite and proustite) found using x-ray diffraction on iron-travertine deposits, are related to oxide and sulfide minerals enriched in Fe, Sr and Cu found, using optical microscopy. The oxide and sulfide minerals are like crystals inside cavities of iron-carbonate matrix, which correspond to a later crystallization, after an iron-travertine precipitation. Moreover, the iron-oxide minerals are good hosts to induce the Fe-Cu sulfide grainy crystallization (framboid textures). From this, it seems that base metals (Cu in this current work) can crystallize over a Fe-oxide mineral surface. Oxide and sulfide mineral crystallization are similar to the case of travertine deposits in Greece and Russia, where hot spring deposits host metal crystals inside carbonate matrix cavities (Kanellopoulos et al., 2017; Okrugin, Andreeva, Chubarov, Yablokova, & Shishkanova, 2015).

5.2 Diagenetic events

The central and eastern zones at Jaraña contain mineralogical and optical characteristics suitable for a comparison between these two zones and, also, to identify the diagenesis events. The analysis is based on the four deposit types identified at Jaraña: jarosite, gypsum, manganese-travertine and iron-travertine deposits. Hot spring deposits at Jaraña reveal three diagenetic events: early, middle and late. The analysis focuses on the following components: filaments, plants, diatoms, basal fragments, minerals, cement and polymictic grains. The diagenetic descriptions for the four types of deposits are represented in figure 5.8 and the lines represent the precipitation of ancient, subaerial and subaqueous precipitates.

The subrecent jarosite deposits register an early time with plants and filaments. During a middle time, iron cement precipitation predominates and small iron crystals precipitate above the jarosite surface. Finally, a late time of deposition registers the presence of diatoms, which could represent the end of jarosite precipitation, apparently under subaqueous conditions (Figure 5.8A).

Gypsum deposits precipitate under subaerial conditions and during the early time of precipitation to trap carbonate fragments or incorporate carbonate clasts into their structures. During a middle time, gypsum has two stages of crystallization: platy and prismatic. Platy gypsum crystals coexist with diatoms during their formation and build up columns forming convex laminations. When the first crystallization is complete, carbonate cement with polymictic grains covers the platy gypsum surface. The second crystallization reveals prismatic crystals filled in spaces created by convex laminations, and prismatic crystals form bunches of crystals. Finally, during a late time of precipitation, sulfide minerals crystallize and fill gypsum cavities; this sulfide crystallization was only registered in the central zone but the finding suggests that gypsum deposits could be good host for sulfide crystals (Figure 5.8B).

Travertine deposits precipitate under subaqueous conditions and precipitate two deposit types based on iron and manganese. The figure 5.8C shows the diagenetic events for iron-travertine deposits in orange lines and for manganese travertine deposits in black lines. The iron-travertine deposits are shown during an early time, trapping iron fragments and incorporating them into their structure. Fragments contain a greater quantity of filaments and diatoms. The middle time of precipitation is dominated by cement deposition; cement consists on iron, calcite, silica and hematite. The first cement deposition mainly contains iron and could be interbedded with hematite laminations; these laminations contain a greater amount of polymictic grains, filaments and diatoms. The iron cement laminations, alternate with calcite, and, when iron cement precipitation stops, a silica laminated horizon precipitates. Parallel to the decrease of iron cement deposition, filaments decrease in amount but diatoms remain constant. Silica laminated horizons are interbedded with carbonate horizons, but when silica precipitation is over, the carbonate and iron cement deposition increases, alternating between them. During this last stage of cement deposition, the amount of polymictic grains is variable but filaments disappear and it is rare to find diatoms. Finally, the late time of deposition is characterized by the filling of cavities with carbonate fluids and minerals. Carbonate fluids, iron-oxide minerals and Cu-Fe sulfide minerals fill the small cavities inside the iron-travertine matrix (Figure 5.8C).

The manganese-travertine deposits showed a similar diagenetic behaviour as the iron-travertine deposits, but with different compositions. During an early time of deposition, manganese-travertine deposits trap carbonate fragments and incorporate them into their structure, while filaments and diatoms surround the fragments. The middle time of cement deposition is characterized by manganese precipitation, which decreases in the last stages. The manganese horizons may be interbedded with iron-laminated horizons and polymictic grains, the latter of which are variable during manganese precipitation. Manganese precipitation buries diatoms, and laminations are interbedded with grainy calcite, but when manganese precipitation decreases, fibrous and fragmental calcite crystals increase in size. Finally, the late time of precipitation is characterized by the filling of cavities. Carbonate fluids filled the holes left by chemical dissolution but no sulfide or oxide minerals crystallized (Figure 5.8C).

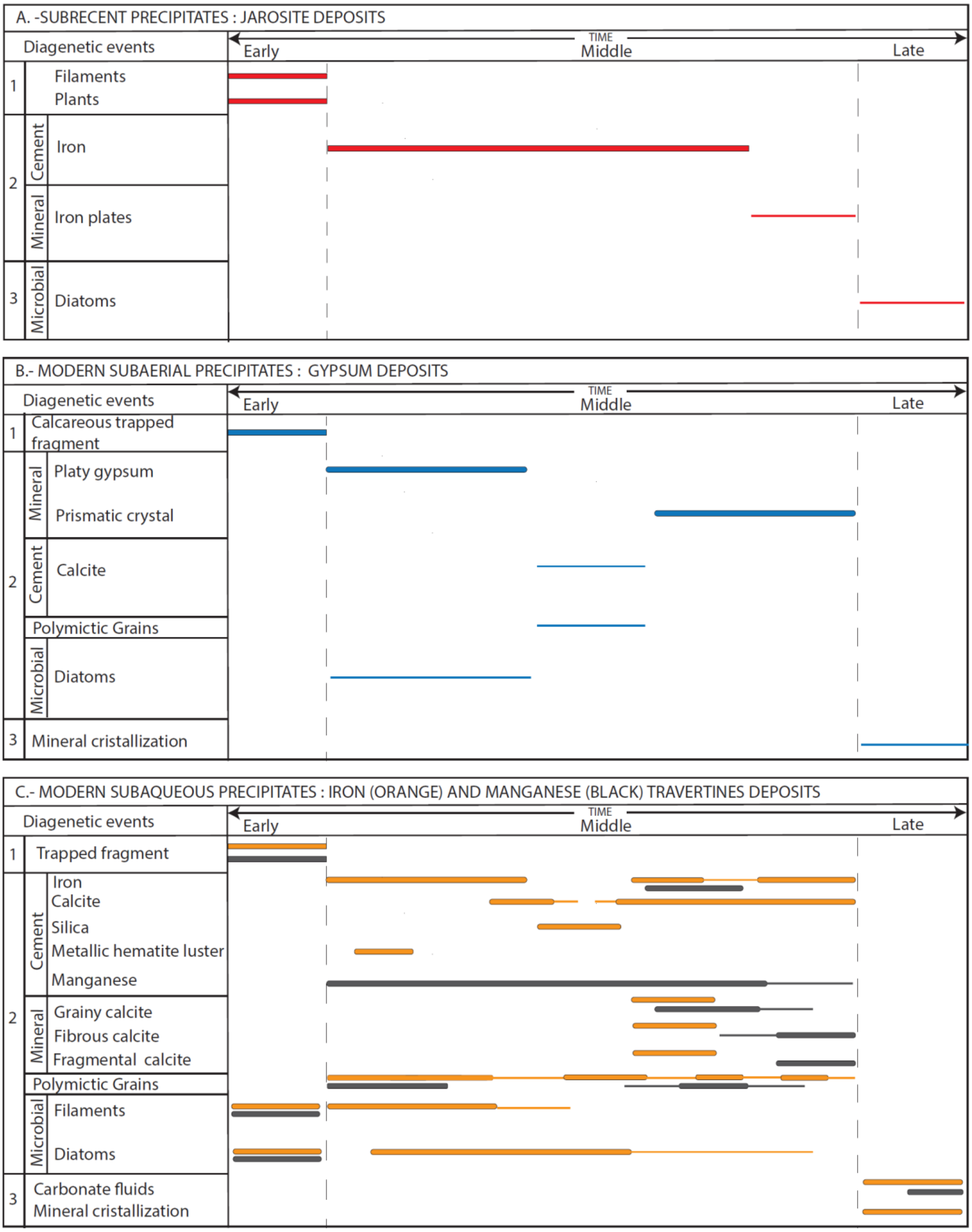

Figure 5.8 Relative timing relationships and distribution of diagenetic processes for subrecent and modern subaerial and subaqueous precipitates recorded at the Jaraña hot springs. Thicker lines represent the high amounts of components and thin lines the low amounts of components.

5.3 Conceptual Model of the Jaraña Geothermal System

The hot spring deposits at Jaraña are part of a dynamic geothermal system. The Jaraña geothermal system is supplied by meteoric water that falls over the peak Mountains (5300 m). Meteoric water percolates over and through country rocks: sandstones, limestones, red bed conglomerates rich in calcareous cement and andesite lavas, thereby providing Ca, Fe, Si and Na elements. The iron-copper sulfide minerals within subvolcanic rocks, are suitable for providing Fe, Cu, As and S elements (Figure 5.9). In addition, the Jaraña hot springs occur above a breccia iron-cemented outcrop, surrounded by silicified rocks, providing a potential source for Fe and Si. Meteoric water circulates through the Jaraña country rock, and deep faults provide a mechanism to heat the fluids. The ascendant heated fluids react with the host rocks driving potential dissolution during water-rock exchange (Faulds et al., 2012). The host rock surrounding the hot springs areas are mainly based on quartz minerals. Silicified rocks contain trace element concentration completely different from those registered on hot springs deposits at Jaraña. Therefore, the host rocks around do not appear to be a source for the Jaraña hot springs.

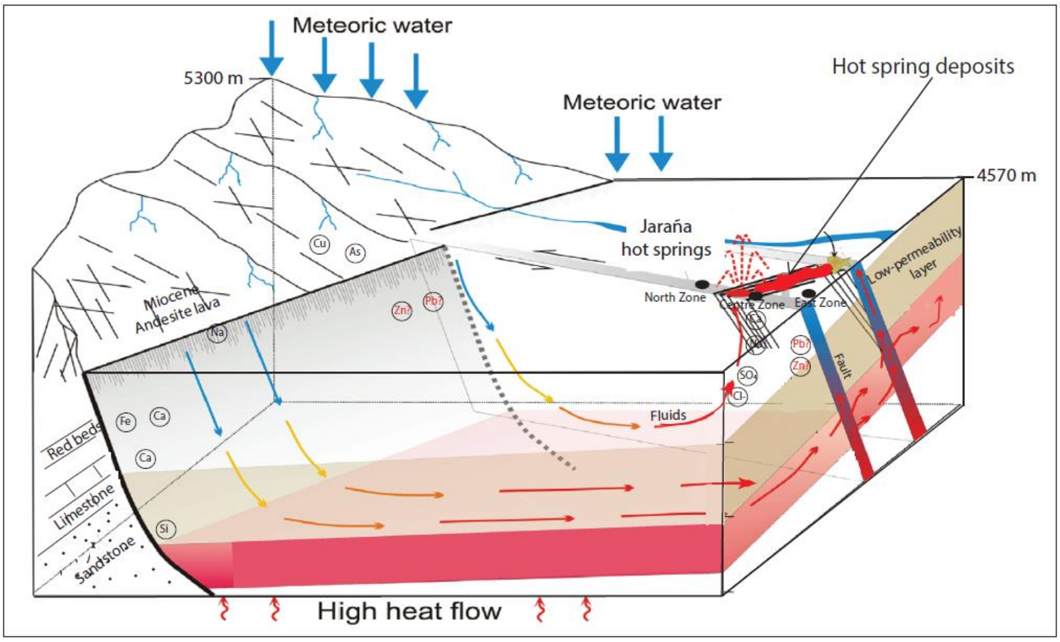

Figure 5.9 conceptual model of the Jaraña geothermal system, modified from Moeck (2014).

Thermal water emerges on the surface as a vent, sustaining thermal pools with variable deepness in the northern, central and eastern zones. Thermal waters concentrate high amounts of Na, Ca, Cl and SO_4 between 100 to 1000 mg/L among the three zones (Figure 5.10). The saturation of Ca and SO_4 in thermal waters brings suitable conditions for gypsum precipitation (Tang et al., 2014; Vogel et al., 2010). Gypsum deposits at Jaraña have a subaerial emplacement; build convex laminations of gypsum crystals that form branches shaped columnar nodules. Also, gypsum deposits concentrates Ca and Si above 1 Wt %. The major concentrations of Si inside gypsum structures could explain the blue colour luminescence detected during the cathodoluminescence analysis. Moreover, the highest concentrations of Na, Mg and K in gypsum deposits from the central zone are not reflected with thermal water composition (Figure 5.10). Thus, thermal waters from the central zone contain the highest amount of Ca and Mg and thermal waters from the eastern zone contain the highest amount of K. However, the high concentration of Ca and Mg in thermal waters and gypsum deposits in the central zone could be an influence for a later sulfide mineral crystallization. The neutral pH, high amount of Ca and SO_4 in thermal waters at Jaraña, becomes important for a gypsum precipitation but not for Jarosite precipitation. Jarosite deposits need an acid pH, and a high amount of Fe and SO_4 to precipitate in hot spring terrains (Jones & Renaut, 2007). Studies in Waiotapu at New Zealand showed that jarosite deposits precipitates from thermal water with Fe in the range of 4.2-5.6 mg/L and SO_4 in the range of 255-263 mg/L. Actual element concentrations in thermal water seems to be suitable for jarosite precipitation; however, pH conditions result unsuitable. Therefore, jarosite deposits at Jaraña are the record of previous hot springs emergences.

Hot springs at Jaraña precipitate iron and manganese travertine deposits under subaqueous conditions with thermal water having Ca saturation between 100 to 1000 mg/L, HCO_3 above 100 mg/L but lower concentration of Fe. Studies in Sperchios hot springs in Greece showed that iron-travertine deposits precipitate from thermal waters with Fe in the range of 0.005–11 mg/L (Kanellopoulos et al., 2017). Chocolate Pots at Yellowstone have iron-silica deposits that precipitate from thermal waters with Fe in the range of 5.8–5.9 mg/L (Parenteau et al., 2014). Thermal waters at Jaraña contain a similar range of concentrations of Fe (0.1 to 10 mg/L); thus, iron-travertine deposits could be comparable to studies in Greece or United States (Kanellopoulos et al., 2017; Parenteau et al., 2014). In contrast, studies in Sambe and Hokkaido hot springs, indicate that manganese-travertine deposits precipitate from thermal water with low Mn (0.9–3.05 mg/L) and Fe (<0.01–0.56 mg/L) saturations (Mita & Maruyama, 1994; Sasaki et al., 2013). Thermal waters at Jaraña contain lower concentrations of Mn (0.1–1 mg/L) compared to Fe (0.1-10 mg/L). The saturation of Mn in thermal waters is lower compared with the cases in Japan (Mita & Maruyama, 1994; Sasaki et al., 2013).

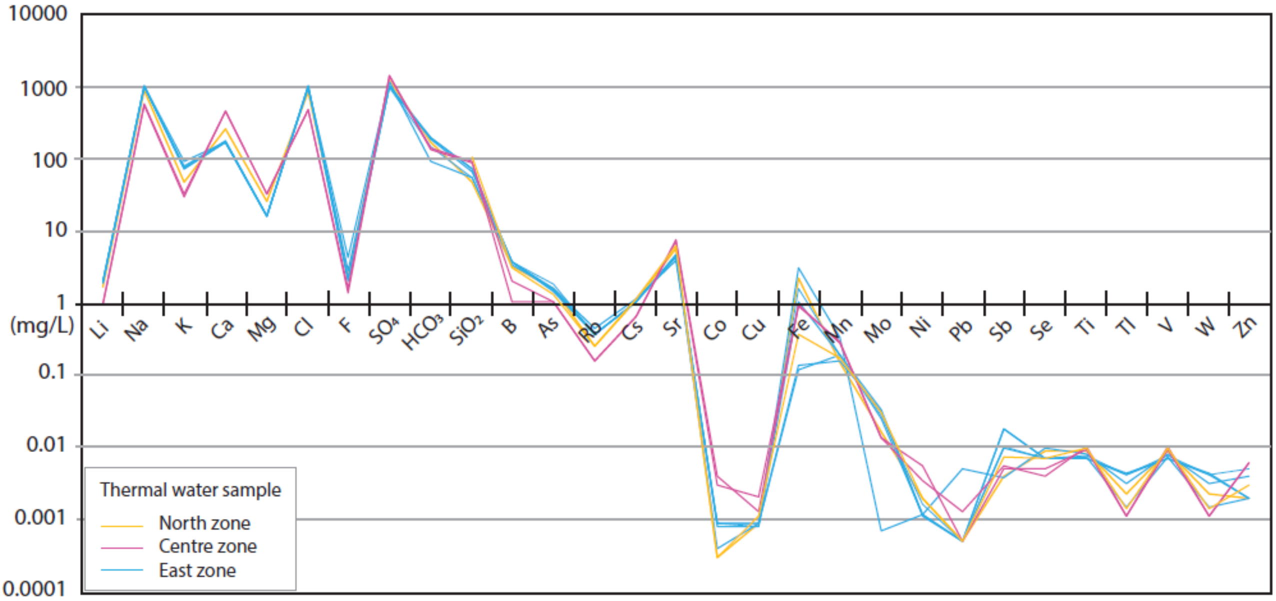

Figure 5.10 Jaraña hot spring chemistry comparing the northern, central and eastern zones (data from Cruz, (2016)).

Apparently, the Jaraña geothermal system shows that hot spring deposits in subaerial areas have a greater affinity with sulfate ligands, different from subaqueous areas that have a greater affinity for carbonate ligands. Conditions for subaerial precipitation requires high concentrations of Ca, Na, Mg and SO_4 in thermal waters but for subaqueous precipitation is not necessary high amounts of Fe or Mn in thermal waters. Therefore, microbials have an important influence on the concentration and precipitation of Fe and Mn from thermal waters (Chafetz et al., 1998; Sasaki et al., 2013). The pennate diatoms seem to have an important role for concentrating and precipitationg Fe and Mn in subaqueous deposits. However, pennate diatoms and filaments could be inducing the highest concentration on base metals and REE's, precipitation as laminated horizons of hematite mineral, and crystallization as grains of Cu-Fe sulfides and iron-oxide minerals.

The all-geothermal system at Jaraña seems to be connected among country rocks (source), thermal water (carrier) and hot spring deposits (host). Among the group of elements in country rocks only Ca, Na, SO_4, HCO_3 and SiO_2 have high concentrations in thermal waters. Moreover, hot spring deposits distribute these elements in subaerial and subaqueous areas. The subaqueous areas induced by microbial communities are suitable to increase metal elements, which are in low concentration in thermal waters (Figure 5.11).

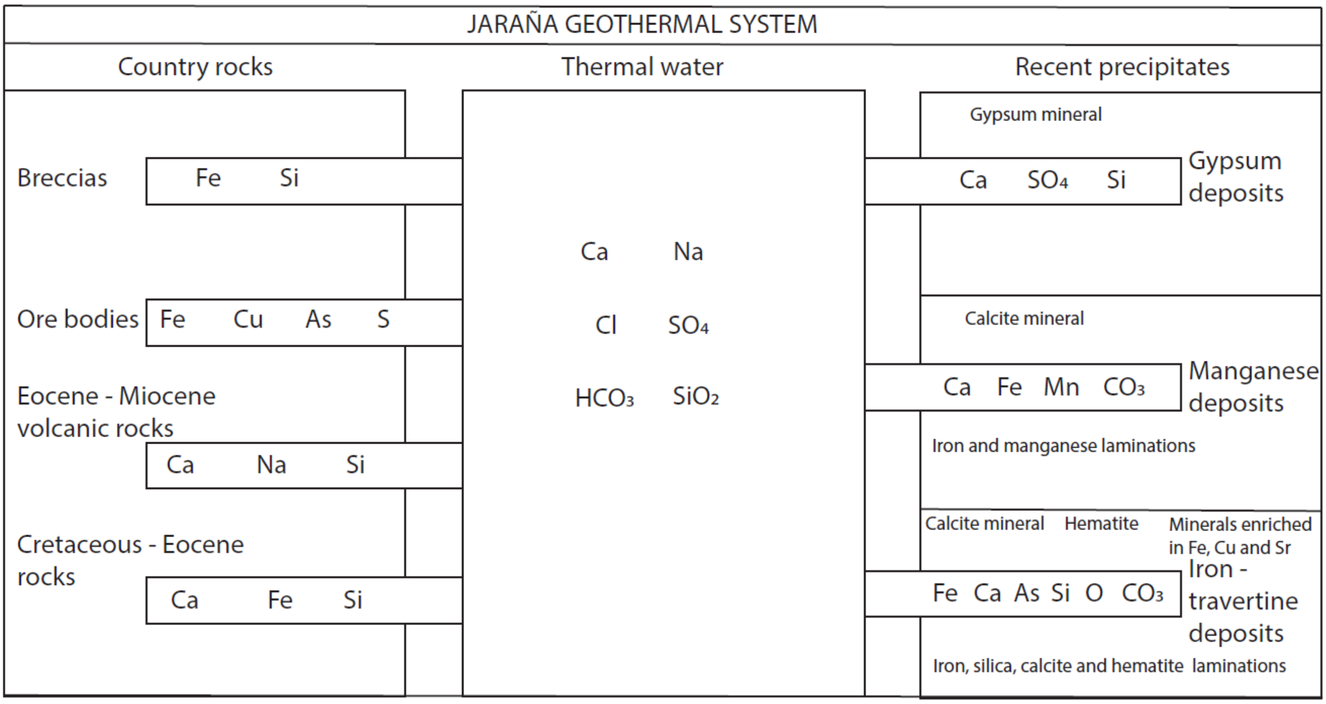

Figure 5.11 Schematic graphic illustrate country rocks, thermal water, and recent precipitates element distribution at Jaraña geothermal system.

6 CONCLUSIONS

The study of hot spring deposits at Jaraña, conducted at high altitudes in the Peruvian central Andes, reveal the following conclusions:

1) Jaraña hot springs register four deposits types, of which, two of them are sulfate deposits and the other two are travertine deposits. The sulfate deposits are jarosite and gypsum based, whereas the travertine deposits are iron and manganese based.
2) Subrecent and recent deposits reflect changes in thermal waters. The jarosite deposits (subrecent deposits) are the register of the acidic thermal water conditions inside a previous geothermal system. Currently, hot springs emerge from the ground, sustain thermal pools and generate run-off channels. Hot springs induce a subaerial build-up and generate a subaqueous precipitation. The subaerial build-up is based on gypsum deposits and the subaqueous precipitation on iron and manganese travertine deposits. Conditions for precipitation between iron and manganese travertine deposits are different; therefore, iron-travertine deposits precipitate on thermal pools with variable depth or forming spring conduits, while manganese-travertine deposits are on shallow water areas.
3) Morphologies between subrecent and recent deposits are different. Subrecent deposits (jarosite deposits) contain network fabric morphology and recent deposits contain a variable range of nodular and botryoidal morphologies. The recent precipitates such as gypsum deposits contain a nodular-branched type, iron-travertine deposits have clumped nodular humps, and manganese-travertine deposits develop nodular with smooth surface, growing perpendicular to the water level. From a vertical cross section view, gypsum deposits show columns laterally linked with convex laminations; iron-travertine deposits contain wavy laminated horizons with small rounded nodules and manganese-travertine deposits display laminated horizons with calcite crystals.
4) The crystal habit is common in gypsum and manganese-travertine deposits rather than jarosite or iron-travertine deposits. Gypsum deposits contain two gypsum crystal types, platy with twinning and prismatic; and manganese-travertine deposits contain three-calcite crystal type, acicular, fragmented and grainy.
5) The laminated horizons are common only in subaqueous travertine deposits. However, iron-travertine deposits contain a greater variation of laminations compared with manganese-travertine deposits. Iron-travertine deposits have four types of laminated horizons with iron, carbonate, silica and hematite mineral composition, which can be mixed. In contrast, manganese-travertine deposits contain two type of laminated horizons with manganese and iron oxide minerals, which are not mixed between them but fill the spaces between calcite crystals.
6) The microbial communities are the main factor inducing the precipitation at Jaraña hot springs. Microbials have a carbonate composition and look like green to orange mats floating above the thermal water surface; also, all hot spring deposits contain pennate diatoms. Only iron-travertine deposits contain diatoms and filaments inside laminated horizons. Microbial communities have a strong influence on the precipitation process, concentration of metals and a later mineral crystallization at Jaraña. Moreover, diatoms appear in hot spring deposits with high amount of Si.
7) Ca, Fe and Si represent the main chemical concentrations above 1 Wt %. The four deposit types at Jaraña contain variable ranges of Ca and Fe in major concentrations. However, jarosite and iron-travertine deposits register the highest amount of Fe, compared with gypsum and manganese deposits that register the highest amount in Ca. Furthermore, the silica (Si) element has major concentrations in recent precipitates.
8) The highest concentrations of base metals, REE's and metalloids (As, Sb) were found in iron-travertine deposits. Only iron-travertine deposits host base metals, REE's and metalloids in greater amounts compared with other deposits types at Jaraña, concentration is influenced by Fe (III) precipitation. The increase on Si amount generates the highest concentrations of Cu, and the increase in Fe produces the highest concentrations of Zn and Pb. Furthermore, laminated horizons with high Fe concentrations but low in Si are favourable for the highest amounts on As.
9) Sulfide and oxide minerals are like crystals inside carbonate matrix cavities only in iron-travertine deposits, and sulfide minerals in small proportion inside gypsum cavities. The iron-travertine deposits

contain greater evidence of iron-oxide and Fe-Cu sulfide minerals compared with gypsum deposits that contain Fe-Cu sulfide minerals.

10) The three zones at Jaraña showed differences in the morphological, mineralogical and chemical composition. The central zone showed favourable conditions to precipitate gypsum and iron-travertine deposits with iron-oxide and Fe-Cu sulfate minerals as crystals. Furthermore, the central zone had appropriate conditions to precipitate iron-travertine deposits with a greater thickness and variability in morphologies. In contrast, the eastern zone was favourable to precipitate manganese-travertine deposits.
11) The hot spring deposits at Jaraña are inside a strategic geologic position appropriate for metal concentrations. Host rocks and exhumed Cu-Fe ore bodies provide the following elements: Ca, Si, Fe, Cu, S and As. However, the Zn and Pb elements concentrated as trace elements on iron-travertine deposits suggest that other ore mineralized bodies with Zn and Pb could be hidden. This determines the importance of iron-travertine deposits as footprints for base metals.
12) The contributions of this study are important for the environmental sciences. Similarly, the metal concentration in hot spring deposits could be used as a key for mineral exploration. Additionally, the chemical and mineralogical variation on subrecent and recent deposits contributes to the analysis of changes inside a geothermal system

REFERENCES

Acosta, J. G., Rivera, R., Valencia, M. M., Chirif, L. H., Huanacuni, D., Rodríguez, I., … Santisteban, A. (2010). *Mapa metalogenético del Perú 2009: Memoria*. (Instituto Geológico Minero y Metalúrgico, Ed.). Lima.

Aguilar, R. (2012). *Magmatismo, Tectónica y Metalogenia de los Centros Volcánicos Miocénicos entre Condoroma y Paratia (Cusco-Puno), sur del Perú*. Universidad Nacional de San Antonio Abad del Cusco.

Alshuaibi, A. A., & Khalaf, F. I. (2015). Calcareous thrombolitic crust on Late Quaternary beachrocks in Kuwait , Arabian Gulf. *Arabian Journal of Geosciences*, *8*(11), 9721–9732. http://doi.org/10.1007/s12517-015-1869-5

Bramburger, A. J., Haffner, G. D., Hamilton, P. B., Hinz, F., & Hehanussa, P. E. (2006). An examination of species within the genus Surirella from the Malili Lakes , Sulawesi Island , Indonesia , with descriptions of 11 new taxa, *21*(1), 1–56. http://doi.org/10.1080/0269249X.2006.9705650

Brock, T. D. (1978). *Thermophilic Microorganisms and Life at High Temperatures*. New York : Springer-Verlag.

Campbell, K. A., Farmer, J. D., & Des Marais, D. (2002). Ancient hydrocarbon seeps from the Mesozoic convergent margin of California.pdf. *Geofluids*, *2*, 63–94.

Campbell, K. A., Guido, D. M., Gautret, P., Foucher, F., Ramboz, C., & Westall, F. (2015). Geyserite in hot-spring siliceous sinter: Window on Earth’s hottest terrestrial (paleo)environment and its extreme life. *Earth-Science Reviews*, *148*, 44–64. http://doi.org/10.1016/j.earscirev.2015.05.009

Campbell, K. A., Rodgers, K. A., Brotheridge, J. M. A., & Browne, P. R. L. (2002). An unusual modern silica-carbonate sinter from Pavlova spring, Ngatamariki, New Zealand. *Sedimentology*, *49*(4), 835–854. http://doi.org/10.1046/j.1365-3091.2002.00473.x

Carlotto, V. S., Jaillard, E., Carlier, G., Cárdenas, J. D., Cerpa, L. M., Flores, T., … Ibarra, I. (2005). Las cuencas terciarias sinorogénicas en el Altiplano y en la Cordillera Occidental del sur del Perú. In Sociedad Geológica del Perú (Ed.), *Alberto Giesecke Matto* (pp. 103–106). Lima: Sociedad Geológica del Perú.

Cereceda, C., Cerpa, L., Mamani, M., Torres, D., Muñoz, L., & Aguilar, R. (2010). Características geoquímicas del volcanismo Cenozoico del Sur del Perú en el sector Condoroma-Ocuviri : Implicancias en la estratigrafía volcánica y mineralización. In *Congreso Peruano de Geología, 15* (Vol. 9, pp. 2–7). Cusco: Sociedad Geológica del Perú.

Cerpa, L., Cereceda, C., Torres, D., Muñoz, L., Aguilar, R., Martinez, J., & Chacón, A. (2012). Controles Tectono-Magmáticos en el Sur del Perú (72 ° -70 ° 30’ y 14^{o}-16^{o}S). Implicancias Metalogenéticas. In *Congreso Peruano de Geología, 16* (pp. 22–25). Lima: Sociedad Geológica del Perú.

Chafetz, H. S., Akdim, B., Julia, R., & Reid, A. (1998). Mn-and Fe-rich black Travertine Shrubs: Bacterially (and Nanobacterially) Induced Precipitates. *Journal of Sedimentary Research*, *68*(3), 404–412. http://doi.org/073-130X/98/068-0404/$03.00

CLIMATE-DATA.ORG. (2018). CLIMATE-DATA.ORG. Retrieved from https://es.climate-data.org/america-del-sur/peru/puno/santa-lucia-27442/

Cruz, V. (2016). Hidrogeoquímica de aguas termales y mineralizadas de la zona de Jaraña, Paratía, Puno. In *Congreso Peruano de Geología, 18* (p. 5). Lima: Sociedad Geológica del Perú.

Faulds, J. E., Hinz, N., Kreemer, C., & Coolbaugh, M. (2012). Regional Patterns of Geothermal Activity in the Great Basin Region , Western USA : Correlation With Strain Rates Distribution of Geothermal Fields. *Geothermal Resources Council Transactions*, *36*, 897–902. Retrieved from https://pangea.stanford.edu/ERE/db/IGAstandard/record_detail.php?id=14060

Ferris, F. G. (2000). Microbe-Metal Interactions in Sediments. In R. E. Riding & S. M. Awramik (Eds.), *Microbial Sediments* (pp. 121–126). Springer-Verlag Berlin Heidelberg.

Finland, G. S. of. (2005). FOREGS-EuroGeoSurveys Geochemical Baseline Database. Retrieved from http://weppi.gtk.fi/publ/foregsatlas/text/Mn.pdf

Fornari, M., Baldellón, E., Espinoza, F., Ibarra, I., Jimenez, N., & Mamani, M. (2002). Ar-Ar dating of late oligocene-early miocene volcanism in the altiplano. In *International Symposium on Andean Geodynamics, 5* (Vol. 02, pp. 223–226). Toulouse: Université Paul Sabatier.

Fournier, R., Kennedy, B. M., Aoki, M., & Thompson, J. M. (1994). Correlation of gold in siliceous sinters with 3He/4He in hot spring waters of Yellowstone National Park, *58*(24), 5401–5419.

Giggenbach, W. F. (1980). Geothermal mineral equilibria. *Geochimica et Cosmochima Acta*, *45*, 393–410.

Guido, D. M., & Campbell, K. A. (2011). Jurassic hot spring deposits of the Deseado Massif (Patagonia, Argentina): Characteristics and controls on regional distribution. *Journal of Volcanology and Geothermal Research*, *203*(1–2), 35–47. http://doi.org/10.1016/j.jvolgeores.2011.04.001

Guido, D. M., & Campbell, K. A. (2018). Upper Jurassic travertine at El Macanudo, Argentine Patagonia: A fossil geothermal field modified by hydrothermal silicification and acid overprinting. *Geological Magazine*, *155*(6), 1394–1412. http://doi.org/10.1017/S0016756817000498

Gutscher, M. A., Olivet, J. L., Aslanian, D., Eissen, J. P., & Maury, R. (1999). The “lost Inca Plateau”: Cause of flat subduction beneath Peru? *Earth and Planetary Science Letters*, *171*(3), 335–341. http://doi.org/10.1016/S0012-821X(99)00153-3

Hamilton, A., Campbell, K., Rowland, J., & Browne, P. (2017). The Kohuamuri siliceous sinter as a vector for epithermal mineralisation, Coromandel Volcanic Zone, New Zealand. *Mineralium Deposita*, *52*(2), 181–196. http://doi.org/10.1007/s00126-016-0658-8

Handley, K. M., Campbell, K. A., Mountain, B. W., & Browne, P. R. L. (2005). Abiotic–biotic controls on the origin and development of spicular sinter: in situ growth experiments, Champagne Pool, Waiotapu, New Zealand. *Geobiology*, *3*(2), 93–114.

Hedenquist, J. W., & Lowenstern, J. B. (1994). The role of magmas in the formation of hydrothermal ore deposits. *Nature*. http://doi.org/10.1038/370519a0

Herbert Jr, R. B. (1995). Precipitation of Fe oxyhydroxides and jarosite from acidic groundwater. *GFF*, *117*(2), 81–85. http://doi.org/10.1080/11035899509546203

INGEMMET. (2018). GEOCATMIN. Retrieved from http://geocatmin.ingemmet.gob.pe/

International Geothermal Association. (2014). *Best Practices Guide for Geothermal Exploration*. Bochum.

Jaillard, E., Soler, P., Carlier, G., & Mourier, T. (1990). Geodynamic evolution of the northern and central Andes during early to middle Mesozoic times: a Tethyan model. *Journal of the Geological Society*, *147*(6), 1009–1022. http://doi.org/10.1144/gsjgs.147.6.1009

Jones, B., & Renaut, R. W. (2003). Hot spring and geyser sinters: the integrated product of precipitation, replacement, and deposition. *Canadian Journal of Earth Sciences*, *40*(11), 1549–1569. http://doi.org/10.1139/e03-078

Jones, B., & Renaut, R. W. (2007). Selective mineralization of microbes in Fe-rich precipitates (jarosite, hydrous ferric oxides) from acid hot springs in the Waiotapu geothermal area, North ISland, New Zealand. *Sedimentary Geology*, *194*, 77–98.

Kale, A., & Karthick, B. (2015). The Diatoms. *Indian Academy of Sciences*, *20*(10), 919–930.

Kanellopoulos, C., Mitropoulos, P., Valsami-Jones, E., & Voudouris, P. (2017). A new terrestrial active mineralizing hydrothermal system associated with ore-bearing travertines in Greece (northern Euboea Island and Sperchios area). *Journal of Geochemical Exploration*, *179*(May), 9–24. http://doi.org/10.1016/j.gexplo.2017.05.003

Klein, C., Dana, J. D., & Hurlbut, C. S. (1993). *Manual of Mineralogy (after James D. Dana)* (21th ed.). New York: New York: Wiley 1993.

Landrum, J. T., Bennett, P. C., Engel, A. S., Alsina, M. A., Pastén, P. A., & Milliken, K. (2009). Partitioning geochemistry of arsenic and antimony , El Tatio Geyser Field , Chile. *Applied Geochemistry*, *24*(4), 664–676. http://doi.org/10.1016/j.apgeochem.2008.12.024

Laurent, G. C., Edoardo, P., Ian, S. R., Peacock, D. C. P., Roger, S., Ragnar, P., … Vladimir, M. (2016). Origin and diagenetic evolution of gypsum and microbialitic carbonates in the Late Sag of the Namibe Basin (SW Angola). *Sedimentary Geology*, *342*, 133–153. http://doi.org/10.1016/j.sedgeo.2016.06.015

Lynne, B. Y. (2012). Mapping vent to distal-apron hot spring paleo-flow pathways using siliceous sinter architecture. *Geothermics*, *43*, 3–24. http://doi.org/10.1016/j.geothermics.2012.01.004

Lynne, B. Y., & Campbell, K. A. (2003). Diagenetic transformations (opal-A to quartz) of low- and mid-temperature microbial textures in siliceous hot-spring deposits, Taupo Volcanic Zone, New Zealand. *Canadian Journal of Earth Sciences*, *40*(11), 1679–1696. http://doi.org/10.1139/e03-064

Lynne, B. Y., Campbell, K. A., Perry, R. S., Browne, P. R. L., & Moore, J. N. (2006). Acceleration of sinter diagenesis in an active fumarole, Taupo volcanic zone, New Zealand. *Geology*, *34*(9), 749–752. http://doi.org/10.1130/G22523.1

Mackenzie, W. S., & Adams, A. E. (1951). *A colour atlas of rocks and minerals in thin section*. (Manson Pub. c1994, Ed.). London.

McHenry, L. J., Carson, G. L., Dixon, D. T., & Vickery, C. L. (2017). Secondary minerals associated with Lassen fumaroles and hot springs : Implications for martian hydrothermal deposits. *American Mineralogist*, *102*, 1418–1434.

McKenzie, E. J., Brown, K. L., Cady, S. L., & Campbell, K. A. (2001). Trace metal chemistry and silicification of microorganisms in geothermal sinter, Taupo volcanic zone, New Zealand. *Geothermics*, *30*(4), 483–502. http://doi.org/10.1016/S0375-6505(01)00004-9

Merinero, R. L., Hernández, R., & Martínez, J. (2010, September). Carbonatos Metanógenos y Pirita Framboidal Autigénica : Geomarcadores de la Actividad de Organismos Quimiosintéticos en el Golfo de Cádiz . *Revista de La Sociedad Española de Mineralogía*, (12), 29–37.

Mita, N., & Maruyama, A. (1994). A growing produced deposit, *28*.

Moeck, I. S. (2014). Catalog of geothermal play types based on geologic controls. *Renewable and Sustainable Energy Reviews*, *37*, 867–882. http://doi.org/10.1016/j.rser.2014.05.032

Nicholson, K. N. (1993). *Geothermal Fluids. Chemistry and Exploration Techniques*. Berlin: Springer-Verlag.

Nicholson, K., & Parker, R. J. (1990). Geothermal sinter towards a diagnosticsignature and a sinter geothermometer. In *12th New Zealand Geothermal Workshop* (pp. 97–102).

Nicolau, C. B. (2013). *Physico-Chemical and Environmental Controls on Siliceous Sinter Formation At the High-Altitude El Tatio Geothermal Field , Northern Chile*. Universidad de Chile.

Okrugin, V. M., Andreeva, E. D., Chubarov, V. M., Yablokova, D. A., & Shishkanova, K. O. (2015). Sulfides of the Modern Kamchatka Hydrothermal Systems, (April), 19–25.

Pajuelo, D., Condorhuaman, A., Cruz, V., & Zegarra, E. (2016). Características geológicas de la zona geotérmica de Pinaya-región Puno (pp. 1–4). Lima-Perú: XVIII Congreso Peruano de Geología.

Parenteau, M. N., Jahnke, L. L., Farmer, J. D., & Cady, S. L. (2014). Production and Early Preservation of Lipid Biomarkers in Iron Hot Springs. *Astrobiology*, *14*(6), 502–521. http://doi.org/10.1089/ast.2013.1122

Renaut, R. W., & Jones, B. (2000). Microbial Precipitates Around Continental Hot Springs and Geysers. In R. E. Riding & S. M. Awramik (Eds.), *Microbial Sediments* (pp. 187–195). Springer-Verlag Berlin Heidelberg.

Renaut, R. W., & Jones, B. (2011). Hydrothermal Environments, Terrestrial. In J. Reitner & T. Volker (Eds.), *Encyclopedia of Geobiology* (1st ed., p. 927). Göttingen: Springer Netherlands.

Rice, C. M., Ashcroft, W. A., Batten, D. J., Boyce, J., Fallick, A. E., Hole, M. J., … Ab, H. (1995). A Devonian auriferous hot spring system , Rhynie , Scotland. *Journal of the Geological Society, London*, *152*, 229–250.

Riding, R. E., & Awramik, S. M. (2000). *Microbial Sediments*. (R. E. Riding & S. M. Awramik, Eds.). Springer-Verlag Berlin Heidelberg. http://doi.org/10.1007/978-3-662-04036-2

Rosenbaum, G., Giles, D., Saxon, M., Betts, P. G., Weinberg, R. F., & Duboz, C. (2005). Subduction of the Nazca Ridge and the Inca Plateau: Insights into the formation of ore deposits in Peru. *Earth and Planetary Science Letters*, *239*(1–2), 18–32. http://doi.org/10.1016/j.epsl.2005.08.003

Rowland, J. V., & Sibson, R. H. (2004). Structural controls on hydrothermal flow in a segmented rift system, Taupo Volcanic Zone, New Zealand. *Geofluids*, *4*(4), 259–283. http://doi.org/10.1111/j.1468-8123.2004.00091.x

Rudnick, R. L., & Gao, S. (2013). *Composition of the Continental Crust*. *Treatise on Geochemistry: Second Edition* (2nd ed., Vol. 4). Elsevier Ltd. http://doi.org/10.1016/B978-0-08-095975-7.00301-6

Sasaki, K., Uejima, Y., Sakamoto, A., Yu, Q., Ishibashi, J., Okibe, N., & Hirajima, T. (2013). Geochemical and Microbiological Analysis of Sambe Hot Springs, Shimane Prefecture, Japan. *Resource Geology*, *63*(2), 155–165. http://doi.org/10.1111/rge.12002

Scarlett, N., Grey, I. E., & Brand, H. E. A. (2012). Fundamental studies into the formation of jarosite related precipitates, (August).

Scholle, P. A., & Ulmer-Scholle, D. S. (2003). *A color guide to the petrography of carbonate rocks: grains, textures, porosity, diagenesis*. American Association of Petroleum Geologists. http://doi.org/https://doi.org/10.1306/M77973

Sillitoe, R. H. (2015). Epithermal paleosurfaces. *Mineralium Deposita*, *50*(7), 767–793. http://doi.org/10.1007/s00126-015-0614-z

Smith, D. J. (2008). *From Slab To Sinter: the Magmatic-Hydrothermal System of Savo Volcano, Solomon Islands*. University of Leicester. Retrieved from http://hdl.handle.net/2381/8207

Stahl, R. S., Fanning, D. S., & James, B. R. (1993). Goethite and Jarosite Precipitation from Ferrous Sulfate Solutions. *Soil Science Society of America Journal*, *57*(1), 280. http://doi.org/10.2136/sssaj1993.03615995005700010047x

Stolz, J. F. (2000). Structure of Microbial Mats and Biofilms. In R. E. Riding & S. M. Awramik (Eds.), *Microbial Sediments* (pp. 1–8). Springer-Verlag Berlin Heidelberg.

Takashima, C., Kano, A., Naganuma, T., & Tazaki, K. (2008). Laminated iron texture by iron-oxidizing bacteria in a calcite travertine. *Geomicrobiology Journal*, *25*(3–4), 193–202. http://doi.org/10.1080/01490450802081887

Takashima, C., Okumura, T., Nishida, S., Koike, H., & Kano, A. (2011). Bacterial symbiosis forming laminated iron-rich deposits in Okuoku-hachikurou hot spring, Akita Prefecture, Japan. *Island Arc*, *20*(2), 294–304. http://doi.org/10.1111/j.1440-1738.2011.00768.x

Tang, M., Ehreiser, A., & Li, Y. L. (2014). What lurks in the martian rocks and soil? Investigations of sulfates, phosphates, and perchlorates. Gypsum in modern kamchatka volcanic hot springs and the lower cambrian black shale: Applied to the microbial-mediated precipitation of sulfates on Mars. *American Mineralogist*, *99*(10), 2126–2137. http://doi.org/10.2138/am-2014-4754

Tassara, A. (2005). Interaction between the Nazca and South American plates and formation of the Altiplano Puna plateau: Review of a flexural analysis along the Andean margin (15° 34°S). *Tectonophysics*, *399*(1–4), 39–57. http://doi.org/10.1016/j.tecto.2004.12.014

Taylor, R. (2009). *Ore Textures. Recognition and Interpretation* (1st ed.). Queensland: Springer-Verlag Berlin Heidelberg. http://doi.org/10.1007/978-3-642-01783-4

Terra, J. G. S., Spadini, A. R., França, A. B., Leite, C., Zambonato, E. E., Costa, L., … Maria, S. (2010). *Classificações Clássicas De Rochas Carbonáticas*. *B. Geoci. Petrobras, Rio de Janeiro* (Vol. 18). Rio de Janeiro.

Uchida, A., Yokoyama, T., Watanabe, K., & Izawa, E. (2001). Gold content in siliceous deposits formed from acidic and iron-rich geothermal waters at Hatchobaru, central Kyushu, Japan. *Resource Geology*, *51*(3), 269–271. http://doi.org/10.1111/j.1751-3928.2001.tb00099.x

Valdivia, E., & Rodríguez, R. (2003). *Memoria descriptiva de la revisión y actualización del cuadrángulo de Lagunillas (32-u), escala 1:100 000*. *Instituto Geológico Minero y Metalúrgico*. Lima.

Valdivieso, L. G. (2015). *Proyecto de exploración sabina , comparación con los depósitos Arasi y Pinaya , franja metalogenética XXI , sur del Perú*. Lima-Perú.

Vargas, V., & Cruz, V. (2010). Geothermal Map of Perú. In *World Geothermal Congress* (pp. 25–29). Bali, Indonesia: Proceedings World Geothermal Congress 2010.

Vogel, M. B., Des Marais, D. J., Parenteau, M. N., Jahnke, L. L., Turk, K. A., & Kubo, M. D. Y. (2010). Biological influences on modern sulfates: Textures and composition of gypsum deposits from Guerrero Negro, Baja California Sur, Mexico. *Sedimentary Geology*, *223*(3–4), 265–280. http://doi.org/10.1016/j.sedgeo.2009.11.013

Warren, J. (2016). *Evaporites* (2nd ed.). Springer International Publishing. http://doi.org/10.1007/978-3-319-13512-0

West Japan Engineering Consultants. (2012). *PLAN MAESTRO PARA EL DESARROLLO DE LA ENERGÍA GEOTÉRMICA EN EL PERÚ*. Perú.

Winsborough, B. M. (2000). Diatoms and Benthic Microbial Carbonates. In R. E. Riding & S. M. Awramik (Eds.), *Microbial Sediments* (pp. 76–83). Springer-Verlag Berlin Heidelberg.

APPENDICES

APPENDIX I: MINERALOGY

Figure A1 Hand sample photography and x-ray diffraction results.

NORTH ZONE


JR- 01
2 cm

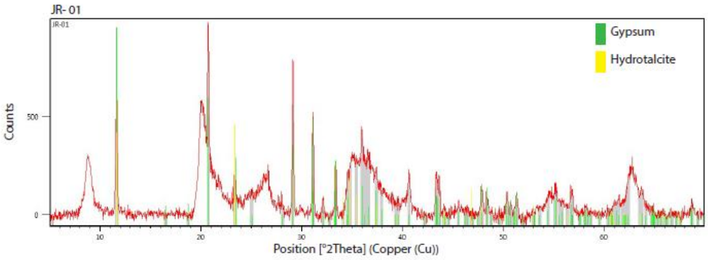
JR- 01
JR-01
Counts
500
0
10
20
30
40
50
60
Position [°2Theta] (Copper (Cu))
Gypsum
Hydrotalcite

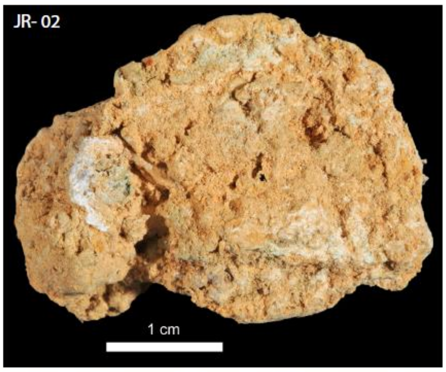
JR- 02
1 cm

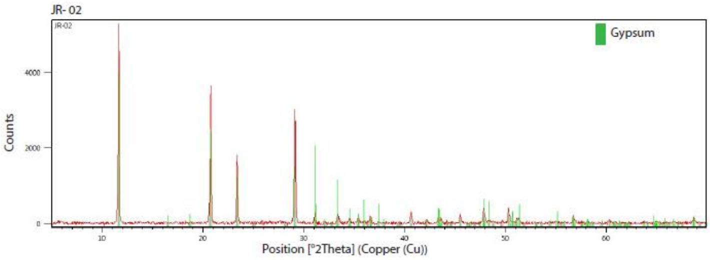
JR- 02
JR-02
Counts
4000
2000
0
10
20
30
40
50
60
Position [°2Theta] (Copper (Cu))
Gypsum

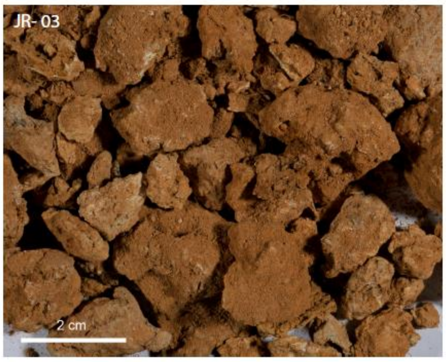
JR- 03
2 cm

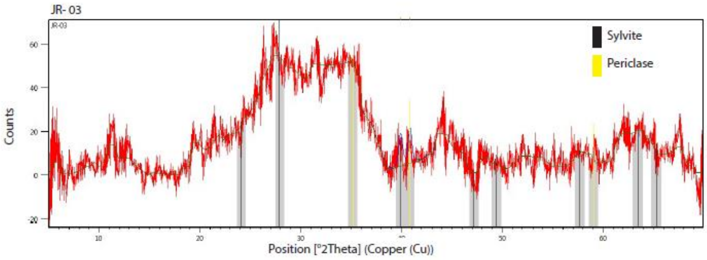
JR- 03
JR-03
Counts
60
40
20
0
-20
10
20
30
40
50
60
Position [°2Theta] (Copper (Cu))
Sylvite
Periclase


JR- 04
2 cm

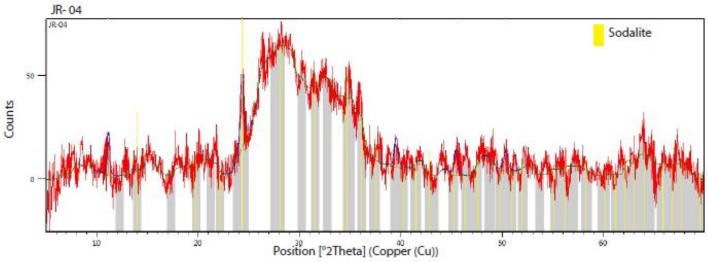
JR- 04
JR-04
Counts
50
0
10
20
30
40
50
60
Position [°2Theta] (Copper (Cu))
Sodalite


JR- 05
1 cm

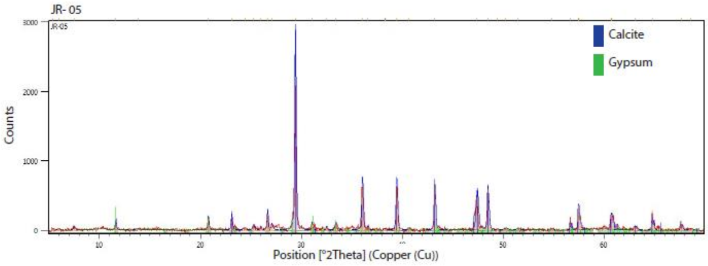
JR- 05
JR-05
Counts
3000
2000
1000
0
10
20
30
50
60
Position [°2Theta] (Copper (Cu))
Calcite
Gypsum

CENTRE ZONE


JR- 06
1 cm

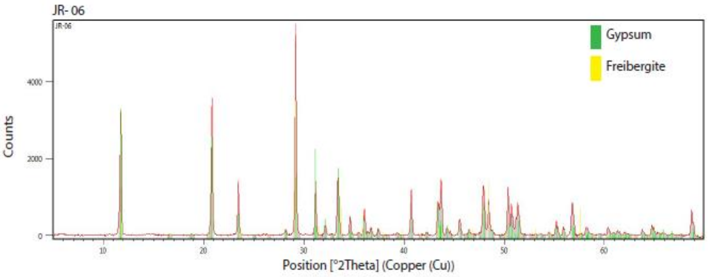
JR- 06
JR-06
Counts
4000
2000
0
10
20
30
40
50
60
Position [°2Theta] (Copper (Cu))
Gypsum
Freibergite

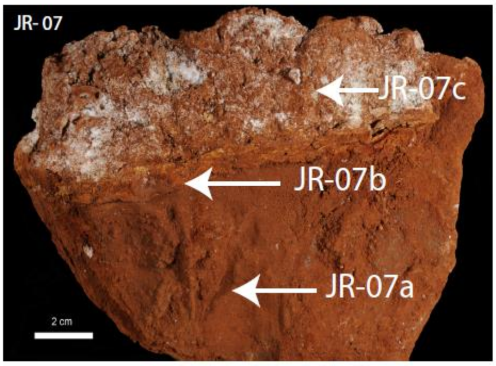
JR- 07
JR-07c
JR-07b
JR-07a
2 cm

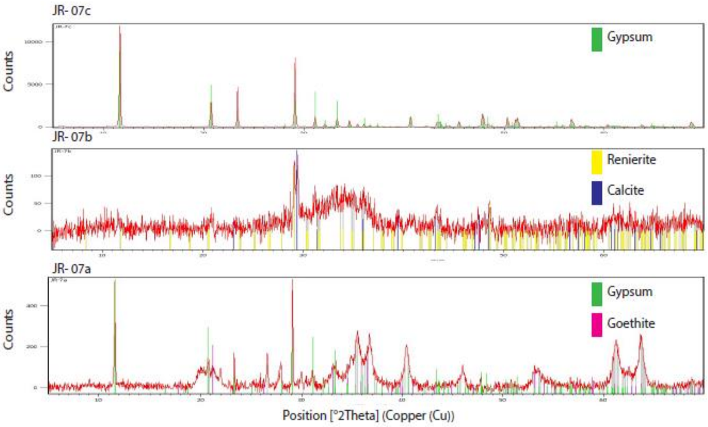
JR- 07c
Counts
10000
5000
0
Gypsum
JR- 07b
Counts
100
50
0
Renierite
Calcite
JR- 07a
Counts
400
200
0
Gypsum
Goethite
10
20
30
40
50
60
Position [°2Theta] (Copper (Cu))


JR- 08
2 cm

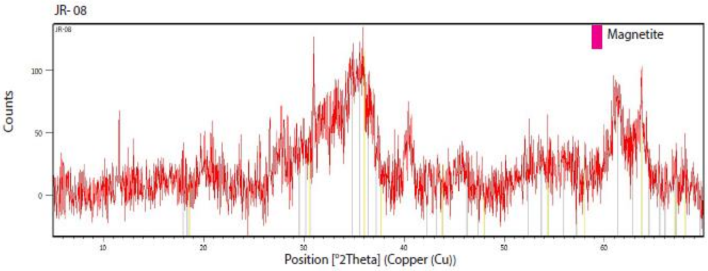
JR- 08
JR-08
Counts
100
50
0
10
20
30
40
50
60
Position [°2Theta] (Copper (Cu))
Magnetite

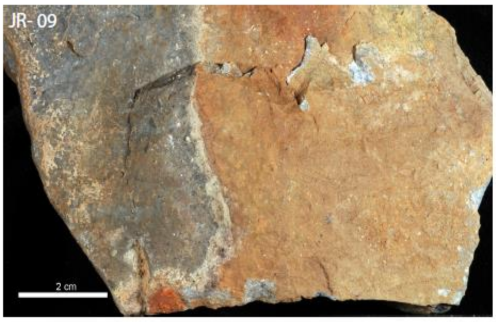
JR- 09
2 cm

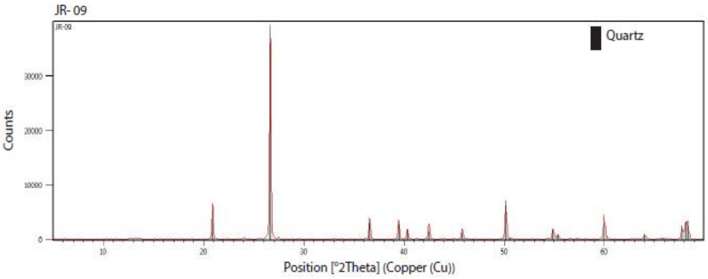
JR- 09
JR-09
Counts
30000
20000
10000
0
10
20
30
40
50
60
Position [°2Theta] (Copper (Cu))
Quartz

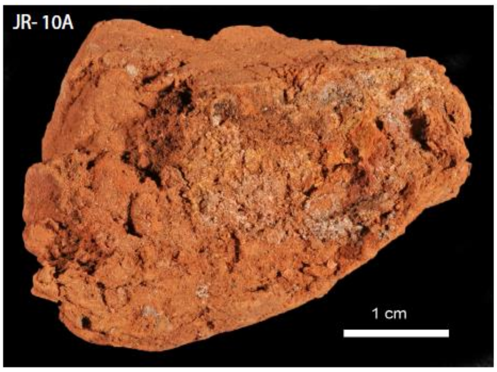
JR- 10A
1 cm

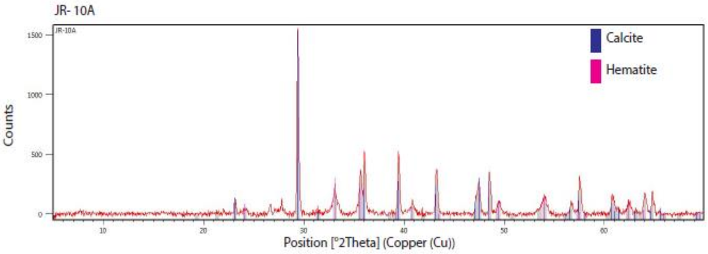
JR- 10A
JR-10A
Counts
1500
1000
500
0
10
20
30
40
50
60
Position [°2Theta] (Copper (Cu))
Calcite
Hematite

CENTRE ZONE


JR- 10B
1 cm

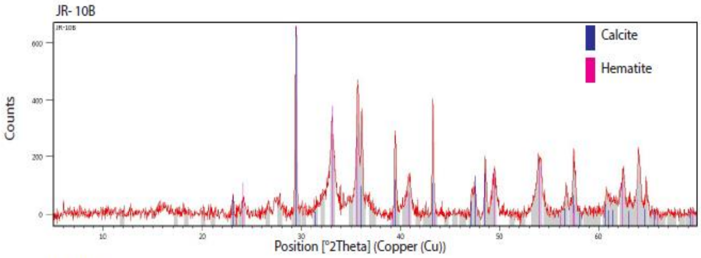
JR- 10B
Counts
Position [°2Theta] (Copper (Cu))
Calcite
Hematite

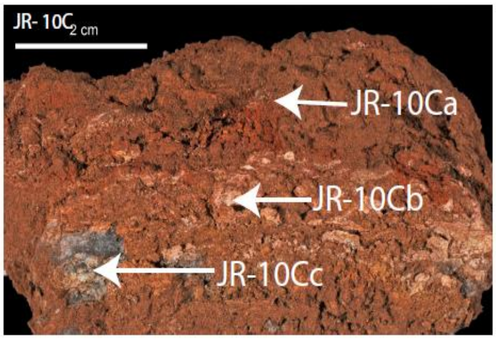
JR- 10C
2 cm
JR-10Ca
JR-10Cb
JR-10Cc

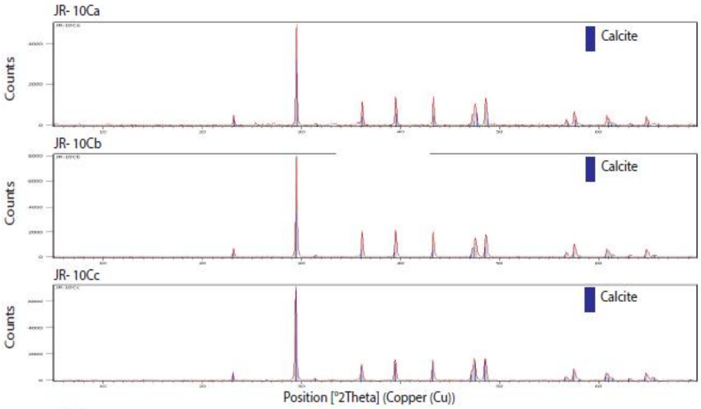
JR- 10Ca
Counts
Calcite
JR- 10Cb
Counts
Calcite
JR- 10Cc
Counts
Calcite
Position [°2Theta] (Copper (Cu))

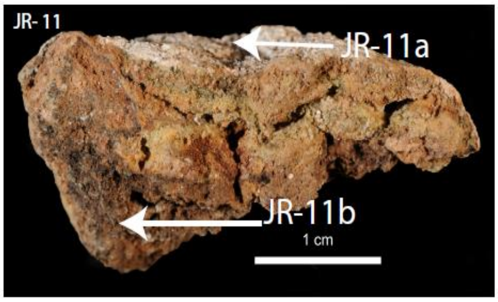
JR- 11
JR-11a
JR-11b
1 cm

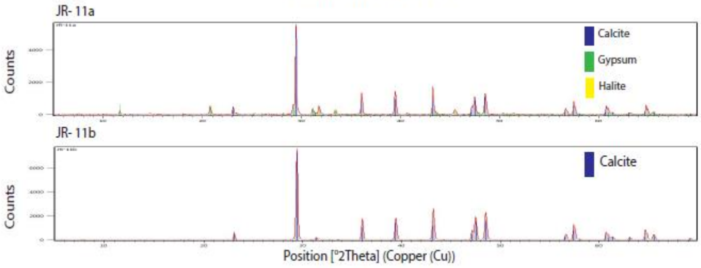
JR- 11a
Counts
Calcite
Gypsum
Halite
JR- 11b
Counts
Calcite
Position [°2Theta] (Copper (Cu))

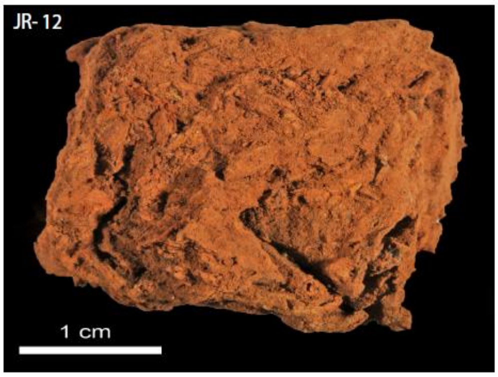
JR- 12
1 cm

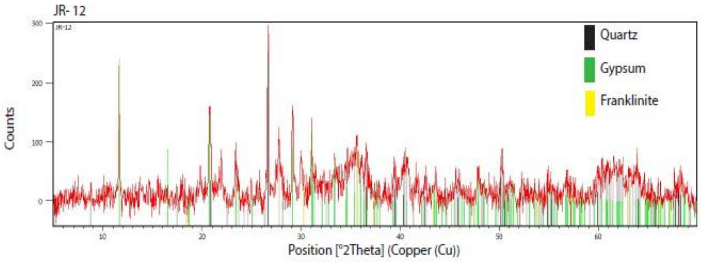
JR- 12
Counts
Position [°2Theta] (Copper (Cu))
Quartz
Gypsum
Franklinite

CENTRE ZONE

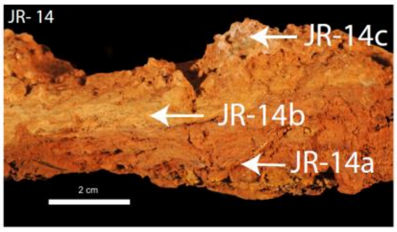

JR-14c_d

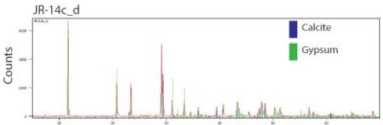

JR-14c_repeated

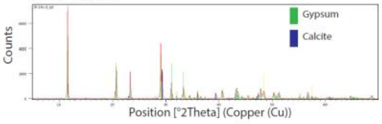

JR-14b_d

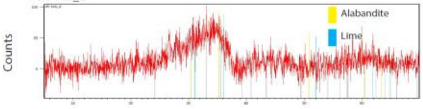

JR-14a_d

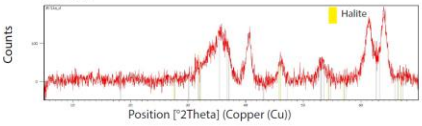

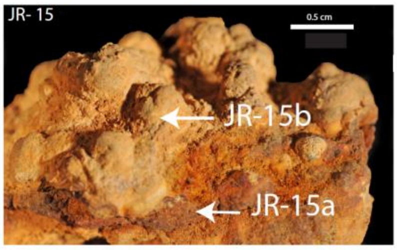

JR- 15b

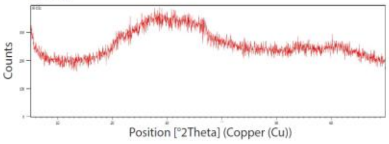

JR- 15a

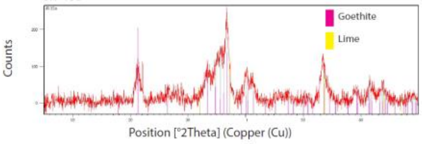

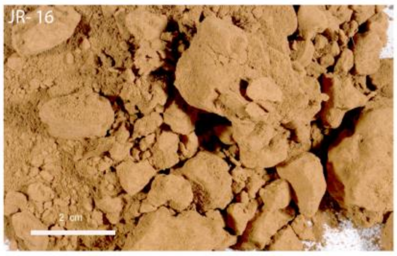

JR- 16

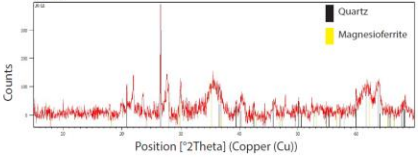

JR- 17

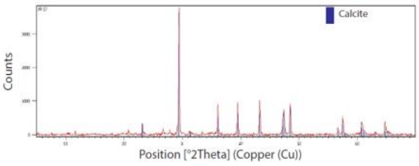

JR- 18

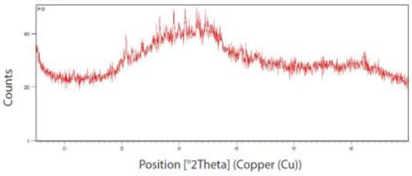

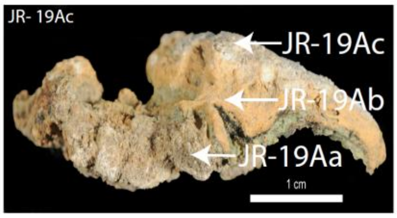

JR- 19Ac

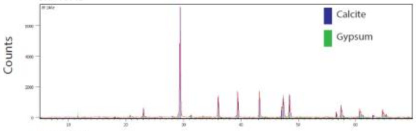

JR- 19Aa

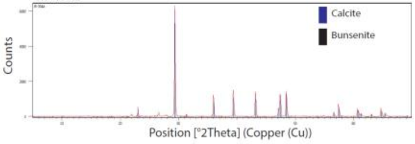

JR- 19Ab

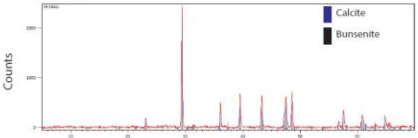

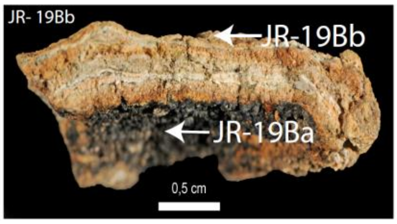

JR- 19Bb

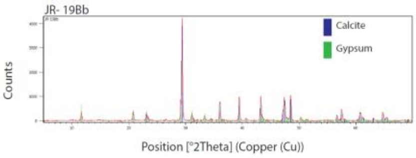

JR- 19Ba

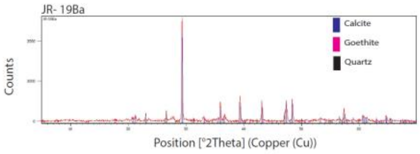

CENTRE ZONE

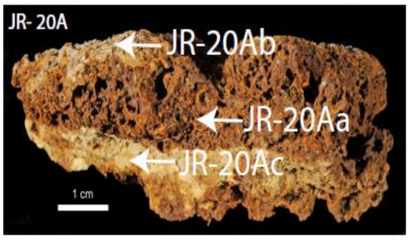
JR- 20A
JR-20Ab
JR-20Aa
JR-20Ac
1 cm

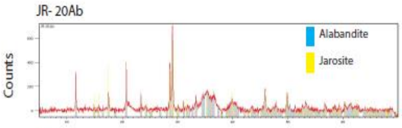
JR- 20Ab
Counts
Alabandite
Jarosite

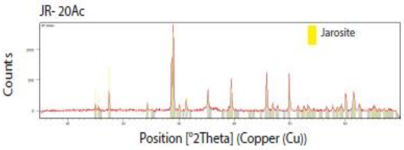
JR- 20Ac
Counts
Jarosite
Position [°2Theta] (Copper (Cu))

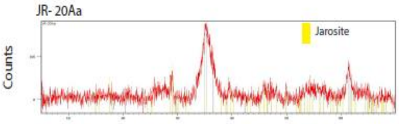
JR- 20Aa
Counts
Jarosite

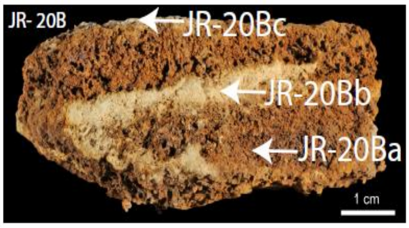
JR- 20B
JR-20Bc
JR-20Bb
JR-20Ba
1 cm

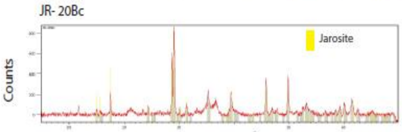
JR- 20Bc
Counts
Jarosite

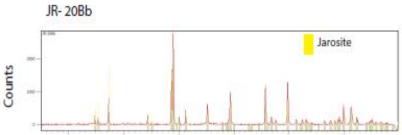
JR- 20Bb
Counts
Jarosite

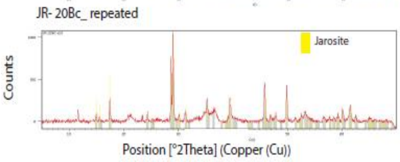
JR- 20Bc_ repeated
Counts
Jarosite
Position [°2Theta] (Copper (Cu))

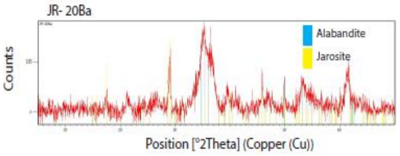
JR- 20Ba
Counts
Alabandite
Jarosite
Position [°2Theta] (Copper (Cu))


JR- 21A
1 cm

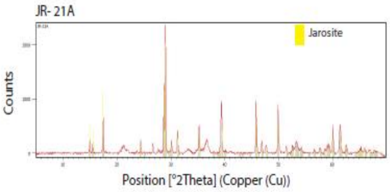
JR- 21A
Counts
Jarosite
Position [°2Theta] (Copper (Cu))


JR- 21B
2 cm

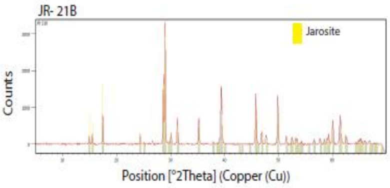
JR- 21B
Counts
Jarosite
Position [°2Theta] (Copper (Cu))


JR- 22
2 cm

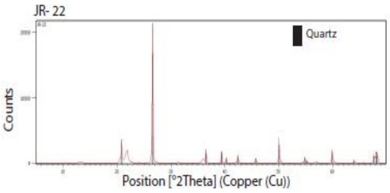
JR- 22
Counts
Quartz
Position [°2Theta] (Copper (Cu))

EAST ZONE

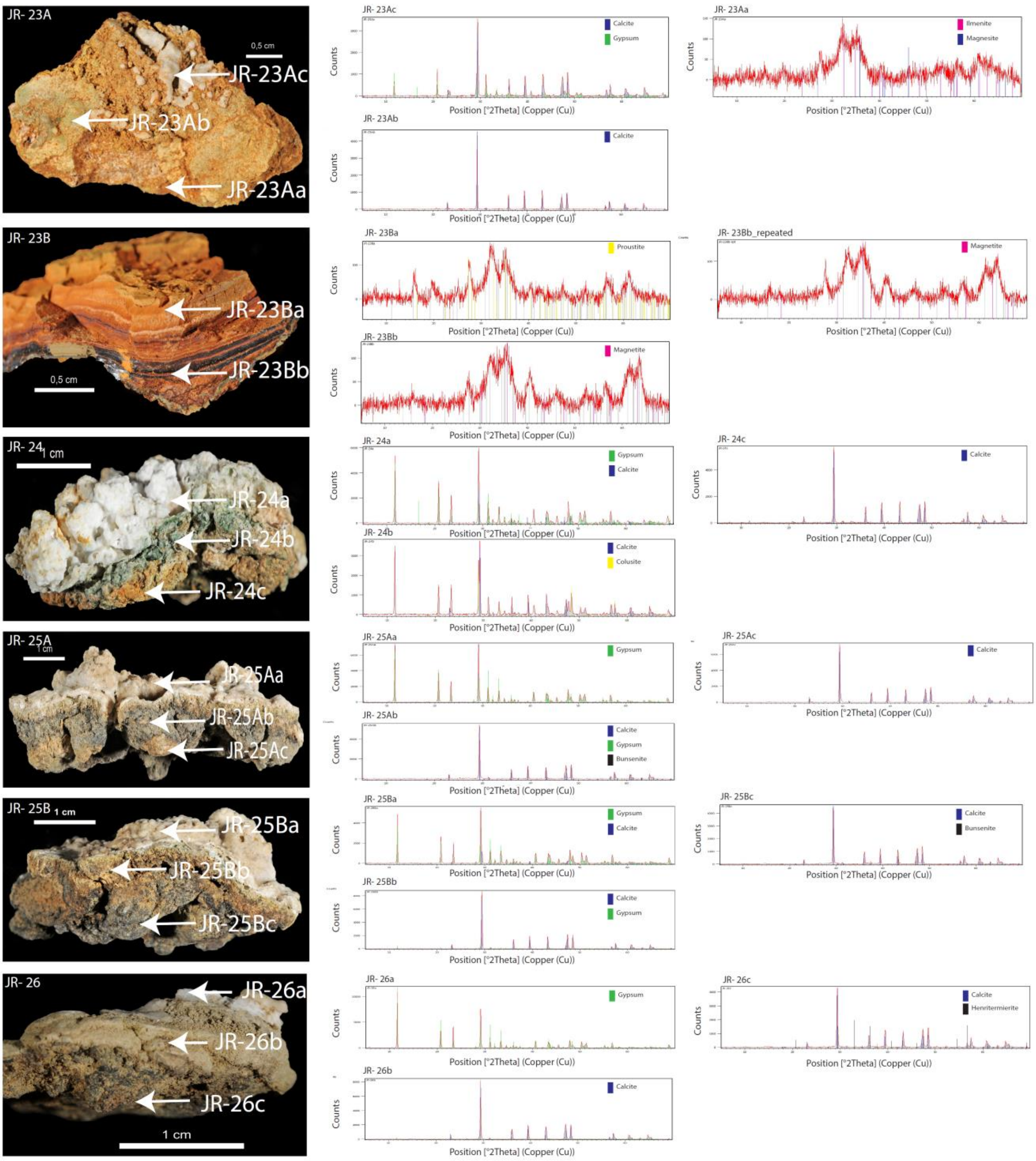
JR- 23A
0,5 cm
JR-23Ac
JR-23Ab
JR-23Aa
JR- 23Ac
Calcite
Gypsum
Counts
Position [°2Theta] (Copper (Cu))
JR- 23Aa
Ilmenite
Magnesite
JR- 23Ab
Calcite
JR- 23B
JR-23Ba
JR-23Bb
0,5 cm
JR- 23Ba
Proustite
JR- 23Bb_repeated
Magnetite
JR- 23Bb
Magnetite
JR- 24
1 cm
JR-24a
JR-24b
JR-24c
JR- 24a
Gypsum
Calcite
JR- 24c
Calcite
JR- 24b
Calcite
Colusite
JR- 25A
1 cm
JR-25Aa
JR-25Ab
JR-25Ac
JR- 25Aa
Gypsum
JR- 25Ac
Calcite
JR- 25Ab
Calcite
Gypsum
Bunsenite
JR- 25B
1 cm
JR-25Ba
JR-25Bb
JR-25Bc
JR- 25Ba
Gypsum
Calcite
JR- 25Bc
Calcite
Bunsenite
JR- 25Bb
Calcite
Gypsum
JR- 26
JR-26a
JR-26b
JR-26c
1 cm
JR- 26a
Gypsum
JR- 26c
Calcite
Henritermierite
JR- 26b
Calcite

APPENDIX II: CHEMICAL DATA

Table A1 EDS results–trace elements

Element		CENTRE ZONE											
		JR-10C CRYSTAL_LAYER 1_ORANGE	JR-10C MATRIX_LAYER 2_WHITE	JR-10C CRYSTAL_LAYER 2	JR-10C CRYSTAL_LAYER 2	JR-10C CRYSTAL_LAYER 2	JR-10C CRYSTAL_LAYER 2	JR-10C CRYSTAL_LAYER 2	JR-10C CRYSTAL_LAYER 1	JR-10C WHITE HORIZON	JR-10C GRAY HORIZON	JR-10C RED HORIZON	JR-10C RED HORIZON
Ca	(Wt%)	28.2	38.4	11.5	13.0	1.93	3.58	64.6	16.3	29.2	35.3	20.9	8.87
Fe	(Wt%)	5.23	5.77	21.3	18.6	70.8	33.3	11.0	6.67	11.9	16.2	24.4	34.1
Al	(Wt%)	-	0.94	0.59	-	1.06	1.02	-	-	0.79	0.97	0.92	0.43
Na	(Wt%)	1.22	0.91	0.57	0.34	0.23	0.52	0	1.77	0.56	0.52	0.79	0.32
K	(Wt%)	-	-	-	-	-	-	-	-	-	-	-	0.30
Mg	(Wt%)	-	-	-	-	-	-	-	-	-	1.06	0.87	0.94
P	(Wt%)	-	0.89	0.14	0.47	0.46	0.64	0.79	0.56	-	-	-	-
Si	(Wt%)	2.98	3.67	9.70	3.54	2.71	2	2.66	2.93	5.99	3.98	6.82	9.60
Mn	(Wt%)	0.36	0.73	10.7	1.51	0.68	0.28	1.42	0.31	1.11	1.00	1.44	1.14
Sr	(Wt%)	-	8.70	7.02	33.6	2.22	4.64	-	-	-	-	-	-
As	(Wt%)	3.67	3.95	2.87	3.94	3.66	3.00	0	8.35	-	-	8.58	10.95
C	(Wt%)	27.5	13.3	12.6	5.64	3.97	8.14	4.47	24.9	17.6	13.9	11.0	9.55
O	(Wt%)	29.6	19.7	22.3	15.5	11.9	9.61	13.8	37.0	27.2	21.5	23.7	22.9
S	(Wt%)	1.30	1.85	0.77	2.80	0.34	5.26	1.29	1.02	3.28	5.63	0.63	0.22
Cl	(Wt%)	-	-	-	-	-	-	-	0.24	2.34	-	-	0.61
Ba	(Wt%)	-	-	-	0.98	0.14	-	-	-	-	-	-	-
Cu	(Wt%)	-	1.25	0	-	-	28.0	-	-	-	-	-	-

Element		CENTRE ZONE							
		JR-14 DARK ORANGE HORIZON	JR-14 ORANGE HORIZON	JR-14 OFF YELLOW HORIZON	JR-14 ORANGE HORIZON	JR-14 ORANGE HORIZON	JR-14 WHITE HORIZON	JR-20A SURFACE	JR-20A CRYSTAL AND SURFACE
Ca	(Wt%)	2.13	2.19	2.53	2.13	2.13	1.17	0.15	0.18
Fe	(Wt%)	38.0	21.7	38.6	33.9	26.2	2.98	67.0	64.3
Al	(Wt%)	4.85	1.75	5.15	5.44	3.31	1.36	-	-
Na	(Wt%)	0.19	0.27	0.11	0.16	0.31	0.65	-	-
K	(Wt%)	0.30	0.44	0.29	0.35	0.46	0.40	-	-
Mg	(Wt%)	0.61	0.27	0.74	0.48	0.50	0.33	-	-
P	(Wt%)	-	-	-	-	-	-	-	-
Si	(Wt%)	12.7	33.7	9.46	16.6	22.5	47.2	1.06	0.13
Mn	(Wt%)	0.43	0.26	0.4	0.34	0.5	0.26	0.48	0.50
Sr	(Wt%)	-	-	-	-	-	-	-	-
As	(Wt%)	7.92	2.63	10.58	8.43	6.25	1.4	0.43	3.18
C	(Wt%)	6.23	7.47	5.40	4.99	7.74	10.1	6.71	6.14
O	(Wt%)	26.7	29.3	26.7	27.2	30.1	33.1	17.1	18.6
S	(Wt%)	0	0	0	0	0	0.57	7.07	6.92
Cl	(Wt%)	0	0.03	0.05	0.04	0	0.51	-	-
Ba	(Wt%)	-	-	-	-	-	-	-	-
Cu	(Wt%)	-	-	-	-	-	-	-	-

		EAST ZONE					
Element		JR25B FILAMENT	JR25B INNER NODULE_BLACK PRECIPITATE	JR25B BLACK HORIZON	JR25B ORANGE HORIZON	JR25B ACICULAR CRYSTALS FAN	JR-25B ROUNDED CRYSTAL
Ca	(Wt%)	50.86	36.29	9.18	6.33	35.2	15.0
Fe	(Wt%)	1.18	2.33	17.83	24.53	7.52	14.0
Al	(Wt%)	-	-	-	-	-	-
Na	(Wt%)	-	-	-	-	-	-
K	(Wt%)	-	-	-	-	-	-
Mg	(Wt%)	-	-	-	-	-	-
P	(Wt%)	-	-	-	-	-	-
Si	(Wt%)	1.35	9.01	12.19	19.76	7.56	13.2
Mn	(Wt%)	0.55	3.19	24.51	2.91	0.66	0.61
Sr	(Wt%)	-	-	-	-	-	-
As	(Wt%)		-	2.71	3.05	1.05	0.00
C	(Wt%)	14.3	16.7	9.32	15.4	16.5	28.5
O	(Wt%)	30.0	31.5	23.8	27.1	30.3	28.3
S	(Wt%)	1.73	1.08	0.5	0.95	1.24	0.43
Cl	(Wt%)	-	-	-	-	-	-
Ba	(Wt%)	-	-	-	-	-	-
Cu	(Wt%)	-	-	-	-	-	-

Table A2 4-acid digest results major concentrations

	NORTH ZONE	CENTRE ZONE													EAST ZONE				
Element	JR-03	JR-06	JR-07a	JR-10Ca	JR-10Cc	JR-11a	JR-12	JR-14b_d	JR-14c_d	JR-19Ab	JR-19Ac	JR-20Aa	JR-20Bc	JR-21B	JR-22	JR-23Ba	JR-23Bb	JR-24a	JR-25Ba	JR-25Bc
Ca (Wt%)	0.36	17.05	0.82	23.6	>25.0	20.4	3.16	1.61	5.75	9.40	24.4	0.06	0.88	0.09	0.02	3.91	2.77	19.1	19.2	>25.0
Fe (Wt%)	20.6	0.12	28.7	10.1	3.68	0.98	20.7	27.2	13.3	13.8	1710.00	38.3	34.7	26.9	0.09	27.5	34.5	0.04	0.07	3.09
Al (Wt%)	6.44	0.06	5.00	0.57	0.28	0.14	1.75	1.76	1.87	2.54	0.39	0.07	0.13	0.84	0.11	0.01	0.04	0.03	0.03	0.09
Na (Wt%)	0.22	1.76	1,290	0.34	0.29	3.51	0.8	0.32	0.38	0.66	0.40	0.47	0.39	0.44	0.01	0.12	0.09	0.19	0.09	0.19
K (Wt%)	0.11	0.10	0.42	0.19	0.11	0.28	0.52	0.19	0.23	0.68	0.16	0.15	1.63	4.29	0.05	0.06	0.03	0.02	0.02	0.07
Mg (Wt%)	0.05	0.33	0.17	0.44	0.54	1.05	0.23	0.13	0.23	0.29	0.53	0.01	0.01	0.05	<0.01	0.11	0.06	0.15	0.09	0.12
P (Wt%)	0.02	0.001	0.04	0.01	0.01	0.01	0.17	0.01	0.004	0.04	0.01	0.56	0.26	0.08	0.003	0.02	0.03	<0.001	0.001	0.01
Ti (Wt%)	0.01	0.002	0.05	0.03	0.01	0.01	0.12	0.01	0.01	0.16	0.02	0.01	0.01	0.07	0.56	<0.001	<0.001	0.002	0.002	0.004
Mn (ppm)	38	50.0	246	4930	2890	1875	445	661	943	6280	3230.00	8.00	5.00	28.8	1.00	777	935	23.3	193	34600
Sr (ppm)	182	4990	710	3530	4900	5840	1385	1110	1815	2090	5670.00	25.5	387	339	10.1	1475	1265	5190	4750	3160
As (ppm)	>10000	562	>10000	>10000	6190	2600	>10000	>10000	>10000	>10000	5220.00	>10000	7400	1090	30.5	>10000	>10000	150.0	285	4320
S (Wt%)	0.70	>10.0	0.91	0.60	1.08	7.20	1.43	0.17	0.26	1.18	1.67	4.08	6.78	9.51	0.03	0.10	0.06	>10.0	>10.0	0.73

Table A3 4-acid digest results minor concentrations

	NORTH ZONE	CENTRE ZONE														EAST ZONE				
Element	JR-03	JR-06	JR-07a	JR-10Ca	JR-10Cc	JR-11a	JR-12	JR-14b_d	JR-14c_d	JR-19Ab	JR-19Ac	JR-20Aa	JR-20Bc	JR-21B	JR-22	JR-23Ba	JR-23Bb	JR-24a	JR-25Ba	JR-25Bc
Li (ppm)	25.0	70.7	208	34.1	50.4	108	26.5	20.4	20.1	31.8	30.2	10.8	6.30	3.90	19.4	4.30	2.50	44.2	16.1	31.6
Rb (ppm)	9.01	8.66	53.3	15.2	10.8	26.8	40.0	23.1	35.0	59.7	18.7	3.48	46.7	67.8	5.70	5.69	2.23	2.65	3.71	9.39
Cs (ppm)	38.8	23.2	103	27.6	41.6	72.4	78.0	108	191	105	54.7	6.51	24.8	31.8	11.8	14.8	7.67	10.2	23.1	38.8
Be (ppm)	6.86	0.21	22.9	45.2	24.5	6.63	31.5	18.6	17.8	45.1	6.32	0.06	0.05	0.17	0.09	16.0	25.8	0.03	0.07	3.19
Ba (ppm)	38.0	16.0	389	371	217	133	329	209	199	830	331	9.00	24.0	126	77.0	89.0	191	16.0	24.0	650
Sc (ppm)	5.32	0.16	18.8	1.68	0.56	0.30	2.69	2.22	1.68	4.74	0.66	1.25	1.04	1.86	0.60	0.03	0.14	<0.01	<0.01	<0.01
Y (ppm)	25.0	0.23	29.0	5.20	2.19	0.59	13.6	10.4	6.46	11.1	1.69	0.09	0.37	1.04	0.97	1.20	7.27	0.09	0.07	0.28
La (ppm)	1.65	0.14	3.89	2.69	1.31	0.73	9.28	10.9	6.34	11.6	1.71	0.36	1.27	5.04	0.69	0.18	0.15	0.19	0.42	0.55
Ce (ppm)	5.46	0.25	7.73	5.37	2.59	1.27	18.3	23.5	14.0	22.2	3.38	0.68	2.77	8.96	1.32	0.13	0.52	0.27	0.30	0.92
Pr (ppm)	-	0.03	1.02	0.63	0.32	-	-	-	-	-	-	0.08	-	1.01	0.15	-	-	0.03	0.04	0.11
Nd (ppm)	-	0.11	4.94	2.23	1.16	-	-	-	-	-	-	0.28	-	3.43	0.50	-	-	0.11	0.12	0.45
Sm (ppm)	-	0.04	3.65	0.53	0.25	-	-	-	-	-	-	0.03	-	0.49	0.10	-	-	0.03	0.02	0.07
Eu (ppm)	-	0.01	1,815	0.24	0.10	-	-	-	-	-	-	0.01	-	0.11	0.01	-	-	0.01	0.01	0.01
Gd (ppm)	-	0.04	7.87	1.08	0.44	-	-	-	-	-	-	0.03	-	0.32	0.10	-	-	0.02	0.02	0.06
Tb (ppm)	-	0.01	1,025	0.14	0.05	-	-	-	-	-	-	0.00	-	0.04	0.02	-	-	0.002	0.002	0.01
Dy (ppm)	-	0.03	5.82	0.75	0.34	-	-	-	-	-	-	0.02	-	0.22	0.14	-	-	0.01	0.01	0.05
Ho (ppm)	-	0.01	0.98	0.13	0.05	-	-	-	-	-	-	0.00	-	0.04	0.03	-	-	0.002	0.002	0.01
Er (ppm)	-	0.02	2.23	0.27	0.11	-	-	-	-	-	-	0.01	-	0.10	0.10	-	-	0.01	0.004	0.02
Tm (ppm)	-	0.002	0.25	0.03	0.01	-	-	-	-	-	-	<0.002	-	0.02	0.02	-	-	<0.002	<0.002	0.003
Yb (ppm)	-	0.02	1.37	0.17	0.07	-	-	-	-	-	-	0.01	-	0.11	0.11	-	-	0.01	0.01	0.02
Lu (ppm)	-	0.002	0.20	0.02	0.01	-	-	-	-	-	-	<0.002	-	0.02	0.01	-	-	<0.002	<0.002	0.003
Th (ppm)	0.36	0.04	1,480	0.94	0.40	0.24	4.06	0.32	0.23	5.13	0.59	0.32	0.30	2.04	1.47	<0.004	<0.004	0.05	0.05	0.13
U (ppm)	20.1	0.06	0.98	0.27	0.11	0.07	0.95	7.12	3.62	1.26	0.23	0.25	0.20	0.44	1.11	0.05	0.12	0.01	0.02	0.03
Zr (ppm)	3.90	0.70	15.7	9.40	4.5	2.40	37.6	3.60	2.50	48.2	6.30	1.80	2.90	24.2	26.6	0.20	0.30	0.80	0.90	1.20
Nb (ppm)	0.35	0.06	1.47	0.88	0.39	0.24	3.38	0.33	0.23	4.59	0.58	0.14	0.22	2.11	6.35	0.03	0.01	0.06	0.06	0.12
Mo (ppm)	111	1.57	3.13	15.5	5.79	2.05	39.6	38.7	6.33	19.6	2.48	112	62.1	8.15	7.42	2.73	2.6	0.66	0.17	12.7
Hf (ppm)	0.12	0.02	0.42	0.25	0.11	0.09	0.98	0.10	0.07	1,355	0.20	0.05	0.08	0.62	0.71	<0.004	0.01	0.02	0.02	0.03
Ta (ppm)	0.03	0.81	0.37	1.26	3.53	0.02	0.24	0.02	0.02	0.32	0.04	0.51	0.02	1.05	0.33	<0.01	0.03	0.03	0.13	0.04
W (ppm)	13.2	0.40	193	152	51.0	9.92	18.0	11.3	2.20	98.2	7.23	0.08	0.11	0.39	710	55.2	79.3	0.86	0.64	132
Re (ppm)	0.002	<0.002	0.002	0.003	<0.002	<0.002	<0.002	0.01	0.002	0.003	<0.002	0.01	0.01	<0.002	0.01	<0.002	0.002	<0.002	<0.002	0.002
V (ppm)	23.6	1.60	96.1	6.80	3.10	1.70	25.8	10.2	4.50	33.4	5.00	590	546	188	13.9	0.50	0.30	0.30	0.30	1.00
Cr (ppm)	2.00	0.50	9.10	3.00	1.80	2.70	11.4	3.30	1.90	16.1	2.80	12.4	10.4	8.90	10.3	0.30	0.40	0.30	0.40	1.00
Co (ppm)	6.70	0.29	8.60	1.60	0.68	0.36	1.18	43.2	58.8	4.56	1.50	0.96	1.01	1.34	62.7	0.37	0.48	0.08	0.073	1.08
Ni (ppm)	11.7	0.53	19.8	2.98	1.66	1.70	2.59	27.1	37.0	10.2	2.72	1.62	1.26	2.14	0.78	0.76	0.81	0.15	0.21	1.13
Cu (ppm)	1.67	1.33	26.8	7.38	3.62	2.87	5.79	185	109	8.72	4.43	4.71	10.8	20.8	5.23	0.15	0.03	0.93	1.11	2.28
Zn (ppm)	68.0	4.50	297	21.5	10.8	5.30	25.0	669	565	111	21.0	7.20	17.0	11.8	7.90	297	423	1.90	2.20	27.2
Ag (ppm)	0.01	0.002	0.10	0.01	0.01	0.02	0.02	0.01	0.01	0.06	0.01	0.03	0.01	0.02	0.02	0.01	<0.002	0.004	0.02	0.08
Cd (ppm)	0.17	0.25	0.34	0.03	0.05	0.01	0.01	13.0	15.9	0.07	0.10	0.12	0.08	0.05	0.43	0.04	0.04	0.01	0.01	0.04
Ga (ppm)	0.63	0.24	12.4	5.28	2.64	0.75	5.55	0.76	0.51	11.5	1.51	11.7	11.5	8.82	0.34	0.66	1.29	0.13	0.16	1.05
In (ppm)	0.01	<0.005	0.02	<0.005	0.01	0.01	0.02	0.01	0.01	0.03	0.01	<0.005	0.02	0.04	<0.005	0.02	0.01	<0.005	<0.005	0.01
Sn (ppm)	0.11	0.22	0.26	1.14	0.39	0.17	0.42	0.56	0.26	0.50	0.13	0.06	0.09	0.57	2.96	0.02	0.22	0.04	0.05	0.1
Tl (ppm)	1,095	0.66	21.4	10.8	20.0	3.51	14.5	6.48	12.5	36.1	5.53	0.39	4.42	7.93	0.57	2.31	1.90	0.27	0.15	12.8
Pb (ppm)	1.95	0.42	118	4.85	2.81	1.70	8.05	6.22	3.88	17.8	2.86	0.60	1.52	9.32	47.3	27.9	415	0.30	0.38	1.36
Bi (ppm)	0.01	0.01	1.27	0.09	0.09	0.01	0.18	0.03	0.06	0.14	0.03	0.02	0.01	0.19	0.39	<0.005	<0.005	0.01	0.01	0.02
Ge (ppm)	0.43	0.32	37.7	0.15	0.11	0.31	0.22	0.71	0.13	0.17	0.06	0.25	0.29	0.19	<0.05	0.20	0.3	0.06	0.18	0.06
Sb (ppm)	32.8	8.53	268	232	99.0	23.4	116	133	62.7	170	26.4	7.72	4.59	1.71	5.72	104	540	3.05	1.37	16.6
Te (ppm)	<0.04	<0.04	0.11	<0.04	<0.04	<0.04	0.07	0.04	0.08	0.07	<0.04	0.53	0.43	0.34	0.18	<0.04	<0.04	<0.04	<0.04	<0.04
Se (ppm)	0.30	0.40	1.20	0.50	0.60	0.50	0.90	0.20	<0.2	0.30	0.60	2.60	2.00	0.70	0.50	0.40	0.20	0.40	0.20	0.40

Table A4 Laser Ablation ICP-MS results, major elements

	NORTH ZONE						
Element	JR-06-LS-1	JR-06-LS-2	JR-06-LS-3	JR-06-LS-4	JR-06-LS-5	JR-06-CLAST-2	JR-06-CLAST-3
Ca (Wt%)	17,1	17,1	17,1	17,1	17,1	1,61	1,61
Fe (Wt%)	0,02	0,05	0,01	0,03	0,03	0,001	0,001
Al (Wt%)	0,01	0,05	0,002	0,01	0,02	0,0003	0,0002
Mg (Wt%)	0,11	1,42	0,88	0,42	0,81	0,01	0,01
Ti (Wt%)	0,0004	0,01	0,0003	-	0,002	0,00003	0,00003
Si (Wt%)	0,98	3,92	6,41	2,53	3,50	0,01	0,01
Mn (Wt%)	0,0001	0,001	0,0001	-	0,0003	0,00001	0,00001
Sr (Wt%)	0,22	0,36	0,14	0,20	0,30	0,01	0,01
As (Wt%)	0,01	0,01	0,01	0,01	0,005	0,0002	0,0002

	CENTRE ZONE																							
Element	JR-10C-HA-1	JR-10C-HA-2	JR-10C-HA-3	JR-10C-HA-4	JR-10C-HA-5	JR-10C-HB-1	JR-10C-HB-2	JR-10C-HB-3	JR-10C-HB-4	JR-10C-HB-5	JR-10C-HC-1	JR-10C-HC-2	JR-10C-HC-4	JR-10C-HC-5	JR-10C-HD-1	JR-10C-HD-2	JR-10C-HD-3	JR-10C-HD-4	JR-10C-HD-5	JR-11-HA-1	JR-11-HA-2	JR-11-HA-3	JR-11-HA-4	JR-11-HA-5
Ca (Wt%)	24,3	24,3	24,3	24,3	24,3	24,3	24,3	24,3	24,3	24,3	24,3	24,3	24,3	24,3	24,3	24,3	24,3	24,3	24,3	20,4	20,4	20,4	20,4	20,4
Fe (Wt%)	0,89	1,84	1,02	0,99	2,07	2,10	2,71	2,28	0,89	3,03	1,13	2,23	1,31	1,63	3,59	3,78	2,43	1,52	1,97	0,89	0,66	0,35	0,82	0,46
Al (Wt%)	0,07	0,03	0,03	0,16	0,05	0,18	0,08	0,08	0,02	0,13	0,01	0,04	0,03	0,05	0,52	0,12	0,17	0,02	0,10	0,07	0,06	0,12	0,04	0,02
Mg (Wt%)	2,37	2,01	1,84	2,16	1,96	2,29	3,09	2,93	2,35	6,22	1,84	3,84	1,77	1,88	30,4	8,33	4,81	1,64	2,85	0,95	0,92	0,97	0,88	0,78
Ti (Wt%)	0,004	0,002	0,001	0,002	0,001	0,01	0,002	0,004	0,002	0,003	0,001	0,002	0,002	0,001	0,01	0,004	0,01	0,00	0,003	0,001	0,002	0,001	0,001	0,001
Si (Wt%)	1,52	1,92	3,52	1,75	3,33	5,24	6,65	4,53	4,61	5,33	0,56	1,65	0,78	2,31	12,8	5,27	2,90	0,64	2,79	0,28	0,34	0,30	0,32	0,16
Mn (Wt%)	0,11	0,14	0,07	0,12	0,05	0,11	0,13	0,14	0,05	0,13	0,07	0,13	0,09	0,11	0,28	0,20	0,17	0,13	0,13	0,90	0,90	0,21	0,21	0,23
Sr (Wt%)	0,16	0,24	0,20	0,20	0,19	0,22	0,24	0,24	0,17	0,25	0,32	0,27	0,28	0,27	0,26	0,30	0,41	0,26	0,32	0,14	0,14	0,12	0,10	0,13
As (Wt%)	0,13	0,29	0,17	0,16	0,30	0,32	0,40	0,36	0,14	0,51	0,23	0,45	0,24	0,29	0,58	0,43	0,46	0,26	0,37	0,14	0,11	0,08	0,11	0,09

	CENTRE ZONE																								
Element	JR-11-HB-1	JR-11-HB-2	JR-11-HB-3	JR-11-HB-4	JR-11-HB-5	JR-11-HC-1	JR-11-HC-2	JR-11-HC-3	JR-11-HC-4	JR-11-HC-5	JR-14-HA-1	JR-14-HA-2	JR-14-HA-3	JR-14-HA-4	JR-14-HA-5	JR-14-HB-1	JR-14-HB-2	JR-14-HB-3	JR-14-HB-4	JR-14-HB-5	JR-14-HEE-1	JR-14-HEE-2	JR-14-HEE-3	JR-14-HEE-4	JR-14-HEE-5
Ca (Wt%)	20,4	20,4	20,4	20,4	20,4	20,4	20,4	20,4	20,4	20,4	1,61	1,61	1,61	1,61	1,61	1,61	1,61	1,61	1,61	1,61	1,61	1,61	1,61	1,61	1,61
Fe (Wt%)	0,14	0,34	1,18	0,20	0,18	0,22	0,67	1,27	0,28	0,57	17,7	21,0	17,5	31,1	36,93	19,2	18,0	19,5	21,2	17,25	0,84	1,56	2,54	2,73	0,40
Al (Wt%)	0,08	0,02	0,96	0,04	0,09	0,07	0,04	0,38	0,07	0,21	2,33	3,15	2,01	2,50	5,36	1,10	1,86	1,66	2,17	0,92	0,08	0,08	0,21	0,20	0,06
Mg (Wt%)	0,86	0,93	1,01	1,02	0,89	0,96	0,99	1,09	0,92	0,97	0,38	0,47	0,58	0,52	0,80	0,63	0,49	0,69	1,17	0,58	0,45	0,55	1,64	1,36	1,26
Ti (Wt%)	0,0005	0,0005	0,001	0,003	0,0005	0,001	0,001	0,001	0,0004	0,001	0,001	0,001	0,01	0,001	0,003	0,06	0,002	0,002	0,001	0,0002	0,0002	0,0003	0,001	0,000	0,0001
Si (Wt%)	0,09	0,13	0,68	0,19	0,10	0,23	0,29	0,73	0,25	0,23	11,3	14,3	11,6	12,5	25,5	10,1	13,7	20,2	36,45	10,6	6,30	9,70	21,5	22,6	4,34
Mn (Wt%)	0,17	0,47	0,76	0,60	0,19	0,08	0,56	0,23	0,26	0,44	0,04	0,03	0,05	0,05	0,04	0,05	0,03	0,04	0,03	0,05	0,01	0,01	0,02	0,02	0,01
Sr (Wt%)	0,12	0,14	0,10	0,12	0,12	0,11	0,14	0,13	0,12	0,13	0,08	0,07	0,08	0,07	0,08	0,07	0,07	0,07	0,06	0,07	0,01	0,01	0,02	0,02	0,01
As (Wt%)	0,07	0,09	0,17	0,08	0,07	0,07	0,14	0,22	0,09	0,12	4,61	4,59	6,14	6,35	6,28	6,25	4,42	6,64	4,03	5,48	0,03	0,09	0,09	0,14	0,02

	CENTRE ZONE																								
Element	JR-14-HC-1	JR-14-HC-2	JR-14-HC-3	JR-14-HC-4	JR-14-HC-5	JR-14-HD-1	JR-14-HD-2	JR-14-HD-3	JR-14-HD-4	JR-14-HD-5	JR-15-HA-1	JR-15-HA-2	JR-15-HA-3	JR-15-HA-4	JR-15-HA-5	JR-15-HB-1	JR-15-HB-2	JR-15-HB-3	JR-15-HB-4	JR-15-HB-5	JR-15-HC-1	JR-15-HC-2	JR-15-HC-3	JR-15-HC-4	JR-15-HC-5
Ca (Wt%)	1,61	-	-	-	-	1,61	1,61	1,61	1,61	1,61	1,17	1,17	1,17	1,17	1,17	1,17	1,17	1,17	1,17	1,17	1,17	1,17	1,17	1,17	1,17
Fe (Wt%)	0,74	-	-	-	-	15,8	19,5	20,0	21,0	19,8	1,35	0,60	0,53	0,85	0,80	6,77	7,26	6,18	6,82	7,35	2,79	1,69	1,87	2,55	3,45
Al (Wt%)	0,35	-	-	-	-	6,56	2,29	2,72	2,78	3,04	2,23	0,67	0,79	1,83	0,53	2,42	4,92	3,42	4,31	2,60	1,04	1,35	0,69	4,26	3,82
Mg (Wt%)	1,69	-	-	-	-	0,59	0,84	0,73	0,70	0,81	0,52	0,71	0,81	0,38	0,52	0,47	0,35	0,30	0,39	0,34	2,39	1,39	1,41	0,62	0,50
Ti (Wt%)	-	-	-	-	-	0,0002	0,03	0,00	0,00	0,00	0,002	0,01	0,01	0,01	0,00	0,00	-	0,0003	0,0002	0,0005	0,03	0,01	0,003	0,001	-
Si (Wt%)	46,0	-	-	-	-	13,6	16,0	15,7	16,7	16,2	89,7	60,7	49,6	87,6	51,2	26,0	18,3	19,4	26,1	26,7	65,7	92,6	73,6	48,8	35,7
Mn (Wt%)	0,02	-	-	-	-	0,04	0,06	0,10	0,04	0,02	0,01	0,01	0,02	0,00	0,01	0,02	0,02	0,02	0,02	0,02	0,06	0,02	0,04	0,01	0,02
Sr (Wt%)	0,02	-	-	-	-	0,07	0,07	0,07	0,07	0,07	0,06	0,03	0,03	0,05	0,03	0,04	0,04	0,04	0,04	0,04	0,02	0,04	0,04	0,05	0,04
As (Wt%)	0,06	-	-	-	-	3,15	3,34	3,34	3,70	3,98	0,13	0,04	0,03	0,03	0,05	0,57	1,06	0,67	0,58	0,60	0,06	0,07	0,06	0,47	0,71

	CENTRE ZONE																			
Element	JR-15-HC-1C	JR-15-HC-2C	JR-15-HC-3C	JR-15-HC-4C	JR-15-HD-1	JR-15-HD-2	JR-15-HD-3	JR-15-HD-4	JR-15-HD-5	JR-15-CLAST-1	JR-15-CLAST-2	JR-15-CLAST-3	JR-19B-HA-1	JR-19B-HA-2	JR-19B-HA-3	JR-19B-HA-4	JR-19B-HA-5	JR-19B-HB-1	JR-19B-HB-2	JR-19B-HB-3	JR-19B-HB-5
Ca (Wt%)	1,17	1,17	1,17	1,17	1,17	1,17	1,17	1,17	1,17	0,06	0,06	0,06	9,40	9,40	9,40	9,40	9,40	24,4	24,4	24,4	24,4
Fe (Wt%)	1,41	1,72	0,38	2,38	2,79	3,89	3,28	3,39	2,78	5,66	10,5	10,5	1,17	0,72	0,56	0,38	0,24	0,03	0,02	0,02	0,02
Al (Wt%)	2,89	3,81	0,27	2,42	3,47	2,72	2,96	2,87	2,89	1,09	0,23	0,15	0,12	0,06	0,02	0,04	0,01	0,36	0,002	0,002	0,003
Mg (Wt%)	0,32	0,62	0,13	0,43	0,36	0,35	0,38	0,39	0,37	0,06	0,05	0,04	0,93	0,62	0,66	0,84	0,52	2,09	2,32	2,17	2,90
Ti (Wt%)	0,00	0,01	0,00	-	0,00	0,00	0,00	0,00	0,00	0,00005	-	0,0001	0,004	0,001	0,001	0,0009	0,0005	0,0005	0,0005	0,0005	0,0005
Si (Wt%)	31,6	41,0	8,60	42,7	10,4	8,44	12,5	13,0	8,71	1,02	1,27	1,37	1,74	1,22	0,50	0,70	0,17	5,61	5,63	4,47	7,84
Mn (Wt%)	0,01	0,01	0,01	0,02	0,01	0,01	0,01	0,01	0,01	0,00	0,01	0,01	0,02	0,02	0,01	0,08	0,02	0,03	0,03	0,02	0,01
Sr (Wt%)	0,02	0,03	0,01	0,05	0,06	0,06	0,07	0,07	0,06	0,002	0,002	0,002	0,07	0,07	0,07	0,07	0,08	0,23	0,25	0,29	0,32
As (Wt%)	0,14	0,19	0,02	0,11	0,34	0,45	0,33	0,33	0,31	0,10	0,15	0,15	0,19	0,13	0,11	0,07	0,07	0,07	0,08	0,09	0,09

	EAST ZONE																								
Element	JR-23A-HA-1	JR-23A-HA-2	JR-23A-HA-3	JR-23A-HA-4	JR-23A-HA-5	JR-23A-HB-1	JR-23A-HB-2	JR-23A-HB-3	JR-23A-HB-4	JR-23A-HB-5	JR-23A-HC-1	JR-23A-HC-2	JR-23A-HC-3	JR-23A-HC-4	JR-23A-HC-5	JR-23A-HD-1	JR-23A-HD-2	JR-23A-HD-3	JR-23A-HD-4	JR-23A-HD-5	JR-25-HA-1	JR-25-HA-2	JR-25-HA-3	JR-25-HA-4	JR-25-HA-5
Ca (Wt%)	3,91	3,91	3,91	3,91	3,91	3,91	3,91	3,91	3,91	3,91	3,91	3,91	3,91	3,91	3,91	3,91	3,91	3,91	3,91	3,91	25,00	25,0	25,0	25,0	25,0
Fe (Wt%)	60,2	35,1	49,7	41,0	48,8	14,4	14,3	16,3	15,6	14,9	42,1	23,5	16,3	21,4	19,8	22,6	34,9	47,5	33,8	29,1	10,4	0,78	0,61	2,55	18,2
Al (Wt%)	0,04	0,03	0,04	0,03	0,05	0,01	0,01	0,01	0,01	0,01	0,17	0,02	0,01	0,01	0,01	0,04	0,03	0,04	0,07	0,02	0,03	0,03	0,02	0,04	0,17
Mg (Wt%)	1,22	0,74	1,11	0,85	1,03	0,56	0,50	0,50	0,43	0,40	0,93	0,55	0,43	0,50	0,46	0,50	0,69	0,87	0,67	0,57	2,12	0,89	0,97	2,10	5,88
Ti (Wt%)	0,0003	0,0003	0,0003	0,0003	0,0003	0,0002	0,0002	0,0002	0,0002	0,0002	-	0,0001	0,0001	0,0001	0,0001	0,0005	-	-	0,0001	0,0001	0,001	0,001	0,001	0,001	0,001
Si (Wt%)	19,8	11,3	17,4	12,9	16,6	6,90	7,44	6,76	7,06	6,08	12,55	7,39	5,37	6,71	6,38	6,74	9,07	11,73	10,12	7,16	17,23	4,77	2,09	4,07	26,36
Mn (Wt%)	0,14	0,10	0,12	0,11	0,12	0,07	0,07	0,07	0,07	0,06	0,10	0,08	0,07	0,07	0,07	0,06	0,08	0,10	0,08	0,08	5,04	0,64	1,36	11,6	31,9
Sr (Wt%)	0,11	0,08	0,10	0,09	0,10	0,07	0,07	0,07	0,07	0,06	0,09	0,08	0,08	0,08	0,08	0,08	0,08	0,09	0,08	0,08	0,29	0,14	0,14	0,35	0,84
As (Wt%)	4,61	3,97	4,09	4,25	4,22	5,52	6,90	5,38	6,14	7,12	4,61	4,69	4,71	4,70	4,29	4,08	4,72	5,35	4,24	4,81	0,89	0,09	0,10	0,51	1,89

Table A5 Laser Ablation ICP-MS results, trace elements

		NORTH ZONE						
Element		JR-06-LS-1	JR-06-LS-2	JR-06-LS-3	JR-06-LS-4	JR-06-LS-5	JR-06-CLAST-2	JR-06-CLAST-3
Li	(ppm)	7,13	14,1	13,4	11,5	12,7	0,65	0,60
Rb	(ppm)	1,51	7,57	11,6	8,97	7,22	0,03	0,02
Cs	(ppm)	7,17	35,2	64,8	26,8	36,2	0,04	0,03
Be	(ppm)	-	-	-	-	-	-	-
Ba	(ppm)	0,21	4,76	0,11	0,43	1,46	0,01	0,01
La	(ppm)	-	0,35	-	-	-	-	-
Ce	(ppm)	-	0,62	-	-	-	-	-
Nd	(ppm)	-	0,28	-	-	-	-	-
Sm	(ppm)	-	-	-	-	-	-	-
Gd	(ppm)	-	-	-	-	-	-	-
Dy	(ppm)	-	-	-	-	-	-	-
Er	(ppm)	-	-	-	-	-	-	-
Yb	(ppm)	-	-	-	-	-	-	-
Th	(ppm)		0,13	-	-	-	-	-
U	(ppm)	0,05	0,05	-	-	-	-	-
Mo	(ppm)	-	-	-	-	-	-	-
W	(ppm)	-	-	-	-	-	-	-
Re	(ppm)	-	-	-	-	-	-	-
V	(ppm)	-	0,88	-		0,25	-	-
Cr	(ppm)	-	-	-	26,3	-	0,20	0,19
Co	(ppm)	-	0,07	-	-	0,10	-	-
Ni	(ppm)	-	-	-	-	0,46	-	-
Cu	(ppm)	0,35	0,73	0,21	1,24	0,57	0,05	0,04
Zn	(ppm)	0,94	1,17	-	-	1,46	0,10	-
Ag	(ppm)	-	-	-	-	-	-	-
Cd	(ppm)	-	-	-	-	-	-	-
Ga	(ppm)	-	0,08	-	-	-	-	-
Sn	(ppm)	3,77	0,89	1,40	10,4	4,56	0,54	0,46
Tl	(ppm)	0,46	2,11	2,58	2,94	1,92	0,02	0,02
Pb	(ppm)	0,84	0,44	0,28	2,32	0,45	0,10	0,07
Bi	(ppm)	-	-	-	-	-	-	-
Ge	(ppm)	-	0,83	0,66	-	-	-	-
B	(ppm)	126	566	1070	436	618	2,27	2,18
Sb	(ppm)	0,99	5,00	7,01	2,88	4,79	-	-
Au	(ppm)	-	-	-	-	-	-	-
Hg	(ppm)	-	-	-	-	-	-	-
Mn	(ppm)	0,82	5,14	0,81	-	2,84	0,08	0,06
Sr	(ppm)	2151	3591	1370	2013	3019	124	123
As	(ppm)	53,5	96,4	100	140	49,1	1,63	1,54
Cl	(ppm)	-	-	-	-	-	-	-

	CENTRE ZONE																							
Element	JR-10C-HA-1	JR-10C-HA-2	JR-10C-HA-3	JR-10C-HA-4	JR-10C-HA-5	JR-10C-HB-1	JR-10C-HB-2	JR-10C-HB-3	JR-10C-HB-4	JR-10C-HB-5	JR-10C-HC-1	JR-10C-HC-2	JR-10C-HC-4	JR-10C-HC-5	JR-10C-HD-1	JR-10C-HD-2	JR-10C-HD-3	JR-10C-HD-4	JR-10C-HD-5	JR-11-HA-1	JR-11-HA-2	JR-11-HA-3	JR-11-HA-4	JR-11-HA-5
Li (ppm)	12,1	8,01	8,84	7,39	9,62	13,9	21,0	18,7	11,6	46,4	14,1	20,4	13,0	9,1	247	77,3	53,2	11,8	21,3	17,8	16,8	7,40	7,98	7,34
Rb (ppm)	3,42	1,95	2,16	1,92	2,22	2,70	3,17	2,79	1,68	4,10	0,81	1,63	0,99	1,33	17,1	7,25	3,23	1,02	2,95	2,88	4,09	2,18	1,97	1,13
Cs (ppm)	6,20	4,91	6,12	3,47	5,95	8,52	11,7	9,17	6,63	12,8	1,39	3,64	2,35	4,13	94,1	43,1	12,2	2,76	6,76	3,62	6,76	6,05	3,26	1,73
Be (ppm)	10,8	15,7	8,20	9,61	13,9	20,9	28,7	23,7	5,95	27,4	5,11	11,6	6,75	9,03	30,3	23,7	15,9	8,64	14,5	7,27	6,55	5,18	7,32	4,60
Ba (ppm)	38,6	80,5	60,6	53,1	65,3	84,2	85,6	90,0	50,8	104	98,1	102	87,2	97,0	221	99,5	444	80,8	133	208	222	67,1	72,3	79,5
La (ppm)	0,44	0,18	0,12	0,23	0,16	0,40	0,46	0,63	0,22	0,51	0,06	0,23	0,13	0,32	1,89	0,71	1,17	0,10	0,44	13,1	0,10	0,07	0,04	0,03
Ce (ppm)	6,23	0,29	0,25	0,43	0,32	0,67	0,81	1,19	0,16	1,12	0,12	0,40	0,23	0,72	3,56	1,31	1,31	0,21	0,79	0,06	0,15	0,21	0,11	0,04
Nd (ppm)	0,59	-	-	-	-	0,31	0,33	0,66	-	0,51	-	-	-	0,23	1,39	0,57	0,37	-	0,25	-	-	-	-	-
Sm (ppm)	-	-	-	-	-	-	-	-	-	-	-	-	-	-	-	-	-	-	-	-	-	-	-	-
Gd (ppm)	-	-	-	-	-	-	-	0,29	-	-	-	-	-	-	-	0,38	-	-	-	-	-	-	-	-
Dy (ppm)	-	-	-	-	-	-	-	-	-	-	-	-	-	-	-	0,31	-	-	-	-	-	-	-	-
Er (ppm)	-	-	-	-	-	-	-	-	-	-	-	-	-	-	-	-	-	-	-	-	-	-	-	-
Yb (ppm)	-	-	-	-	-	-	-	-	-	-	-		-	-	-	-	-	-	-	-	-	-	-	-
Th (ppm)	0,18	-	-	0,06	0,14	0,11	0,28	0,13	-	0,15	-	0,06	-	0,07	0,76	0,21	0,30	-	0,15	-	-	-	-	-
U (ppm)		-	-	-	-	-	-	-	-	-	-	-	-	-	0,18	0,06	0,06	-	-	-	-	-	-	-
Mo (ppm)	0,54	1,91	0,70	0,89	1,88	2,22	2,98	2,15	0,71	3,23	1,00	2,42	1,33	1,44	4,33	4,89	2,52	1,76	2,22	3,76	4,05	0,58	1,51	1,10
W (ppm)	5,99	23,1	9,17	8,73	24,6	25,4	36,3	28,8	9,78	41,7	13,1	32,1	15,1	17,9	52,9	61,9	34,3	22,3	26,9	28,0	24,3	3,26	23,7	14,8
Re (ppm)	-	-	-	-	-	-	-	-	-	-	-	-	-	-	-	-	-	-	-	-	-	-	-	-
V (ppm)	0,46	0,27	0,42	0,43	0,50	1,35	0,79	0,95	0,21	1,11	0,15	0,46	0,24	0,57	5,04	1,52	1,77	0,30	0,46	0,31	0,65	0,13	0,35	0,22
Cr (ppm)	2,91	1,81	3,20	1,86	4,10	-	2,10	1,61	2,25	2,37	-	-	1,55	-	-	2,99	1,87	-	-	-	-	1,54	1,70	1,53
Co (ppm)	0,16	0,10	-	0,11	0,13	0,14	0,16	0,23	0,09	0,25	0,07	0,11	0,09	0,09	0,73	0,32	0,21	0,09	0,15	0,46	0,55	0,09	0,26	0,18
Ni (ppm)	0,50	-	-	0,69	0,81	0,48	0,74	0,55	0,36	1,64	0,35	0,53	0,32	0,38	2,66	1,17	0,82	0,50	0,65	2,62	2,83	0,67	1,52	0,92
Cu (ppm)	0,85	1,01	0,79	0,79	2,41	0,96	1,55	1,17	0,43	4,49	0,22	0,55	0,28	0,31	3,47	2,99	0,92	0,35	0,59	4,72	6,88	4,30	3,18	1,50
Zn (ppm)	2,77	4,28	2,79	3,83	5,25	8,92	12,0	6,71	1,42	13,1	2,14	5,17	2,23	3,63	21,2	13,4	8,84	4,40	5,81	2,50	3,44	2,42	1,75	1,52
Ag (ppm)	-	-	-	-	-	-	-	-	-	-	-	-	-	-	-	-	-	-	-	-	-	-	-	-
Cd (ppm)	-	-	-	-	-	-	-	-	-	-	-	-	-	-	-	-	-	-	-	-	-	-	-	-
Ga (ppm)	0,99	0,99	1,14	0,67	1,04	1,89	2,43	2,13	0,91	3,41	0,26	0,53	0,43	0,48	4,71	1,78	1,53	0,36	1,01	0,51	0,59	0,27	0,24	0,16
Sn (ppm)	-	-	-	-	-	-	-	-	-	-	-	-	-	-	-	1,06	-	-	-	-	-	-	-	-
Tl (ppm)	0,26	0,64	0,30	0,23	0,61	0,84	1,13	0,99	0,25	1,43	0,54	1,10	0,65	0,72	3,18	14,9	1,62	0,78	1,28	14,5	16,3	3,35	5,52	3,50
Pb (ppm)	0,58	0,57	0,58	0,71	1,21	0,98	0,93	0,74	0,17	9,22	0,24	0,47	0,27	0,34	2,91	2,85	4,66	0,35	0,63	0,25	0,66	0,21	0,24	0,20
Bi (ppm)	-	-	-	-	-	-	-	-	-	-	-	-	-	-	0,08	-	0,11	-	-	-	-	-	-	-
Ge (ppm)	4,41	4,79	3,42	3,18	5,19	6,61	10,1	8,70	6,38	25,4	2,67	11,0	3,4	3,53	129	24,2	14,6	3,42	6,72	1,56	1,71	0,99	1,56	0,77
B (ppm)	35,1	46,4	84,6	31,5	104	80,6	97,0	61,8	122	85,9	42,8	50,5	35,0	52,9	189	83,2	63,3	34,5	52,4	62,3	60,8	35,1	58,5	39,6
Sb (ppm)	12,3	38,3	16,5	17,4	43,2	45,9	61,7	45,5	15,5	88,9	20,6	54,2	28,0	34,1	120	110	62,1	34,5	48,1	22,5	23,1	5,87	14,3	9,20
Au (ppm)	-	-	-	-	-	-	-	-	-	-	-	-	-	-	-	-	-	-	-	-	-	-	-	-
Hg (ppm)	-	-	-	-	-	-	-	-	-	-	-	-	-	-	-	-	-	-	-	-	-	-	-	-
Mn (ppm)	1133	1390	707	1197	461	1134	1328	1352	500	1310	678	1255	868	1136	2807	1954	1729	1263	1252	8997	8978	2060	2148	2277
Sr (ppm)	1552	2384	1991	1981	1947	2235	2357	2414	1723	2498	3247	2680	2791	2650	2620	2990	4141	2640	3241	1402	1412	1183	1046	1350
As (ppm)	1260	2861	1712	1563	3048	3170	4003	3630	1369	5100	2299	4454	2449	2879	5781	4281	4609	2649	3726	1416	1120	790	1116	866
Cl (ppm)	989	779	2116	-	2877	-	893	802	1195	1369	-	-	-	-	1039	1983	-	-	-	-	-	-	-	-

	CENTRE ZONE																								
Element	JR-11-HB-1	JR-11-HB-2	JR-11-HB-3	JR-11-HB-4	JR-11-HB-5	JR-11-HC-1	JR-11-HC-2	JR-11-HC-3	JR-11-HC-4	JR-11-HC-5	JR-14-HA-1	JR-14-HA-2	JR-14-HA-3	JR-14-HA-4	JR-14-HA-5	JR-14-HB-1	JR-14-HB-2	JR-14-HB-3	JR-14-HB-4	JR-14-HB-5	JR-14-HEE-1	JR-14-HEE-2	JR-14-HEE-3	JR-14-HEE-4	JR-14-HEE-5
Li (ppm)	4,08	8,60	14,5	9,56	4,98	3,53	10,13	10,08	5,52	9,26	31,7	20,7	27,4	28,6	151	5,41	4,02	13,0	16,6	9,11	4,03	4,25	17,0	13,1	14,6
Rb (ppm)	0,49	1,45	5,64	2,78	0,81	1,16	2,24	6,32	0,93	1,86	24,7	26,1	23,4	30,0	96,2	15,9	15,0	105	124	28,6	4,50	5,56	12,2	11,8	2,37
Cs (ppm)	0,63	1,74	13,3	2,28	0,91	4,01	3,97	20,96	1,69	2,51	117	115	98,8	137	532	85,8	71,9	622	728	176	29,9	37,9	77,6	69,7	15,6
Be (ppm)	3,98	5,09	9,93	3,93	4,65	3,16	7,18	8,40	4,63	6,77	24,4	22,1	26,5	24,2	18,0	18,7	17,9	16,1	12,3	18,8	0,87	1,52	3,48	3,38	1,11
Ba (ppm)	51,2	125	213	162	64,64	31,94	202,46	78,70	79,8	138	119	126	133	166	225	124	107	131	137	123	6,74	11,6	23,8	28,9	6,21
La (ppm)	0,04	-	0,06	-	-	0,04	-	0,12	-	-	9,29	12,1	8,45	65,0	7,72	5,96	11,8	4,33	4,23	5,63	0,17	0,72	0,45	0,80	0,14
Ce (ppm)	0,06	-	0,11	-	-	0,09	-	0,24	-	0,05	18,4	24,6	16,5	20,2	15,2	11,8	24,3	8,01	7,73	11,80	0,28	1,53	0,82	1,64	0,28
Nd (ppm)	-	-	-	-	-	-	-	-	-	-	9,68	13,5	8,55	11,5	8,81	6,25	13,1	4,32	4,17	6,77	0,13	0,90	0,43	0,96	0,14
Sm (ppm)	-	-	-	-	-	-	-	-	-	-	2,11	2,81	1,74	2,41	1,84	1,36	2,69	1,02	0,84	1,52	-	0,21	-	0,21	-
Gd (ppm)	-	-	-	-	-	-	-	-	-	-	2,21	2,86	2,01	2,59	1,99	1,40	2,72	0,88	0,92	1,50	-	0,19	-	-	-
Dy (ppm)	-	-	-	-	-	-	-	-	-	-	1,59	2,04	1,29	1,85	1,25	0,87	1,77	0,62	0,52	0,99	-	0,15	-	-	-
Er (ppm)	-	-	-	-	-	-	-	-	-	-	0,62	0,88	0,62	0,82	0,68	0,42	0,88	0,36	-	0,50	-	0,07	-	-	-
Yb (ppm)	-	-	-	-	-	-	-	-	-	-	0,45	0,61	0,45	0,56	-	-	0,50	-	-	0,38	-	-	-	-	-
Th (ppm)	-	-	-	-	-	-	-	-	-	-	0,08	-	0,28	-	0,15	-	-	-	-		-	-	-	-	-
U (ppm)	-	-	-	-	-	-	-	-	-	-	2,12	2,21	2,44	3,63	3,76	2,45	1,25	2,88	3,07	2,41	0,18	0,28	0,69	0,66	0,21
Mo (ppm)	0,35	1,93	3,79	3,00	0,71	-	1,37	0,94	0,38	1,20	3,53	3,28	4,36	6,56	8,31	3,86	1,56	4,53	9,80	3,44	0,18	-	0,32	0,26	-
W (ppm)	1,08	4,56	12,95	7,30	1,70	1,21	5,68	7,32	2,06	5,41	2,28	2,04	2,64	4,81	7,77	4,90	1,65	5,37	7,89	6,31	-	-	0,26	-	-
Re (ppm)	-	-	-	-	-	-		-	-	-	-	-	-	-	-	-	-	-	-	-	-	-	-	-	-
V (ppm)	-	-	0,18	0,32	-	-	0,10	0,38	-	-	1,70	1,89	4,15	2,75	4,69	4,94	1,77	1,77	2,40	1,45	0,30	0,20	0,35	0,29	0,08
Cr (ppm)	-	-	2,36	1,88	2,16	-			-	-	-	-	-	4,01	7,16	-	-	-	-	-	-	0,92	-	-	0,65
Co (ppm)	0,05	0,08	0,14	0,08	-	0,07	0,12	0,17	0,10	0,09	6,93	7,62	6,37	11,5	22,2	8,13	7,05	16,3	29,5	9,3	15,5	15,7	56,6	39,4	36,9
Ni (ppm)	0,35		0,76	-	0,45	-	-	0,48	-	0,44	8,70	9,62	9,94	13,4	26,6	8,45	8,43	18,2	19,2	8,7	10,0	10,8	37,8	25,4	22,6
Cu (ppm)	0,74	1,01	3,09	2,25	1,40	0,74	1,00	2,02	0,93	1,15	144	178	143	224	333	132	127	187	225	122	9,64	21,2	26,0	64,0	7,63
Zn (ppm)	2,07	2,05	5,58	5,57	3,04	2,07	7,89	8,28	3,60	8,87	509	534	602	803	1212	859	669	1204	1142	772	65,5	104	169	113	162
Ag (ppm)	-	-	-	-	-	-	-	-	-	-	-	-	-	-	-	-	-	-	-	-	-	-	-	-	-
Cd (ppm)	-	-	-	-	-	-	-	-	-	-	12,6	10,4	18,3	11,5	10,1	14,4	11,4	13,2	6,76	12,6	1,47	2,02	2,94	2,09	2,81
Ga (ppm)	-	0,15	0,74	0,14	-	-	0,23	0,50	0,15	0,28	0,34	0,32	0,69	0,42	0,63	0,51	0,30	0,32	0,45	0,26	0,06				
Sn (ppm)	0,62	-	0,85	-	1,57	-	0,71	-	-	0,69	-	-	-	-	-	-	-	-	-	-	-	-	-	-	-
Tl (ppm)	1,38	6,31	15,0	11,8	2,90	0,48	8,35	4,61	3,97	6,70	5,18	5,34	6,60	6,21	11,28	8,39	6,71	14,2	11,7	7,47	2,46	4,34	8,12	7,26	4,02
Pb (ppm)	0,15	0,11	0,43	0,21	0,23	0,20	0,39	0,47	0,19	0,36	3,15	3,46	3,86	5,78	5,06	1,62	3,37	3,10	2,36	0,91	0,43	0,73	1,04	1,17	0,12
Bi (ppm)	-	-	-	-	-	-	-	-	-	-	-	-	-	-	-	-	-	-	-	-	0,02	0,03	0,05	-	-
Ge (ppm)	-	0,64	2,76	-	-	-	1,32	3,30	0,70	1,16	18,3	19,9	19,6	28,3	57,3	23,8	20,7	56,4	64,3	28,4	2,86	4,66	10,0	9,67	6,90
B (ppm)	25,3	35,2	80,7	42,6	47,93	24,75	69,52	74,33	28,6	51,6	38,3	43,0	40,9	51,8	73,3	52,2	55,2	97,0	111	46,3	86,0	121	189	293	31,9
Sb (ppm)	2,60	8,42	23,0	9,10	3,32	2,33	14,02	19,06	7,01	14,1	108	122	121	162	227	206	183	241	223	169	3,94	9,39	14,9	15,5	4,77
Au (ppm)	-	-	-	-	-	-	-	-	-	-	-	-	-	-	-	-	-	-	-	-	-	-	-	-	-
Hg (ppm)	-	-	-	-	-	-	-	-	-	-	-	-	-	-	-	-	-	-	-	-	-	-	-	-	-
Mn (ppm)	1693	4701	7564	6022	1929	783	5613	2338	2636	4443	425	334	515	460	360	459	286	437	336	475	77	99	183	172	134
Sr (ppm)	1222	1350	1022	1216	1179	1101	1402	1253	1200	1346	759	750	792	704	762	700	735	664	590	735	96	104	171	184	86
As (ppm)	724	898	1728	810	674	736	1379	2210	916	1207	46107	45909	61415	63472	62791	62531	44188	66448	40262	54827	260	923	879	1395	174
Cl (ppm)	-	-	-	-	-	-	-	-	-	-	-	-	-	-	-	-	-	-	-	-	-	-	-	-	-

		CENTRE ZONE																								
Element		JR-14-HC-1	JR-14-HC-2	JR-14-HC-3	JR-14-HC-4	JR-14-HC-5	JR-14-HD-1	JR-14-HD-2	JR-14-HD-3	JR-14-HD-4	JR-14-HD-5	JR-15-HA-1	JR-15-HA-2	JR-15-HA-3	JR-15-HA-4	JR-15-HA-5	JR-15-HB-1	JR-15-HB-2	JR-15-HB-3	JR-15-HB-4	JR-15-HB-5	JR-15-HC-1	JR-15-HC-2	JR-15-HC-3	JR-15-HC-4	JR-15-HC-5
Li	(ppm)	14,4	-	-	-	-	5,33	3,17	3,76	2,61	4,42	17,6	3,53	6,27	5,30	6,58	2,37	7,81	5,63	7,53	3,67	16,4	12,7	9,49	4,51	4,62
Rb	(ppm)	4,62	-	-	-	-	17,4	26,3	27,4	30,9	32,8	63,6	17,1	15,7	61,1	16,6	46,0	32,3	20,8	25,3	27,7	29,9	39,1	33,8	13,4	10,3
Cs	(ppm)	34,0	-	-	-	-	83,3	166	163	143	178	445	123	93,5	453	115	268	192	114	150	155	198	242	234	92,5	64,7
Be	(ppm)	-	-	-	-	-	48,9	40,4	34,3	36,3	25,6	2,74	-	-	1,98	-	5,96	4,75	6,60	5,54	6,51	-	5,39	-	7,71	8,61
Ba	(ppm)	37,6	-	-	-	-	98,8	113	118	144	116	158	230	139	90,4	87,3	90,4	75,5	72,1	92,4	71,4	56,2	84,1	26,9	106	77,5
La	(ppm)	-	-	-	-	-	14,4	10,3	8,61	8,04	8,80	1,79	2,45	2,48	1,17	7,36	9,87	5,36	10,8	9,23	9,96	6,97	13,2	5,94	8,89	9,39
Ce	(ppm)	-	-	-	-	-	32,0	21,1	17,1	14,6	20,0	3,58	4,69	3,95	2,27	12,8	19,5	10,3	21,9	19,8	19,3	14,2	23,6	12,1	18,6	20,3
Nd	(ppm)	-	-	-	-	-	18,8	11,8	9,05	7,61	10,6	1,54	2,32	1,55	1,02	4,86	8,47	4,41	9,78	8,63	8,43	7,57	9,83	6,56	9,00	9,49
Sm	(ppm)	-	-	-	-	-	4,10	2,63	1,88	1,47	2,10	-	-	0,26	-	0,84	1,46	0,82	1,71	1,51	1,36	-	1,12	-	1,56	1,79
Gd	(ppm)	-	-	-	-	-	4,27	2,77	2,27	1,71	2,48	-	0,41	-	-	0,86	1,18	0,74	1,47	1,33	1,18	-	-	-	1,15	1,57
Dy	(ppm)	-	-	-	-	-	3,02	1,93	1,49	1,27	1,72	-	-	-	-	0,43	0,76	0,43	0,84	0,75	0,68	-	-	-	0,84	0,96
Er	(ppm)	-	-	-	-	-	1,45	0,98	0,75	0,60	0,77	-	-	-	-	0,21	0,33	0,18	0,37	0,29	0,29	-	-	-	-	0,43
Yb	(ppm)	-	-	-	-	-	1,04	0,69	0,49	-	0,58	-	-	-	-	-	-	-	0,29	-	0,21	-	-	-	-	-
Th	(ppm)	-	-	-	-	-	-	-	-	0,27	0,12	0,12	0,23	0,47	0,20	0,09	-	-	-	-	-	0,56	6,78	-	-	-
U	(ppm)	2,89	-	-	-	-	4,21	3,66	5,11	5,44	8,00	3,05	3,71	2,43	2,15	17,2	2,37	5,84	2,65	4,06	3,10	10,68	5,92	10,0	3,71	2,83
Mo	(ppm)	-	-	-	-	-	2,20	2,93	5,10	2,67	3,48	6,52	1,07	0,90	2,54	3,47	0,52	1,92	0,69	1,08	0,77	2,80	1,40	-	0,89	0,72
W	(ppm)	-	-	-	-	-	1,61	3,78	4,58	3,56	2,66	0,69	-	-	0,45	-	-	0,78	0,34	0,53	0,46	-	-	-	-	-
Re	(ppm)	-	-	-	-	-	-	-	-	-	-	-	-	-	-	-	-	-	-	-	-	-	-	-	-	-
V	(ppm)	-	-	-	-	-	1,93	13,68	4,66	3,71	4,30	1,51	1,68	4,03	1,66	1,87	1,95	2,98	1,71	2,47	2,36	16,7	6,96	10,4	1,45	0,95
Cr	(ppm)	78,6	-	-	-	-		43,98	3,68	5,36	-	-	-	-	-	-	-	-	-	-	-	-	11,7	25,7	6,02	-
Co	(ppm)	41,7	-	-	-	-	28,6	30,0	47,9	23,1	11,0	54,3	29,7	27,2	9,07	111	17,1	26,7	39,7	26,1	64,2	361	118	252	42,2	22,5
Ni	(ppm)	34,2	-	-	-	-	9,17	18,0	16,3	13,5	13,3	33,2	19,6	19,2	6,32	65,7	18,9	26,9	26,7	25,8	41,1	256	75,5	193	28,3	17,0
Cu	(ppm)	16,7	-	-	-	-	107	138	148	144	147	118	39,6	31,7	19,5	121	80,2	80,0	174	77,7	199	268	168	208	241	144
Zn	(ppm)	110	-	-	-	-	543	646	586	603	574	371	176	203	97,2	514	278	394	569	378	699	745	401	598	303	294
Ag	(ppm)	-	-	-	-	-	-	-	-	-	-	-	-	-	-	-	-	-	-	-	-	-	-	-	-	-
Cd	(ppm)	-	-	-	-	-	8,98	12,4	11,3	11,0	10,6	2,77	-	1,37	-	4,06	2,58	4,74	6,44	4,20	8,46	-	2,88	4,22	2,58	2,61
Ga	(ppm)	-	-	-	-	-	0,37	0,96	0,48	0,73	0,59	-	0,42	1,12	0,29	0,34	0,24	0,17	0,25	0,21	0,22	1,70	1,75	-	-	0,26
Sn	(ppm)	-	-	-	-	-	-	-	-	-	-	-	1,17	-	-	10,5	-	-	1,70	1,02	-	-	-	-	-	-
Tl	(ppm)	4,52	-	-	-	-	6,41	8,08	8,48	9,77	8,00	37,33	8,63	6,75	28,3	9,23	9,14	9,00	7,07	7,48	8,61	15,4	22,2	17,0	7,43	7,64
Pb	(ppm)	-	-	-	-	-	3,37	2,65	1,89	2,31	2,90	2,04	4,11	2,74	1,37	4,97	2,84	6,50	4,54	5,03	3,14	13,2	4,18	5,18	2,04	1,94
Bi	(ppm)	-	-	-	-	-	-	-	-	-	-	-	-	-	-	-	-	-	-	-	-	-	-	-	-	-
Ge	(ppm)	-	-	-	-	-	12,4	18,2	18,0	18,3	18,6	13,9	11,5	8,43	17,5	23,2	13,5	12,7	10,2	12,2	13,3	30,4	17,0	22,2	10,0	9,87
B	(ppm)	1222	-	-	-	-	79,4	115	107	109	116	577	736	769	693	908	93,2	61,9	74,2	118	103	800	890	810	495	388
Sb	(ppm)	14	-	-	-	-	29,4	57,2	45,3	40,1	69,3	10,9	5,06	5,29	6,19	9,40	15,1	13,3	12,2	15,9	16,5	47,9	35,1	44,4	17,9	12,3
Au	(ppm)	-	-	-	-	-	-	-	-	-	-	-	-	-	-	-	-	-	-	-	-	-	-	-	-	-
Hg	(ppm)	-	-	-	-	-	-	-	-	-	-	-	-	-	-	-	-	-	-	-	-	-	-	-	-	-
Mn	(ppm)	201	-	-	-	-	368	561	996	434	243	66,91	139	151	46,5	149	190	221	202	202	226	553	206	371	147	156
Sr	(ppm)	197	-	-	-	-	701	747	738	746	720	585,07	332	308	550	270	397	386	408	407	400	205	448	386	472	382
As	(ppm)	595	-	-	-	-	31546	33354	33358	37010	39794	1303,62	447	326	347	513	5729	10553	6740	5794	6023	609	664	579	4695	7087
Cl	(ppm)	-	-	-	-	-	-	-	-	-	-	-	-	-	-	-	-	-	-	-	-	-	-	-	-	-

		CENTRE ZONE																				
Element		JR-15-HC-1C	JR-15-HC-2C	JR-15-HC-3C	JR-15-HC-4C	JR-15-HD-1	JR-15-HD-2	JR-15-HD-3	JR-15-HD-4	JR-15-HD-5	JR-15-CLAST-1	JR-15-CLAST-2	JR-15-CLAST-3	JR-19B-HA-1	JR-19B-HA-2	JR-19B-HA-3	JR-19B-HA-4	JR-19B-HA-5	JR-19B-HB-1	JR-19B-HB-2	JR-19B-HB-3	JR-19B-HB-5
Li	(ppm)	13,7	15,4	1,08	4,09	2,00	1,55	2,71	2,76	1,59	1,42	1,80	1,64	9,77	4,81	5,22	5,52	2,88	8,37	9,37	8,48	9,99
Rb	(ppm)	21,7	32,5	2,41	15,9	29,5	20,2	43,5	52,0	22,5	0,54	0,26	0,31	2,90	1,63	0,80	1,53	0,42	1,13	0,97	0,84	1,24
Cs	(ppm)	141	218	15,3	95,5	126,1	84,6	192	255	95,7	1,49	1,34	1,30	6,65	3,07	1,96	3,66	0,73	4,55	5,20	3,55	6,62
Be	(ppm)	1,58	1,76	0,37	3,42	7,48	7,66	5,15	4,69	7,20	-	-	-	5,69	3,51	2,55	2,39	1,40	-	-	-	-
Ba	(ppm)	16,1	30,2	32,0	299	115	117	120	126	119	2,13	1,70	1,88	32,5	31,0	25,5	37,9	26,1	73,0	72,4	208	413
La	(ppm)	1,12	1,65	0,58	4,92	6,88	7,06	4,79	4,73	7,04	0,06	0,05	0,06	0,37	0,24	0,12	0,14	0,05	-	-	-	-
Ce	(ppm)	2,32	3,60	1,03	10,3	14,2	14,9	8,32	8,02	15,3	0,16	0,13	0,13	0,65	0,56	0,27	0,24	0,09	-	-	-	-
Nd	(ppm)	1,07	1,75	0,46	5,10	6,87	7,07	3,55	3,50	7,26	0,06	0,07	0,09	0,32	-	0,13	-	-	-	-	-	-
Sm	(ppm)	-	0,42	0,10	1,12	1,25	1,29	0,59	0,55	1,28	-	-	-	-	-	-	-	-	-	-	-	-
Gd	(ppm)	-	0,33	0,07	0,78	1,10	1,11	0,53	0,58	1,12	-	-	-	-	-	-	-	-	-	-	-	-
Dy	(ppm)	0,17	0,22	0,05	0,59	0,68	0,68	0,39	0,34	0,73	-	-	-	-	-	-	-	-	-	-	-	-
Er	(ppm)	-	-	-	-	0,34	0,31	0,18	0,17	0,32	-	-	-	-	-	-	-	-	-	-	-	-
Yb	(ppm)	-	-	-	-	0,23	0,24	0,13	-	0,30	-	-	-	-	-	-	-	-	-	-	-	-
Th	(ppm)	-	-	-	-			-	-	-	-	-	-	0,13	0,26	0,04	-	-	-	-	-	-
U	(ppm)	2,86	3,85	0,73	4,84	0,23	0,21	0,59	0,62	0,13	0,28	0,30	0,32		0,04	-	-	-	-	-	-	0,08
Mo	(ppm)	4,21	6,01	0,12	-	0,17	0,15	0,40	0,21	-	6,94	8,63	11,97	0,27	0,30	0,15	0,30	-	-	-	-	-
W	(ppm)	0,54	0,76	-	-	-	-	0,32	0,15	-	0,13	0,19	0,24	1,38	1,30	0,78	-	-	-	-	-	-
Re	(ppm)	-	-	-	-	-	-	-	-	-	-	-	-	-	-	-	-	-	-	-	-	-
V	(ppm)	1,35	4,14	0,17	0,92	0,19	0,29	0,36	0,37	0,16	0,90	1,32	1,13	1,00	0,71	0,23	0,31	0,11	-	-	-	-
Cr	(ppm)	-	2,59	-	-	-	-	-	-	-	-	0,98	0,88	-	1,83	0,99	1,92	0,67	-	-	-	-
Co	(ppm)	9,56	14,8	2,71	10,9	5,43	5,14	5,70	6,45	4,07	2,30	2,89	3,62	0,16	0,10	0,05	0,19	0,04	0,11	0,07	-	-
Ni	(ppm)	8,63	11,3	2,07	9,61	5,60	5,48	5,99	6,60	4,59	2,70	3,07	3,63	0,64	0,30	-	0,38	-	0,66	-	-	0,32
Cu	(ppm)	87,8	100	25,7	156	107	123	85,7	75,0	124	39,1	67,9	70,4	0,80	0,46	0,28	0,47	0,17	1,01	-	0,23	0,34
Zn	(ppm)	80,5	88,2	26,5	187	159	204	134	142	166	36,2	46,2	57,7	2,83	1,75	1,20	1,52	1,19	4,04	-	-	0,98
Ag	(ppm)	-	-	-	-	-	-	-	-	-	-	-	-	-	-	-	-	-		-	-	-
Cd	(ppm)	1,35	1,22	0,52	1,66	2,31	2,76	1,72	1,76	2,13	0,28	0,42	0,45	-	-	-	-	-		-	-	-
Ga	(ppm)	-	0,31	-	-	0,14	0,16	0,11	-	0,14	0,54	0,10	0,04	0,39	0,24	0,14	0,21	0,05	0,33	-	-	-
Sn	(ppm)	-	-	-	-	-	-	-	-	0,57	4,41	0,78	0,77	-	-	-	-	-	2,13	-	-	-
Tl	(ppm)	22,7	30,9	3,68	27,3	3,30	2,99	4,13	4,96	2,84	0,33	0,38	0,41	0,58	0,34	0,28	0,39	0,15	0,18	0,15	0,14	0,19
Pb	(ppm)	2,72	3,01	0,29	3,89	0,90	1,02	0,43	0,42	0,87	1,72	0,55	0,33	0,77	0,53	0,33	0,28	0,15	1,68	-	-	-
Bi	(ppm)	-	-	-	-	-	-	-	-	-	-	-	-	-	-	-	-	-	-	-	-	-
Ge	(ppm)	5,44	6,71	1,25	9,09	4,29	5,25	4,78	5,72	3,81	6,80	12,2	12,8	2,90	1,64	1,47	1,32	0,44	3,81	4,03	3,72	5,40
B	(ppm)	235	270	109	661	23,2	24,7	21,7	19,7	20,8	16,3	23,8	28,7	40,9	35,7	25,4	37,2	14,9	112	107	87,6	140
Sb	(ppm)	9,2	11,5	2,12	10,0	1,68	3,95	2,40	2,09	2,41	2,71	5,04	4,60	5,96	4,24	3,94	2,54	1,61	5,02	4,72	3,42	5,58
Au	(ppm)	-	-	-	-	-	-	-	-	-	-	-	-	-	-	-	-	-	-	-	-	-
Hg	(ppm)	-	-	-	-	-	-	-	-	-	-	-	-	-	-	-	-	-	-	-	-	-
Mn	(ppm)	105	108	60	162	84	104	101	106	81	47	73	83	219	192	112	794	160	320	262	151	87,0
Sr	(ppm)	214	286	122	485	626	634	662	662	641	15	18	20	696	683	749	741	831	2288	2548	2850	3153
As	(ppm)	1417	1942	215	1131	3353	4470	3254	3276	3093	977	1472	1467	1901	1311	1100	710	740	743	810	892	892
Cl	(ppm)	-	-	-	-	-	-	-	-	-	-	-	-	-	-	-	-	-	-	-	-	-

Element	EAST ZONE																								
	JR-23A-HA-1	JR-23A-HA-2	JR-23A-HA-3	JR-23A-HA-4	JR-23A-HA-5	JR-23A-HB-1	JR-23A-HB-2	JR-23A-HB-3	JR-23A-HB-4	JR-23A-HB-5	JR-23A-HC-1	JR-23A-HC-2	JR-23A-HC-3	JR-23A-HC-4	JR-23A-HC-5	JR-23A-HD-1	JR-23A-HD-2	JR-23A-HD-3	JR-23A-HD-4	JR-23A-HD-5	JR-25-HA-1	JR-25-HA-2	JR-25-HA-3	JR-25-HA-4	JR-25-HA-5
Li (ppm)	5,21	3,19	4,37	3,65	4,31	1,85	1,99	1,72	1,62	2,01	3,85	2,89	2,89	3,01	2,29	2,58	3,51	4,57	3,13	2,94	17,67	6,87	7,96	23,0	83,1
Rb (ppm)	1,07	0,62	0,78	0,82	0,93	2,99	3,29	2,34	2,60	3,47	1,86	1,34	1,21	1,34	1,26	1,18	1,41	1,85	1,52	1,26	19,8	2,96	3,03	15,1	51,7
Cs (ppm)	4,74	2,26	3,59	3,11	3,82	8,23	9,04	6,65	6,97	5,39	6,84	3,80	2,31	3,28	3,12	3,80	5,17	7,27	5,95	4,16	80,7	15,8	12,4	38,2	163
Be (ppm)	48,3	33,9	44,8	37,1	42,2	13,9	13,2	14,0	12,4	10,7	24,5	16,3	14,1	14,2	14,7	25,9	29,9	39,8	35,4	26,5	13,7	1,75	1,02	4,59	28,0
Ba (ppm)	316	167	241	227	252	36,3	36,6	36,1	38,6	32,5	243	123	73,4	101	85,2	103	195	293	153	174	1758	231	454	2517	6227
La (ppm)		0,08	0,11	0,08	0,09	0,04	-	-	-	-	-	0,85	-	0,03	-	0,08	0,06	0,08	0,12	0,06	0,18	0,22	0,11	0,04	0,32
Ce (ppm)	0,35	0,24	0,34	0,37	0,27	0,03	0,04	0,07	0,04	0,03	0,11	0,06	0,04	0,06	0,04	0,27	0,15	0,19	0,54	0,18	0,34	0,42	0,23	0,07	0,50
Nd (ppm)	0,72	0,53	0,66	0,95	0,68	-	-	-	-	-	-	-	-	-	-	0,59	-	0,39	1,26	0,36	-	0,17	-	-	-
Sm (ppm)	0,79	0,52	0,75	0,96	0,72	-	-	-	-	-	-	-	-	-	-	0,68	-	-	1,31	0,37	-	-	-	-	-
Gd (ppm)	1,53	1,12	1,35	1,95	1,49	-	-	-	-	-	-	-	-	-	-	1,22	0,57	0,73	2,71	0,72	-	-	-	-	-
Dy (ppm)	0,75	0,48	0,55	1,14	0,73	-	-	-	-	-	-	-	-	-	-	0,55	0,27	-	1,18	0,34	-	-	-	-	-
Er (ppm)	-	-	-	0,38	-	-	-	-	-	-	-	-	-	-	-	0,20	-	-	0,33	-	-	-	-	-	-
Yb (ppm)	-	-	-	-	-	-	-	-	-	-	-	-	-	-	-	-	-	-	-	-	-	-	-	-	-
Th (ppm)	-	-	-	-	-	-	-	-	-	-	-	-	-	-	-	-	-	-	-	-	-	-	-	-	-
U (ppm)	0,12	0,15	0,13	0,12	0,13	0,14	0,13	0,13	0,11	0,13	-	-	-	-	-	0,14	0,13	0,16	0,18	0,13	-	-	-	-	-
Mo (ppm)	3,18	2,41	2,89	2,53	2,74	1,51	1,61	1,64	1,73	1,39	3,56	2,32	1,77	2,15	1,91	2,43	3,17	3,73	3,12	2,61	5,95	0,87	2,92	32,5	45,8
W (ppm)	197	131	201	131	174	31,4	34,2	30,2	32,0	29,5	39,6	19,3	13,2	18,2	16,9	80,3	110	158	145	79,1	154	22,6	72,6	620	938
Re (ppm)	-	-	-	-	-	-	-	-	-	-	-	-	-	-	-	-	-	-	-	-	-	-	-	-	-
V (ppm)	-	-	0,24	-	-	-	-	-	-	-	-	-	-	-	-	-	-	-	-	-	0,20	0,20	-	0,19	0,58
Cr (ppm)	-	-	-	-	-	-	3,09	3,46	3,13	2,96	-	-	-	-	-	-	-	-	-	-	-	1,73	-	-	8,03
Co (ppm)	0,69	0,41	0,64	0,52	0,64	0,21	0,21	0,20	0,21	0,18	0,41	0,25	0,17	0,23	0,19	0,25	0,35	0,47	0,33	0,30	1,41	0,25	0,32	4,61	8,10
Ni (ppm)	2,28	1,49	2,14	1,63	1,86	0,40	0,44	0,53	0,46	0,40	1,22	0,58	0,37	0,53	0,51	0,84	1,11	1,60	1,25	0,92	0,60	-	0,38	2,24	6,45
Cu (ppm)	0,38	0,29	0,37	0,35	0,46	0,33	0,24	0,28	0,27	0,34	0,72	0,36	0,22	0,28	0,27	0,20	0,29	0,32	0,21	0,29	0,87	0,49	0,44	0,87	5,10
Zn (ppm)	1213	746	1108	815	1032	251	327	248	292	278	658	385	265	326	280	486	663	949	785	572	53,2	11,1	11,0	69,9	199
Ag (ppm)	-	-	-	-	-	-	-	-	-	-	-	-	-	-	-	-	-	-	-	-	-	-	-	-	-
Cd (ppm)	-	-	-	-	-	-	-	-	-	-	-	-	-	-	-	-	-	-	-	-	-	-	-	-	-
Ga (ppm)	1,25	0,77	1,21	0,88	1,15	0,74	0,81	0,70	0,70	0,64	0,67	0,41	0,27	0,32	0,37	0,91	1,18	1,75	1,64	0,81	1,21	0,29	0,21	1,10	4,29
Sn (ppm)	-	-	-	-	-	-	-	-	-	-	2,85	1,05	-	-	-	-	4,33	-	-	-	-	-	-	-	-
Tl (ppm)	4,39	2,49	3,47	2,79	3,70	1,96	2,85	1,90	2,36	3,26	2,57	1,71	1,46	1,60	1,42	1,65	2,20	2,82	2,18	1,91	21,0	2,37	5,36	36,2	108
Pb (ppm)	203	132	228	308	265	6,14	6,43	5,35	6,54	5,50	9,30	4,08	3,13	4,76	4,55	138	60,6	79,9	473	87,7	3,82	1,74	3,48	7,00	13,1
Bi (ppm)	-	-	-	-	-	-	-	-	-	-	-	-	-	-	-	-	-	-	-	-	-	-	-	-	-
Ge (ppm)	80,0	46,9	68,0	52,6	64,2	19,3	24,2	20,3	22,0	20,4	42,0	24,2	16,8	21,0	18,8	26,8	38,0	53,0	39,4	32,5	13,9	2,13	2,31	12,1	44,0
B (ppm)	59,7	44,3	51,8	48,1	53,5	49,8	61,2	49,3	51,1	67,8	42,9	37,8	34,9	36,8	36,4	31,9	41,9	43,6	38,3	35,9	167	39,5	27,7	96,2	392
Sb (ppm)	727	590	853	553	655	122	144	130	143	131	228	118	74,1	93,1	89,8	567	592	843	886	477	25,0	3,75	6,47	47,5	132
Au (ppm)	-	-	-	-	-	-	-	-	-	-	-	-	-	-	-	-	-	-	-	-	-	-	-	-	-
Hg (ppm)	-	-	-	-	-	-	-	-	-	-	-	-	-	-	-	-	-	-	-	-	-	-	-	-	-
Mn (ppm)	1391	1004	1214	1114	1207	677	721	705	722	640	1005	753	690	748	690	636	839	969	780	758	50362	6368	13577	116294	319428
Sr (ppm)	1056	842	989	935	969	709	680	690	693	637	919	787	761	767	767	788	828	941	824	815	2891	1393	1448	3454	8405
As (ppm)	46121	39740	40889	42472	42193	55220	68982	53767	61393	71204	46115	46906	47132	47034	42880	40810	47173	53536	42374	48138	8871	925	1022	5106	18920
Cl (ppm)	-	-	-	-	-	-	-	-	-	-	-	-	-	-	-	-	-	-	-	-	-	-	-	-	-

	EAST ZONE																								
Element	JR-23A-HA-1	JR-23A-HA-2	JR-23A-HA-3	JR-23A-HA-4	JR-23A-HA-5	JR-23A-HB-1	JR-23A-HB-2	JR-23A-HB-3	JR-23A-HB-4	JR-23A-HB-5	JR-23A-HC-1	JR-23A-HC-2	JR-23A-HC-3	JR-23A-HC-4	JR-23A-HC-5	JR-23A-HD-1	JR-23A-HD-2	JR-23A-HD-3	JR-23A-HD-4	JR-23A-HD-5	JR-25-HA-1	JR-25-HA-2	JR-25-HA-3	JR-25-HA-4	JR-25-HA-5
Li (ppm)	5,21	3,19	4,37	3,65	4,31	1,85	1,99	1,72	1,62	2,01	3,85	2,89	2,89	3,01	2,29	2,58	3,51	4,57	3,13	2,94	17,67	6,87	7,96	23,0	83,1
Rb (ppm)	1,07	0,62	0,78	0,82	0,93	2,99	3,29	2,34	2,60	3,47	1,86	1,34	1,21	1,34	1,26	1,18	1,41	1,85	1,52	1,26	19,8	2,96	3,03	15,1	51,7
Cs (ppm)	4,74	2,26	3,59	3,11	3,82	8,23	9,04	6,65	6,97	5,39	6,84	3,80	2,31	3,28	3,12	3,80	5,17	7,27	5,95	4,16	80,7	15,8	12,4	38,2	163
Be (ppm)	48,3	33,9	44,8	37,1	42,2	13,9	13,2	14,0	12,4	10,7	24,5	16,3	14,1	14,2	14,7	25,9	29,9	39,8	35,4	26,5	13,7	1,75	1,02	4,59	28,0
Ba (ppm)	316	167	241	227	252	36,3	36,6	36,1	38,6	32,5	243	123	73,4	101	85,2	103	195	293	153	174	1758	231	454	2517	6227
La (ppm)		0,08	0,11	0,08	0,09	0,04	-	-	-	-	-	0,85	-	0,03	-	0,08	0,06	0,08	0,12	0,06	0,18	0,22	0,11	0,04	0,32
Ce (ppm)	0,35	0,24	0,34	0,37	0,27	0,03	0,04	0,07	0,04	0,03	0,11	0,06	0,04	0,06	0,04	0,27	0,15	0,19	0,54	0,18	0,34	0,42	0,23	0,07	0,50
Nd (ppm)	0,72	0,53	0,66	0,95	0,68	-	-	-	-	-	-	-	-	-	-	0,59	-	0,39	1,26	0,36	-	0,17	-	-	-
Sm (ppm)	0,79	0,52	0,75	0,96	0,72	-	-	-	-	-	-	-	-	-	-	0,68	-	-	1,31	0,37	-	-	-	-	-
Gd (ppm)	1,53	1,12	1,35	1,95	1,49	-	-	-	-	-	-	-	-	-	-	1,22	0,57	0,73	2,71	0,72	-	-	-	-	-
Dy (ppm)	0,75	0,48	0,55	1,14	0,73	-	-	-	-	-	-	-	-	-	-	0,55	0,27	-	1,18	0,34	-	-	-	-	-
Er (ppm)	-	-	-	0,38	-	-	-	-	-	-	-	-	-	-	-	0,20	-	-	0,33	-	-	-	-	-	-
Yb (ppm)	-	-	-	-	-	-	-	-	-	-	-	-	-	-	-	-	-	-	-	-	-	-	-	-	-
Th (ppm)	-	-	-	-	-	-	-	-	-	-	-	-	-	-	-	-	-	-	-	-	-	-	-	-	-
U (ppm)	0,12	0,15	0,13	0,12	0,13	0,14	0,13	0,13	0,11	0,13	-	-	-	-	-	0,14	0,13	0,16	0,18	0,13	-	-	-	-	-
Mo (ppm)	3,18	2,41	2,89	2,53	2,74	1,51	1,61	1,64	1,73	1,39	3,56	2,32	1,77	2,15	1,91	2,43	3,17	3,73	3,12	2,61	5,95	0,87	2,92	32,5	45,8
W (ppm)	197	131	201	131	174	31,4	34,2	30,2	32,0	29,5	39,6	19,3	13,2	18,2	16,9	80,3	110	158	145	79,1	154	22,6	72,6	620	938
Re (ppm)	-	-	-	-	-	-	-	-	-	-	-	-	-	-	-	-	-	-	-	-	-	-	-	-	-
V (ppm)	-	-	0,24	-	-	-	-	-	-	-	-	-	-	-	-	-	-	-	-	-	0,20	0,20	-	0,19	0,58
Cr (ppm)	-	-	-	-	-	-	3,09	3,46	3,13	2,96	-	-	-	-	-	-	-	-	-	-	-	1,73	-	-	8,03
Co (ppm)	0,69	0,41	0,64	0,52	0,64	0,21	0,21	0,20	0,21	0,18	0,41	0,25	0,17	0,23	0,19	0,25	0,35	0,47	0,33	0,30	1,41	0,25	0,32	4,61	8,10
Ni (ppm)	2,28	1,49	2,14	1,63	1,86	0,40	0,44	0,53	0,46	0,40	1,22	0,58	0,37	0,53	0,51	0,84	1,11	1,60	1,25	0,92	0,60	-	0,38	2,24	6,45
Cu (ppm)	0,38	0,29	0,37	0,35	0,46	0,33	0,24	0,28	0,27	0,34	0,72	0,36	0,22	0,28	0,27	0,20	0,29	0,32	0,21	0,29	0,87	0,49	0,44	0,87	5,10
Zn (ppm)	1213	746	1108	815	1032	251	327	248	292	278	658	385	265	326	280	486	663	949	785	572	53,2	11,1	11,0	69,9	199
Ag (ppm)	-	-	-	-	-	-	-	-	-	-	-	-	-	-	-	-	-	-	-	-	-	-	-	-	-
Cd (ppm)	-	-	-	-	-	-	-	-	-	-	-	-	-	-	-	-	-	-	-	-	-	-	-	-	-
Ga (ppm)	1,25	0,77	1,21	0,88	1,15	0,74	0,81	0,70	0,70	0,64	0,67	0,41	0,27	0,32	0,37	0,91	1,18	1,75	1,64	0,81	1,21	0,29	0,21	1,10	4,29
Sn (ppm)	-	-	-	-	-	-	-	-	-	-	2,85	1,05	-	-	-	-	4,33	-	-	-	-	-	-	-	-
Tl (ppm)	4,39	2,49	3,47	2,79	3,70	1,96	2,85	1,90	2,36	3,26	2,57	1,71	1,46	1,60	1,42	1,65	2,20	2,82	2,18	1,91	21,0	2,37	5,36	36,2	108
Pb (ppm)	203	132	228	308	265	6,14	6,43	5,35	6,54	5,50	9,30	4,08	3,13	4,76	4,55	138	60,6	79,9	473	87,7	3,82	1,74	3,48	7,00	13,1
Bi (ppm)	-	-	-	-	-	-	-	-	-	-	-	-	-	-	-	-	-	-	-	-	-	-	-	-	-
Ge (ppm)	80,0	46,9	68,0	52,6	64,2	19,3	24,2	20,3	22,0	20,4	42,0	24,2	16,8	21,0	18,8	26,8	38,0	53,0	39,4	32,5	13,9	2,13	2,31	12,1	44,0
B (ppm)	59,7	44,3	51,8	48,1	53,5	49,8	61,2	49,3	51,1	67,8	42,9	37,8	34,9	36,8	36,4	31,9	41,9	43,6	38,3	35,9	167	39,5	27,7	96,2	392
Sb (ppm)	727	590	853	553	655	122	144	130	143	131	228	118	74,1	93,1	89,8	567	592	843	886	477	25,0	3,75	6,47	47,5	132
Au (ppm)	-	-	-	-	-	-	-	-	-	-	-	-	-	-	-	-	-	-	-	-	-	-	-	-	-
Hg (ppm)	-	-	-	-	-	-	-	-	-	-	-	-	-	-	-	-	-	-	-	-	-	-	-	-	-
Mn (ppm)	1391	1004	1214	1114	1207	677	721	705	722	640	1005	753	690	748	690	636	839	969	780	758	50362	6368	13577	116294	319428
Sr (ppm)	1056	842	989	935	969	709	680	690	693	637	919	787	761	767	767	788	828	941	824	815	2891	1393	1448	3454	8405
As (ppm)	46121	39740	40889	42472	42193	55220	68982	53767	61393	71204	46115	46906	47132	47034	42880	40810	47173	53536	42374	48138	8871	925	1022	5106	18920
Cl (ppm)	-	-	-	-	-	-	-	-	-	-	-	-	-	-	-	-	-	-	-	-	-	-	-	-	-

		EAST ZONE															
Element		JR-25-HB-1	JR-25-HB-2	JR-25-HB-3	JR-25-HB-4	JR-25-HB-5	JR-25-HC-1	JR-25-HC-2	JR-25-HC-3	JR-25-HC-4	JR-25-HC-5	JR-25-HC-6	JR-25-HD-1	JR-25-HD-2	JR-25-HD-3	JR-25-HD-4	JR-25-HD-5
Li	(ppm)	8,83	11,6	18,7	8,07	20,3	5,59	10,0	10,9	12,3	15,8	13,7	12,3	6,08	3,55	8,71	7,33
Rb	(ppm)	4,87	10,4	17,1	3,31	18,6	0,38	1,98	1,50	0,75	0,59	1,00	2,34	4,72	1,52	2,92	8,32
Cs	(ppm)	15,7	33,0	56,2	9,43	53,3	0,73	8,51	7,15	2,84	1,90	4,29	17,5	34,7	9,01	19,7	58,1
Be	(ppm)	2,91	5,92	9,90	1,76	9,12	-	-	0,97	0,76	-	-	-	-	-	-	-
Ba	(ppm)	283	1087	1601	208	2424	45,5	37,1	40,3	38,5	33,2	65,06	1,94	9,69	7,19	3,23	6,01
La	(ppm)	-	0,08	0,14	0,01	0,14	-	-	-	-	-	-	-	-	-	0,06	-
Ce	(ppm)	0,04	0,17	0,26	0,02	0,29	-	-	-	-	-	-	0,40	-	-	0,13	-
Nd	(ppm)	-	-	-	-	-	-	-	-	-	-	-	-	-	-	-	-
Sm	(ppm)	-	-	-	-	-	-	-	-	-	-	-	-	-	-	-	-
Gd	(ppm)	-	-	-	-	-	-	-	-	-	-	-	-	-	-	-	-
Dy	(ppm)	-	-	-	-	-	-	-	-	-	-	-	-	-	-	-	-
Er	(ppm)	-	-	-	-	-	-	-	-	-	-	-	-	-	-	-	-
Yb	(ppm)	-	-	-	-	-	-	-	-	-	-	-	-	-	-	-	-
Th	(ppm)	-	-	-	-	-	-	-	-	-	-	-	-	-	-	0,04	
U	(ppm)	-	-	-	-	-	-	-	-	-	-	-	-	-	-	-	-
Mo	(ppm)	7,37	7,52	11,4	6,44	22,4	-	-	-	-	-	0,36	-	-	-	-	-
W	(ppm)	49,0	123	182	49,0	347	-	0,42	0,37	0,79	0,67	3,10	-	-	-	-	-
Re	(ppm)	-	-	-	-	-	-	-	-	-	-	-	-	-	-	-	-
V	(ppm)	-	0,15	0,19	-	0,25	-	-	-	-	-	-	-	-	-	-	-
Cr	(ppm)	-	-	-	-	2,43	-	-	1,83	2,13	-	3,56	-	-	-	-	-
Co	(ppm)	1,40	0,94	1,45	1,06	1,73	0,09	-	0,07	0,08	-	-	0,05	-	0,04	0,06	-
Ni	(ppm)	1,05	0,83	1,08	0,91	1,41	-	0,88	-	-	-	-	-	-	-	0,15	-
Cu	(ppm)	0,49	0,84	1,19	0,42	1,67	3,12	12,2	0,65	0,29	0,48	1,10	-	2,73	-	0,21	2,49
Zn	(ppm)	23,7	38,5	55,9	19,4	66,8	5,23	8,71	4,82	3,31	2,03	3,14	-	-	-	-	3,57
Ag	(ppm)	-	-	-	-	-	-	-	-	-	-	-	-	-	-	-	-
Cd	(ppm)	-	-	-	-	-	-	-	-	-	-	-	-	-	-	-	-
Ga	(ppm)	0,43	0,75	1,12	0,33	1,31	-	-	0,10	-	-	-	-	-	-	-	-
Sn	(ppm)						-	-	-	-	-	-	-	-	-	-	2,32
Tl	(ppm)	8,61	21,1	32,1	6,31	42,8	0,18	0,95	0,85	0,57	0,42	2,03	0,05	0,22	-	0,08	0,32
Pb	(ppm)	7,87	4,79	8,36	4,54	19,1	28,3	37,8	7,60	4,04	6,34	9,15	0,15	0,18	0,15	0,19	23,3
Bi	(ppm)	-	-	-	-	-	-	-	-	-	-	-	-	-	-	-	-
Ge	(ppm)	5,15	7,09	11,4	3,22	12,3	-	1,83	0,85	0,66	0,50	1,94	1,18	1,77	0,69	1,55	5,80
B	(ppm)	48,1	75,5	125	30,21	127	-	198	50,2	39,4	39,9	73,1	191	398	109	214	669
Sb	(ppm)	12,8	25,8	39,3	9,96	49,9	-	1,11	1,34	1,47	1,73	1,73	0,82	1,63	0,37	0,98	4,83
Au	(ppm)	-	-	-	-	-	-	-	-	-	-	-	-	-	-	-	-
Hg	(ppm)	-	-	-	-	-	-	-	-	-	-	-	-	-	-	-	-
Mn	(ppm)	32993	51992	78185	26391	111871	626	614	1032	1007	808	1917	14,6	43,3	9,30	19,7	68,2
Sr	(ppm)	1097	1662	2296	960	3006	1773	1542	1593	1598	1522	1276	2402	2168	2535	3153	1686
As	(ppm)	2308	3466	5884	1282	5667	544	1006	1040	775	677	600	65,0	161	74,6	56,3	149
Cl	(ppm)	-	-	-	-	-	-	-	-	-	-	-	-	-	-	-	-

APPENDIX III: LIST OF CODE NUMBER

Table A6 Samples Archived in the Geological Collection, School of Environment. the University of Auckland.

AU Rock Number	Field Number	Rock Name
68044	JR-01	Travertine
68045	JR-02	Travertine
68046	JR-03	Travertine
68047	JR-04	Travertine
68048	JR-05	Travertine
68049	JR-06	Gypsum
68050	JR-07	Travertine
68051	JR-08	Travertine
68052	JR-09	Chert
68053	JR-10A	Travertine
68054	JR-10B	Travertine
68055	JR-10C	Travertine
68056	JR-11	Travertine
68057	JR-12	Travertine
68058	JR-14	Travertine
68059	JR-15	Travertine

AU Rock Number	Field Number	Rock Name
68060	JR-16	Travertine
68061	JR-17	Travertine
68062	JR-18	Travertine
68063	JR-19A	Travertine
68064	JR-19B	Travertine
68065	JR-20A	Jarosite
68066	JR-20B	Jarosite
68067	JR-21A	Jarosite
68068	JR-21B	Jarosite
68069	JR-22	Chert
68070	JR-23A	Travertine
68071	JR-23B	Travertine
68072	JR-24	Gypsum
68073	JR-25A	Travertine
68074	JR-25B	Travertine
68075	JR-26	Travertine